UNRAVELLING ELECTRONIC STRUCTURE IN MODULATING FUNCTIONAL PROPERTIES OF MATERIALS FOR ENERGY APPLICATIONS

PREETI BHUMLA

DEPARTMENT OF PHYSICS
INDIAN INSTITUTE OF TECHNOLOGY DELHI
NOVEMBER 2023

UNRAVELLING ELECTRONIC STRUCTURE IN MODULATING FUNCTIONAL PROPERTIES OF MATERIALS FOR ENERGY APPLICATIONS

by

PREETI BHUMLA

Department of Physics

Submitted

in fulfillment of the requirements of the degree of Doctor of Philosophy

to the

INDIAN INSTITUTE OF TECHNOLOGY DELHI

NOVEMBER 2023

Dedicated to my beloved parents

Certificate

This is to certify that the thesis entitled "**Unravelling Electronic Structure in Modulating Functional Properties of Materials for Energy Applications**," being submitted by **Preeti Bhumla** to the Indian Institute of Technology Delhi for the award of the degree of **Doctor of Philosophy** in Physics, is a record of bonafide research work carried out by her under my supervision and guidance. She has fulfilled the requirements for the submission of the thesis, which, to the best of my knowledge, has reached the required standard. The material contained in the thesis has not been submitted in part or in full to any other university or institute for the award of any degree or diploma.

Prof. Saswata Bhattacharya
Thesis Supervisor
Department of Physics,
Indian Institute of Technology Delhi,
Hauz Khas, New Delhi 110016, India.
Date:.....
Place: New Delhi

Acknowledgments

First and foremost, I would like to extend my deepest gratitude and heartfelt appreciation to my thesis advisor, Prof. Saswata Bhattacharya, for his unwavering support and guidance. He introduced me to the world of computational physics and has been a constant source of inspiration throughout my academic journey. His scientific acumen, intuitive insights, expert guidance and passion for physics have played a pivotal role in my growth as a student and researcher. He always had faith in my abilities, which motivated me to choose a career in research, for which I am sincerely thankful. I would like to acknowledge his invaluable assistance in enhancing my presentation and scientific writing skills.

I would like to thank all my colleagues and collaborators from our dynamic research group, DISCERE (DISCovering Electronic CorRElation): Dr. Shikha Saini, Dr. Pooja Basera, Dr. Ekta Arora, Dr. Arunima Singh, Dr. Deepika Gill, Dr. Manjari Jain, Sajjan Sheoran, Ankita Phutela, Sanchi Monga, Ruman Moulik, Riya Gupta, Shantanu Pathak and Divyanshi Tyagi for their constant motivation and support. Their encouragement, love and affection have greatly contributed to my personal and professional development.

I would also like to thank my other collaborators: Prof. Venkat Krishnan, Prof. Sreedevi Upadhyayula, Dr. Ashutosh Kumar, Dr. Shailesh Pathak and Dr. Hushan Chand for fruitful discussions and collaborations.

I am grateful to the Indian Institute of Technology Delhi (IIT Delhi) for providing me all the necessary facilities to carry out my research and providing travel grant for participating in conferences. I am thankful to University Grants Comission (UGC) and Council for Scientific and Industrial Research (CSIR) for funding my research and conference travel.

I would like to take this opportunity to thank my student research committee members: Prof. J. P. Singh, Prof. Hemant K. Kashyap and Prof. Rohit Narula for their evaluation of my research work from time to time. Their intriguing questions and invaluable comments have guided me

to look deeper into the problems.

A special thanks to my friends– Dimple, Pratiksha, Rekha, Rimple, Shakti, Mohit, and Arjun for being with me through thick and thin, constantly supporting me. I wish you all the best.

I will forever be indebted to my parents and brother for their unconditional love, support, and encouragement. This thesis would not have been possible without them. I deeply appreciate all the sacrifices and hardships they endured for my sake. I am thankful for everything they have done, and no words can truly convey my feelings. So, I humbly refrain from attempting to capture them in writing.

Most importantly, I would like to thank myself for not giving up and for persevering through difficult times. I heartily congratulate myself on the completion of my Ph.D. degree.

Lastly, I would like to thank almighty for his blessings, seek forgiveness for any mistakes, and request strength for what lies ahead.

Preeti Bhumla

Abstract

Energy materials encompass a wide range of materials crucial for various energy-related processes, including energy generation, storage, and transformation. With the world facing an ever-increasing need for energy resources, the advancement and utilization of energy materials are paramount for ensuring a sustainable future. Here, we study–catalysts for methane activation and hydrogen production, and perovskites for solar cells and thermoelectric devices.

Methane is a potent greenhouse gas, making its conversion into valuable products essential. However, the efficient activation of methane poses a significant challenge due to its strong C-H bonds (4.5 eV), low polarizability, and negligible electron affinity. To circumvent this challenge, an appropriate catalyst is required. In view of this, we study the transition metal, Ni_4 in a reactive atmosphere of O_2 and CH_4 gas. It adsorbs these gases and form intermediate phases $[Ni_4O_x(CH_4)_y]$. We examine the thermodynamic stability of these phases at finite temperatures and pressures using *ab initio* atomistic thermodynamics (*ai*AT). Additionally, to account for anharmonicity in the vibrational free energy contribution to the configurational entropy, we employ thermodynamic integration method. The inclusion of anharmonic effects proves crucial in detecting the activation of the C-H bond.

After this, we explore the perovskite materials for energy applications. Lead halide perovskites have gained considerable attention due to their unique characteristics in optoelectronics and spintronics. We study inorganic $CsPbF_3$ perovskite in terms of its spintronic applications. The presence of spin-orbit coupling (SOC) arising from lead (Pb) in the non-centrosymmetric phase of $CsPbF_3$ indicates the possibility of Rashba-Dresselhaus (RD) splitting within this material. We investigate this RD splitting and reversible spin textures in $R3c$ phase employing the perturbative ***k.p*** formalism alongside first-principles calculations. Subsequently, we investigate the vacancy-ordered double perovskites (VODPs) and their prospective applications in optoelectronics and thermoelectrics. These VODPs exhibit bandgaps in the visible region, making them promising candidates for optoelectronic devices. Notably, they possess

ultralow thermal conductivity, rendering them appealing for thermoelectric applications. In our work, we thoroughly investigate the thermoelectric properties of these VODPs. Furthermore, we enhance the thermoelectric characteristics of the GeTe semiconductor by manipulating its electronic structure and lattice dynamics through doping.

We employ a robust methodological approach that integrates different levels of theories combined into one multi-scale simulation to address the various properties of materials. In this thesis, the state-of-the-art methodologies utilized to obtain the desired objectives are: (i) density functional theory (DFT) for ground-state properties, (ii) cascade genetic algorithm (cGA) to determine global minimum structures (ii) *ab initio* atomistic thermodynamics to predict the stability, (iii) many-body perturbation theory (GW) for excited-state properties, (iv) climbing image nudged elastic band (CINEB) method to calculate activation energies, and (v) boltzmann transport theory to compute thermoelectric properties.

सार

ऊर्जा सामग्री में ऊर्जा उत्पादन, भंडारण और परिवर्तन सहित विभिन्न ऊर्जा-संबंधित प्रक्रियाओं के लिए महत्वपूर्ण सामग्रियों की एक विस्तृत श्रृंखला शामिल है। दुनिया को ऊर्जा संसाधनों की लगातार बढ़ती आवश्यकता का सामना करने के साथ, एक स्थायी भविष्य सुनिश्चित करने के लिए ऊर्जा सामग्रियों की उन्नति और उपयोग सर्वोपरि है। यहां, हम मीथेन सक्रियण और हाइड्रोजन उत्पादन के लिए उत्प्रेरक, और सौर कोशिकाओं और थर्मोइलेक्ट्रिक उपकरणों के लिए पेरोव्स्काइट्स का अध्ययन करते हैं।

मीथेन एक शक्तिशाली ग्रीनहाउस गैस है, जिसका मूल्यवान उत्पादों में रूपांतरण आवश्यक है। हालाँकि, मीथेन का कुशल सक्रियण इसके मजबूत सी-एच बांड (4.5 ईवी), कम ध्रुवीकरण और नगण्य इलेक्ट्रॉन बंधुता के कारण एक महत्वपूर्ण चुनौती पेश करता है। इस चुनौती से निपटने के लिए एक उपयुक्त उत्प्रेरक की आवश्यकता है। इसे देखते हुए, हम O_2 और CH_4 गैस के प्रतिक्रियाशील वातावरण में संक्रमण धातु, Ni_4 का अध्ययन करते हैं। यह इन गैसों को सोख लेता है और मध्यवर्ती चरण $[Ni_4O_x(CH_4)_y]$ बनाता है। हम एब इनिटियो एटमिस्टिक थर्मोडायनामिक्स (एआईएटी) का उपयोग करके सीमित तापमान और दबाव पर इन चरणों की थर्मोडायनामिक स्थिरता की जांच करते हैं। इसके अतिरिक्त, कॉन्फ़िगरेशन एन्ट्रापी में कंपन मुक्त ऊर्जा योगदान में असंगतता को ध्यान में रखते हुए, हम थर्मोडायनामिक एकीकरण विधि को नियोजित करते हैं। सी-एच बांड की सक्रियता का पता लगाने में एनार्मोनिक प्रभावों का समावेश महत्वपूर्ण साबित होता है।
इसके बाद, हम ऊर्जा अनुप्रयोगों के लिए पेरोव्स्काइट सामग्रियों का पता लगाते हैं। ऑप्टोइलेक्ट्रॉनिक्स और स्पिंट्रोनिक्स में अपनी अनूठी विशेषताओं के कारण लेड हैलाइड पेर-ओव्स्काइट्स ने काफी ध्यान आकर्षित किया है। हम इसके स्पिंट्रोनिक अनुप्रयोगों के संदर्भ में अकार्बनिक $CsPbF_3$ पेरोव्स्काइट का अध्ययन करते हैं। $CsPbF_3$ के गैर-सेंट्रोसिमेट्रिक चरण में लेड (Pb) से उत्पन्न होने वाली स्पिन-ऑर्बिट युग्मन (SOC) की उपस्थिति इस सामग्री के भीतर रशबा-ड्रेसलहाउस (RD) के विभाजन की संभावना को इंगित करती है। हम आर3सी चरण में इस आरडी विभाजन और प्रतिवर्ती स्पिन बनावट की जांच करते हैं, जिसमें पहले-सिद्धांतों की गणना के साथ-साथ गड़बड़ी केपी औपचारिकता को नियोजित किया जाता है। इसके बाद, हम रिक्ति-आदेशित डबल पेरोव्स्काइट्स (वीओडीपी) और ऑप्टोइलेक्ट्रॉनिक्स और थर्मोइलेक्ट्रिक्स में उनके संभावित अनुप्रयोगों की जांच करते हैं। ये वीओडीपी दृश्य क्षेत्र में बैंडगैप प्रदर्शित करते हैं, जिससे वे ऑप्टोइलेक्ट्रॉनिक उपकरणों के लिए आशाजनक उम्मीदवार बन जाते हैं। विशेष रूप से, उनमें अल्ट्रालो तापीय चालकता होती है, जो उन्हें थर्मोइलेक्ट्रिक अनुप्रयोगों के लिए आकर्षक बनाती है। अपने काम में, हम इन वीओडीपी के थर्मोइलेक्ट्रिक गुणों की गहन जांच करते हैं। इसके अलावा, हम डोपिंग के माध्यम से इसकी इलेक्ट्रॉनिक संरचना और जाली गतिशीलता में हेरफेर करके GeTe सेमीकंडक्टर की थर्मोइलेक्ट्रिक विशेषताओं को बढ़ाते हैं।

हम एक मजबूत पद्धतिगत दृष्टिकोण अपनाते हैं जो सामग्रियों के विभिन्न गुणों को संबोधित करने के लिए विभिन्न स्तरों के सिद्धांतों को एक बहु-स्तरीय सिमुलेशन में एकीकृत करता है। इस थीसिस में, वांछित उद्देश्यों को प्राप्त करने के लिए उपयोग की जाने वाली अत्याधुनिक पद्धतियां हैं: (i) ग्राउंड-स्टेट गुणों के लिए घनत्व कार्यात्मक सिद्धांत (डीएफटी), (ii) वैश्विक न्यूनतम संरचनाओं को निर्धारित करने के लिए कैस्केड जेनेटिक एल्गोरिदम (सीजीए)। (ii) स्थिरता की भविष्यवाणी करने के लिए एबी इनिटियो परमाणु थर्मोडायनामिक्स, (iii) उत्तेजित-अवस्था गुणों के लिए कई-शरीर गड़बड़ी सिद्धांत (जीडब्ल्यू), (iv) सक्रियण ऊर्जा की गणना करने के लिए इमेज नज्ड इलास्टिक बैंड (CINEB) पर चढ़ने की विधि, और (v) थर्मोइलेक्ट्रिक गुणों की गणना करने के लिए बोल्ट्ज़मैन परिवहन सिद्धांत।

List of Publications

1. **Preeti Bhumla**, Manish Kumar, and Saswata Bhattacharya, "Theoretical Insights into C-H Bond Activation of Methane by Transition Metal Clusters: The Role of Anharmonic Effects", Nanoscale Adv. **3**, 575 (2021).

2. **Preeti Bhumla**, Deepika Gill, Sajjan Sheoran, and Saswata Bhattacharya, "Origin of Rashba Spin-splitting and Strain Tunability in Ferroelectric Bulk $CsPbF_3$", J. Phys. Chem. Lett. **12**, 9539 (2021).

3. **Preeti Bhumla**, Manjari Jain, Sajjan Sheoran, and Saswata Bhattacharya, "Vacancy-ordered Double Perovskites Cs_2BI_6 (B = Pt, Pd, Te, Sn): An Emerging Class of Thermoelectric Material", J. Phys. Chem. Lett. **13**, 11655 (2022).

4. Ashutosh Kumar*, **Preeti Bhumla***, Duraisamy Sivaprahasam, Saswata Bhattacharya, and Nita Dragoe, "Effect of Crystal Field Engineering and Fermi Level Optimization on Thermoelectric Properties of $Ge_{1.01}Te$: Experimental Investigation and Theoretical Insight", Phys. Rev. Mater. **7**, 045402 (2023) (*Equal contribution).

5. Ashutosh Kumar, **Preeti Bhumla**, Taras Parashchuk, Saswata Bhattacharya, and Krzysztof T. Wojciechowski, "Engineering Electronic Structure and Lattice Dynamics to Achieve Enhanced Thermoelectric Performance of Mn-Sb Co-doped GeTe", Chem. Mater. **33**, 3611 (2021).

6. Ashutosh Kumar, **Preeti Bhumla**, Artur Kosonowski, Karol Wolski, Szczepan Zapotoczny, Saswata Bhattacharya, and Krzysztof T. Wojciechowski, "Synergistic Effect of Work Function and Acoustic Impedance Mismatch for Improved Thermoelectric Performance in GeTe-WC Composite", ACS Appl. Mater. Interfaces **14**, 44527 (2022).

7. Hushan Chand, Ashish Kumar*, **Preeti Bhumla***, Banavath Raju Naik, Viswanath Balakrishnan, Saswata Bhattacharya, and Venkata Krishnan, "Low-Cost Scalable Prepara-

tion of Ultrathin Boron Nanosheets and their Catalytic Application", Adv. Mater. Interf. **9**, 2200508 (2022) (*Equal contribution).

8. Shailesh Pathak, **Preeti Bhumla**, Shashank Bahri, Sreedevi Upadhyayula, Saswata Bhattacharya, "O-vacancy Mediated AB_2O_4 Type Ferrospinels for Enhanced Activity in the Sulfuric Acid Decomposition Step of the Iodine-sulfur Cycle for Hydrogen Production", J. Phys. Chem. Lett. **15**, 97 (2023).

9. Shikha Saini, Pooja Basera, Manish Kumar, **Preeti Bhumla**, and Saswata Bhattacharya, "Metastability Triggered Reactivity in Clusters at Realistic Conditions: A Case Study of N-doped (TiO_2) for Photocatalysis", J. Phys. Mater. **4**, 015001 (2020).

10. Deepika Gill, **Preeti Bhumla**, Manish Kumar, and Saswata Bhattacharya, "High-Throughput Screening for Bandgap Engineering by Sublattice Mixing of $Cs_2AgBiCl_6$ from First-Principles", J. Phys. Mater. **4**, 025005 (2021).

11. Manjari Jain, Deepika Gill, **Preeti Bhumla**, Pooja Basera, and Saswata Bhattacharya, "Theoretical Insights of Excitonic Effect in Lead Bromide Perovskites", Appl. Phys. Lett. **118**, 192103 (2021).

12. Sajjan Sheoran, Manish Kumar, **Preeti Bhumla** and Saswata Bhattacharya, "Rashba spin splitting and anomalous spin textures in the bulk ferroelectric oxide perovskite KIO_3", Mater. Adv. **3**, 4170 (2022).

13. Manjari Jain, **Preeti Bhumla**, Manish Kumar, and Saswata Bhattacharya, "Excitonic and Polaronic Effects in Lead Free Double Perovskites from Manybody Perturbation Theory", J. Phys. Chem. C **126**, 6753 (2022).

14. Sajjan Sheoran, **Preeti Bhumla** and Saswata Bhattacharya, "Emergence of cubic ordered full-plane persistent spin textures in lead-free materials", Phys. Rev. Mater. **6**, 094602 (2022).

15. Ankita Phutela, **Preeti Bhumla**, Manjari Jain, and Saswata Bhattacharya, "Exploring strong and weak topological states on isostructural substitutions in $TlBiSe_2$", Sci. Rep. **12**, 21970 (2022).

16. Arunima Singh, Manjari Jain, **Preeti Bhumla**, and Saswata Bhattacharya, "Electrocatalytic study for hydrogen evolution reaction on MoS_2/BP and MoSSe/BP in acidic media", Nanoscale Adv. **5**, 5332 (2023).

17. Megha Arya, **Preeti Bhumla**, Sajjan Sheoran, and Saswata Bhattacharya, "Rashba and Dresselhaus effects in doped methylammonium lead halide perovskite $MAPbI_3$", Phys. Chem. Chem. Phys. **26**, 10419 (2024).

18. Hushan Chand, **Preeti Bhumla**, Subhadip Goswami, Nicolo Allasia, Gianvito Vile, Saswata Bhattacharya, and Venkata Krishnan, "Facile Low-Temperature Synthesis of Novel Carbon Nitrides for Efficient Carbon Dioxide Conversion into Value-Added Chemicals" *(under review)*.

Contents

Certificate i

Acknowledgements ii

Abstract iv

List of Publications viii

List of Figures xvi

List of Tables xxiii

1 Introduction 1

1.1 Energy . . . 1

1.2 Renewable energy sources . . . 1

1.3 Energy materials . . . 4

1.3.1 Catalysis . . . 4

1.3.2 Solar cells . . . 5

1.3.3 Thermoelectricity . . . 6

1.4 Defects in solids . . . 7

1.5 Thermodynamics of point defects . . . 7

1.6 Problems and challenges . . . 9

1.7 A short overview of the thesis . . . 11

2 Theoretical methodology 15

2.1 Computer simulation . . . 15

2.2 First-principles calculation . . . 17

2.3 Many-body problem . . . 18

2.4 Time-independent many-body Schrödinger equation . . . 19
2.4.1 Born–Oppenheimer approximation . . . 20
2.4.2 The Hartree approximation . . . 21
2.4.3 The Hartree–Fock approximation . . . 23
2.5 Density functional theory (DFT) . . . 24
2.5.1 Thomas-Fermi-Dirac approximation . . . 24
2.5.2 The Hohenberg-Kohn theorems . . . 26
2.5.3 The Kohn-Sham ansatz . . . 28
2.5.4 Exchange-correlation functionals . . . 30
2.5.4.1 Local Density Approximation (LDA) . . . 31
2.5.4.2 Generalized Gradient Approximation (GGA) . . . 32
2.5.4.3 Meta-Generalized Gradient Approximation (meta-GGA) . . . 33
2.5.4.4 Hybrid functionals . . . 33
2.6 Basis set . . . 34
2.6.1 Plane waves basis set . . . 35
2.6.2 Pseudopotentials . . . 38
2.6.3 Norm-conserving pseudopotentials . . . 39
2.6.4 Ultrasoft pseudopotentials . . . 40
2.6.5 Projector augmented-wave (PAW) method . . . 40
2.7 Force theorem and geometry optimization . . . 42
2.8 Climbing image nudged elastic band (CINEB) method . . . 43
2.9 Cascade genetic algorithm (cGA) . . . 45
2.10 *Ab initio* atomistic thermodynamics (*aiAT*) . . . 47
2.10.1 Thermodynamic potentials . . . 48
2.10.2 Partition function . . . 48
2.10.3 Chemical potential . . . 50
2.11 Many-body perturbation theory (MBPT): The Green's function approach . . . 52
2.11.1 Green's function . . . 53
2.11.2 Dyson's equation . . . 56
2.11.3 *GW* approximation: Hedin's equations . . . 57
2.11.4 Implementation of the single-shot *GW* (G_0W_0) . . . 58

3 Heterogeneous catalysis in energy applications 60

3.1 Theoretical insights into C−H bond activation of methane by transition metal clusters: the role of anharmonic effects . . . 60

3.1.1 Introduction . . . 60

3.1.2 Computational methods . . . 62

3.1.3 Results and discussion . . . 65

3.1.3.1 Determination of stable phases of the $[Ni_4O_x(CH_4)_y]$ clusters 65

3.1.3.2 Comparing the role F_{vibs} in $\Delta G(T,p)$: Importance of capturing anharmonic effects . . . 68

3.1.3.3 $Ni_4O_6(CH_4)_2$ cluster: Harmonic IR vs Anharmonic IR . . . 71

3.1.3.4 $Ni_4O_7(CH_4)_2$ cluster and C−H bond activation . . . 72

3.1.4 Conclusions . . . 74

3.2 O-vacancy mediated partially inverted ferrospinels for enhanced activity in the sulfuric acid decomposition for hydrogen production . . . 75

3.2.1 Introduction . . . 75

3.2.2 Computational methods . . . 78

3.2.3 Results and discussion . . . 79

3.2.3.1 Thermodynamic stability and activation barrier . . . 79

3.2.4 Conclusions . . . 82

4 Origin of Rashba spin-splitting and strain tunability in ferroelectric bulk $CsPbF_3$ 84

4.1 Introduction . . . 84

4.2 Computational methods . . . 86

4.3 Results and discussion . . . 87

4.3.1 Crystal structure . . . 87

4.3.2 Electronic structure analysis . . . 88

4.3.3 Rashba and Dresselhaus spin-splitting in *R*3*c* phase . . . 92

4.3.4 Effect of strain on Rashba spin-splitting . . . 95

4.4 Conclusions . . . 98

5 Vacancy-ordered double perovskites Cs_2BI_6 (B = Pt, Pd, Te, Sn): an emerging class of thermoelectric materials 100

5.1 Introduction . . . 100

5.2 Computational methods . . . 102
5.3 Results and discussion . . . 103
5.3.1 Crystal structure . . . 103
5.3.2 Stability of Cs_2BI_6 (B = Pt, Pd, Te, Sn) vacancy-ordered double perovskites . . . 103
5.3.2.1 Structural stability . . . 103
5.3.2.2 Thermodynamic stability . . . 105
5.3.2.3 Mechanical stability . . . 106
5.3.3 Electronic structure analysis . . . 108
5.3.4 Thermoelectric properties of Cs_2BI_6 (B = Pt, Pd, Te, Sn) vacancy-ordered double perovskites . . . 109
5.3.5 Relation between anharmonicity and lattice thermal conductivity . . . 111
5.3.6 Conclusions . . . 115

6 Low lattice thermal conductivity and its role in thermoelectric performance of CsNaS and RbNaS alkali metal sulfides 117
6.1 Introduction . . . 117
6.2 Computational methods . . . 118
6.3 Results and discussion . . . 118
6.3.1 Dynamical stability . . . 118
6.3.2 Electronic properties . . . 120
6.3.3 Lattice thermal conductivity (κ_l) . . . 120
6.3.4 Gruneisen parameter (γ) and phonon lifetime (τ) . . . 121
6.4 Conclusions . . . 122

7 Enhancing thermoelectric properties via crystal field engineering and low thermal conductivity 123
7.1 Engineering electronic structure and lattice dynamics to achieve enhanced thermoelectric performance of Mn–Sb co-doped GeTe . . . 123
7.1.1 Introduction . . . 123
7.1.2 Computational methods . . . 124
7.1.3 Results and discussion . . . 125
7.1.3.1 Electronic structure . . . 125

7.1.3.2 Lattice thermal conductivity (κ_{ph}) . . . 129
7.1.4 Conclusions . . . 130
7.2 Effect of crystal field engineering and Fermi level optimization on thermoelectric properties of $Ge_{1.01}Te$ . . . 131
7.2.1 Introduction . . . 131
7.2.2 Computational methods . . . 133
7.2.3 Results and discussion . . . 133
7.2.3.1 Electronic properties . . . 133
7.2.3.2 Thermoelectric properties . . . 137
7.2.3.3 Phonon dispersion calculation . . . 139
7.2.4 Conclusions . . . 140

8 Epilogue and outlook 142

List of Figures

1.1 Global energy consumption in 2019. 2

1.2 Different energy materials as alternatives to conventional fuels. 4

1.3 Energy materials studied in the present work. 5

1.4 Seebeck effect. 6

1.5 Challenges encountered in calculating the different properties of materials. . . . 9

1.6 Overview of the thesis. 12

2.1 Multi-scale simulation in different length and time scales. 16

2.2 Schematic representation of mapping of interacting system to a non-interacting many-electron system through the same ground-state electron density. 28

2.3 Flow chart to solve the Kohn-Sham equations self-consistently. 30

2.4 Jacob's ladder of density functional approximations. 32

2.5 Schematic representation of pseudopotential technique. The all-electron wave function corresponding to Coulomb potential is shown by red color. The pseudo wave function corresponding to pseudopotential is shown by blue color. 38

2.6 Schematic diagram to show the various forces acting on the elastic band during the optimization. 44

2.7 Flow chart of cascade genetic algorithm. 46

2.8 Schematic representation of excited-state spectroscopies, namely, direct photoemission, inverse photoemission, and optical absorption. Here, IP and EA represent the ionization potential and electron affinity, respectively. Also, E_N is the total energy of N-electron system. Moreover, $E_g^{GW} = IP - EA$ is the quasiparticle (QP) band gap and $E_g^{BSE} = IP - EA - E_B$ is the optical band gap, where E_B is the exciton binding energy. 53

2.9 Schematic representation of spectral function in the case of non-interacting (electrons) single-particle excitation and interacting single-particle like (QP) excitation. 55

2.10 Illustration of a QP formation in the case of photoemission spectroscopy. 55

2.11 Schematic representation of the Dyson's equation, which relates the non-interacting (G_0) and interacting (G) Green's functions via the self-energy operator (Σ). Here, the black arrow describes the propagation of a non-interacting particle and the viloet color represents screening process of different orders. . . 57

2.12 Schematic representation of the self-consistent Hedin's equations. 58

3.1 Structures of different isomers of Ni_4O_7 clusters obtained from PBE (represented by dashed blue line) and HSE06 (represented by dashed red line) exchange-correlation (ε_{xc}) functionals. Dashed circles represent the global minima from the two functionals. 64

3.2 Histogram of aiMD simulation for $Ni_4O_6CH_4$ cluster at T = 600 K. 65

3.3 2D projection of 3D phase diagram obtained for $Ni_4O_x(CH_4)_y$ clusters in the reactive atmosphere of O_2 and CH_4. In this plot $\Delta G(T,p)$ is computed (a) when only DFT total energies are included, (b) DFT+$F_{vibs}^{harmonic}$ are included and (c) DFT+$F_{vibs}^{anharmonic}$ are included to compute $F(T)$ of respective configurations as shown in Equation 3.2. Colored regions show the most stable compositions in a wide range of pressure at T = 800 K. 68

3.4 Logarithm of probability of occurrence (in %) of $Ni_4O_7(CH_4)_2$, $Ni_4O_8CH_4$, $Ni_4O_6CH_4$ and $Ni_4O_6(CH_4)_2$ clusters in all the three cases (DFT, DFT+$F_{vibs}^{harmonic}$ and DFT+$F_{vibs}^{anharmonic}$) at (a) T = 800 K and p_{O_2} = 1 atm, p_{CH_4} = 1 atm (b) T = 800 K and $p_{O_2} = 10^{-10}$ atm, p_{CH_4} = 1 atm. 70

3.5 Infrared (IR) spectra of $Ni_4O_6(CH_4)_2$ for both harmonic (upper panel) as well as the anharmonic (lower panel) case. The possible vibrational modes are also shown corresponding to those respective peaks. 72

3.6 (a) Infrared (IR) spectra of $Ni_4O_7(CH_4)_2$ for both harmonic as well as the anharmonic case. Contour plots of electronic charge density associated with (001) plane of (b) CH_4 (delocalization of charge within C−H bonds) and (c) $Ni_4O_7(CH_4)_2$ cluster (localization of charge within C−H bonds). 73

3.7 Radial distribution function (RDF) plot at 0 K and 1000 K for (a) $FeCo_2O_4$ and $CoFe_2O_4$ clusters over SiC-Pretrt, respectively. 79

3.8 Free energy profiles for the adsorption and dissociation of SO_3 on the surfaces of $CoFe_2O_4$/SiC-Pretrt and $FeCo_2O_4$/SiC-Pretrt catalysts, respectively, were calculated using HSE06 ϵ_{xc} functional. 80

3.9 Reaction profiles for the decomposition of SO_3 with the initial state (IS), transition state (TS), and final state (FS) on (a) $CoFe_2O_4$ and (b) $FeCo_2O_4$ clusters with oxygen (O) vacancy were calculated using HSE06 ϵ_{xc} functional. Structures and charge density difference contours for SO_3 adsorbed on top of (c) $CoFe_2O_4$ and (d) $FeCo_2O_4$ clusters with O-vacancy. Cyan and yellow colors represent the negative and positive charge, respectively. 81

3.10 Projected density of states (pDOS) for (a) isolated SO_3, and SO_3, adsorbed over the cluster (b) $CoFe_2O_4$ and $FeCo_2O_4$ clusters, respectively. Here, red and blue colors correspond to O and S states, respectively. The energy range (y-axis) is the same for all figures. 82

4.1 Crystal structure of $CsPbF_3$ (a) cubic $Pm\bar{3}m$ phase and (b) rhombohedral $R3c$ phase. Cs, Pb and F atoms are indicated by red, grey and yellow colors, respectively. Phonon band structure of $CsPbF_3$ (c) cubic $Pm\bar{3}m$ phase and (d) rhombohedral $R3c$ phase. 88

4.2 Band structure of cubic $Pm\bar{3}m$ phase of $CsPbF_3$, calculated using (a) PBE (b) PBE+SOC. (c) Projected density of states (pDOS), calculated using HSE06+SOC. 89

4.3 (a) Optimized crystal structure of $CsPbF_3$ in rhombohedral $R3c$ phase. Cs, Pb and F atoms are indicated by red, grey and yellow colors, respectively. (b) The first hexagonal Brillouin zone showing the high symmetry path for band structure calculations in $R3c$ phase of $CsPbF_3$. Electronic band structure of $CsPbF_3$ for $R3c$ phase, calculated using (c) PBE (d) PBE+SOC. The conduction and valence bands considered in the discussion are indicated by orange color. (e) Schematic representation of bands showing Rashba splitting. (f) Splitting of conduction band minimum (CBm) and valence band maximum (VBM) of the chosen bands along the M-Γ-K path. The inset shows the enlarged view of Cbm. (g) Projected density of states (pDOS) in $R3c$ phase of $CsPbF_3$ calculated using HSE06+SOC. The Fermi energy is set to zero in the energy axis. 90

4.4 (a) Band structure of $R3c$ phase using G_0W_0@HSE+SOC. (b) Imaginary part (Im (ε)) of the dielectric function for $R3c$ phase of $CsPbF_3$ calculated using HSE06+SOC and G_0W_0@HSE+SOC. 91

4.5 Imaginary part (Im (ε)) of the dielectric function for $Pm\bar{3}m$ phase of $CsPbF_3$ calculated using HSE06+SOC and G_0W_0@HSE+SOC ϵ_{xc} functional, respectively. 91

4.6 Band structure of cubic $Pm\bar{3}m$ phase of $CsPbF_3$, calculated using (a) PBE+SOC (b) HSE+SOC (c) G_0W_0@HSE+SOC, respectively. 92

4.7 (a) Schematic representation of spin textures in Rashba splitting. Spin projected constant energy contour plots of spin texture calculated in k_x-k_y plane centered at Γ point. The upper and lower panels represent the spin textures calculated at constant energy: (b) $E=E_F + 2.5$ eV and (c) $E=E_F - 0.2$ eV, respectively. Electronic band structures showing spin-splitting of (d) CBm and (e) VBM around Γ point, respectively. Band structure is plotted along $(\frac{2\pi}{a}0.25, 0, 0) - (0, 0, 0) - (\frac{2\pi}{a}0.16, \frac{2\pi}{b}0.16, 0)$ direction of momentum space, which is $M - \Gamma - K$ direction. DFT and ***k.p*** band structures are plotted with dashed lines and dots, respectively. In the color scale, red depicts spin-up while blue depicts spin-down states. 93

4.8 Band structures of $CsPbF_3$ ($R3c$ phase) under uniaxial strain of $\pm 5\%$, calculated using PBE+SOC for path (a) Γ-M-K-Γ-A-L and (b) M-Γ-K. (c) Rashba spin-splitting energy (δE) (d) offset momentum (δk) (e) Rashba parameters (α_R and α_D) as a function of strain. The values are calculated for CBm in $R3c$ phase. Note that δE is same along both M-Γ and Γ-K directions. 96

4.9 (a) Climbing image nudged elastic band (CINEB) calculation for the polarization switching process in $CsPbF_3$ perovskite. Two ferroelectric (FE) structures in the ground state with opposite direction of electric polarization are shown. E_b is the activation barrier energy for the polarization switching process. Reversible in-plane spin textures calculated at constant energy E = E_F+2.5 eV with oppposite spin polarization: (b) -P (c) +P. 97

5.1 Schematic of the relationship between ABX_3 perovskite and A_2BX_6 (vacancy-ordered) double perovskite. 101

5.2 $\Delta G(T, P)$ of Cs_2BI_6 vacancy-ordered double perovskites calculated using PBE and HSE06 ε_{xc} functionals. 106

5.3 Band structures of (a) Cs_2PtI_6, (b) Cs_2PdI_6, (c) Cs_2TeI_6 and (d) Cs_2SnI_6 vacancy-ordered double perovskites, calculated using HSE06+SOC ε_{xc} functional. 108

5.4 Projected density of states (pDOS) of (a) Cs_2PtI_6, (b) Cs_2PdI_6, (c) Cs_2TeI_6 and (d) Cs_2SnI_6 vacancy-ordered double perovskites, calculated using HSE06+SOC ε_{xc} functional. 109

5.5 Seebeck coefficient (S) as a function of (a) chemical potential (μ) and (b) carrier concentration (n) at 300, 500 and 800 K. (c) Thermoelectric figure of merit (zT) as a function of temperature (T) for Cs_2PtI_6, Cs_2PdI_6, Cs_2TeI_6 and Cs_2SnI_6, calculated using HSE06 ϵ_{xc} functional. 111

5.6 Calculated (a) electronic thermal conductivity, (b) lattice thermal conductivity and (c) total thermal conductivity in Cs_2BI_6 vacancy-ordered double perovskites, calculated using PBE ε_{xc} functional. 112

5.7 Harmonic (U_h) and anharmonic energy (U_{ah}) of (a) Cs_2PtI_6 (b) Cs_2PdI_6 (c) Cs_2TeI_6 and (d) Cs_2SnI_6 as a function of temperature (T), calculated using HSE06 ϵ_{xc} functional. 113

5.8 (a) Phonon dispersion plots and (b) two dimensional ELF of (110) plane passing through Cs, Pt, Pd, Te, Sn and I atoms of Cs_2PtI_6, Cs_2PdI_6, Cs_2TeI_6 and Cs_2SnI_6, calculated using PBE ϵ_{xc} functional. The ELF values of 0.0, 0.5, and 1.0 are interpreted as absence, uniform electron gas like, and localized electrons, respectively. 114

6.1 Crystal structure of (a) CsNaS (b) RbNaS having P4/nmm symmetry. Cs, Rb, Na and S atoms are indicated by pink, green, yellow and purple colors, respectively. Phonon band structure of (a) CsNaS (b) RbNaS alkali metal sulfides. . . 119

6.2 Band structures of (a) CsNaS and (b) RbNaS, calculated using PBE ϵ_{xc} functional. 120

6.3 Lattice thermal conductivity as a function of temperature of (a) CsNaS and (b) RbNaS alkali metal sulfides. 121

6.4 Gruneisen parameter (γ) of (a) CsNaS and (b) RbNaS alkali metal sulfides. . . 122

6.5 Phonon lifetimes (τ) of (a) CsNaS and (b) RbNaS alkali metal sulfides. 122

7.1 (a) and (b) are two configurations of Mn–Sb co-doped system with different energies. 126

7.2 Electronic band structures of rhombohedral (a) $Ge_{22}Te_{24}$, (b) $Ge_{21}MnTe_{24}$, (c) $Ge_{20}MnSbTe_{24}$, and (d) $Ge_{19}MnSb_2Te_{24}$. The Ge vacancies are considered during the calculation to attest to the high carrier concentration. The band gap appears at the Γ point in a $2\times2\times2$ supercell containing 48 atoms. The VBM and CBM occur at the L point in the pristine GeTe fold onto the Γ point in the supercell. (e) Density of states of pristine GeTe ($Ge_{24}Te_{24}$), GeTe with Ge vacancies ($Ge_{22}Te_{24}$), Mn-doped GeTe ($Ge_{21}MnSb_{24}$), and Mn–Sb co-doped GeTe ($Ge_{20}MnSbTe_{24}$, $Ge_{19}MnSb_2Te_{24}$) samples. 127

7.3 Phonon dispersion curve for (a) $Ge_{24}Te_{24}$ and (b) $Ge_{21}MnSb_2Te_{24}$ in a rhombohedral structure. 128

7.4 Charge density plot for a plane with Miller indices (001) at a distance of 13Åfrom the origin for (a) $Ge_{24}Te_{24}$ showing all Ge atoms and (b) $Ge_{21}MnSb_2Te_{24}$ showing Ge and Sb atoms. 129

7.5 (a) and (b) represent two configurations of $Ge_{20}TiBi_2Te_{24}$ with different relative energies, calculated using PBE exchange-correlation functional. 134

7.6 (a) Band structure of $Ge_{25}Te_{24}$ supercell, where the principal valence band (light hole) maximum (VBM) and conduction band minimum (CBM) occur at the Γ point due to the folding of the L point onto Γ. (b) The unfolded band structure of $Ge_{25}Te_{24}$ supercell showing VBM and CBM at L point. 135

7.7 Electronic band structures of (a) $Ge_{23}Te_{24}$, (b) $Ge_{22}TiTe_{24}$, (c) $Ge_{21}TiBiTe_{24}$, and (d) $Ge_{20}TiBi_2Te_{24}$. The Ge vacancies are theoretically induced during the calculation to attest to the large experimental value of carrier concentration. The band gap appears at the Γ point in a $2 \times 2 \times 2$ supercell containing 48 atoms. The VBM and CBM occur at the L point in the pristine GeTe fold onto the Γ point in the supercell. (e) Density of states of GeTe with excess Ge ($Ge_{25}Te_{24}$), GeTe with Ge vacancies ($Ge_{23}Te_{24}$), Ti-doped GeTe ($Ge_{22}TiTe_{24}$), and Ti–Bi co-doped GeTe ($Ge_{21}TiBiTe_{24}$, $Ge_{20}TiBi_2Te_{24}$) samples. 136

7.8 (a) Electrical conductivity (σ), (b) Seebeck coefficient (α), (c) electronic thermal conductivity (κ_e), (d) power factor ($\alpha^2\sigma$), and (e) figure of merit (zT) as a function of chemical potential (μ) are calculated at 300 K for different GeTe compositions: $Ge_{23}Te_{24}$, $Ge_{22}TiTe_{24}$, $Ge_{21}TiBiTe_{24}$ and $Ge_{20}TiBi_2Te_{24}$. Electrical conductivity, Seebeck coefficient, thermal conductivity, power factor, and figure of merit are reported by scaling them with τ. 138

7.9 (a) Calculated Seebeck coefficient (α) as a function of chemical potential (μ) for different GeTe compositions at (a) 300 K, (b) 500 K, and (c) 800 K. 138

7.10 Phonon dispersion curve for (a) $Ge_{24}Te_{24}$ and (b) $Ge_{21}TiBi_2Te_{24}$ in a rhombohedral structure. 139

7.11 Charge density plot of a plane with Miller indices (001) at a distance of 9.5 Å from the origin for (a) $Ge_{25}Te_{24}$ supercell showing all Ge atoms, and (b) $Ge_{20}TiBi_2Te_{24}$ supercell showing Ge and Bi atoms. 140

List of Tables

4.1 Optimized lattice parameters of $Pm\bar{3}m$ phase, a = 4.80652 Å. 87

4.2 Optimized lattice parameters of $R3c$ phase, a = 6.80864 Å, c = 16.30620 Å. Hexagonal settings are used. 88

4.3 Band gap (in eV) of $Pm\bar{3}m$ and $R3c$ phases using different ϵ_{xc} functionals. . . 91

4.4 Rashba parameters for band-splitting at Γ point in $R3c$ phase. 94

4.5 RD parameters as a function of strain for CBm in $R3c$ phase. 98

5.1 Calculated lattice parameters (Å) of Cs_2BI_6 (B = Pt, Pd, Te, Sn) vacancy-ordered double perovskites using different exchange-correlation (ε_{xc}) functionals. 104

5.2 Goldschmidt tolerance factor (t), octahedral factor (μ) and new tolerance factor (τ) of Cs_2BI_6 vacancy-ordered double perovskites. 105

5.3 $\Delta G(T, P)$ of Cs_2BI_6 perovskites calculated using PBE and HSE06 ε_{xc} functionals 106

5.4 Calculated elastic constants C_{ij} (GPa), Bulk modulus B (GPa), Shear modulus G (GPa), Young's modulus E (GPa), Pugh's ratio B/G, Poisson's ratio ν and elastic anisotropy $\boldsymbol{A}$ of Cs_2BI_6 vacancy-ordered double perovskites. 107

5.5 Band gap (eV) of Cs_2BI_6 vacancy-ordered double perovskites calculated using different ϵ_{xc} functionals. 109

5.6 Energies (eV) of Cs_2BI_6 (B = Pt, Pd, Te, Sn) vacancy-ordered double perovskites at different k-grids calculated using PBE ε_{xc} functional. 110

5.7 Effective mass of electrons m^* in terms of rest mass of electron m_0, electronic dielectric constant ϵ_∞ and ionic static dielectric constant ϵ_{static} of Cs_2BI_6 perovskites. 115

5.8 Calculated polaron parameters corresponding to electrons in Cs_2BI_6 perovskites. ω_{LO} (THz), α_e, m_P, l_P (Å) and μ_P ($cm^2V^{-1}s^{-1}$) are the optical phonon frequency, Fröhlich coupling constant, polaron mass, polaron radii and polaron mobility, respectively. 115

7.1 Lattice parameters (a, c), c/a for $Ge_{1.01-x-y}Ti_xBi_yTe$ ($0.00 \leq x \leq 0.02$, $0.00 \leq y \leq 0.08$) at 300 K. 134

CHAPTER 1

Introduction

1.1 Energy

Energy serves as a vital driving force for the overall development of society. Presently, the world predominantly relies on fossil fuels, such as oil, coal, and natural gas for its energy supply [1, 2, 3]. The global energy consumption is illustrated in Fig. 1.1. These fossil fuels are primarily composed of hydrocarbons, which are chemical compounds consisting of carbon and hydrogen atoms. The energy within these fuels is stored in the C–H bonds. When these compounds undergo combustion in the presence of oxygen, these bonds break, releasing the stored energy in the form of heat. However, it is important to note that these fossil fuels contribute significantly to global greenhouse gas emissions, accounting for approximately one-third of the total. The increasing energy demands, coupled with the depletion of fossil fuel reserves and their associated greenhouse gas emissions, pose significant challenges. To address these challenges, a transition towards renewable energy sources is essential.

1.2 Renewable energy sources

Renewable energy is derived from natural sources that renew themselves more quickly than we use them. For instance, sunlight and wind are examples of such constantly replenishing sources. These sources of renewable energy are abundant and can be found all around us. Renewable energy sources have been recognized as a sustainable solution to mitigate the global energy shortage [4]. The cost-effectiveness, environmental friendliness, and abundant availability of renewable energy sources make them an attractive alternative for meeting energy demands. The common renewable energy sources are:

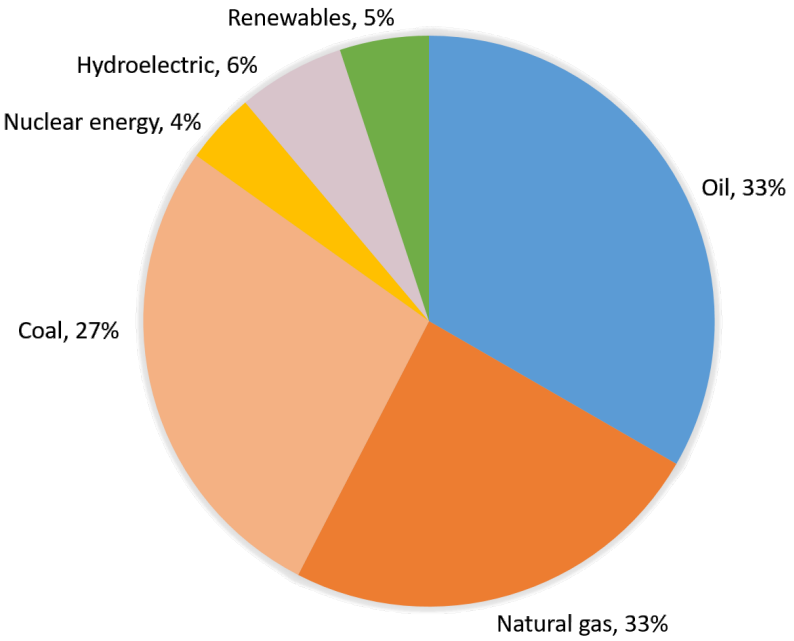

Figure 1.1: Global energy consumption in 2019.

Solar energy

Sunlight is one of the most abundant source of renewable energy received by earth. Solar technologies convert sunlight by using photovoltaics and solar cells. These cells are made from semiconductor materials. When sunlight makes contact with the cells, it ejects electrons from their atomic bonds, enabling these electrons to move through the cell, thereby generating electricity. Research has indicated that solar energy holds the potential to cater to the world's energy demands effectively, as it is a naturally abundant and freely accessible energy source without associated costs.

Hydropower

Hydropower is a source of renewable energy that harnesses the power of moving water to generate electricity. It captures the energy of water as it flows from higher to lower elevations. This energy can be derived from both reservoirs and rivers. Reservoir hydropower plants utilize stored water in a reservoir, whereas run-of-river hydropower plants make use of the natural flow of the river. Typically, a hydropower system involves the use of a dam on a river to create a large water reservoir and the stored water is then released through turbines, resulting in power generation.

Bioenergy

Bioenergy is generated from a wide range of organic materials collectively known as biomass. This includes materials like wood, charcoal, dung, and agricultural crops. Additionally, the construction and agricultural products industries, generate significant amounts of unused or residual biomass, which can also be harnessed as a source of bioenergy. The combustion of biomass does result in greenhouse gas emissions, albeit at lower levels compared to burning conventional fuels such as coal, oil, or gas.

Geothermal energy

The Earth's core can attain scorching temperatures of up to 9000^0 F. This intense heat, known as geothermal energy, radiates outward from the core, warming the surrounding layers of the Earth. As a result, underground reservoirs of hot water and steam are formed. These geothermal reservoirs can be mainly harnessed for the generation of electricity. Remarkably, the potential for geothermal energy within the uppermost 6 miles of the Earth's crust is estimated to be 50,000 times the energy contained in all the world's oil and gas resources combined.

Ocean energy

Ocean energy encompasses various forms of renewable energy derived from the sea, including thermal energy from temperature differences between surface and deep waters, mechanical energy from tides, waves, and currents, and kinetic energy from the movement of ocean water. The primary ocean technologies for harnessing this energy include wave, tidal, and ocean thermal systems. These diverse approaches collectively contribute to the utilization of the ocean's vast energy potential.

Wind energy

Wind energy involves using the kinetic energy of moving air to produce mechanical power. Wind turbines play a pivotal role in the conversion of kinetic energy into mechanical power. This mechanical energy can serve various purposes, such as grinding grain or pumping water, and it can also be converted into electricity through the operation of a generator.

1.3 Energy materials

Energy materials, in a broad sense, are materials that are essential for various forms of energy production, storage, and conversion. These materials play a vital role in generating and managing energy in different applications. As the world confronts growing energy demands and environmental challenges, the development and implementation of advanced energy materials are essential for a sustainable and prosperous future. The different energy materials are shown in Fig. 1.2.

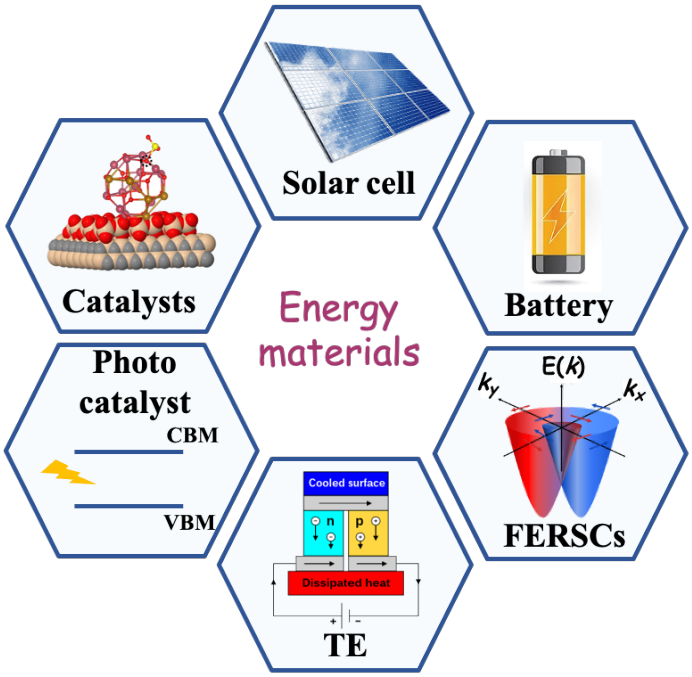

Figure 1.2: Different energy materials as alternatives to conventional fuels.

In line with this, our study explores the field of catalysis, optoelectronics, and thermoelectricity as promising avenues to cater to energy needs. Here, we focus on energy materials–catalysts for methane activation and H_2 production, perovskites for solar cells and thermoelectric devices, and these areas constitute the main topics of our thesis (see Fig. 1.3).

1.3.1 Catalysis

Catalysis is a process that involves the acceleration of a chemical reaction by a catalyst. The catalyst itself remains unchanged in terms of its chemical composition after the reaction [5]. In other words, it speeds up the reaction without being consumed or permanently altered in the process. Catalysts work by lowering the activation energy required for a chemical reaction

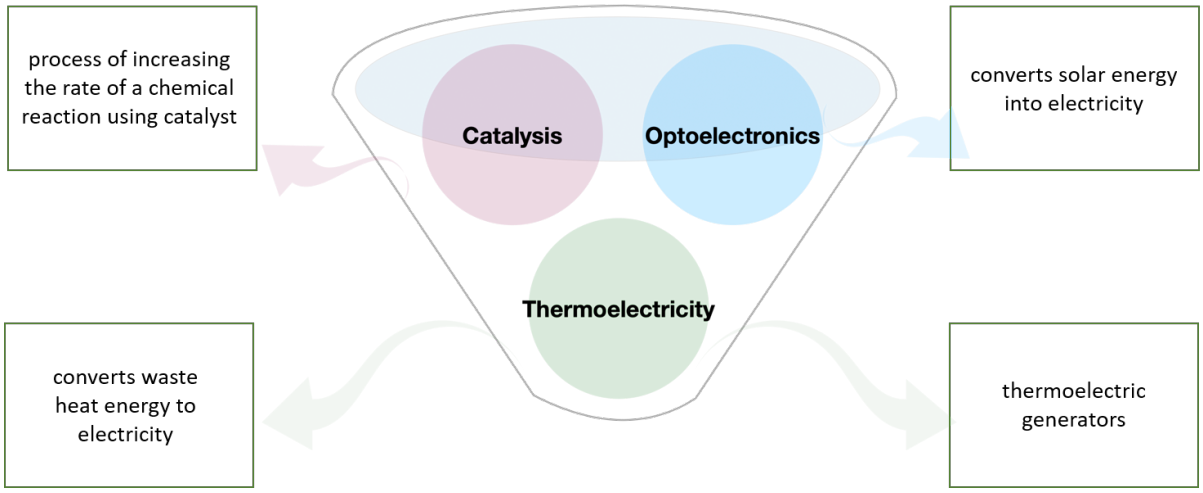

Figure 1.3: Energy materials studied in the present work.

to occur. Activation energy is the minimum energy input necessary for reactants to transform into products. By reducing this energy barrier, a catalyst enables the reaction to proceed more rapidly and efficiently. Catalysis is essential in various industrial and biological processes, as it allows for the control and optimization of chemical reactions. Typically, catalysts are categorized into three primary types:

- **Homogeneous catalysts:** These catalysts exist within the same phase as the reactants and products.
- **Heterogeneous catalysts:** These catalysts operate in a different phase from the reactants. Generally, catalysts are in solid form while reactants exist in gaseous or liquid states.
- **Enzymes and biocatalysts:** Enzyme catalysts primarily consist of proteins.

One significant advantage of heterogeneous catalysts lies in their ease of separation from reactants and products, allowing for their reuse. Furthermore, these catalysts are resilient even under extreme operating conditions, making them the preferred choice for large-scale industrial production. In this thesis, we have studied the heterogeneous catalysis for methane activation and H_2 production.

1.3.2 Solar cells

Solar cells are the devices that convert sunlight into electricity. They are a fundamental component of solar panels and are used to harness solar energy for various applications. Solar cells work based on the principle of the photovoltaic effect, which is the generation of an electric

current when certain materials are exposed to light. In this thesis, we have investigated perovskites materials regarding solar cell applications owing to their suitable optical band gap, high absorption coefficient, low trap density, and reasonable manufacturing cost.

1.3.3 Thermoelectricity

Waste heat represents a significant global concern, exerting a profound influence on the Earth's climate system. Studies indicate that over half of the energy generated is dissipated as heat, encompassing a wide spectrum from household to industrial waste heat [6, 7, 8]. Addressing waste heat and its recovery has become a critical challenge. Thermoelectricity, also known as the Seebeck effect, is one of the methods, in which electricity is generated when there is a temperature difference (ΔT) between two different materials or junctions. The phenomenon is illustrated in Fig. 1.4. Thermoelectricity has the advantage of being a solid-state technology,suggesting that it has no moving parts and is highly reliable. However, it is currently less efficient at converting heat to electricity compared to other methods, such as steam turbines. Continuous research endeavors aim to enhance the effectiveness of thermoelectric materials, catering to a broad spectrum of practical applications.

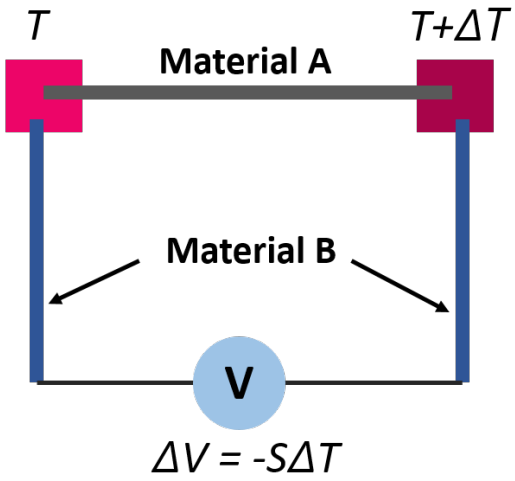

Figure 1.4: Seebeck effect.

1.4 Defects in solids

Point defects are of utmost importance in the field of semiconductors, capable of significantly altering their electronic and optical properties. Vacancies and interstitials, in particular, are intrinsic to real crystals, forming part of the normal thermal equilibrium. Often, experimental identification of these defects and their impact on various properties can be challenging. In such cases, first-principles-based theoretical investigations prove invaluable, offering a complement to experiments and serving as a predictive tool.

Even at low concentrations, defects can exert a profound influence on critical physical and chemical properties of materials, particularly those governing matter transport and its associated characteristics. Additionally, they play a pivotal role in influencing thermal conductivity through phonon scattering, electronic conduction as acceptors or donors, and optical properties by introducing electronic states with optical transitions. Point defects are instrumental in tailoring the properties of semiconductors, making them suitable for electronic, thermoelectric and optoelectronic devices. Therefore, understanding the impact of point defects on electronic and optical properties holds great significance. This methodology is widely adopted by research groups globally, and numerous textbooks and overviews on this pivotal subject are available [9, 10, 11]. In the following section, we delve into a thermodynamic formalism for point defect formation and explore the fundamental principles governing doping and alloying.

1.5 Thermodynamics of point defects

Thermodynamically, point defects are an inherent feature of crystals in thermal equilibrium. To illustrate this concept, we can take the example of a vacancy defect in a monoatomic Bravais lattice. A vacancy represents a point defect where an ion is absent from its regular lattice site. The equilibrium concentration of vacancies, denoted as n, can be determined by minimizing the relevant thermodynamic potential, which, in this case, is the Gibbs free energy G under constant pressure p conditions [12].

$$G = U - TS + pV \tag{1.1}$$

Here, U denotes the internal energy of the crystal, T is the temperature, V corresponds to the volume, and S represents the entropy. To derive the relationship between G and n, let us consider a crystal with a total of $(N+n)$ ion sites, where n represents the number of vacancies.

The volume $V(n)$ can be approximated as approximately equal to $(N+n)v_0$, where v_0 is the volume per ion in the perfect crystal. The configurational entropy S^{config}, resulting from the presence of a fixed number of vacancies, is given by:

$$S^{\text{config}} = k_{\text{B}} \ln \frac{(N+n)!}{N!n!} \tag{1.2}$$

where k_{B} is the Boltzmann constant. The Gibbs free energy is given as

$$G(n) = F_0(n) - TS^{\text{config}}(n) + p(N+n)v_0 \tag{1.3}$$

where $F_0(n) = U - TS$ is the Helmholtz free energy of the imperfect crystal consisting of n vacant sites. Utilizing Stirling's formula (for large $N, \ln N! \approx N(\ln N - 1)$) and considering $n << N$, we get

$$\frac{\partial G}{\partial n} = \frac{\partial F_0}{\partial n} + pv_0 - k_B T \ln \frac{N}{n} \tag{1.4}$$

For small n,

$$\frac{\partial F_0}{\partial n} \approx \left.\frac{\partial F_0}{\partial n}\right|_{n=0} = \mathcal{E} \tag{1.5}$$

where $\mathcal{E}$ stands as the defect formation energy and remains independent of n. Consequently, the number of vacancies that minimizes G can be expressed as:

$$n = Ne^{-(\mathcal{E}+pv_0)/k_{\text{B}}T} \tag{1.6}$$

At atmospheric pressures, the contribution of pv_0 is insignificantly small compared to E, and hence,

$$n = Ne^{-\mathcal{E}/k_{\text{B}}T} \tag{1.7}$$

Equation 1.7 suggests that point defects with lower formation energy tend to exist in higher concentrations, particularly at $T > 0$.

Point defects can arise through various mechanisms, such as thermal processes (associated with thermodynamic equilibrium growth), chemical reactions involving impurities, and exposure to radiation or mechanical damage. Hume-Rothery [13] proposed a set of empirical criteria for significant impurity solubility. One of these criteria stipulates that the atomic diameters of the impurity species and the host atom should not differ by more than 14%. Beyond this threshold, excessive lattice distortion occurs, limiting solubility. Other requirements include a small electronegativity difference between the host and guest atoms and structural similarity between the host and guest atom crystal structures.

1.6 Problems and challenges

Exploring the defect physics of semiconductors is essential for achieving optimal performance in practical applications. The initial step in this endeavor involves assessing the thermodynamic stability under realistic experimental conditions, considering factors like temperature, pressure, and Fermi level. However, even this initial phase is characterized by complexity. It's noteworthy that the free energy of formation of an isolated defect can undergo significant reduction, often by several eVs, in the presence of charge carriers within the material. The process of disentangling the relative stabilities of various types of materials is a challenging task. Subsequent to this, a detailed investigation of the electronic structure, optical properties, and the positions of band edges in the material, tailored for specific applications, becomes imperative. In this pursuit, numerous unknown parameters come into play, including the selection of an appropriate exchange-correlation functional within density functional theory (DFT) [14, 15], considerations regarding thermodynamic stability, the presence of trap states within the forbidden region, optimization of optical absorption, and identifying favorable positions of the VBM (valence band maximum) and CBm (conduction band minimum). Addressing these aspects meticulously is crucial for identifying a material that suits the intended purpose. It's worth noting that, to date, a comprehensive study encompassing all these facets, supported by a robust methodology, has been missing.

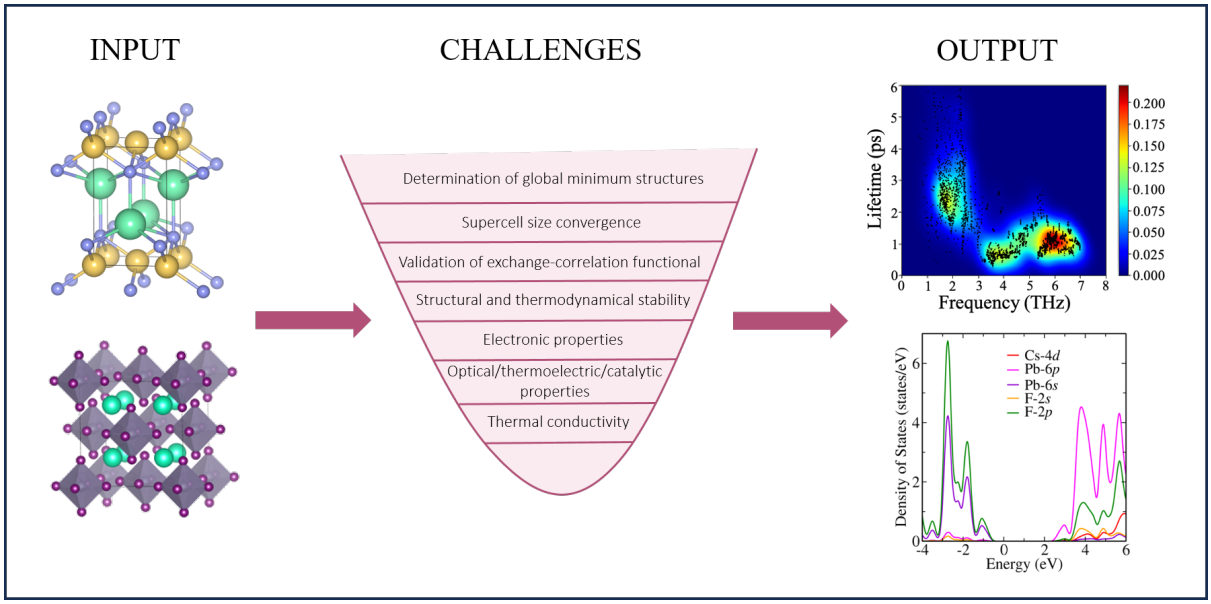

Figure 1.5: Challenges encountered in calculating the different properties of materials.

In the realm of theoretical calculations, the determination of a material's ground-state properties is efficiently carried out through DFT [16]. However, the precision of computational outcomes is frequently limited by the approximations made in exchange-correlation functionals. Another significant challenge, especially in defect calculations, pertains to achieving convergence in the supercell size for an isolated defect. While systematic improvements can be made until convergence is achieved, constraints imposed by computational resources place severe limitations on the extent to which such convergence can be realized.

To compute the formation energy of a defect, the supercell approach is employed. Within this method, a single defect is encompassed within a larger cell, which is periodically replicated. Given that realistic defect concentrations are typically lower than the defect concentration within a cell, interactions between the defect and its periodic images are misleading and necessitate correction [17]. Consequently, the supercell size must be substantial enough to confine the defect within the system. Additionally, an efficient k-point sampling of the Brillouin zone is vital for achieving convergence in the relevant physical quantity.

Local or semi-local exchange-correlation functionals employed within DFT, such as LDA and PBE, tend to significantly underestimate the band gap of materials.As a result, computations of formation energies and charge transition levels for defects in semiconductors using LDA or GGA often yield inaccurate results. Furthermore, these approaches fall short in capturing charge localization stemming from narrow bands or local distortions in the vicinity of defects, primarily due to the electron's self-interaction error. This challenge can be mitigated by adopting hybrid functionals like HSE06, which yield improved defect energetics. However, it is essential to strike a balance by incorporating an appropriate amount of exact exchange mixing to accurately replicate the experimental band gap [18]. Fig. 1.5 illustrates a schematic of the computational obstacles that may arise when designing a material for diverse applications, such as photovoltaics, catalysis and thermoelectricity.

To delve into the properties of excited states, it becomes imperative to extend beyond DFT. Accurate determination of these properties is achieved through quasiparticle calculations rooted in Green's function methods under the Many-Body Perturbation Theory (MBPT) framework. Notably, this involves utilizing the GW approximation [19] and the Bethe-Salpeter equation (BSE) approach [20, 21]. Practically, these calculations are contingent on the DFT orbitals. Therefore, a crucial step involves comparing the theoretical results with experimental data to gauge the reliability of the computational approach. In general, the single-shot GW (G_0W_0)

method provides accurate predictions of band gaps. However, it's important to acknowledge that GW and BSE calculations pose significant computational challenges due to their high cost and demanding memory requirements. In the scope of this thesis work, we have judiciously addressed these parameters to conduct our calculations.

1.7 A short overview of the thesis

- **Chapter 2:** In this chapter, we discuss the theoretical framework that underpins our research. A concise exploration of the first-principles-based DFT is provided. It is a crucial tool for unraveling the structural and electronic characteristics of materials. Additionally, we touch upon *ab initio* atomistic thermodynamics, a pivotal aspect in studying the thermodynamic stability of the materials. Subsequently, we discuss the cGA and CINEB approach to find the global minimum structures and activation energies of reactions, respectively. Our discussion extends to the MBPT approaches, with a specific focus on the GW approximation. These methodologies are instrumental in comprehending the optical properties of different materials.

- **Chapter 3:** In this chapter, we explore the catalytic conversion of methane (greenhouse gas) into syngas, which can be further used in producing valuable products such as methanol, liquid hydrocarbons and ammonia. However, methane is extremely inert since C-H bonds in it possess high bond strength (4.5 eV), low polarizability and negligible electron affinity. As a result, the efficient activation of methane has been a major challenge. To circumvent this problem, a suitable catalyst is required. For this, we have considered a prototypical model system of nickel (Ni_4, which has already been experimentally synthesized and has high selectivity) in a reactive atmosphere of O_2 and CH_4 gas molecules under realistic conditions. Typically, in the presence of a reactive atmosphere, clusters adsorb surrounding gas molecules and form intermediate phases [$Ni_4O_x(CH_4)_y$] at thermodynamic equilibrium. The latter generally proves to be an active material for applications in the field of heterogeneous catalysis. We have investigated the role of environment [i.e., temperature (T), partial pressure of oxygen (p_{O_2}) and partial pressure of methane (p_{CH_4})] to understand the thermodynamic stability of these $Ni_4O_x(CH_4)_y$ ($0 \leq x \leq 8$, $0 \leq y \leq 3$) clusters. Moreover, to incorporate the anharmonicity in the vibrational free energy contribution to the configurational entropy, we have evaluated the excess free energy of

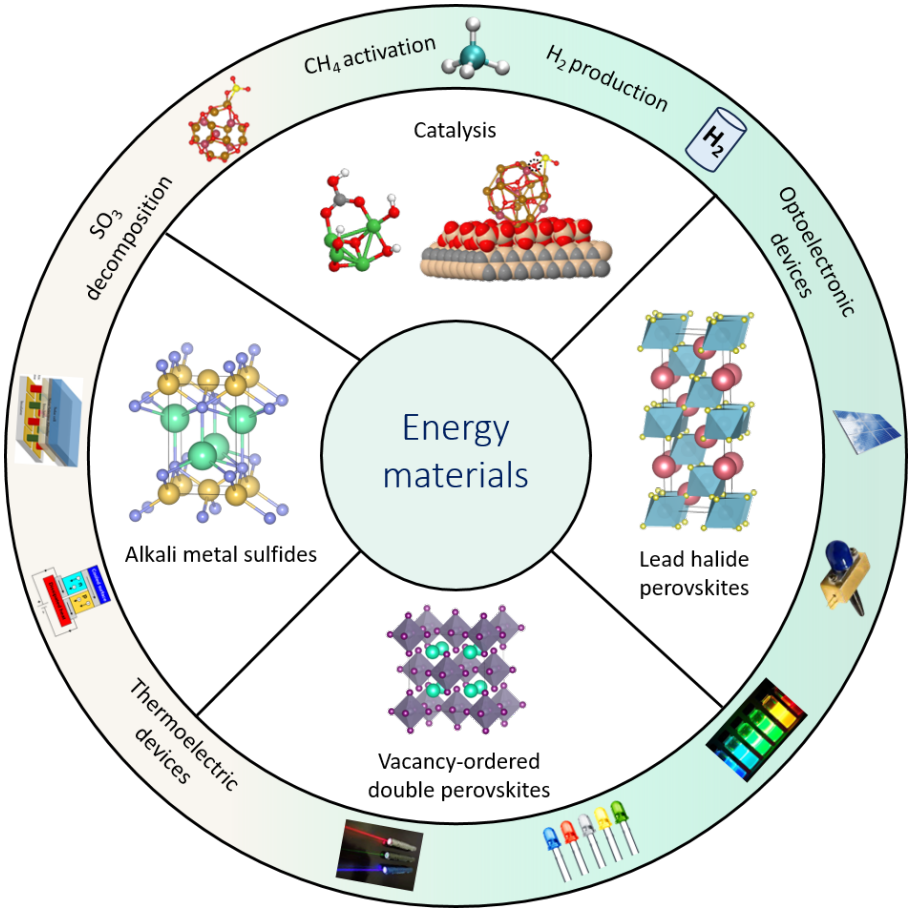

Figure 1.6: Overview of the thesis.

the clusters numerically by thermodynamic integration method with *ab initio* molecular dynamics (*ai*MD) simulation inputs. While finding the accurate thermodynamic stability, we have seen that the inclusion of anharmonicity introduces new stable phases that are entirely ignored by DFT and DFT+$F_{vibs}^{harmonic}$. This has a significant impact on detecting the activation of the C-H bond, where the harmonic IR is unable to capture the correct vibrational modes. Additionally, using DFT calculations, we conduct a study on the decomposition of SO_3 in the Iodine-Sulfur (I-S) cycle for hydrogen production.

- **Chapter 4:** This chapter offers a comprehensive investigation of ferroelectric $CsPbF_3$ perovskite, with a particular emphasis on Rashba-Dresselhaus (RD) splitting. Our approach utilizes first-principles calculations, viz., DFT with semilocal and hybrid functionals (HSE06), in combination with SOC and many-body perturbation theory (G_0W_0). In order to gain a deeper understanding of the observed spin splitting, we analyze spin textures using the ***k.p*** model Hamiltonian. Our findings reveal the absence of an out-of-plane spin component, signifying the dominance of Rashba splitting over Dresselhaus splitting.

Notably, we observe that the strength of Rashba spin splitting can be significantly tuned with the application of uniaxial strain (±5%). Furthermore, the reversible spin textures in $CsPbF_3$ perovskite suggest promising implications for perovskite-based spintronic applications.

- **Chapter 5:** This chapter presents a systematic study of vacancy-ordered double perovskites (VODPs) as potential optoelectronic and thermoelectric materials, utilizing DFT and Boltzmann transport theory. The lack of polyhedral connectivity in VODPs introduces additional degrees of freedom, resulting in lattice anharmonicity. This anharmonic lattice dynamics leads to a strong electron-phonon coupling, which can be accurately described by the Fröhlich mesoscopic model. We investigate the lattice anharmonicity further through ab initio molecular dynamics and the electron localization function. Among the materials studied, Cs_2PtI_6 exhibits the highest degree of anharmonicity, followed by Cs_2PdI_6, Cs_2TeI_6, and Cs_2SnI_6. Additionally, the computed average thermoelectric figure of merit (zT) for Cs_2PtI_6, Cs_2PdI_6, Cs_2TeI_6, and Cs_2SnI_6 is 0.88, 0.85, 0.95, and 0.78, respectively, underscoring their potential in renewable energy applications.

- **Chapter 6:** This chapter outlines an approach to enhance the thermoelectric characteristics of GeTe-based materials via simultaneous Ti and Bi codoping ($Ge_{1.01-x-y}Ti_xBi_yTe$) at cation sites, combined with Ge self-doping. This strategy involves a comprehensive optimization of both electronic properties, achieved through crystal field engineering and precise Fermi level adjustment, and thermal properties, obtained via point-defect scattering. Pristine GeTe exhibits a high carrier concentration (n) owing to intrinsic Ge vacancies, resulting in a low Seebeck coefficient (α) and elevated thermal conductivity (κ). Additionally, the phonon dispersion calculations indicate a decrease in group velocity within Ti-Bi co-doped GeTe, further supporting the observed κ_{ph} reduction. Through a combination of Ge vacancy optimization and crystal field engineering, an improved α is achieved by introducing excess Ge and Ti doping. This enhancement is further refined by manipulating the band structure through Bi doping. The resultant synergy of improved α and optimized Fermi level leads to an increased power factor in Ti-Bi codoped $Ge_{1.01}Te$. The experimental findings are corroborated by theoretical computations of band structure and thermoelectric parameters using DFT and Boltztrap calculations.

- **Chapter 7:** In this chapter, we present an enhanced energy conversion efficiency (η)

achieved through a two-step optimization of TE properties in Mn–Sb co-doped GeTe, involving the manipulation of electronic structure and lattice dynamics. The introduction of Mn and Sb via co-doping effectively improves the TE properties of GeTe, as evidenced by both experimental results and first-principles-based theoretical calculations. DFT calculations reveal that Mn–Sb co-doping leads to improved band convergence and optimal Fermi level positioning. This, in turn, contributes to the enhancement of the Seebeck coefficient (α). The synergistic effects of the optimized α and σ result in a notable increase in the power factor ($\alpha^2\sigma$) for the Mn–Sb co-doped GeTe system. The combined improvement in α and reduction in κ_{ph} leads to an impressive maximum figure-of-merit (zT) of 1.67 at 773 K.

- **Chapter 8:** This chapter concludes the research conducted in this thesis and provides a concise overview of potential future projects.

CHAPTER 2

Theoretical methodology

2.1 Computer simulation

Computer simulation involves running programs on a network of interconnected computers to model real-world processes through an abstract representation. It plays a crucial role in scientific research and innovation, serving to support, validate, or rule out theoretical and experimental hypotheses. Mathematical modeling combined with computer simulations finds applications in a wide range of fields like physics, chemistry, biology, climatology, as well as human-related systems including medical science, economics, social science, security, and engineering. Simulations are particularly valuable when tackling systems too complex for analytical solutions. Therefore, "computer simulation" has become the third essential component of scientific inquiry, alongside theory and experimentation. Simulations serve as valuable tools for investigating experiments that may not always be feasible in a laboratory due to resource limitations. Consequently, computer simulations play a crucial role as a bridge between theoretical and experimental aspects of research. Furthermore, modern computer simulations have advanced to the extent that they can shed light on the contributions of even minor components that impact the entire system. This has given rise to the interdisciplinary field of "Computational Materials Science," which involves the exploration of novel materials, the study of material behaviors and underlying mechanisms, and the quest for efficient theories or methodologies pertaining to materials.

Today's advancements in computer architecture have expanded the horizons of problem-solving across various length and time scales. Multi-scale computer simulation encompasses a range of length scales, from the atomic nucleus to electronic structures, atomistic and nanoscale, mesoscale, and onward to micro/macro-scale. It also spans diverse time scales, from picoseconds to months and years. In physics, multi-scale computer simulations enable the

study of material properties and their responses to different environmental conditions. These simulations rely on several levels of methodology, illustrated in Fig. 2.1. The distinct levels are as follows: (i) atomistic methods, which include Electronic Structure calculations, Molecular Dynamics, and Monte Carlo simulations, (ii) mesoscale methods, such as Dislocation Dynamics and Phase Field modeling, and (iii) continuum methods, like Finite Element and Finite Difference approaches. The results obtained at one level inform and enhance the understanding of phenomena at other levels, while preserving the relevant physical principles. Multi-scale modeling is especially valuable in computational materials engineering as it allows predictions of material properties and system behavior based on atomic structure and elementary process information. Computational techniques are employed to determine ground-state and excited-state properties, including geometries, ground-state energies, charge densities, band gaps, optical and vibrational spectra, and more. The selection of a modeling approach depends upon the particular phenomena and properties under investigation, enabling a customized strategy for addressing various research inquiries.

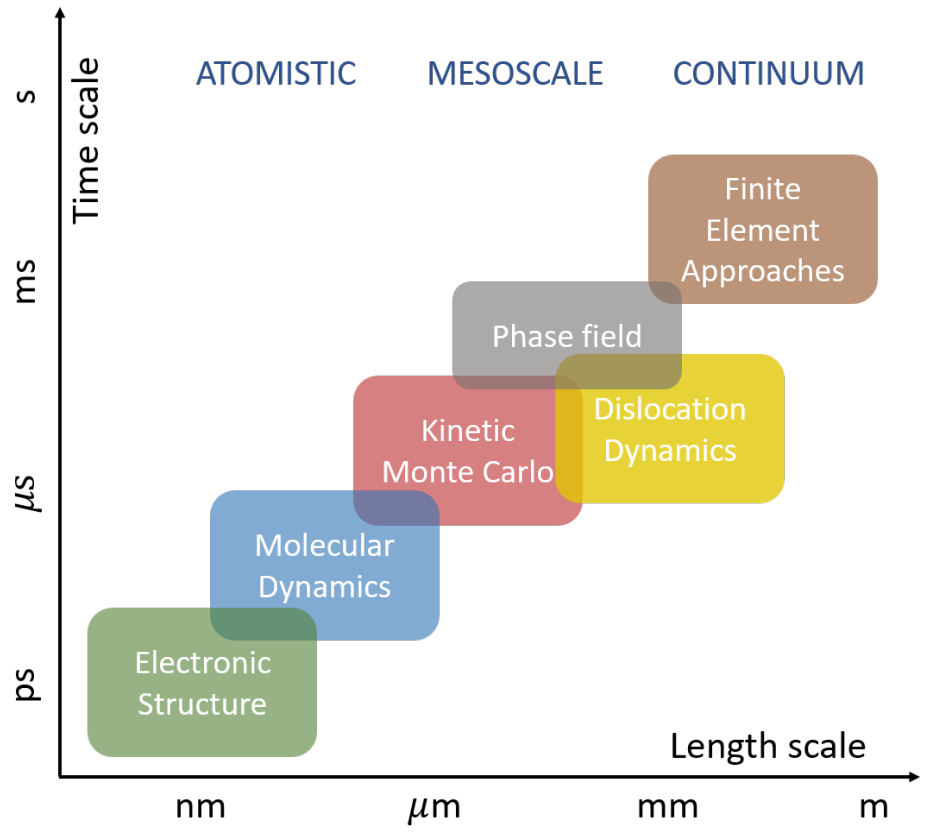

Figure 2.1: Multi-scale simulation in different length and time scales.

In this thesis, we employ first-principles electronic structure calculations to design materials for energy applications in catalysis, optoelectronics and thermoelectricity. The framework of our thesis is outlined as follows: We begin with a brief explanation of the fundamental concept behind first-principles calculations, elucidating how the properties of condensed matter systems can be unveiled through a quantum mechanical approach by solving the many-electron Schrödinger equation. After that, we discuss the foundations of density functional theory (DFT), which serves as a practical method for dealing quantum systems with many electrons. Additionally, we categorize the exchange-correlation functionals, which encompass various approximations. To find the global minimum structures, we employ cascade Genetic Algorithm (cGA). Further, we determine the transition states and activation barriers of reactions using climbing image nudged elastic band (CINEB) method. Finally, to investigate the excited-state properties of the systems, we introduce Green's function methods, specifically, the GW approximation.

2.2 First-principles calculation

A "first-principles calculation" refers to a calculation based on established scientific principles, following the fundamental laws of physics without reliance on empirical laws or parameter fitting. This approach is primarily rooted in the principles of quantum mechanics and offers a comprehensive understanding of the electronic, optical, and magnetic properties of materials and molecules. Our environment consists of condensed matter, which comprises stable systems of atoms and molecules, primarily in solid or liquid phases. The fundamental building blocks of condensed matter are atoms, composed of a positively charged nucleus surrounded by negatively charged electron clouds. Consequently, the interactions between atoms, including covalent, ionic, chemical, and molecular bonding, can be traced back to the interactions of their constituents-specifically, electrons and nuclei. These foundational interactions underpin the physics of condensed matter systems. Accurately modeling these basic interactions presents a considerable challenge. Achieving precise modeling of these interactions is crucial because it should naturally yield complex physical phenomena arising from these interactions in our calculations. The principles governing the interactions between electrons and nuclei in condensed matter are relatively straightforward. The dynamics of these particles are governed by the mathematical framework of basic quantum mechanics, mainly the Schrödinger equation.

Solving this equation allows for the determination of properties related to condensed matter. However, the numerical formulation of this equation poses significant challenges, mainly due to the size and complexity of the problem. While we have a complete understanding of the fundamental laws essential for the mathematical treatment of a significant portion of physics and chemistry, the resulting equations are highly intricate and challenging to solve. Therefore, ongoing research in this field focuses on the development of efficient and accurate computational techniques to address many-body problems.

2.3 Many-body problem

Many-body physics is instrumental in understanding the collective behavior of many interacting quantum particles. The behavior of a system is governed by the fundamental equation of quantum mechanics, the Schrödinger equation. Solving the Schrödinger equation yields the many-body wave function, describing the quantum state of a system, from which all physical phenomena can be derived. However, solving the many-electron Schrödinger equation is practically unattainable except for very basic cases, like the H-atom, He^+, and harmonic oscillators, due to the computational limitations of computers regarding speed and memory. Given these constraints, numerical solutions are only feasible for systems with a limited number of electrons. Since determining an exact solution is computationally formidable, the common approach is to transform the problem into a closely related one for which an exact solution is known. The disparity between the two, assumed to be small, is then treated as a perturbation to the exactly solvable problem. This way, an approximate solution is derived for the many-electron problem, which is subsequently refined with minor corrections to improve the previously obtained approximate values. Addressing the many-electron system begins with the Born-Oppenheimer approximation, which decouples the motion of electrons and nuclei. Given the considerable difference in mass between electrons and nuclei, the nuclei can be considered at rest with respect to the electrons. Although this approximation simplifies the many-electron problem, dealing with electron-electron interactions remains a challenge. For an N-electron system, there are $3N$ variables. Two primary approaches are commonly employed to solve the N-electron system: (i) the wave function-based approach and (ii) DFT. In the former, the N-electron wave function is the primary focus, whereas the latter focuses on the 3D electron density. A classic wave function method developed by Hartree in 1928 treats electrons as

independent entities, with each electron interacting solely through a central potential created by other electrons and nuclei. Therefore, the total wave function is represented as the product of *N* independent electron wave functions. However, this approach fails to adhere to the antisymmetric nature of electrons, which are fermions. In 1930, Fock replaced the Hartree product of wave functions with the Slater determinant, satisfying the required antisymmetric condition. This approximation is known as the Hartree–Fock approximation, considering direct Coulomb and exact exchange interactions among electrons. Nonetheless, it falls short of addressing electronic correlation, leading to significant deviations from experimental results. To overcome these limitations, post-Hartree–Fock methods were developed to incorporate electronic correlation into the many-electron wave function. These methods include Møller-Plesset (MP) perturbation theory, configuration interaction (CI), coupled cluster (CC) methods, multiconfigurational self-consistent field (MCSCF), and quantum Monte Carlo (QMC) methods. However, the precision of these accurate methods comes at a steep computational cost, rendering them applicable only to systems composed of a small number of atoms.

In the pursuit of practical solutions to the many-electron problem, approaches based on DFT have been developed to address systems containing a large number of interacting particles while also considering electronic correlation. DFT was originally conceived as an exact theory for dealing with many-electron systems, where the energy is expressed as a functional of the electronic density. However, the precise relationship between energy and density remains unknown. Consequently, DFT is applied with appropriate approximations to account for exchange and correlation effects. DFT has achieved remarkable success in determining the properties of diverse materials, owing to its effective balance of accuracy and computational efficiency. Furthermore, DFT provides reliable estimations of ground-state properties. When predicting excited-state properties, calculations using *ab initio* many-body perturbation theory, such as the GW approximation and the Bethe-Salpeter equation (BSE) approach, offer better performance.

2.4 Time-independent many-body Schrödinger equation

The initial step in the quantum mechanical approach to determine the electronic structure of matter involves the Schrödinger equation, which is given as

$$\hat{H}\Psi_k\left(\mathbf{r}_1, \mathbf{r}_2, \ldots, \mathbf{r}_N, \mathbf{R}_1, \mathbf{R}_2, \ldots, \mathbf{R}_M\right) = E_k\Psi_k\left(\mathbf{r}_1, \mathbf{r}_2, \ldots, \mathbf{r}_N, \mathbf{R}_1, \mathbf{R}_2, \ldots, \mathbf{R}_M\right) \qquad (2.1)$$

$\hat{H}$ is the Hamiltonian operator for a system of M nuclei and N electrons. The Hamiltonian operator $\hat{H}$ can be expressed as follows

$$\begin{aligned}\hat{H} = &-\sum_{i=1}^{N}\frac{\hbar^2}{2m_e}\nabla_i^2 - \sum_{I=1}^{M}\frac{\hbar^2}{2M_I}\nabla_I^2 - \sum_{i=1}^{N}\sum_{I=1}^{M}\frac{Z_I e^2}{|\mathbf{R}_I - \mathbf{r}_i|} \\ &+ \frac{1}{2}\sum_{i=1}^{N}\sum_{j\neq i}^{N}\frac{e^2}{|\mathbf{r}_i - \mathbf{r}_j|} + \frac{1}{2}\sum_{I=1}^{M}\sum_{J\neq I}^{M}\frac{Z_I Z_J e^2}{|\mathbf{R}_I - \mathbf{R}_J|}\end{aligned} \tag{2.2}$$

Here, indices i and j run over N electrons, while I and J run over M nuclei within the system. m_e stands for the mass of an electron, and M_I represents the mass of nucleus I. Z_I represents the nuclear charge of nucleus I. The first two terms within Equation 2.2 account for the kinetic energies of the N electrons and M nuclei, respectively. The last three terms describe the attractive electrostatic interaction between the nuclei and electrons, as well as the repulsive interactions between electron-electron and nucleus-nucleus pairs. The wavefunction, $\Psi_k\left(\mathbf{r}_1, \mathbf{r}_2, \ldots, \mathbf{r}_N, \mathbf{R}_1, \mathbf{R}_2, \ldots, \mathbf{R}_M\right)$ denotes the state k of the system, while E_k represents the corresponding energy (eigenvalue). The wave function itself does not depict a physical quantity; however, its square, denoted as $|\Psi|^2$ [1], gives the probability density. In simpler terms, $|\Psi|^2$ represents the likelihood of finding a particle at a specific point in space at a given moment in time. To be physically valid, the wave function should exhibit continuity, double differentiability, and square integrability. For an introductory overview of quantum mechanics, please refer to Ref [22].

2.4.1 Born–Oppenheimer approximation

The solution of Schrödinger equation is not feasible for many-electron system due to the high dimensionality (i.e., where all the particles have three degrees of freedom) and the constraints on the wave function. Consequently, approximations are employed to solve the Schrödinger equation. The primary and fundamental approximation is the Born–Oppenheimer or adiabatic approximation, in which the motion of the electrons and nuclei is considered independently. Given the significantly greater mass of nuclei compared to electrons, the motions of electrons and nuclei can be treated as separate processes. The positions of electrons rapidly adjust in response to any nuclear movement, with the motion of electrons depending on the nuclear positions parametrically. Hence, within the Born–Oppenheimer approximation, the wave functions

[1] $|\Psi|^2 = \Psi^*\Psi$, where Ψ^* is the complex conjugate of Ψ.

of electrons and nuclei can be separated as

$$\Psi_{total} = \psi_{electronic} \times \psi_{nuclear}$$

$$\Psi\left(\mathbf{r}_1, \mathbf{r}_2, \ldots, \mathbf{r}_N, \mathbf{R}_1, \mathbf{R}_2, \ldots, \mathbf{R}_M\right) = \psi\left(\mathbf{r}_1, \mathbf{r}_2, \ldots, \mathbf{r}_N; \mathbf{R}_1, \mathbf{R}_2, \ldots, \mathbf{R}_M\right) \times \psi\left(\mathbf{R}_1, \mathbf{R}_2, \ldots, \mathbf{R}_M\right) \tag{2.3}$$

The contributions from the nuclei (including the kinetic energy of nuclei and the energy of internuclear repulsion) can be introduced subsequently, once the electronic properties are determined. As a result, the motions of the nuclei and electrons can be treated separately, and the Hamiltonian for the electronic structure theory can be expressed as:

$$\hat{H} = \hat{T} + \hat{V}_{ext} + \hat{V}_{int} \tag{2.4}$$

In the atomic units, $\hbar = m_e = e = \frac{4\pi}{\epsilon_0} = 1$. The kinetic energy operator for the electrons $\hat{T}$ is given as

$$\hat{T} = -\sum_{i=1}^{N} \frac{1}{2} \nabla_i^2 \tag{2.5}$$

The potential ($\hat{V}_{ext}$) acting on the electrons due to the nuclei is given as

$$\hat{V}_{ext} = \sum_{i=1}^{N} \sum_{I=1}^{M} V_I\left(|\mathbf{r}_i - \mathbf{R}_I|\right) \tag{2.6}$$

and $\hat{V}_{int}$ represents the electron-electron interaction,

$$\hat{V}_{int} = \frac{1}{2} \sum_{i=1}^{N} \sum_{j \neq i}^{N} \frac{1}{|\mathbf{r}_i - \mathbf{r}_j|} \tag{2.7}$$

Even with application of Born–Oppenheimer approximation, solving the Schrödinger equation with the electronic Hamiltonian remains a challenging task. Therefore, additional approximations are required to address the Schrödinger equation, as discussed in the subsequent sections.

2.4.2 The Hartree approximation

Hartree introduced a significant method in 1984 to derive the most accurate single-electron wavefunction. For the Schrödinger equation to be solved, the variables as functions of electron coordinates must be separable. These variables should be separable in a manner that depends solely on the coordinates of individual electrons. Consequently, an approximate Hamiltonian was devised to account for the electron interactions in an averaged manner. By solving the Schrödinger equation, the precise single-electron eigenfunctions of this approximate Hamiltonian can be determined. In the Hartree approximation, the multi-electron wavefunction is

expressed as a product of individual single-electron wavefunctions.

$$\Psi\left(\mathbf{r}_1, \mathbf{r}_2, \ldots, \mathbf{r}_N\right) = \phi_1\left(\mathbf{r}_1\right)\phi_2\left(\mathbf{r}_2\right)\ldots\phi_N\left(\mathbf{r}_N\right) \tag{2.8}$$

where $\mathbf{r}_i$ encompasses the spatial and spin coordinate for each electron, and $\phi_i\left(\mathbf{r}_j\right)$ represents a single-electron spin-orbital. This equation implies that the electrons are treated as independent entities and only interact with the average electron density. With this assumption, the electronic Hamiltonian can be defined as

$$\hat{H}_{el} = \sum_{i=1}^{N}\hat{h}_i + \hat{V}_{int} \tag{2.9}$$

where

$$\hat{h}_i = -\frac{1}{2}\nabla_i^2 + \hat{v}_i \tag{2.10}$$

and $\hat{h}_i$ is dependent on the coordinates $\mathbf{r}_i$ of the i-th electron. $\hat{V}_{int}$ is approximated by summing up the interactions of each electron with the averaged electron density of the remaining N-1 electrons as follows

$$\hat{V}_{int} \approx \sum_{i=1}^{N}\hat{g}_i\left(\mathbf{r}\right) \tag{2.11}$$

where

$$\hat{g}_k\left(\mathbf{r}\right) = \int \rho^{(k)}\left(\mathbf{r}'\right)\frac{1}{|\mathbf{r}-\mathbf{r}'|}d\mathbf{r}' \tag{2.12}$$

and

$$\rho^{(k)}\left(\mathbf{r}\right) = \sum_{\substack{i=1\\ i\neq k}}^{N}|\phi_i\left(\mathbf{r}\right)|^2 \tag{2.13}$$

As a result of these approximations, the many-electron Schrödinger equation simplifies into N independent single-electron equations

$$\left(-\frac{1}{2}\nabla_i^2 + \hat{v}_i + \hat{g}_i\right)\phi_i\left(\mathbf{r}\right) = \epsilon_i\phi_i\left(\mathbf{r}\right) \tag{2.14}$$

ϵ_i represents the energy of the i-th electron. In practice, we initialize with an initial guess for the orbitals, ϕ_i (e.g., based on the hydrogen atom wave function). Subsequently, we compute the spin-orbitals, $\hat{g}_i$, derived from these initial guesses. We then solve the N independent single-electron equations to determine N new spin-orbitals. These new spin-orbitals serve as our starting point, and we iterate until we achieve convergence. The resulting converged orbitals are referred to as self-consistent field spin-orbitals. We utilize these *self-consistent field* spin-orbitals to construct the many-electron wave function Ψ and proceed to compute the ground state's total energy, denoted as E. It's important to note that the total energy is not equivalent to the sum of individual orbital energies ϵ_i because the electron-electron interaction is accounted

for twice in our effective potential formulation. As a result, the corrected total energy is given by

$$E = \sum_{i=1}^{N} \epsilon_i - \frac{1}{2} \sum_{i=1}^{N} \sum_{j \neq i}^{N} J_{ij} \tag{2.15}$$

J_{ij} denotes the Coulomb interaction between electrons i and j. These interactions are commonly referred to as Coulomb integrals, and are given as

$$J_{ij} = \int \int \frac{\rho_i (\mathbf{r}_1) \rho_j (\mathbf{r}_2)}{|\mathbf{r}_1 - \mathbf{r}_2|} d\mathbf{r}_1 d\mathbf{r}_2 = \int \int |\phi_i (\mathbf{r}_1)|^2 \frac{1}{|\mathbf{r}_1 - \mathbf{r}_2|} |\phi_j (\mathbf{r}_2)|^2 d\mathbf{r}_1 d\mathbf{r}_2 \tag{2.16}$$

$$J_{ij} = \int \int \phi_i^* (\mathbf{r}_1) \phi_i (\mathbf{r}_1) \frac{1}{|\mathbf{r}_1 - \mathbf{r}_2|} \phi_j^* (\mathbf{r}_2) \phi_j (\mathbf{r}_2) d\mathbf{r}_1 d\mathbf{r}_2 \tag{2.17}$$

The Hartree approximation provides a crucial starting point for developing methods to deal with many-electron systems.

2.4.3 The Hartree–Fock approximation

A significant limitation of the Hartree approximation is its failure to account for the antisymmetry property of the electronic wave function. This results in a violation of the Pauli exclusion principle, rendering the description of the electronic component incomplete. The primary aim of the Hartree-Fock approximation is to fix this shortcoming. In this approach, the variational wave function takes the form of a Slater determinant, which ensures satisfaction of the antisymmetric condition. The Pauli exclusion principle naturally arises from this condition, stating that two fermions cannot simultaneously occupy the same orbital.

For N orbitals, the Slater determinant is written as

$$\Psi (\mathbf{r}_1, \mathbf{r}_2, \ldots, \mathbf{r}_N) = \frac{1}{\sqrt{N!}} \begin{vmatrix} \phi_1 (\mathbf{r}_1) & \phi_2 (\mathbf{r}_1) & \cdots & \phi_N (\mathbf{r}_1) \\ \phi_1 (\mathbf{r}_2) & \phi_2 (\mathbf{r}_2) & \cdots & \phi_N (\mathbf{r}_2) \\ \vdots & \vdots & \ddots & \vdots \\ \phi_1 (\mathbf{r}_N) & \phi_2 (\mathbf{r}_N) & \cdots & \phi_N (\mathbf{r}_N) \end{vmatrix} \tag{2.18}$$

$\mathbf{r}_i$ incorporates the spatial coordinates and a spin coordinate for the i-th electron, while $\phi_i (\mathbf{r}_j)$ denotes the i-th single-electron spin orbital. Consequently, the total energy is calculated as follows:

$$E = \langle \Psi | H | \Psi \rangle = \sum_{i=1}^{N} H_i + \frac{1}{2} \sum_{i=1}^{N} \sum_{j=1}^{N} (J_{ij} - K_{ij}) \tag{2.19}$$

where

$$H_i = \int \phi_i^* (\mathbf{r}) \hat{h}_i \phi_i (\mathbf{r}) \, d\mathbf{r} \tag{2.20}$$

K_{ij} is called as *exchange* integral, given as

$$K_{ij} = \int \int \phi_i^* (\mathbf{r}_1) \phi_j (\mathbf{r}_1) \frac{1}{|\mathbf{r}_1 - \mathbf{r}_2|} \phi_i (\mathbf{r}_2) \phi_j^* (\mathbf{r}_2) \, d\mathbf{r}_1 d\mathbf{r}_2 \tag{2.21}$$

This exchange term results from the Pauli exclusion principle, introducing repulsion between electrons of the same spin.

While the Hartree–Fock approximation addresses exact exchange, it overlooks electronic correlation, a significant factor in bond formation and breaking. Moreover, there are also cases where different wave functions that follow the exclusion principle can't be represented by the Hartree-Fock method's single Slater determinant. To accommodate these correlation effects, more complex methods, such as post-Hartree–Fock approaches, are necessary. However, these methods are computationally intensive and become even more demanding as the system's size increases. In contrast, density functional theory offers a conceptually straightforward and computationally feasible approach that incorporates both exchange and correlation effects.

2.5 Density functional theory (DFT)

In DFT, the fundamental quantity is electron density, which is a scalar function of position. This differs from the traditional wave function approach to solving the Schrödinger equation. Using electron density simplifies the many-electron system problem by reducing its dimensionality from 3N to 3, and it retains its three-dimensional nature even as more electrons are added. This feature makes DFT suitable for efficiently handling systems with a large number of atoms. As a result, DFT finds extensive use in studying many-electron systems, including atoms, molecules, and solids. Its primary application is in describing the ground-state properties of these systems, which are functions of electron density. The subsequent sections will delve into the development of DFT.

2.5.1 Thomas-Fermi-Dirac approximation

Instead of utilizing wave function-based methods like Hartree and Hartree–Fock, a different approach emerged in 1927 through the work of Thomas and Fermi. Thomas and Fermi suggested

the use of electronic density as the fundamental variable for computing the energy of many-electron systems. In their original work, they proposed an expression for the kinetic energy of these systems, approximating it as a functional of density. Their approach assumed the system as non-interacting electrons uniformly distributed with density matching the local density at any given point. They employed fermion statistical mechanics to calculate the kinetic energy for this uniform electron gas model confined within a box.

$$T_{TF}\left[n\right] = C_1 \int n^{\frac{5}{3}}\left(\mathbf{r}\right) d\mathbf{r} \tag{2.22}$$

here $C_1 = \frac{3}{10}\left(3\pi^2\right)^{\frac{2}{3}} n(\mathbf{r})$ = 2.871 in atomic units and $n\left(\mathbf{r}\right)$ represents the electronic density of a uniform electron gas, approximately 2.871 in atomic units. Notably, the exchange and correlation among electrons were neglected in this formulation. The introduction of exchange effects can be achieved through a local approximation, taking into account Slater's expression for the uniform electron gas, as proposed by Dirac in 1930 and later by Slater in 1951.

$$E_X\left[n\right] = C_2 \int n^{\frac{4}{3}}\left(\mathbf{r}\right) d\mathbf{r} \tag{2.23}$$

where $C_2 = -\frac{3}{4}\left(\frac{3}{\pi}\right)^{\frac{1}{3}}$ = 0.739 in atomic units. Thus, in presence of external potential $V_{ext}\left(\mathbf{r}\right)$, the energy functional for electrons is written as

$$\begin{aligned} E_{TFD}\left[n\right] = C_1 \int n^{\frac{5}{3}}\left(\mathbf{r}\right) d^3r + \int V_{ext}\left(\mathbf{r}\right) n\left(\mathbf{r}\right) d^3r + C_2 \int n^{\frac{4}{3}}\left(\mathbf{r}\right) d^3r \\ + \frac{1}{2}\int \frac{n\left(\mathbf{r}\right) n\left(\mathbf{r}'\right)}{\left|\mathbf{r}-\mathbf{r}'\right|} d^3r d^3r' \end{aligned} \tag{2.24}$$

Here, the last term represents the classical electrostatic Hartree energy. When the approximated exchange term is included, the theory is referred to as *Thomas-Fermi-Dirac* (TFD).

The ground-state electron density and energy are determined by minimizing the functional $E[n]$ for all potential $n\left(\mathbf{r}\right)$, with the condition that the total integrated charge matches the number of electrons.

$$\int n\left(\mathbf{r}\right) d^3r = N \tag{2.25}$$

By employing the Lagrange multipliers method, one can obtain the solution through an unconstrained minimization of the functional.

$$\Omega_{TF}\left[n\right] = E_{TF}\left[n\right] - \mu\left\{\int n\left(\mathbf{r}\right) d^3r - N\right\} \tag{2.26}$$

where the Lagrange multiplier μ represents the Fermi energy. Equation 2.26 can be written as

$$\frac{1}{2}\left(3\pi^2\right)^{\frac{2}{3}} n^{\frac{2}{3}}\left(\mathbf{r}\right) + V\left(\mathbf{r}\right) - \mu = 0 \tag{2.27}$$

where $V(\mathbf{r}) = V_{ext}(\mathbf{r}) + V_{Hartree}(\mathbf{r}) + V_x(\mathbf{r})$ is the total potential.

The fact that this model is constructed with crude approximations and lacks essential physics, particularly correlation effects, renders it unsuitable for accurately describing the electronic structure of matter.

2.5.2 The Hohenberg-Kohn theorems

Back in 1964, Hohenberg and Kohn laid the foundation of modern density functional theory with two fundamental theorems in their renowned paper [23].

Theorem I: *In the case of a system of interacting electrons subjected to an external potential* $V_{ext}(\mathbf{r})$*, the* $V_{ext}(\mathbf{r})$ *can be uniquely determined based on the electronic ground-state density* $n(\mathbf{r})$*, except for a trivial additive constant.*

To prove this, let us assume the existence of two distinct potentials, $V_{ext}(\mathbf{r})$ and $V'_{ext}(\mathbf{r})$, which result in the same ground-state density $n(\mathbf{r})$. These potentials correspond to two different Hamiltonians, H and H'. Solving the Schrödinger equation for each Hamiltonian yields distinct wave functions Ψ and Ψ'. Subsequently, the ground-state energies for Ψ and Ψ' are computed as $E = \langle\Psi|H|\Psi\rangle$ and $E' = \langle\Psi'|H'|\Psi'\rangle$. It is worth noting that we have considered the non-degenerate case here, although the proof of the Hohenberg-Kohn theorem can be extended to the degenerate case as well [24]. Additionally, by employing the variational principle, we can establish that E and E' must yield the same energy due to their representation of the ground state. Applying variational principle as

$$E < \langle\Psi'|H|\Psi'\rangle = \langle\Psi'|H'|\Psi'\rangle + \langle\Psi'|H - H'|\Psi'\rangle = E' + \int n(\mathbf{r})\left[V_{ext}(\mathbf{r}) - V'_{ext}(\mathbf{r})\right] d\mathbf{r} \quad (2.28)$$

Likewise, when we calculate E', we can interchange the indices in Equation 2.28, resulting in the following form

$$E' < \langle\Psi|H'|\Psi\rangle = \langle\Psi|H|\Psi\rangle + \langle\Psi|H' - H|\Psi\rangle = E + \int n(\mathbf{r})\left[V'_{ext}(\mathbf{r}) - V_{ext}(\mathbf{r})\right] d\mathbf{r} \quad (2.29)$$

On adding Equation 2.28 and 2.29, we obtain

$$E + E' < E + E' \quad (2.30)$$

This leads to a conflicting inequality. Hence, our initial presumption was incorrect, and the ground-state density exclusively determines the potential.

Corollary I: Given that $n(\mathbf{r})$ uniquely specifies $V_{ext}(\mathbf{r})$, and $V_{ext}(\mathbf{r})$ subsequently defines the Hamiltonian, which, in turn, gives the many-body wave functions. Consequently, the system's

properties are entirely defined when only the ground-state density $n(\mathbf{r})$ is known.

Theorem II: *A universal energy functional $E[n]$ that relies on the density $n(\mathbf{r})$ can be established, and it remains applicable for any number of particles and any external potential $V_{ext}(\mathbf{r})$. In the case of a specific potential $V_{ext}(\mathbf{r})$, the $E[n]$ corresponds to the exact ground-state energy of the system, representing the global minimum for the correct ground-state density, $n(\mathbf{r})$.*

To establish this, we confine our analysis to densities that are V-representable, indicating they can be represented by a potential. It is worth noting that a more comprehensive proof, without this constraint, can be found in Ref [25]. Given that the entirety of a system's properties can be deduced from the density functional, we can express the energy functional as follows:

$$\begin{aligned} E_{HK}[n] &= T[n] + E_{int}[n] + \int V_{ext}(\mathbf{r})\, n(\mathbf{r})\, d\mathbf{r} \\ &= F_{HK}[n] + \int V_{ext}(\mathbf{r})\, n(\mathbf{r})\, d\mathbf{r} \end{aligned} \tag{2.31}$$

where

$$F_{HK}[n] = T[n] + E_{int}[n] \tag{2.32}$$

represents the universal functional of $n(\mathbf{r})$, encompassing both the kinetic and interaction energies of electrons within the system.

Given that $V_{ext}(\mathbf{r})$ relies on nuclear coordinates, its contribution is inherently specific to the system. Now, let us contemplate a system with a ground-state density $n_1(\mathbf{r})$, which corresponds to the potential $V_{ext}^1(\mathbf{r})$. In this context, the energy can be viewed as the expected value of the Hamiltonian.

$$E_1 = E_{HK}[n_1] = \langle \Psi_1 | H | \Psi_1 \rangle \tag{2.33}$$

where Ψ_1 corresponds to the ground state wave function. Let us now explore an alternative density, $n_2(\mathbf{r})$, associated with a different wave function Ψ_2. We can then apply the variational principle

$$E_1 = E_{HK}[n_1] = \langle \Psi_1 | H | \Psi_1 \rangle < \langle \Psi_2 | H | \Psi_2 \rangle = E_{HK}[n_2] = E_2 \tag{2.34}$$

Consequently, the Hohenberg-Kohn functional, derived from the actual ground-state density, yields the minimum energy when compared to any other arbitrary density. This implies that if we have knowledge of the density functional, we can ascertain the ground-state energy and density by minimizing it with respect to density variations. It is important to note that this

functional exclusively pertains to the ground state, and it does not offer insights into excited states.

While these theorems establish the existence of a universal functional, $F_{HK}[n]$, they do not provide a specific method for its determination. The Kohn-Sham equations, however, offer a framework for addressing the many-electron system.

2.5.3 The Kohn-Sham ansatz

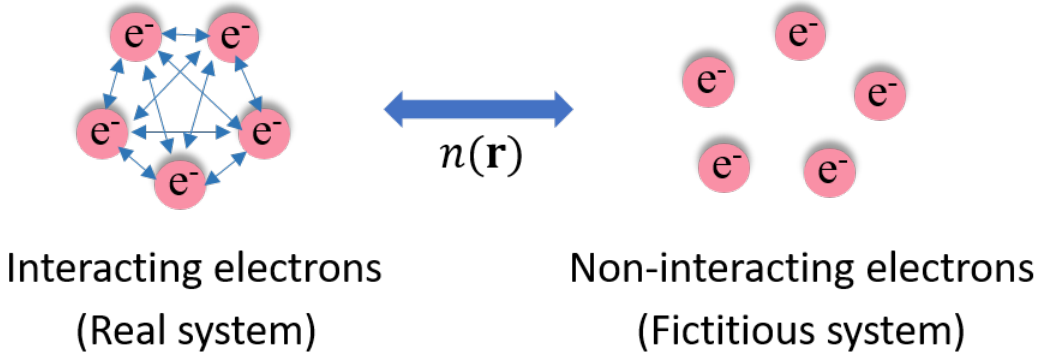

Figure 2.2: Schematic representation of mapping of interacting system to a non-interacting many-electron system through the same ground-state electron density.

In 1965, Kohn and Sham proposed a method [26] for the determination of the unknown functional $F_{HK}[n]$. Their approach involved the introduction of a non-interacting particle system and the crucial assumption that the ground-state density of the original interacting system matched that of the auxiliary non-interacting system (see Fig. 2.2 for the schematic representation). The auxiliary Hamiltonian was designed to incorporate the conventional kinetic energy operator and an effective local potential, $V_{eff}^{\sigma}(\mathbf{r})$, for an electron with spin σ located at the position $\mathbf{r}$.

$$\hat{H}_{aux}^{\sigma} = -\frac{1}{2}\nabla^2 + V_{eff}^{\sigma}(\mathbf{r}) \tag{2.35}$$

The eigenstates, denoted as $\psi_i^{\sigma}(\mathbf{r})$, represent the Kohn-Sham orbitals corresponding to the lowest eigenvalues ϵ_i^{σ} of the Hamiltonian described above. The density of the auxiliary system is expressed as follows

$$n(\mathbf{r}) = \sum_{\sigma} n(\mathbf{r}, \sigma) = \sum_{\sigma} \sum_{i=1}^{N^{\sigma}} |\psi_i^{\sigma}(\mathbf{r})|^2 \tag{2.36}$$

The expression for the kinetic energy T_s in the independent-electron auxiliary system is written as a functional of Kohn-Sham orbitals.

$$T_s = -\frac{1}{2}\sum_{\sigma}\sum_{i=1}^{N^\sigma}\langle\psi_i^\sigma|\nabla^2|\psi_i^\sigma\rangle = \frac{1}{2}\sum_{\sigma}\sum_{i=1}^{N^\sigma}\int|\nabla\psi_i^\sigma(\mathbf{r})|^2 d\mathbf{r} \tag{2.37}$$

and the Hartree energy is given as

$$E_{Hartree}[n] = \frac{1}{2}\int\frac{n(\mathbf{r})\,n(\mathbf{r}')}{|\mathbf{r}-\mathbf{r}'|}d\mathbf{r}d\mathbf{r}' \tag{2.38}$$

Hence, the total energy within the Kohn-Sham framework may be represented as

$$E_{KS} = T_s[n] + \int V_{ext}(\mathbf{r})\,n(\mathbf{r})\,d\mathbf{r} + E_{Hartree}[n] + E_{xc}[n] \tag{2.39}$$

The exchange-correlation energy E_{xc} consists of ll the many-body interactions of exchange and correlation and can be written as

$$E_{xc}[n] = F_{HK}[n] - (T_s[n] + E_{Hartree}[n]) \tag{2.40}$$

or

$$E_{xc}[n] = \langle\hat{T}\rangle - T_s[n] + \langle\hat{V}_{int}\rangle - E_{Hartree}[n] \tag{2.41}$$

$\langle\hat{T}\rangle$ represents the kinetic energy, and $\langle\hat{V}_{int}\rangle$ signifies the internal interaction energy within the original many-body interacting system. $E_{xc}[n]$ plays a pivotal role in binding atoms together to form molecules and solids. Consequently, the Kohn-Sham equations can be formulated as follows

$$H_{KS}^\sigma\psi_i^\sigma(\mathbf{r}) = \epsilon_i^\sigma\psi_i^\sigma(\mathbf{r}) \tag{2.42}$$

where

$$H_{KS}^\sigma(\mathbf{r}) = -\frac{1}{2}\nabla^2 + V_{KS}^\sigma(\mathbf{r}) \tag{2.43}$$

and

$$\begin{aligned} V_{KS}^\sigma(\mathbf{r}) &= V_{ext}(\mathbf{r}) + \frac{\delta E_{Hartree}}{\delta n(\mathbf{r},\sigma)} + \frac{\delta E_{xc}}{\delta n(\mathbf{r},\sigma)} \\ &= V_{ext}(\mathbf{r}) + V_{Hartree}(\mathbf{r}) + V_{xc}^\sigma(\mathbf{r}) \end{aligned} \tag{2.44}$$

The above mentioned equations can be iteratively solved in a self-consistent manner, as depicted in Fig. 2.3. Nevertheless, the exact functional form of $E_{xc}[n]$ as a function of density n remains unknown. Therefore, specific approximations are employed to deduce the exchange-correlation functional.

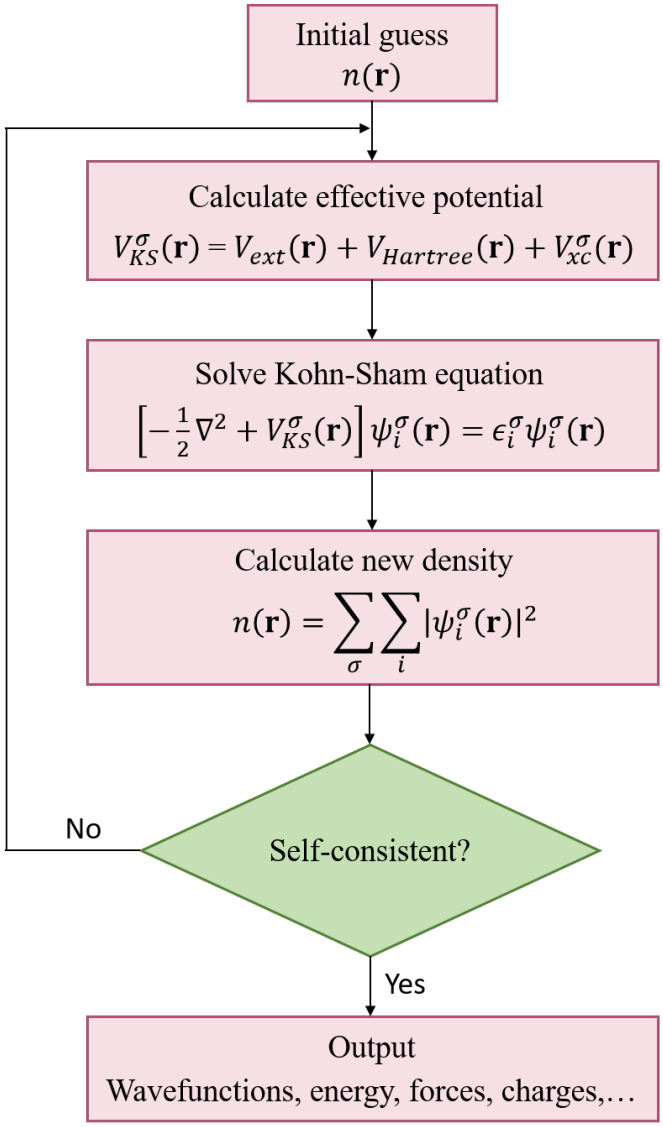

Figure 2.3: Flow chart to solve the Kohn-Sham equations self-consistently.

2.5.4 Exchange-correlation functionals

The exchange and correlation energy is defined as the difference between the exact total energy of a system and the classical Hartree energy. Unless dealing with exceptionally straightforward cases, achieving an exact treatment of exchange and correlation is practically impossible, making the use of approximations essential. The accuracy of a DFT calculation depends on how closely the chosen approximate exchange and correlation methods align with the exact values.

2.5.4.1 Local Density Approximation (LDA)

Back in 1965, Kohn–Sham introduced an approximation for the exchange-correlation functional, $E_{xc}[n]$, where it was modeled as a function primarily influenced by the local or near-local electron density. This functional not only corrects self-interaction but also elucidates the repulsion between electrons.

$$E_{xc}^{LDA}[n] = \int n(\mathbf{r})\, \varepsilon_{xc}^{unif}(n(\mathbf{r}))\, d\mathbf{r} \tag{2.45}$$

Here, $\varepsilon_{xc}^{unif}(n(\mathbf{r}))$ represents the exchange-correlation energy per electron within an electron gas possessing a uniform density, $n(\mathbf{r})$. LDA holds exact accuracy for systems with uniform densities and remains dependable for cases where $n(\mathbf{r})$ exhibits gradual spatial variations.

$$\frac{|\nabla n|}{n} \ll k_F = \left(3\pi^2 n\right)^{\frac{1}{3}} \tag{2.46}$$

and

$$\frac{|\nabla n|}{n} \ll k_S = \frac{2}{\sqrt{\pi}}\left(3\pi^2 n\right)^{\frac{1}{6}} \tag{2.47}$$

where k_F and k_S denote the Fermi and Thomas-Fermi wave vector. From Wigner approximation (1938), $\varepsilon_{xc}^{unif}(n)$ can be expressed as

$$\varepsilon_{xc}^{unif}(n) = \varepsilon_{x}^{unif}(n) + \varepsilon_{c}^{unif}(n) \tag{2.48}$$

Dirac in 1930 formulated $\varepsilon_{x}^{unif}(n)$ as

$$\varepsilon_{x}^{unif}(n) = -\frac{3}{4\pi}\left(3\pi^2 n\right)^{\frac{1}{3}} = -\frac{3}{4\pi}k_F = -\frac{3}{4\pi}\frac{\left(\frac{9\pi}{4}\right)^{\frac{1}{3}}}{r_s} \tag{2.49}$$

and Seitz radius, $r_s = \left(\frac{3}{4\pi n}\right)^{\frac{1}{3}}$, corresponds to the radius of a sphere that, on average, encloses a single electron. In 1938, Wigner formulated $\varepsilon_{x}^{unif}(n)$ as

$$\varepsilon_{c}^{unif}(n) \approx -0.056\left(\frac{n^{\frac{1}{3}}}{0.079 + n^{\frac{1}{3}}}\right) \approx -\frac{0.44}{7.8 + r_s} \tag{2.50}$$

With exact high and low density limits, Quantum Monte Carlo (QMC) calculations provide an accurate ε_{c}^{unif}.

Fig. 2.4 illustrates Jacob's ladder, showcasing a hierarchy of exchange-correlation functional approximations. This ladder of density functional approximations for exchange-correlation energy extends from the basic Hartree level to the more sophisticated realm of chemical precision [27]. As we move up this ladder, we observe an increase in complexity, accuracy, cost, and time commitment.

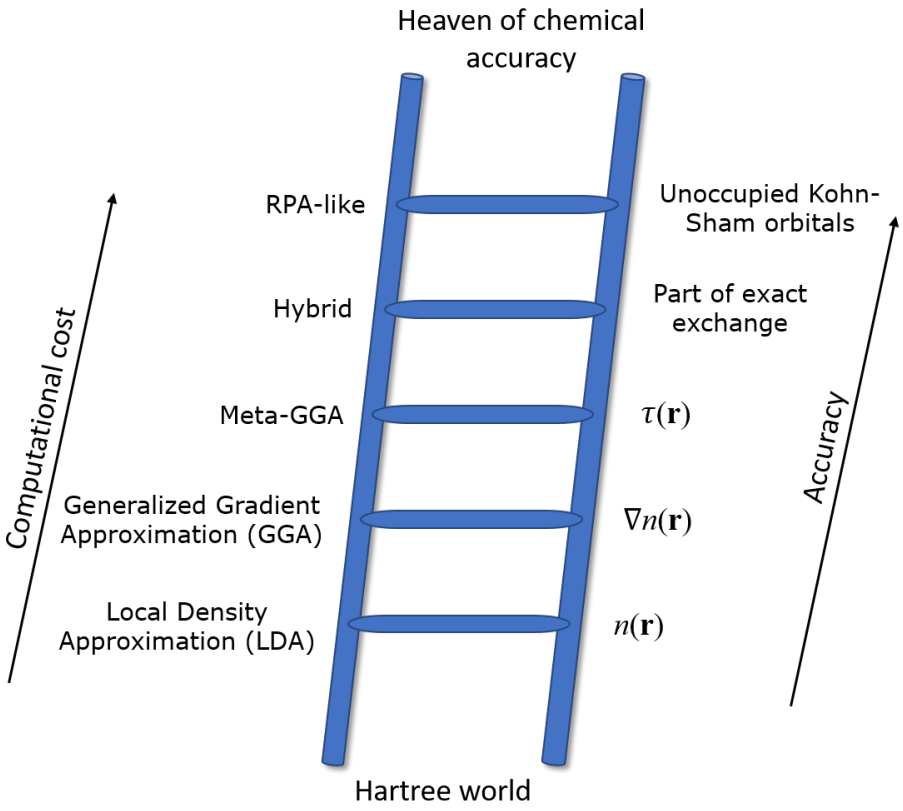

Figure 2.4: Jacob's ladder of density functional approximations.

2.5.4.2 Generalized Gradient Approximation (GGA)

It has become evident that relying solely on approximations based on a homogeneous electron gas is unreasonable for materials with highly variable densities. Consequently, there is a need to consider both the electronic density and its gradient. This semi-local approximation is referred to as the generalized gradient approximation. The expression for the exchange-correlation energy depends on $n(\mathbf{r})$ and $|\nabla n(\mathbf{r})|$. The concept of GGA was introduced by Langreth and Mehl in 1983 [28].

$$E_{xc}^{GGA}[n] = \int n(\mathbf{r})\, \varepsilon_{xc}^{GGA}(n, |\nabla n|)\, d\mathbf{r} \tag{2.51}$$

In 1968, Ma and Bruekner derived the gradient expansion (GE) [29] as follows

$$E_{xc}^{GE} = \int n(\mathbf{r})\, \varepsilon_{xc}^{unif}(n(\mathbf{r}))\, d\mathbf{r} + \int B_{xc}(n) \frac{|\nabla n|^2}{n^{\frac{4}{3}}} d\mathbf{r} \tag{2.52}$$

The coefficient $B_{xc}(n)$ is approximately determined and comprises an exchange component, which remains independent of electron density, and a correlation component, which exhibits weak dependence on n. While it proves exact for slowly varying electron densities, up to the order of $|\nabla n|^2$, this is not the case for real systems composed of atoms, where the correlation

component introduces significant errors. Hence, the GE falls short as an appropriate approximation for real systems. Consequently, a more rigorous treatment of the gradient expansion is required, considering all relevant contributions up to the desired order and adhering to the exact constraints imposed by exchange and correlation holes. In order to meet these conditions, modified gradient expansions are introduced, referred to as generalized gradient approximations (GGAs). In 1996, Perdew, Burke, and Ernzerhof (PBE) presented a GGA derivation where all parameters are fundamental constants [30], and this has become widely used. Another GGA functional is BLYP, where parameters are fitted to experimental molecular data.

GGA enhances the accuracy of binding energies of atoms and leads to improved bond lengths. However, it is important to acknowledge that GGA does have limitations in terms of accuracy, as it does not fully account for the non-local effects of the exchange term and does not entirely eliminate the self-interaction error

2.5.4.3 Meta-Generalized Gradient Approximation (meta-GGA)

In 1999, Perdew *et. al.* (PZKB) introduced the concept of meta-GGA and is defined as

$$E_{xc}^{MGGA}[n] = \int n(\mathbf{r})\, \varepsilon_{xc}^{MGGA}(n, |\nabla n|, \tau)\, d\mathbf{r} \tag{2.53}$$

where τ represents the kinetic energy density for the non-interacting system given as

$$\tau(\mathbf{r}) = \sum_{i}^{occup} \frac{1}{2} |\nabla \phi_i(\mathbf{r})|^2 \tag{2.54}$$

and

$$\int \tau(\mathbf{r})\, d\mathbf{r} = T_s[n] \tag{2.55}$$

τ can satisfy some exact constraints that are not satisfied by GGA.

Meta-GGA is a semi-local functional that, despite some improvements, presents certain issues. Notably, it exhibits an incomplete self-interaction correction, which can only be rectified through a non-local approximation.

2.5.4.4 Hybrid functionals

The concept of hybrid functionals was first introduced in 1993 by Becke, who combined a fraction of exact exchange (Hartree-Fock (HF) exchange) with GGA exchange and correlation.

$$E_{xc}^{hyb} = \alpha E_x^{HF} + (1-\alpha) E_x^{GGA} + E_c^{GGA} \tag{2.56}$$

where the coefficient α can either be empirically fitted or theoretically estimated.

Hybrid functionals offer a high level of accuracy by accounting for non-local effects. However, computationally calculating the HF exchange, especially for extended systems, is a challenging task. To address this challenge, Heyd, Scuseria, and Ernzerhof proposed the screened hybrid functional (HSE) [31, 32]. In HSE, the long-range part of HF exchange is screened out through the use of a screened Coulomb potential, reducing computational costs. The Coulomb potential is divided into components for short-range (SR) and long-range (LR) interactions

$$\frac{1}{r} = \underbrace{\frac{1-\text{erf}(\omega r)}{r}}_{\text{SR}} + \underbrace{\frac{\text{erf}(\omega r)}{r}}_{\text{LR}} \tag{2.57}$$

with ω representing the screening parameter that defines the range of separation. The error function is described as follows

$$\text{erf}(\omega r) = \frac{2}{\sqrt{\pi}} \int_0^{\omega r} e^{-x^2} dx \tag{2.58}$$

The exchange-correlation energy is determined as

$$E_{xc}^{HSE} = \alpha E_x^{HF,SR}(\omega) + (1-\alpha) E_x^{PBE,SR}(\omega) + E_x^{PBE,LR}(\omega) + E_c^{PBE} \tag{2.59}$$

The HSE06 functional, employing default values of $\alpha = 0.25$ and $\omega = 0.11$ bohr^{-1}, demonstrates accurate predictions for enthalpies of formation, ionization potentials, electron affinities, band gaps, and lattice constants. These parameters can be adjusted to match experimental data, suggesting the need for empirical adjustments due to some aspects of their construction not being fully understood.

In our thesis, we predominantly utilized the PBE functional of the GGA for structural relaxation and the HSE06 hybrid functional for energy calculations. There are various software packages available for performing DFT calculations, and we conducted our computations using the Vienna ab initio simulation package (VASP).

2.6 Basis set

The expansion of the many-electron wave function relies on a chosen basis set of functions, which significantly influences the computational efficiency of a method. The initial step in implementing a DFT method is selecting an appropriate basis set. Two commonly employed basis

functions are plane waves and Gaussian-type orbitals (GTOs). Plane wave basis sets are typically employed in the context of periodic crystals, while GTOs find more application in molecular systems. When using plane wave basis sets, pseudopotentials are often used to address the interaction between core electrons and nuclei. Notably, the plane wave pseudopotential method is free from basis set superposition error (BSSE), which can be present in methods relying on localized basis sets such as GTOs. Therefore, corrections are required to account for BSSE. In the present thesis, our calculations primarily focus on periodic solids, and we employ the plane wave pseudopotential method for electronic structure calculations.

2.6.1 Plane waves basis set

Efficient numerical methods are essential for solving the single-particle Kohn-Sham equations in extended systems. The prevalent approach to address this challenge involves expanding the single-particle eigenstates of the Kohn-Sham equations using a set of basis functions. This transformation results in the conversion of the Schrödinger equation into an algebraic equation defined by expansion coefficients, which can be solved numerically. In this context, plane waves serve as a highly suitable basis function set for extended systems. Plane waves possess the advantages of orthonormality and energy independence. Consequently, the Schrödinger equation simplifies into a fundamental matrix eigenvalue problem for these expansion coefficients. As plane waves are not dependent on atomic positions, they eliminate Pulay forces, allowing the direct application of the Hellmann-Feynman theorem for atomic force calculations.

The plane wave basis set typically consists of plane waves up to a specified wave vector cutoff. The basis set convergence is primarily determined by a single parameter, the cutoff wave vector length. However, representing the rapid oscillations of valence wave functions in the core region near nuclei requires a substantial number of plane waves. Consequently, plane waves are used in combination with pseudopotentials to approximate the impact of core electrons. Furthermore, the utilization of Fast Fourier Transforms (FFTs) alongside plane waves simplifies various integrals and operations, making plane waves suitable for larger systems.

In this section, we introduce the fundamental terminology used to describe infinitely extended periodic systems, followed by an exploration of the utility of the plane wave basis set for wave function expansion. Subsequent sections will describe the pseudopotential approach.

Bloch's theorem

As per Bloch's theorem, the eigenstates of the single-particle Schrödinger equation within a periodic crystal, described in terms of plane waves, can be represented as

$$\psi\left(\mathbf{r}+\mathbf{T}\right)=e^{i\mathbf{k}\cdot\mathbf{T}}\psi\left(\mathbf{r}\right) \tag{2.60}$$

with respect to every $\mathbf{T}$ in the Bravais lattice and $\mathbf{k}$ represents the wave vector. The permissible values of $\mathbf{k}$ are confined to the reciprocal unit cell, commonly identified as the first Brillouin zone (BZ). For each $\mathbf{k}$ value, distinct independent eigenstates exist, each distinguished by a band index denoted as n.

Bloch's theorem can be alternatively expressed, stating that all the eigenfunctions $\psi_{n\mathbf{k}}$ of the single-particle Schrödinger equation having a periodic potential can be described as a plane wave times a function $u_{n\mathbf{k}}$ with the periodicity of the Bravais lattice [12]

$$\psi_{n\mathbf{k}}\left(\mathbf{r}\right)=e^{i\mathbf{k}\cdot\mathbf{r}}u_{n\mathbf{k}}\left(\mathbf{r}\right) \tag{2.61}$$

where

$$u_{n\mathbf{k}}\left(\mathbf{r}+\mathbf{T}\right)=u_{n\mathbf{k}}\left(\mathbf{r}\right) \tag{2.62}$$

for every $\mathbf{T}$ of the Bravais lattice. This enables the confinement of eigenfunction calculations to a single unit cell, while Equation 2.61 can be used to determine eigenfunctions in other unit cells. Additionally, normalizing the eigenfunctions with respect to a single unit cell is convenient practice.

$$\int_{\Omega_c}|\psi_{n\mathbf{k}}\left(\mathbf{r}\right)|^2d\mathbf{r}=1 \tag{2.63}$$

Given the periodic nature of the functions $u_{n\mathbf{k}}\left(\mathbf{r}\right)$, it is possible to express them as a series of plane waves. Thus, Equation 2.61 is transformed to

$$\psi_{n\mathbf{k}}\left(\mathbf{r}\right)=\sum_{\mathbf{G}}c_{n\mathbf{k}}\left(\mathbf{G}\right)e^{i(\mathbf{k}+\mathbf{G})\cdot\mathbf{r}} \tag{2.64}$$

where $c_{n\mathbf{k}}\left(\mathbf{G}\right)$ are the Fourier coefficients.

The Kohn-Sham equations in terms of Bloch states can be expressed as

$$\left(-\frac{1}{2}\nabla^2+V_{eff}\left(\mathbf{r}\right)\right)\psi_{j\mathbf{k}}\left(\mathbf{r}\right)=\epsilon_{j\mathbf{k}}\psi_{j\mathbf{k}}\left(\mathbf{r}\right) \tag{2.65}$$

where

$$V_{eff}\left(\mathbf{r}\right)=V_{ext}\left(\mathbf{r}\right)+V_{Hartree}\left[n\left(\mathbf{r}\right)\right]+V_{xc}\left[n\left(\mathbf{r}\right)\right] \tag{2.66}$$

and

$$n\left(\mathbf{r}\right)=2\frac{\Omega_c}{\left(2\pi\right)^3}\sum_j\int_{\mathrm{BZ}}\left|\psi_{j\mathbf{k}}\left(\mathbf{r}\right)\right|^2\Theta\left(E_F-\epsilon_{j\mathbf{k}}\right)d\mathbf{k} \tag{2.67}$$

To distinguish between electron density and band index, n is used for electron density, and j for band index. Electron spin is accounted for in Equation 2.67 by a factor of two. The function Θ denotes the step function, yielding a value of one for positive arguments and zero for negative ones. E_F represents the Fermi energy, which determines the upper limit for occupying single-particle states.

Fourier representation of the Kohn-Sham equation

The Kohn-Sham equation adopts a more straightforward form when the wave function is represented using a plane wave basis. Upon replacing Equation 2.64 with Equation 2.65 and conducting some elementary mathematical transformations, we derive the matrix eigenvalue equation [24]:

$$\sum_{\mathbf{G}}\left(\frac{1}{2}|\mathbf{k}+\mathbf{G}|^2\delta_{\mathbf{G}'\mathbf{G}}+V_{eff}\left(\mathbf{G}'-\mathbf{G}\right)\right)c_{\mathbf{G}}^{j\mathbf{k}}=\epsilon_{j\mathbf{k}}c_{\mathbf{G}'}^{j\mathbf{k}} \tag{2.68}$$

In practice, the wave function's Fourier expansion, as described in Equation 2.64, is limited by including only those plane waves with kinetic energies below a specified cutoff value, denoted as E_{cut}:

$$\frac{1}{2}|\mathbf{k}+\mathbf{G}|^2\leq E_{\mathrm{cut}} \tag{2.69}$$

Hence, to achieve convergence for the specific quantity, it is necessary to systematically increase the value of E_{cut}. The Fourier expression for the electron density is given as

$$n\left(\mathbf{G}\right)=\frac{2}{N_{\mathrm{kpt}}}\sum_{j\mathbf{k}}f_{j\mathbf{k}}\sum_{\mathbf{G}'}\left(c_{\mathbf{G}'-\mathbf{G}}^{j\mathbf{k}}\right)^*c_{\mathbf{G}'}^{j\mathbf{k}} \tag{2.70}$$

As the electron density, denoted as n and proportional to ψ^2, demands Fourier components with twice the spatial extent in all directions compared to those required for the wave function ψ.

Computing all these Fourier components as described in Equation 2.70 involves a double summation, which scales with N_G^2, where N_G represents the number of $\mathbf{G}$ vectors required for describing the electron density. This can become computationally expensive for large systems. Furthermore, if the Bloch states are available on a grid comprising NR points in real space, determining the electron density can be carried out within NR operations, effectively as a square. This becomes very expensive for large systems. Moreover, if the Bloch states are known on a grid of N_R points in real space, the electron density can be determined as a square, in N_R

operations. The application of the fast Fourier transform (FFT) facilitates the transformation between the two spaces in $N\ln N$ operations, where $N = N_R = N_G$ [24]. Hence, it is beneficial to employ plane waves as they expedite the evaluation of these expressions by using the Fast Fourier Transform (FFT).

2.6.2 Pseudopotentials

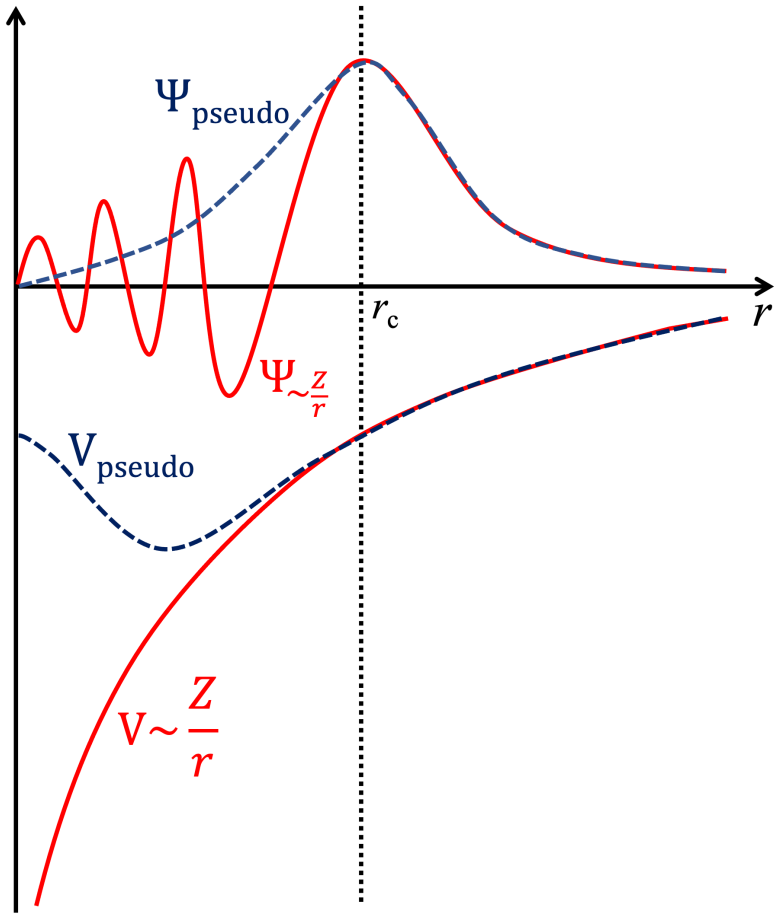

Figure 2.5: Schematic representation of pseudopotential technique. The all-electron wave function corresponding to Coulomb potential is shown by red color. The pseudo wave function corresponding to pseudopotential is shown by blue color.

Solving the Kohn-Sham equations presents computational challenges due to the need to determine wave functions for N electrons. Moreover, a significant number of plane waves are required to effectively expand the tightly bound core orbitals and capture the rapid oscillations within valence electrons' wave functions in the core region [33]. The pseudopotential approach mitigates this complexity by permitting the expansion of electronic wave functions using a smaller basis set of plane waves.

It is a well-established fact that the physical and chemical properties of a material are predominantly governed by valence electrons rather than core electrons. Therefore, the pseudopotential approximation capitalizes on this by substituting the core electrons and their strong ionic potential with a weaker pseudopotential acting on a set of pseudo wave functions in place of true valence wave functions. This concept is schematically illustrated in Fig. 2.5. The Pauli exclusion principle necessitates orthogonality between core wave functions and valence wave functions, which is upheld by the rapid oscillations present in the valence wave functions within the core electron region. he pseudopotentials are designed to ensure that the wave functions of valence electrons match those of an all-electron calculation beyond the core region, as defined by a cutoff radius r_c, as depicted in Fig. 2.5. Within the core region, these pseudopotentials are characterized by nodeless and smooth behavior. Pseudopotentials with larger r_c values yield softer potentials, converging effectively with a smaller basis set of plane waves. However, these soft pseudopotentials exhibit lower transferability, meaning they are less accurate in reproducing valence properties in diverse chemical environments. An additional advantage of employing pseudopotentials is the incorporation of relativistic effects for valence electrons, even when they are treated non-relativistically. In the subsequent sections, we will discuss regarding the pseudopotentials utilized in DFT.

2.6.3 Norm-conserving pseudopotentials

Hamann, Schlüter, and Chiang introduced norm-conserving pseudopotentials [24, 34] in 1979, with subsequent refinements by Kleinman and Bylander. These pseudopotentials possess the crucial characteristic of charge conservation, ensuring superior transferability compared to ultrasoft pseudopotentials. The degree of transferability depends on the choice of the cutoff radius, r_c. When r_c falls within the inert region, a pseudopotential can be effectively applied across various chemical environments. However, transferability diminishes when used outside this inert region. It is worth noting that ultrasoft pseudopotentials can be tailored for transferability, meaning they can be generated for an atom and applied to molecules or solids with comparable accuracy, although the process is challenging. As previously discussed, the congruence between real and pseudo wavefunctions beyond the core region leads to identical charge densities and, consequently, accurate determination of the exchange and correlation energy. The norm of the pseudopotential wavefunction (ψ_{Pseudo}) equals that of the all-electron

wavefunction (ψ).

$$\int_0^{r_c} r^2 \psi^{\star}_{\text{Pseudo}}(r)\psi_{\text{Pseudo}}(r)dr = \int_0^{r_c} r^2 \psi^{\star}(r)\psi(r)dr \tag{2.71}$$

One approach to achieving this is by employing a non-local pseudopotential, where each potential corresponds to distinct components of the pseudopotential's angular momentum. This approach also allows for the determination of the ion's dispersion characteristics in different surroundings.

2.6.4 Ultrasoft pseudopotentials

The effectiveness of norm-conserving pseudopotentials is limited when applied to systems with highly localized valence orbitals like $2p$ and $3d$. This limitation arises from the challenges associated with representing the pseudo wave function using a plane waves basis set. In contrast, ultrasoft pseudopotentials relax the norm-conserving constraint, requiring a smaller number of plane waves. Ultrasoft pseudopotentials are inherently fully nonlocal and transition to a local form outside the core [35]. They depend self-consistently on the charge density, enhancing their transferability. The smoothness of the pseudo wave function can be optimized as the norm-conserving constraint is relaxed. The pseudo wave function can be divided into two parts: (i) the ultrasoft valence wave function, which does not adhere to the norm conservation constraint, and (ii) the core augmentation charge, representing the charge deficit within the core region. The introduction of the ultrasoft valence wave function substantially reduces the plane wave energy cutoff, but the latter feature introduces additional terms in the Kohn-Sham formalism. This complexity results in a higher number of operations required per computational cycle. Despite the increased computational effort, the overall reduction in computational cost achieved by lowering the plane wave energy cutoff is advantageous in many cases.

2.6.5 Projector augmented-wave (PAW) method

In 1994, Blöchl [36] introduced the projector augmented-wave (PAW) method, which integrated concepts from both the pseudopotential approach and the linearized augmented plane wave (LAPW) approach [37, 38]. The fundamental idea is to establish a correspondence between the Kohn-Sham all-electron wave function $|\phi_s^0\rangle$ for state s and a smooth pseudo wave function $|\tilde{\phi}_s^0\rangle$, along with correction terms designed to restore oscillatory behavior within the

core region. This mapping of $|\phi_s^0\rangle$ is achieved through a linear transformation operator $\hat{T}$:

$$|\phi_s^0\rangle = \hat{T}|\tilde{\phi}_s^0\rangle \tag{2.72}$$

Considering that $|\phi_s^0\rangle$ exhibits oscillations near the core region and is smooth beyond a certain threshold, the spatial domain is partitioned into two regions, as per the LAPW method: (i) the augmentation region surrounding the nuclei Ω_a, where a denotes an atom index, and (ii) the interstitial region Ω_i [39]. The definition of Ω_a involves a cutoff radius r_c^a to avoid overlap of augmentation spheres. Since the pseudo wave function should match the all-electron wave function outside Ω_a, the linear transformation $\hat{T}$ is designed to modify $|\phi_s^0\rangle$ solely within the augmentation region. Consequently, $\hat{T}$ can be expressed as follows:

$$\hat{T} = 1 + \sum_a \hat{T}^a \tag{2.73}$$

The contribution of $\hat{T}^a$, which is centered on the atom, alters $|\phi_s^0\rangle$ within Ω_a, the region enclosing the atom. This transformation operator is defined by introducing both the all-electron partial waves φ_j^a and the pseudo partial waves $\tilde{\varphi}_j^a$ within the augmentation region, and can be described as

$$\hat{T} = 1 + \sum_a \sum_j \left(|\varphi_j^a\rangle - |\tilde{\varphi}_j^a\rangle\right) \langle \tilde{p}_j^a| \tag{2.74}$$

In this expression, $|\tilde{p}_j^a\rangle$ represents smooth projector functions. It is important to note that within the augmentation sphere, these projector functions maintain orthogonality with the pseudo partial waves. When this is applied to the all-electron wave function Equation 2.72, the following expression is derived:

$$|\phi_s^0\rangle = |\tilde{\phi}_s^0\rangle + \sum_a \sum_j \left(|\varphi_j^a\rangle - |\tilde{\varphi}_j^a\rangle\right) \langle \tilde{p}_j^a|\tilde{\phi}_s^0\rangle \tag{2.75}$$

The subsequent conditions are valid within the augmentation region, specifically for $\mathbf{r} \in \Omega_a$

$$\begin{aligned} \phi_s^0(\mathbf{r}) &= \phi_s^a(\mathbf{r}) \\ \tilde{\phi}_s^0(\mathbf{r}) &= \tilde{\phi}_s^a(\mathbf{r}) \end{aligned} \tag{2.76}$$

and outside the augmentation region, i.e., when $\mathbf{r} \in \Omega_i$

$$\begin{aligned} \phi_s^0(\mathbf{r}) &= \tilde{\phi}_s^0(\mathbf{r}) \\ \phi_s^a(\mathbf{r}) &= \tilde{\phi}_s^a(\mathbf{r}) \end{aligned} \tag{2.77}$$

where

$$\begin{aligned} \phi_s^a(\mathbf{r}) &= \sum_j \varphi_j^a(\mathbf{r}) \langle \tilde{p}_j^a|\tilde{\phi}_s^0\rangle \\ \tilde{\phi}_s^a(\mathbf{r}) &= \sum_j \tilde{\varphi}_j^a(\mathbf{r}) \langle \tilde{p}_j^a|\tilde{\phi}_s^0\rangle \end{aligned} \tag{2.78}$$

These pseudo wave functions are represented through an expansion in a basis set of plane waves, with a reduced energy cutoff owing to their smooth nature. Both the partial waves and projectors are computed as products of radial functions and spherical harmonics. This approach, known as the PAW method, is recognized for its computational efficiency in electronic structure calculations. In this thesis, DFT calculations have been performed utilizing the PAW method as implemented in VASP.

2.7 Force theorem and geometry optimization

The process of geometry optimization is employed to find the equilibrium configuration where atoms arrange themselves in the ground state. In this process, atoms move in the direction of the force, to minimize the total energy. The equilibrium configuration is achieved when these forces reach a state of equilibrium, typically when they fall within a predefined convergence criterion. These forces are computed using a principle known as the force theorem, or the Hellmann-Feynman theorem [40]. As per this theorem, the force acting on an ion, labeled as I, can be obtained by taking the derivative of the total energy, denoted as E, with respect to the ion's position, $\mathbf{R}_I$.

$$\mathbf{F}_I = -\frac{\partial E}{\partial \mathbf{R}_I} \tag{2.79}$$

where

$$E = \frac{\langle \Psi | H | \Psi \rangle}{\langle \Psi | \Psi \rangle} \tag{2.80}$$

Considering the wave function is normalized, $\langle \Psi | \Psi \rangle = 1$, we get

$$\mathbf{F}_I = -\langle \Psi | \frac{\partial H}{\partial \mathbf{R}_I} | \Psi \rangle - \langle \frac{\partial \Psi}{\partial \mathbf{R}_I} | H | \Psi \rangle - \langle \Psi | H | \frac{\partial \Psi}{\partial \mathbf{R}_I} \rangle \tag{2.81}$$

When $|\Psi\rangle$ is an eigenstate of H, we can write

$$\mathbf{F}_I = -\langle \Psi | \frac{\partial H}{\partial \mathbf{R}_I} | \Psi \rangle - E \frac{\partial}{\partial \mathbf{R}_I} \langle \Psi | \Psi \rangle \tag{2.82}$$

The last term vanishes and we get

$$\mathbf{F}_I = -\langle \Psi | \frac{\partial H}{\partial \mathbf{R}_I} | \Psi \rangle \tag{2.83}$$

Given that Equation 2.83 explicitly relies on the nuclei's positions for the external potential $V_{ext}(\mathbf{r})$ and the nuclei-nuclei interaction term E_{II}, it can be expressed as follows

$$\mathbf{F}_I = -\int d\mathbf{r}\, n(\mathbf{r}) \frac{\partial V_{ext}(\mathbf{r})}{\partial \mathbf{R}_I} - \frac{\partial E_{II}}{\partial \mathbf{R}_I} \tag{2.84}$$

If the chosen basis set is incomplete and reliant on the nuclei positions, it becomes necessary to introduce additional terms, referred to as Pulay correction terms.

In the context of a periodic system, the optimization of the unit cell's shape and volume is essential in addition to the atomic positions. This process involves the calculation of stress, where the application of a strain $\epsilon_{\alpha\beta}$, defined as a spatial scaling $\mathbf{r}_\alpha \rightarrow (\delta_{\alpha\beta} + \epsilon_{\alpha\beta})\,\mathbf{r}_\beta$, leads to the determination of stress $\sigma_{\alpha\beta}$. This is achieved by computing the derivative of the energy concerning the strain, per unit volume [41].

$$\sigma_{\alpha\beta} = -\frac{1}{\Omega}\frac{\partial E}{\partial \epsilon_{\alpha\beta}} \tag{2.85}$$

2.8 Climbing image nudged elastic band (CINEB) method

The nudged elastic band (NEB) method is used for identifying saddle points and determining the minimum energy path (MEP) between reactants and products in various processes, such as chemical reactions, molecular conformation changes, and atomic exchanges [42, 43, 44]. This method entails optimizing a series of intermediate images along the reaction pathway, with each image positioned equidistantly from its neighbors. The optimization process includes the introduction of spring forces connecting the images and considering the force component projection perpendicular to the path. Within this framework, the highest energy configuration among the images corresponds to the saddle point on the MEP, indicating the activation energy barrier. The reactant and product states represent the local minima, and a set of intermediate images between these states is generated through linear interpolation. The interconnection of these images with spring forces forms an elastic band that optimizes the forces along the MEP. However, the traditional elastic band approach faces two main challenges: the sliding down problem and the corner-cutting issue [45, 46, 47]. The former arises when the spring constant is too low, causing the images to shift toward the minima due to the true forces along the path, resulting in decreased resolution around the saddle point. On the other hand, a higher spring constant can lead to spring forces pushing the images away from the true MEP. The convergence of the saddle point is highly sensitive to the choice of the spring constant. To address these challenges, a nudging scheme has been introduced, which eliminates both the parallel and perpendicular components of the true force and spring force. As a result, the total force acting on each image becomes the sum of the perpendicular true force and the spring force

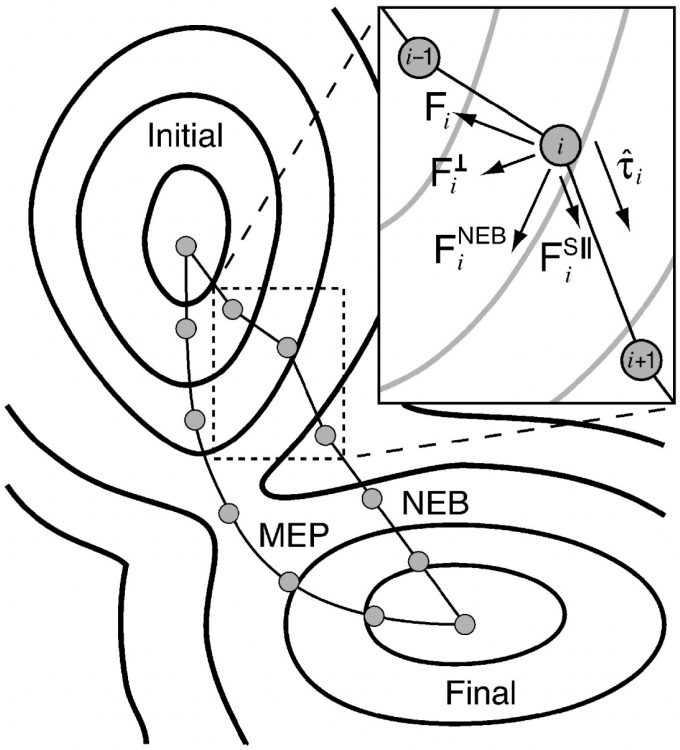

Figure 2.6: Schematic diagram to show the various forces acting on the elastic band during the optimization.

along the local tangent. To illustrate this, let us consider an elastic band with N+1 images [$\mathbf{R}_1$, $\mathbf{R}_2$, ...,$\mathbf{R}_{N-1}$], where $\mathbf{R}_0$ and $\mathbf{R}_N$ represent the initial and final states. Fig. 2.6 shows the forces acting on the i-th image, which can be represented as follows:

$$F_i = F_i^s|_{\parallel} - \nabla E(\mathbf{R}_i)|_{\perp} \tag{2.86}$$

E represents energy, which depends on atomic coordinates. The images along the MEP satisfy the condition: $\nabla E(\mathbf{R}_i)|_{\perp} = 0$. Consequently, the true force expression can be given as

$$\nabla E(\mathbf{R}_i)|_{\perp} = \nabla E(\mathbf{R}_i) - \nabla E(\mathbf{R}_i).\hat{\tau}_i \tag{2.87}$$

For every image i, $\hat{\tau}_i$ is the normalized local tangent and the spring force is given as

$$F_i^s|_{\parallel} = k(|\mathbf{R}_{i+1} - \mathbf{R}_i| - |\mathbf{R}_i - \mathbf{R}_{i-1}|).\hat{\tau}_i \tag{2.88}$$

The spring constant, denoted as k, ensures equal spacing between the images. If this spring constant is allowed to vary as a parameter, it provides greater resolution near the saddle point. This is because the spring constant is connected to the energy of the images. Low-energy images have a weaker spring constant, while those near the saddle point have a stronger one.

However, a limitation of this method is its inability to precisely capture the transition state in the MEP. To address this limitation, a modified approach called the Climbing Image Nudged Elastic Band (CINEB) method has been introduced. This method identifies the highest energy image, labeled as i_{max}, which is not influenced by spring forces and experiences a reversed force – the true force acting in the opposite direction of the elastic band. This imax image is known as the climbing image, and the force acting on it is determined as follows:

$$\begin{aligned} F_{i_{max}} &= -\nabla E(\mathbf{R}_{i_{max}}) + 2\nabla E(\mathbf{R}_{i_{max}})|_{\parallel} \\ &= -\nabla E(\mathbf{R}_{i_{max}}) + 2\nabla E(\mathbf{R}_{i_{max}})|_{\parallel}.\hat{\tau}_i\hat{\tau}_i \end{aligned} \tag{2.89}$$

This approach allows us to identify the climbing image with the highest energy along the path and the images with the lowest energy perpendicular to the path in all directions. Consequently, it ensures the accurate determination of the saddle point's location and guarantees the convergence of the MEP. This makes the CINEB method a suitable choice for accurately calculating the activation barrier of chemical reactions.

2.9 Cascade genetic algorithm (cGA)

The Genetic Algorithm (GA) is a widely applied optimization method inspired by natural evolution processes in scientific and technological fields. It identifies global minima and perform thorough searches of potential energy surfaces (PES) to discover low-energy structures **??**. In this thesis, we have applied the massively parallel cascade genetic algorithm (cGA) for studying metal oxide clusters [48]. In the cGA approach, each subsequent level employs a more accurate level of theory and leverages information from the lower levels. This cascade process helps filter out unsuitable structures, enhancing the search efficiency. The working of cGA is outlined in Fig. 2.7. The initial step involves generating a random pool of structures, ensuring that the minimum distance between neighboring atoms is greater than 1.21 Å. The subsequent stage involves local optimization, where multiple energy and force optimizations occur. This step is computationally intensive and time-consuming, particularly at the ab initio level. To reduce computational costs, local optimization for the initial pool is performed using semi-local functionals and lower-level settings. The most suitable structures falling within an energy range of 2.5 eV from the initial level are advanced to the subsequent stage of the cascade. Here, the chosen structures undergo relaxation using higher-level configurations. Following this relaxation, their single-point energies are determined employing hybrid functionals at a higher level

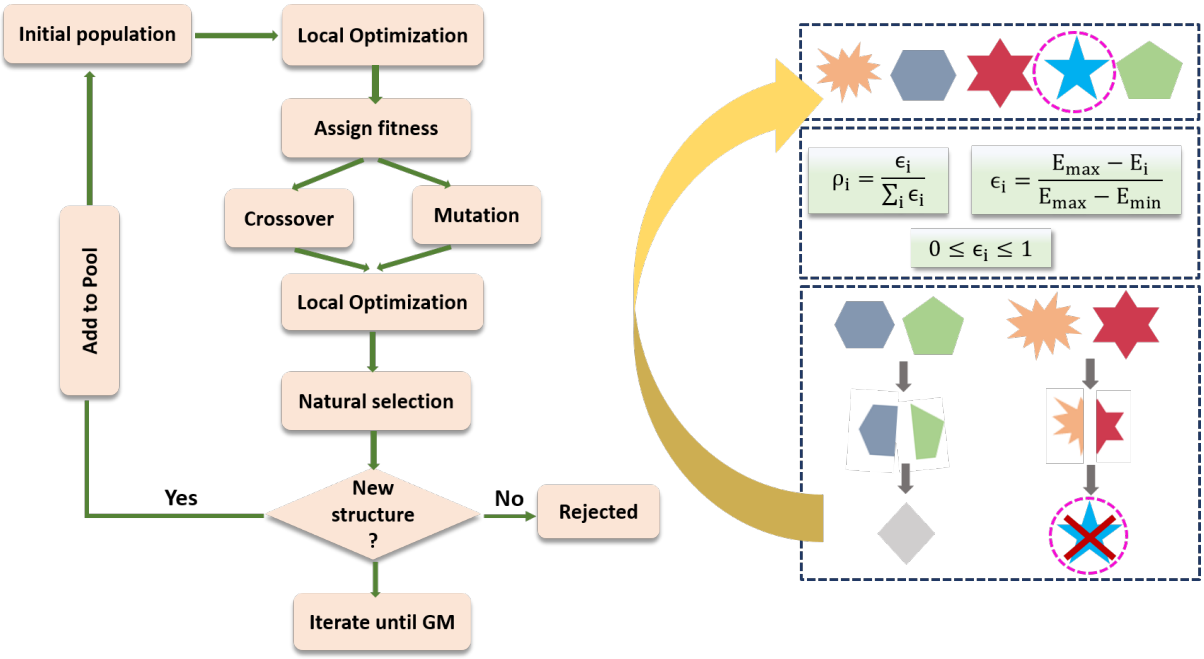

Figure 2.7: Flow chart of cascade genetic algorithm.

of settings. With these energy considerations, a fitness value (ρ_i) normalized to the cluster's energetics is assigned to each ith cluster, given by

$$\rho_i = \frac{\epsilon_i}{\sum_i \epsilon_i} \tag{2.90}$$

where ϵ_i is the relative energy of the ith cluster, defined as:

$$\epsilon_i = \frac{E_{max} - E_i}{E_{max} - E_{min}} \tag{2.91}$$

Here, E_i represents the total energy of the i-th cluster in the population. E_{min} and E_{max} denote the lowest and highest total energies within the population pool, respectively. As per the condition outlined above, it becomes evident that clusters with lower energy (i.e., more negative values) exhibit high fitness, while clusters with higher energy (less negative values) demonstrate low fitness.

$$0 < \rho_i < 1 \tag{2.92}$$

When E_i = E_{max}, the corresponding ρ_i will be 0, indicating poor fitness of the structure. Selection of two structures for crossover and mutation from the pool is guided by the fitness function. The structures with higher fitness values have a greater probability of being chosen. The effectiveness and precision of cGA across various levels of theory and settings concerning advanced theory are extensively discussed in [48]. It is worth noting that selecting an appropriate functional for estimating the fitness function is crucial for a meaningful exploration of the PES.

The fitness function plays a crucial role in determining the selection probabilities for structures from the pool when applying mating operators (crossover and mutation) to generate structures in the next generation. This fitness function dictates the likelihood of structures being selected from the pool for mating operations, such as crossover and mutation, in generating the next generation of structures. Structures with higher fitness values have a greater chance of being selected from the pool, thereby increasing the likelihood of retaining advantageous structural characteristics during the evolutionary process. The performance of cGA relies significantly on the choice of crossover operators. In our approach, we have integrated three distinct crossover methods to achieve the most favorable outcomes as swiftly as feasible, minimizing the overall scanning time.

Subsequently, we also permit the selection of a limited number of structures with high ρ_i values for mating operations to prevent premature convergence to a local minimum in the genetic algorithm scheme. Following local optimization of the offspring with higher-level configurations, their energies and radial distribution functions are employed to assess the uniqueness of the newly constructed structure compared to the ones already present. This ensures that duplicate candidates are not unnecessarily added to the pool. It is worth noting that a new candidate is only included if no identical copy already exists in the pool; otherwise, it is omitted. This iterative process continues until the specified convergence criteria are met. Notably, there is not a strict criterion for determining the convergence threshold in global scanning. A practical approach is to run the cascade genetic algorithm for an extended duration until no significant improvements in fitness values are achieved beyond the current optimal one. In our specific case, we extended the scanning process to at least twice the time needed to discover the genuine global minimum. Furthermore, if no updated lowest minima are found during this extended period, we can reasonably assume that the global minimum has been identified. For additional insights and validation of the cascade genetic algorithm, please refer to [48]. In the cGA, the fitness criteria are determined by calculating the energetics at the hybrid level, providing a more dependable exploration of all low-energy isomers.

2.10 *Ab initio* atomistic thermodynamics (*aiAT*)

DFT determines the ground-state properties via electronic structure calculations at zero-temperature and pressure conditions, operating within the microscopic realm. It enables the

computation of the potential energy surface (PES) $E(\{\mathbf{R}_I\})$, where $\{\mathbf{R}_I\}$ represents the atomic configuration. *ab initio* atomistic thermodynamics takes into account the influence of finite temperature and pressure by leveraging the DFT-derived PES to calculate relevant thermodynamic potentials, such as the Gibbs free energy [49]. Consequently, the integration of thermodynamics with DFT calculations yields macroscopic system properties. This approach is particularly valuable for larger systems, which can be partitioned into smaller subsystems maintaining thermal equilibrium. These interconnected subsystems are characterized by their respective thermodynamic potentials.

2.10.1 Thermodynamic potentials

The state of a thermodynamic system can be described in terms of various thermodynamic potentials. These potentials include the internal energy U, Helmholtz free energy $F = U - TS$, enthalpy $H = U + pV$, and Gibbs free energy $G = U + pV - TS = H - TS = F + pV$. These thermodynamic potentials depend on specific natural variables, namely temperature (T), entropy (S), pressure (p), and volume (V). When a system is held at constant T and V, it minimizes its Helmholtz free energy. Conversely, at constant (T, p), it aims to minimize its Gibbs free energy. In practice, chemical reactions occur under conditions of constant T and p, making the Gibbs free energy the most applicable thermodynamic potential for determining the stable equilibrium geometry under specific environmental conditions.

2.10.2 Partition function

The partition function (q_N) provides insights into how energy is distributed among different energy levels. Essential thermodynamic properties such as average energy (U), Helmholtz free energy (F), Gibbs free energy (G), chemical potential (μ), entropy (S), and pressure (p) can be derived from the partition function and its derivatives.

$$q_N = \sum_i e^{\beta E_i} \tag{2.93}$$

In the above equation, $\beta = \frac{1}{k_B T}$, where i represents the microstate index, and E_i corresponds to the total energy of the system in the specific microstate. The partition function for a continuous system is given by

$$q_N = \frac{1}{h^f} \int e^{\beta E_i} d^f q d^f p \tag{2.94}$$

Here, h represents the Planck constant, while f signifies the number of degrees of freedom. For a molecule consisting of N atoms, it possesses $3N$ degrees of freedom. Among these $3N$ degrees of freedom, three are associated with rotational motion, and the remaining $3N$–6 are vibrational (non-linear molecules). Linear molecules exhibit two rotational degrees of freedom and $3N$–5 vibrational degrees of freedom. For indistinguishable particles:

$$q_N = \frac{1}{h^f N!} \int e^{\beta E_i} d^f q d^f p \tag{2.95}$$

The partition function of an ideal gas made up of N identical molecules is given as

$$q_N = \frac{1}{N!}[q]^N \tag{2.96}$$

and for distinguishable molecules:

$$q_N = [q]^N \tag{2.97}$$

When N = 1 (a single molecule), q represents the partition function of a single molecule. The various modes of motion, such as translational (trans), rotational (rot), vibrational (vib), configurational (conf), electronic (elect), and nuclear (nucl), collectively constitute the total energy of a molecule.

$$q = \sum_i e^{-\beta E_i^{trans} - \beta E_i^{rot} - \beta E_i^{vib} - \beta E_i^{conf} - \beta E_i^{elect} - \beta E_i^{nucl}} \tag{2.98}$$

$$\begin{aligned} q = & \left(\sum_i e^{-\beta E_i^{trans}} \right) \left(\sum_i e^{-\beta E_i^{rot}} \right) \left(\sum_i e^{-\beta E_i^{vib}} \right) \\ & \left(\sum_i e^{-\beta E_i^{conf}} \right) \left(\sum_i e^{-\beta E_i^{elect}} \right) \left(\sum_i e^{-\beta E_i^{nucl}} \right) \end{aligned} \tag{2.99}$$

Therefore, the total partition function for a single molecule is made up of individual contributions, enabling us to compute each component independently. This decomposition is facilitated by the Born–Oppenheimer approximation, which separates the nuclear/electronic part from the vibrational/rotational components. Additionally, the vibrational and rotational components can be treated separately since these motions occur on distinct time scales [50].

$$q = q^{trans} \times q^{rot} \times q^{vib} \times q^{conf} \times q^{elect} \times q^{nucl} \tag{2.100}$$

where

$$q^{trans} = \left(\frac{2\pi m k_B T}{h^2} \right)^{\frac{3}{2}} V = \left(\frac{2\pi m k_B T}{h^2} \right)^{\frac{3}{2}} \frac{k_B T}{p} \tag{2.101}$$

m represents the mass of the molecule, and we have made use of ideal gas approximation to derive this partition function. It is worth noting that the nuclear state remains relatively unchanged during chemical processes, which is why the q^{nucl} term does not significantly affect thermodynamic changes.

$$q^{rot} = \frac{8\pi^2 I_A k_{\mathrm{B}} T}{h^2}, \text{(linear molecules)} \tag{2.102}$$

$$q^{rot} = 8\pi^2 \left(\frac{2\pi k_{\mathrm{B}} T}{h^2}\right)^{\frac{3}{2}} (I_A I_B I_C)^{\frac{3}{2}}, \text{(non-linear molecules)} \tag{2.103}$$

$$q^{vib} = \prod_i \left[e^{-\frac{h\nu_i}{2k_{\mathrm{B}}T}} \left(1 - e^{-\frac{h\nu_i}{k_{\mathrm{B}}T}}\right)^{-1}\right] \tag{2.104}$$

$$q^{conf} = \frac{1}{\sigma} \tag{2.105}$$

$$q^{elect} = \sum_i \left(\mathcal{M}_i e^{-\frac{E_i}{k_{\mathrm{B}}T}}\right) \approx \mathcal{M} e^{-\frac{E^{DFT}}{k_{\mathrm{B}}T}} \tag{2.106}$$

I_A, I_B, and I_C represent the molecule's moment of inertia, while ν_i corresponds to the vibrational frequencies of the molecule. It is important to emphasize that we have adopted the harmonic approximation to account for the vibrational modes. σ denotes the count of symmetry operations based on the molecule's symmetry point group, representing the number of indistinguishable orientations. For diatomic molecules, σ = 1 for heteroatomics and σ = 2 for homoatomics. E^{DFT} signifies the ground-state energy, and $\mathcal{M}$ stands for the spin multiplicity. It is worth mentioning that in this context, we have not considered any interaction among the first excited state and the ground state.

2.10.3 Chemical potential

The chemical potential of oxygen, $\mu_{\mathrm{O}}(T, p_{\mathrm{O_2}})$, as a function of temperature and pressure is determined by establishing thermodynamic equilibrium with the surrounding gas-phase reservoir. This reservoir can be approximated as an ideal gas consisting of N indistinguishable $\mathrm{O_2}$ molecules. Consequently, $\mu_{\mathrm{O}}(T, p_{\mathrm{O_2}})$ is expressed as

$$\mu_{\mathrm{O}}(T, p_{\mathrm{O_2}}) = \frac{1}{2}\mu_{\mathrm{O_2}}(T, p_{\mathrm{O_2}}) = \frac{1}{2}\left(-k_{\mathrm{B}} T \ln Q^{\mathrm{tot}}_{\mathrm{O_2}} + p_{\mathrm{O_2}} V\right)/N \tag{2.107}$$

Here, k_B represents the Boltzmann constant, and V signifies the volume. The evaluation of the partition function for an ideal O_2 gas, $Q^{tot}_{O_2}$, proceeds as follows:

$$Q^{tot}_{O_2} = \frac{1}{N!}\left(q_{O_2}\right)^N = \frac{1}{N!}\left(q^{trans}\, q^{rot}\, q^{vib}\, q^{electr}\, q^{nucl}\right)^N \tag{2.108}$$

q_{O_2} represents the partition function for a single O_2 molecule. This partition function can be further divided into distinct components using Born-Oppenheimer approximation. Using Equation 2.108 and 2.107, we get

$$\begin{aligned}\mu_O(T, p_{O_2}) = &-\frac{1}{2N}\left[k_B T \ln\left(\frac{1}{N!}(q^{trans})^N\right) - p_{O_2} V\right] \\ &+ \frac{1}{2}\mu^{rot} + \frac{1}{2}\mu^{vib} + \frac{1}{2}\mu^{electr} + \frac{1}{2}\mu^{nucl}\end{aligned} \tag{2.109}$$

where, the individual terms can be written as

$$\begin{aligned}-\frac{1}{2N}\left[k_B T \ln\left(\frac{1}{N!}(q^{trans})^N\right) - p_{O_2} V\right] &= -\frac{1}{2} k_B T \ln\left[\left(\frac{2\pi m}{h^2}\right)^{3/2} \frac{(k_B T)^{5/2}}{p_{O_2}}\right] \\ \mu^{rot} &\approx -k_B T \ln\left(\frac{8\pi^2 I k_B T}{\sigma h^2}\right) \\ \mu^{vib} = E^{ZPE} + \Delta\mu^{vib} &= \sum_{i=1}^{M}\left[\frac{\hbar\omega_i}{2} + k_B T \ln\left(1 - \exp\left(-\frac{\hbar\omega_i}{k_B T}\right)\right)\right] \\ \mu^{electr} &\approx E^{total}_{O_2} - k_B T \ln \mathcal{M}\end{aligned} \tag{2.110}$$

The chemical potential of oxygen can be written as

$$\mu_O(T, p_{O_2}) = \mu^{ref}_O + \Delta\mu_O(T, p_{O_2}) \tag{2.111}$$

where $\mu^{ref}_O = \frac{1}{2}E_{O_2} + \frac{1}{2}E^{ZPE}_{O_2}$ is a reference chemical potential while $\Delta\mu_O(T, p_{O_2})$ has all the temperature and pressure dependent contributions

$$\begin{aligned}\Delta\mu_O(T, p_{O_2}) = \frac{1}{2}\Bigg[&-k_B T \ln\left[\left(\frac{2\pi m}{h^2}\right)^{\frac{3}{2}} (k_B T)^{\frac{5}{2}}\right] \\ &+ k_B T \ln p_{O_2} - k_B T \ln\left(\frac{8\pi^2 I k_B T}{h^2}\right) \\ &+ k_B T \ln\left[1 - \exp\left(-\frac{\hbar\omega_O}{k_B T}\right)\right] \\ &- k_B T \ln \mathcal{M} + k_B T \ln \sigma\Bigg]\end{aligned} \tag{2.112}$$

It is crucial to maintain a consistent selection of the chemical potential reference. Additionally, the choice of an appropriate ϵ_{xc} functional is important when calculating energies.

2.11 Many-body perturbation theory (MBPT): The Green's function approach

DFT has proven to be a robust method for evaluating the ground-state properties of many-electron systems such as lattice parameters, phase transitions, charge density, and bulk modulus. In practical DFT applications, the actual interacting system is substituted with a non-interacting fictitious counterpart, both of which share an identical ground-state density. Solving the Kohn-Sham equation for this fictitious system provides us with single-particle eigenstates and eigenvalues. It is important to note, however, that these eigenvalues do not directly represent excitation energies. Instead, they are mathematical tools and do not possess an inherent physical meaning, with the exception of the highest occupied state, which corresponds to the system's exact ionization energy [51, 52]. In many instances, DFT falls short in accurately predicting properties related to excited states, such as band gaps and optical absorption. Consequently, delving beyond DFT becomes imperative when exploring many-body physics. The Green's function formulation of many-body perturbation theory (MBPT) [53] offers a promising approach for addressing these challenges. MBPT encompasses the one-particle Green's function approach, known as the GW method for charged excitations, and the two-particle Green's function approach, referred to as the Bethe-Salpeter Equation (BSE) for neutral excitations.

In experimental settings, the determination of band gaps relies on excited-state spectroscopy techniques. As illustrated in Fig. 2.8, this involves examining both charged and neutral excitations. In direct photoemission, when a sample is exposed to light, an electron is emitted from the material. This process allows for the calculation of the ionization potential (IP) by assessing the total energy difference between a system with N electrons and one with N-1 electrons. Conversely, in inverse photoemission, an electron is introduced into the system, resulting in the emission of a photon. Here, the electron affinity (EA) is determined by evaluating the total energy difference between a system with N electrons and one with N+1 electrons. Both direct and inverse photoemission spectroscopies provide insights into the excitation energy of individual charge carriers, be it electrons or holes. From a theoretical perspective, these processes can be explored using the one-particle Green's function approach, specifically the GW approximation. Furthermore, in the context of optical absorption, when an electron is excited from the valence band to the conduction band upon photon absorption, it may appear as a combination

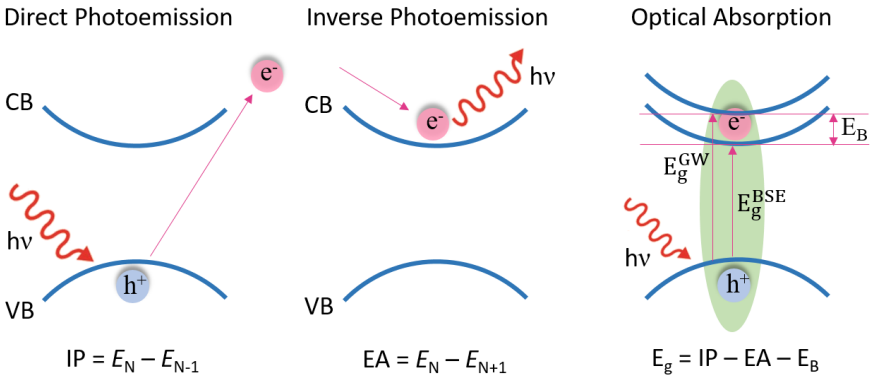

Figure 2.8: Schematic representation of excited-state spectroscopies, namely, direct photoemission, inverse photoemission, and optical absorption. Here, IP and EA represent the ionization potential and electron affinity, respectively. Also, E_N is the total energy of N-electron system. Moreover, $\mathrm{E_g^{GW}} = \mathrm{IP} - \mathrm{EA}$ is the quasiparticle (QP) band gap and $\mathrm{E_g^{BSE}} = \mathrm{IP} - \mathrm{EA} - \mathrm{E_B}$ is the optical band gap, where $\mathrm{E_B}$ is the exciton binding energy.

of direct and inverse photoemission. However, it is crucial to note that the excited electron and hole do not act as independent entities and cannot be studied separately. Instead, they form a bound state known as an exciton. This electron-hole interaction is theoretically well-described through a two-particle Green's function approach, i.e., BSE.

2.11.1 Green's function

Theoretical descriptions of processes involving the injection or ejection of electrons require a framework that connects N-particle and $(N\pm1)$-particle systems. This can be achieved through the use of MBPT. At the core of MBPT is the time-ordered Green's function, $G\left(\mathbf{r}t, \mathbf{r}'t'\right)$, which contains information about excitation energies and lifetimes. The definition of the one-particle Green's function is as follows:

$$\begin{aligned} G\left(\mathbf{r}t, \mathbf{r}'t'\right) = &- i\langle\Psi_0^N|\hat{\psi}(\mathbf{r}t)\hat{\psi}^\dagger(\mathbf{r}'t')|\Psi_0^N\rangle\Theta(t-t') \\ &+ i\langle\Psi_0^N|\hat{\psi}^\dagger(\mathbf{r}'t')\hat{\psi}(\mathbf{r}t)|\Psi_0^N\rangle\Theta(t'-t) \end{aligned} \tag{2.113}$$

where $\Theta(t-t')$ represent the Heaviside step function and is given as

$$\Theta(t-t') = \begin{cases} 1 & \text{if } t > t' \\ 0 & \text{if } t < t' \end{cases}$$

$|\Psi_0^N\rangle$ denotes the ground state of an N-electron system. The field operators $\hat{\psi}^\dagger(\mathbf{r}t)$ and $\hat{\psi}(\mathbf{r}t)$ are responsible for creating and annihilating electrons, respectively, at a given position $\mathbf{r}$ and time t. In the Heisenberg picture, we can express $\hat{\psi}(\mathbf{r}t) = e^{i\hat{H}t}\hat{\psi}(\mathbf{r})e^{-i\hat{H}t}$. When $t > t'$, the Green's function generates an electron in the system at $\mathbf{r}'$ and t', subsequently guiding it to position $\mathbf{r}$, where it is annihilated at time t. Conversely, for $t < t'$, it characterizes the propagation of a hole. This function is commonly referred to as a propagator.

The transition from the time domain to the energy domain to obtain the spectral representation of the Green's function can be achieved through a Fourier transform, resulting in the following mathematical expression

$$G(\mathbf{r},\mathbf{r}',\omega) = \lim_{\eta\to 0^+}\sum_s \psi_s(\mathbf{r})\psi_s^*(\mathbf{r}') \times \left[\frac{\Theta(\epsilon_s - E_F)}{\omega - (\epsilon_s - i\eta)} + \frac{\Theta(E_F - \epsilon_s)}{\omega - (\epsilon_s + i\eta)}\right] \tag{2.114}$$

where the excitation energies (ϵ_s) are

$$\epsilon_s = \begin{cases} E_N - E_{N-1} & \text{for } \epsilon_s < E_F \\ E_{N+1} - E_N & \text{for } \epsilon_s \geq E_F \end{cases}$$

and the transition amplitudes ($\psi_s(\mathbf{r})$) from the N to the $N \pm 1$-body states are expressed as

$$\psi_s(\mathbf{r}) = \begin{cases} \langle \Psi_s^{N-1}|\hat{\psi}(\mathbf{r})|\Psi_0^N\rangle & \text{for } \epsilon_s < E_F \\ \langle \Psi_0^N|\hat{\psi}(\mathbf{r})|\Psi_s^{N+1}\rangle & \text{for } \epsilon_s \geq E_F \end{cases}$$

E_F represents the Fermi level. The inclusion of a small imaginary part η is essential to ensure the convergence of the Fourier transform. Within Equation 2.114, ω represents an energy (frequency). The excitation energies of the many-body system can be determined from the poles of the Green's function. The relationship between the spectral function, which describes the density of excited states, and the Green's function is as follows

$$\begin{aligned} A(\mathbf{r},\mathbf{r}',\omega) &= \frac{1}{\pi}\left|\text{Im } G(\mathbf{r},\mathbf{r}',\omega)\right| \\ &= \sum_s \psi_s(\mathbf{r})\psi_s^*(\mathbf{r}')\delta(\omega - \epsilon_s) \end{aligned} \tag{2.115}$$

When considering non-interacting electrons, the particles exhibit an infinite lifetime. Consequently, the spectral function displays a series of delta peaks, each corresponding to a specific transition (refer to the delta peaks for non-interacting particles in Fig. 2.9). However, experimental observations show that the peak positions exhibit finite widths, typically attributed to

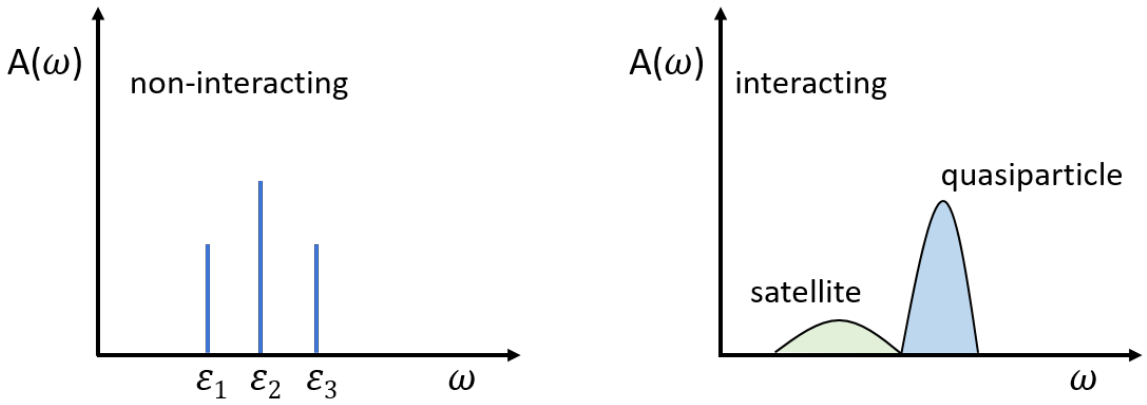

Figure 2.9: Schematic representation of spectral function in the case of non-interacting (electrons) single-particle excitation and interacting single-particle like (QP) excitation.

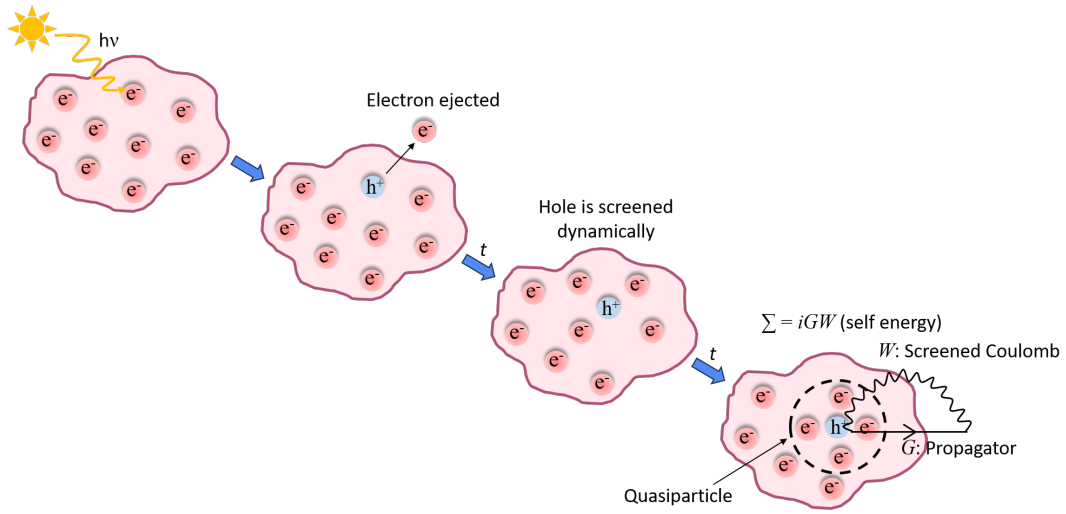

Figure 2.10: Illustration of a QP formation in the case of photoemission spectroscopy.

single-particle-like excitations (QP) (as depicted in Fig. 2.9). These wider peaks are the result of multiple closely positioned delta peaks merging together. Additionally, there is often a broader peak with lower intensity known as the satellite peak. In summary, the spectral function provides insights not only into the position of the QP peak but also into: (i) the excitation's lifetime due to electron-electron interactions, inversely related to the width of the QP peak, and (ii) the spectral weight of the QP. Consequently, the spectral function can also be written as

$$A \approx \frac{1}{\pi} \left| \frac{Z_s}{\omega - (\epsilon_s + i\Gamma)} \right| \tag{2.116}$$

The QP weight, denoted as Z_s, and the peak width, represented as Γ , are significant parameters. Fig. 2.10 illustrates the QP concept in real-space.

A charged particle enveloped by a polarization cloud is considered a QP. In the context

of photoemission spectroscopy, when the system evolves following the ejection or creation of an electron or hole, the surrounding electrons encase the "bare" hole. This surrounding process results in the screening of the hole's interaction with the rest of the system and leads to the concept of self-energy. In other words, it reflects the energy experienced by the particle because of its own presence.

2.11.2 Dyson's equation

Calculating the precise one-particle Green's function is an impractical task, necessitating the use of a viable approximation. The connection between the Green's function and Σ is established through Dyson's equation, as presented below

$$G(\mathbf{r},\mathbf{r}',\omega) = G_0(\mathbf{r},\mathbf{r}',\omega) + \int\int G_0(\mathbf{r},\mathbf{r}'',\omega)\Sigma(\mathbf{r}'',\mathbf{r}''',\omega)G(\mathbf{r}''',\mathbf{r}',\omega)d\mathbf{r}''d\mathbf{r}''' \tag{2.117}$$

Here, the non-interacting Green's function, denoted as $G_0(\mathbf{r},\mathbf{r}',\omega)$, is derived from mean-field theory and satisfies the following equation

$$\hat{h}_0\phi_i^0(\mathbf{r}) = \epsilon_i^0\phi_i^0(\mathbf{r}) \tag{2.118}$$

where the single-particle Hamiltonian is:

$$\hat{h}_0 = -\frac{1}{2}\nabla^2 + V_{\text{ext}}(\mathbf{r}) + \int \frac{n(\mathbf{r}')}{|\mathbf{r}-\mathbf{r}'|}d\mathbf{r}' \tag{2.119}$$

The eigenstates and eigenvalues, denoted as $\phi_i^0(\mathbf{r})$ and ϵ_i^0, respectively, represent the non-interacting system. The non-local self-energy operator Σ, which is dependent on energy (frequency) and non-Hermitian, encompasses all many-body exchange and correlation effects. The Dyson equation can be transformed into an effective single-particle equation, serving to describe the behavior of QP.

$$\hat{h}_0(\mathbf{r})\psi_s(\mathbf{r}) + \int \Sigma(\mathbf{r},\mathbf{r}',\epsilon_s)\psi_s(\mathbf{r}')d\mathbf{r}' = \epsilon_s\psi_s(\mathbf{r}) \tag{2.120}$$

These wavefunctions $\psi_s(\mathbf{r})$ make up a complete set, but lack orthonormality because of the energy-dependent self-energy operator. The Dyson equation may also be expressed algebraically as

$$\begin{aligned} G &= G_0 + G_0\Sigma G_0 + G_0\Sigma G_0\Sigma G_0 + ... \\ G &= G_0 + G_0\Sigma G \end{aligned} \tag{2.121}$$

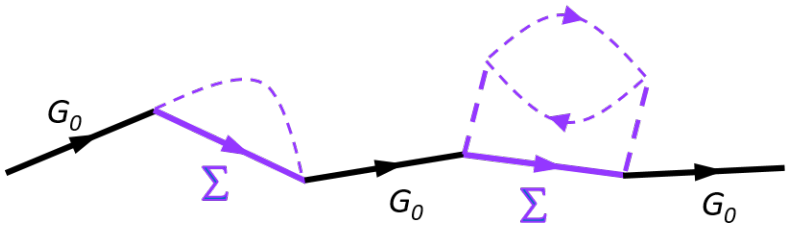

Figure 2.11: Schematic representation of the Dyson's equation, which relates the non-interacting (G_0) and interacting (G) Green's functions via the self-energy operator (Σ). Here, the black arrow describes the propagation of a non-interacting particle and the viloet color represents screening process of different orders.

The schematic illustration of Dyson equation is shown in Fig. 2.11. The various components in Equation 2.121 correspond to single, double, and so on, scattering events with Σ representing the scattering potential. Consequently, the self-energy can be considered as the cumulative effect of all these scattering events. Nonetheless, accurately determining the exact Σ associated with multiple scattering processes is a complex task. Hence, a suitable approximation becomes necessary to assess it.

2.11.3 *GW* approximation: Hedin's equations

With the help of polarizability (P) and the vertex function (Γ), Hedin formulated a system of five self-consistent integro-differential equations in 1965 [19]. These equations connect the self-energy with the Green's function and the screened Coulomb interaction (W).

$$\begin{aligned}
G(1,2) &= G_0(1,2) + \int d(3,4) G_0(1,3)\Sigma(3,4)G(4,2) \\
P(1,2) &= -i \int d(3,4) G(2,3)G(4,2^+)\Gamma(3,4;1) \\
W(1,2) &= v(1,2) + \int d(3,4) W(1,3)P(3,4)v(4,2) \\
\Sigma(1,2) &= i \int d(3,4) G(1,4)W(1^+,3)\Gamma(4,2;3) \\
\Gamma(1,2;3) &= \delta(1,2)\delta(1,3) + \int d(4,5,6,7) \frac{\delta\Sigma(1,2)}{\delta G(4,5)} G(4,6)G(7,5)\Gamma(6,7;3)
\end{aligned} \tag{2.122}$$

Here, we employ the notation $1 = (\mathbf{r}_1, t_1)$, and v represents the unscreened (bare) Coulomb interaction. Additionally, 1^+ denotes $(\mathbf{r}_1, t_1 + \eta)$, with η being a small positive value. Fig. 2.12 shows the self-consistent iterative process diagrammatically. Within this framework, the vertex function encompasses higher-order corrections to the interaction between QPs. Calculating this term can be particularly challenging, given its functional derivative nature and its dependency

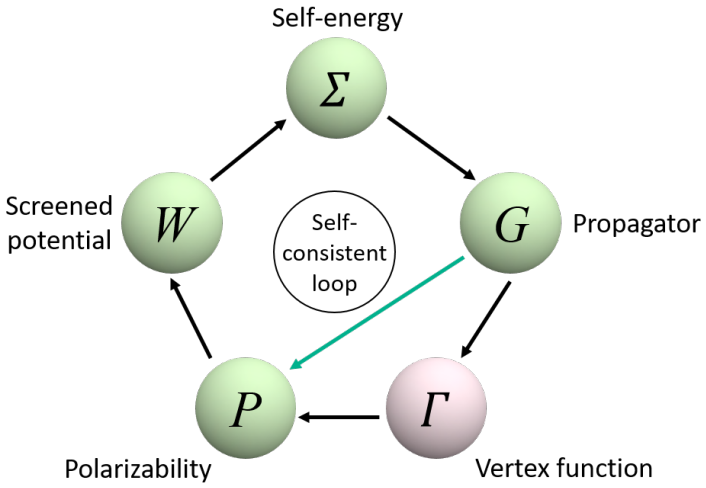

Figure 2.12: Schematic representation of the self-consistent Hedin's equations.

on three spacetime points. As a result, to streamline these equations, approximations are often applied to the vertex function.

Neglecting the functional derivative of the self-energy with respect to the Green's function in the GW approximation results in

$$\begin{aligned} \Gamma(1,2;3) &= \delta(1,2)\delta(1,3) \\ P(1,2) &= -iG(1,2^+)G(2,1) \\ \Sigma(1,2) &= iG(1,2)W(1^+,2) \end{aligned} \tag{2.123}$$

Therefore, in the GW approximation, the self-energy emerges as the outcome of the interplay between the Green's function and the screened Coulomb interaction. The GW approach shares similarities with Hartree-Fock theory, where the dynamically screened Coulomb interaction is replaced by the bare Coulomb interaction.

2.11.4 Implementation of the single-shot *GW* (G_0W_0)

In a standard GW computation, the initial step involves acquiring ground state orbitals and orbital eigenvalues through DFT. Subsequently, GW corrections to the eigenvalues are determined by employing the GW method (single-shot or self-consistent). The choice of the initial approach (LDA/PBE/HSE06) is critical, as it significantly influences the QP energies. Therefore, we need to choose the starting point carefully. In many scenarios, G_0W_0 calculations provide band gap values that align well with experimental data [54, 55]. Additionally, a self-consistent GW (scGW) approach is an option, where both QP energies and their corresponding

orbitals are updated in a self-consistent manner [56]. However, it is worth noting that the scGW method tends to overestimate band gaps compared to experimental measurements [57]. The introduction of self-consistency without considering vertex corrections can lead to discrepancies with experimental results. In our thesis, we primarily employed the single-shot GW approach.

CHAPTER 3

Heterogeneous catalysis in energy applications

3.1 Theoretical insights into C−H bond activation of methane by transition metal clusters: the role of anharmonic effects

3.1.1 Introduction

Methane, the primary component of natural gas, is an abundant, cost-effective, and environmentally friendly energy source [58, 59, 60, 61, 62, 63]. The world's growing dependence on petroleum, coal, and other non-renewable resources has prompted extensive research into more efficient ways to harness natural gas. While carbon dioxide (CO_2) typically garners attention as the primary greenhouse gas, it's worth noting that methane, due to its widespread presence and considerable stability, is actually more potent in terms of its contribution to the greenhouse effect than carbon dioxide. Therefore, there is a growing interest in developing methods to convert methane into valuable chemical products [64]. One critical method for efficiently utilizing the abundant natural gas is the production of synthesis gas (syngas), a gaseous mixture composed of carbon monoxide (CO) and hydrogen (H_2). Syngas plays a vital role in various industrial processes, including the production of methanol, liquid hydrocarbons, ammonia, and dimethyl ether [65, 66, 67]. However, the efficient activation of methane has been a significant challenge due to the strong C−H bonds in methane, characterized by their high bond strength (4.5 eV), low polarizability, and negligible electron affinity, making it one of the least reactive hydrocarbons [68, 69, 70]. Given methane's extreme inertness, transforming it into chemical products presents difficulties. To address this problem, a suitable catalyst must be developed. The catalytic conversion of methane is one of the most appealing fields of study in

both academia and industry [71, 72, 73, 74, 75, 76, 77, 78, 79, 80, 81, 82].

Transition metal (TM) clusters are renowned for their efficient catalytic activity in both homogeneous and heterogeneous reactions [83, 84, 85, 86, 87, 88]. This remarkable catalytic performance can be largely attributed to their partially occupied d-shells, enabling them to exhibit multiple oxidation states in their complexes [89, 90, 91]. When studying heterogeneous catalysis, it is crucial to identify the active species and determine the catalyst's structure [92]. The catalyst assumes various structures under reaction conditions, with different atom numbers and oxidation states, all of which can play a role in the catalytic process to varying degrees. As a result, gaining a comprehensive understanding of catalysis demands a robust methodological approach that integrates various levels of theory into a cohesive multi-scale simulation [93].

Extensive experimental and theoretical investigations have elucidated that the reactivity of small gas-phase metal clusters is strongly influenced by their size, as the number of atoms plays a significant role [94, 95, 96, 97]. Notably, as the cluster size decreases, intriguing size-dependent phenomena become apparent, introducing various size effects with important implications [91, 98, 99, 100]. Furthermore, a material's properties can undergo substantial changes when exposed to operational environments, particularly in the presence of reactive molecules. This naturally gives rise to essential questions, such as determining the composition and structures of species within a real catalyst and understanding how these catalysts alter their structure and catalytic properties upon the adsorption of different ligand molecules. In light of these considerations, there is a compelling need to provide theoretical insights that guide experimental investigations towards understanding the stoichiometry and stability of clusters under realistic conditions. To approach this from a theoretical perspective, we examine a prototypical model system featuring nickel (Ni_4, chosen as a tetrahedral nickel cluster renowned for its high selectivity [101, 102, 103]) in a reactive environment consisting of O_2 and CH_4 gas molecules under realistic conditions. It's worth noting that Ni-based catalysts have gained widespread usage in catalysis due to their cost-effectiveness, high selectivity, and activity, and they have been the focus of extensive research over the years [104, 105, 106, 107, 108, 109]. Typically, in the presence of a reactive atmosphere, clusters adsorb surrounding gas molecules, giving rise to intermediate phases denoted as $[Ni_4O_x(CH_4)_y]$ at thermodynamic equilibrium. These intermediate phases often exhibit high reactivity and find applications in various aspects of heterogeneous catalysis, underscoring the importance of understanding their stable stoichiometries.

In this chapter, we have investigated the role of environment [i.e., temperature (T), partial

pressure of oxygen (p_{O_2}) and partial pressure of methane (p_{CH_4})] to understand the thermodynamic stability of different configurations of $Ni_4O_x(CH_4)_y$ ($0 \leq x \leq 8$, $0 \leq y \leq 3$) clusters in a reactive atmosphere of O_2 and CH_4 molecules. As a first step, a systematic scanning of potential energy surface (PES) is done via cascade genetic algorithm (cGA) [48, 110, 111] approach to obtain the global minimum (GM) configurations of $Ni_4O_x(CH_4)_y$ clusters. Subsequently, we have employed *ab initio* atomistic thermodynamics (*ai*AT) [49, 112] in the framework of density functional theory (DFT) [23, 26] to determine the thermodynamic stability of those configurations under operational conditions. To incorporate the anharmonicity in the vibrational free energy contribution to the configurational entropy, we evaluate the excess free energy of the clusters numerically by thermodynamic integration method with *ab initio* molecular dynamics (*ai*MD) simulation inputs. On analyzing a large dataset, we show that the conventional harmonic approximation miserably fails to estimate the accurate thermodynamic stability. Therefore, consideration of anharmonic effects is of paramount importance to avoid all the possibilities of missing the stable phases of the clusters. If the anharmonic effects are not included, the stable phases would be destabilized erroneously resulting in inaccurate prediction of the stable phases. Further, we have computed the Infrared (IR) spectra of these stable configurations, which also confirm the anharmonicity in such structures. Besides, the latter has significance in the activation of C−H bond, while the harmonic IR spectrum fails to capture it. The sharp peak corresponding to the C−H stretching mode (of the activated C−H bond) in the anharmonic IR spectrum signifies enhanced dipolar interaction in the C−H bond, which results from the localization of charge in C and H atoms of the $Ni_4O_7(CH_4)_2$ cluster, is well captured by the anharmonic IR spectrum. Therefore, to develop a suitable catalyst (with active sites), incorporation of the anharmonic effects is essential in these class of materials.

3.1.2 Computational methods

We have generated a large data set of $Ni_4O_x(CH_4)_y$ ($0 \leq x \leq 8$, $0 \leq y \leq 3$) clusters. We have varied the value of x and y (x = no. of oxygen atoms, y = no. of CH_4 molecules) from zero to the saturation value, which means x and y values are increased with all possible combinations until no more O-atom/CH_4 molecule can be absorbed by the cluster. As a first step, we have used a massively parallel cascade genetic algorithm (cGA) to thoroughly scan the potential energy surface (PES) in determining all possible low-energy structures (including the global minimum). The term "cascade" means a multi-stepped algorithm, where successive steps employ

higher level of theory and each of the next level takes information obtained at its immediate lower level. Typically, a cGA algorithm starts with classical force field and goes upto density functional theory (DFT) with hybrid exchange and correlation (ϵ_{xc}) functionals. Note that it is reported that PBE ϵ_{xc} functional [30] highly overestimates stability of clusters containing larger concentration of O-atoms [92, 97, 110, 113]. This results in a qualitatively wrong prediction of O_2 adsorption for O-rich cases. Such behaviour is not confirmed by more advanced hybrid ϵ_{xc} functionals (e.g., HSE06 [31], PBE0 [114]) as employed in our calculations. Moreover, the spin states of the clusters are also different as found by PBE and PBE0/HSE06 ϵ_{xc} functionals. In view of this, in the cascade algorithm, we have only optimized with PBE but the energetics are computed with PBE0 ϵ_{xc} functional to evaluate the fitness function of the cluster. This is due to the reason that in optimization of the structures, we basically compute the forces amongst atoms, which is determined by gradient of energy i.e., precisely the differences of energies in order to compute the derivative. As a result, the electron's self- interaction present in PBE ϵ_{xc} functional gets canceled out. Therefore, there is not much difference in the structures that we get from PBE and/or PBE0 ϵ_{xc} functionals. In addition, PBE0 ϵ_{xc} functional is computationally much expensive than PBE ϵ_{xc} functional making PBE ϵ_{xc} functional an efficient choice for structural optimization in our system. We have incorporated all these settings in cGA. For details of this cGA implementation, accuracy and validation, we recommend our previous studies as given in Ref. [48, 110, 111].

All DFT calculations have been performed using FHI-aims code, employing an all-electron code with numerical atom centered basis sets [115]. Considering the fact that first-principles based calculations are computationally demanding, lighter (viz., light settings with tier 2 basis set [115]) DFT settings have been implemented in the cGA to find the global minimum structures. The atomic zero-order regular approximation (ZORA) is used for the scalar relativistic correction [116]. The vdW correction is calculated according to the Tkatchenko-Scheffler scheme [117]. The low energy structures obtained from the cGA are further optimized with PBE at higher level settings (viz., tight settings with tier 2 basis set [115]). The atomic forces are converged up to 10^{-5} eV/Å. Finally, the total single point energy is calculated on top of this optimized structure using PBE0 hybrid ϵ_{xc} functional and the global minimum structures are obtained. The role of ϵ_{xc} functionals in identifying global minima is illustrated in Fig. 3.1. The vibrational frequencies are determined of the stable compositions under harmonic approximation using finite displacement method. Next, to capture the anharmonic effects using thermody-

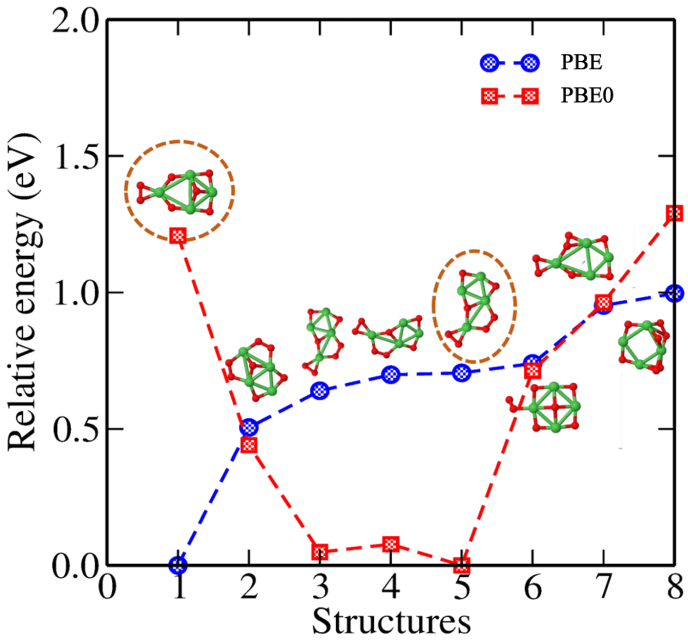

Figure 3.1: Structures of different isomers of Ni_4O_7 clusters obtained from PBE (represented by dashed blue line) and HSE06 (represented by dashed red line) exchange-correlation (ε_{xc}) functionals. Dashed circles represent the global minima from the two functionals.

namic integration method, we have carried out *ab initio* molecular dynamics (*ai*MD) simulations for 8 ps each at different temperatures namely T = 50 K, 100 K, 300 K, 600 K and 800 K in canonical ensemble (i.e., one with constant temperature and volume). We have employed Velocity Verlet scheme [118] for the integration of Newtonian equations with a time-step of 1 fs and the temperature of the system is controlled using Nose-Hoover thermostat [119]. Here, we represent a test case of $Ni_4O_x(CH_4)_y$ (x = 6, y = 1) cluster to validate our *ab initio* molecular dynamics (*ai*MD) simulations. Fig. 3.2 shows the histogram that we have obtained from *ai*MD simulation for $Ni_4O_6CH_4$ cluster at T = 600 K. From the histogram, we infer that average temperature of the simulation is indeed coming around the intended temperature viz., 600 K. Note that here, only the last 1 ps equilibrium stable data is considered after ignoring a large part of the data to avoid any thermal fluctuations. Therefore, Nose-Hoover thermostat is apt to control the temperature during simulation.

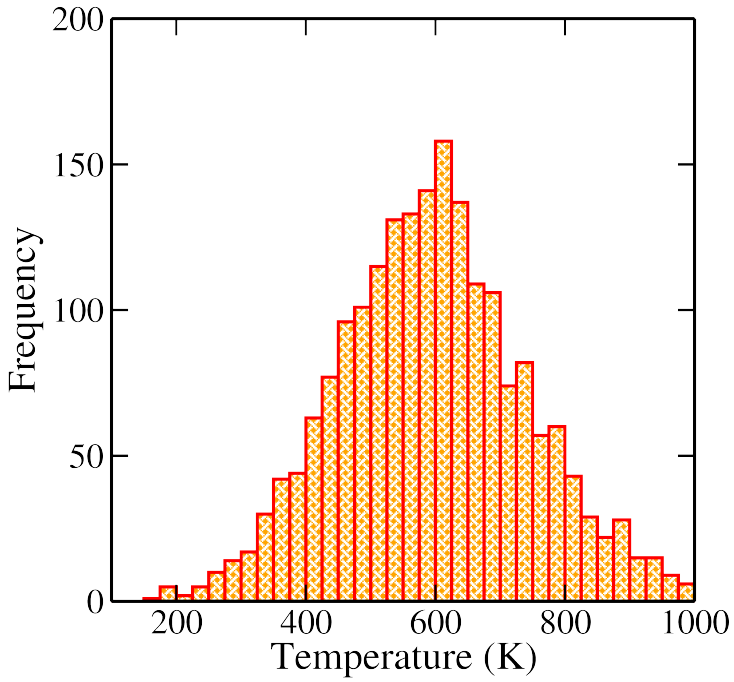

Figure 3.2: Histogram of *ai*MD simulation for $Ni_4O_6CH_4$ cluster at T = 600 K.

3.1.3 Results and discussion

3.1.3.1 Determination of stable phases of the [$Ni_4O_x(CH_4)_y$] clusters

After obtaining all low energy isomers corresponding to different configurations of $Ni_4O_x(CH_4)_y$ clusters from cGA, we study their thermodynamic stability under realistic conditions using *ai*AT approach. Here, we assume that there is an exchange of atoms between the system (Ni_4 cluster) and the surroundings (consisting of O_2 and CH_4 gas molecules) at finite temperatures and pressures, via the following reaction:

$$Ni_4 + \frac{x}{2}O_2 + y\,CH_4 \rightleftharpoons Ni_4O_x(CH_4)_y \tag{3.1}$$

Note that adsorption and desorption of O_2, H_2, H_2O and CO_2 moieties are also taken into account by GA, where all sorts of mutation and crossover operations take place giving rise to all possible structural moieties. Therefore even if the configuration stoichiometrically reads as $Ni_4O_x(CH_4)_y$, it does include all possible moieties.

The Gibbs free energy of formation (ΔG) of all the $Ni_4O_x(CH_4)_y$ structures is then evaluated as a function of T, p_{O_2} and p_{CH_4} by applying *ai*AT. The composition (for a particular value of x, y) having the minimum Gibbs free energy of formation is most likely to be found in the experiments at a specific T, p_{O_2} and p_{CH_4}. $\Delta G(T,p)$ is, therefore, calculated as per the

following equation:

$$\begin{aligned}\Delta G(T, p_{O_2}, p_{CH_4}) = F_{Ni_4O_x(CH_4)_y}(T) - F_{Ni_4}(T) \\ - x \times \mu_O(T, p_{O_2}) - y \times \mu_{CH_4}(T, p_{CH_4})\end{aligned} \tag{3.2}$$

Here, $F_{Ni_4O_x(CH_4)_y}(T)$ and $F_{Ni_4}(T)$ are the Helmholtz free energies of the cluster+ligands [$Ni_4O_x(CH_4)_y$] and the pristine [Ni_4] cluster, respectively. x and y represent the number of oxygen atoms and methane molecules, that are exchanged with the environment in the reactive atmosphere, respectively. $\mu_O(T, p_{O_2})$ and $\mu_{CH_4}(T, p_{CH_4})$ represent the chemical potential of an oxygen atom ($\mu_O = \frac{1}{2}\mu_{O_2}$) and the methane molecule, respectively. The relation of $\mu_O(T, p_{O_2})$ with T and p_{O_2} is governed by the ideal (diatomic) gas approximation. The expression is as follows [120, 121]:

$$\begin{aligned}\mu_{O_2}(T, p_{O_2}) = -k_B T \ln\left[\left(\frac{2\pi m}{h^2}\right)^{\frac{3}{2}} (k_B T)^{\frac{5}{2}}\right] \\ + k_B T \ln p_{O_2} - k_B T \ln\left(\frac{8\pi^2 I_A k_B T}{h^2}\right) \\ + \sum \frac{h\nu_{OO}}{2} + \sum k_B T \ln\left[1 - \exp\left(-\frac{h\nu_{OO}}{k_B T}\right)\right] \\ + E^{DFT}(O_2) - k_B T \ln \mathcal{M} + k_B T \ln \sigma\end{aligned} \tag{3.3}$$

For CH_4 molecule, I_A=I_B=I_C=I, and therefore,

$$\begin{aligned}\mu_{CH_4}(T, p_{CH_4}) = -k_B T \ln\left[\left(\frac{2\pi m}{h^2}\right)^{\frac{3}{2}} (k_B T)^{\frac{5}{2}}\right] \\ + k_B T \ln p_{CH_4} - k_B T \ln\left[8\pi^2\left(\frac{2\pi I k_B T}{h^2}\right)^{\frac{3}{2}}\right] \\ + \sum \frac{h\nu_{CH}}{2} + \sum k_B T \ln\left[1 - \exp\left(-\frac{h\nu_{CH}}{k_B T}\right)\right] \\ + E^{DFT}(CH_4) - k_B T \ln \mathcal{M} + k_B T \ln \sigma\end{aligned} \tag{3.4}$$

The contribution of different terms is given as [48]:

$$\mu_{translational} = -k_B T \ln\left[\left(\frac{2\pi m}{h^2}\right)^{\frac{3}{2}} (k_B T)^{\frac{5}{2}}\right] + k_B T \ln p_{CH_4} \tag{3.5}$$

$$\mu_{rotational} = -k_B T \ln\left[8\pi^2\left(\frac{2\pi I k_B T}{h^2}\right)^{\frac{3}{2}}\right] + k_B T \ln \sigma \tag{3.6}$$

$$\mu_{vibrational} = \sum \frac{h\nu_{CH}}{2} + \sum k_B T \ln\left[1 - \exp\left(-\frac{h\nu_{CH}}{k_B T}\right)\right] \tag{3.7}$$

where the summation runs over all the vibrational modes of methane.

$$\mu_{\text{electronic}} = E^{\text{DFT}} - k_{\text{B}}T \ln \mathcal{M} \tag{3.8}$$

Here k_{B}, h, E^{DFT}, ν_{OO} and ν_{CH} are respectively the Boltzmann constant, Planck constant, total DFT energy and stretching frequencies of O–O and C–H bonds. m, I, $\mathcal{M}$ and σ represent the mass, moment of inertia, spin multiplicity and symmetry no. of the molecule, respectively.

The Helmholtz free energies $F_{\text{Ni}_4\text{O}_x(\text{CH}_4)_y}(T)$ and $F_{\text{Ni}_4}(T)$ consist of respective total DFT energy along with their free energy contributions from translational, rotational, vibrational, symmetry and spin-degeneracy terms [49]. It has been noticed that total DFT energy is the dominant term, which is evaluated in its ground state configuration with respect to both geometry and spin state. The rest of the terms, except contribution from vibrational degrees of freedom (F_{vibs}), are usually considered as invariant since they do not change much (and even if they change, the order is insignificant) due to the dependence on most of the constant terms viz., mass, moment of inertia, universal constants, etc. However, the vibrational contribution is dependent on frequencies of vibration, which are unique for a given structure. Thus, the Helmholtz free energy can be written as follows:

$$F(T) = E^{\text{DFT}} + F_{vibs} + \Delta \tag{3.9}$$

Δ is considered to be the constant term. At low temperature, F_{vibs} usually contributes at the first order after the decimal for a small cluster of few atoms. Thus, while computing $\Delta G(T, p)$, since we take differences of two free energy expressions (i.e., a system with ligands and system without ligands), we assume this to be very small and therefore, can be neglected. However, there exist some systems, where F_{vibs} contributes significantly even after taking the difference of two such terms to compute $\Delta G(T, p)$ [112]. In view of this, though a significant number of works have neglected F_{vibs}, but it is not recommended. Here, we have estimated the role of F_{vibs} via state-of-the-art theoretical techniques at various level of accuracy.

Using Equation 3.2, we have obtained the 3D phase diagram (p_{O_2} vs p_{CH_4} vs $\Delta G(T,p)$) at an experimentally relevant T (here, 800 K) by taking its 2D projection after aligning negative $\Delta G(T, p)$ axis to be vertically up. We have considered all the configurations of $\text{Ni}_4\text{O}_x(\text{CH}_4)_y$ clusters. Note that only those phases that minimize the $\Delta G(T, p)$ at a specific p_{O_2}, p_{CH_4} and $T = 800$ K, are visible (see Fig. 3.3). Each color in the phase diagram represents a stable configuration of the catalyst. All the phase diagrams are constructed at T = 800 K as it is a suitable temperature for methane activation.

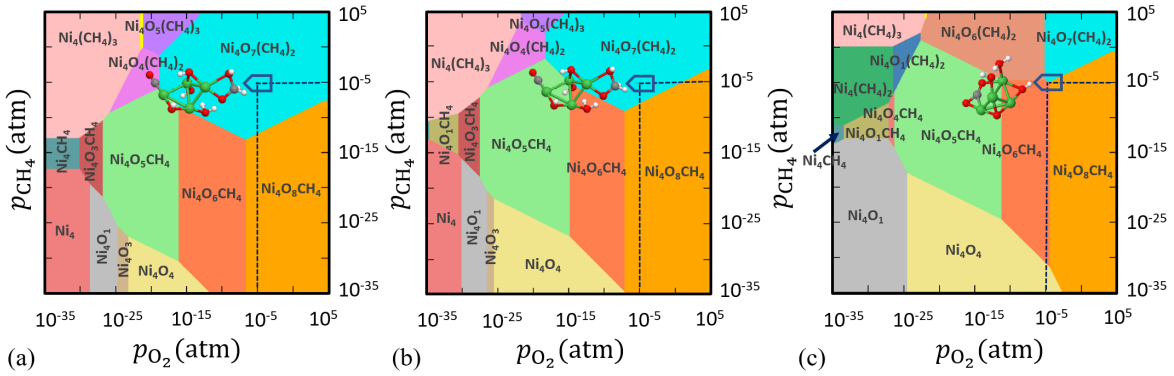

Figure 3.3: 2D projection of 3D phase diagram obtained for $Ni_4O_x(CH_4)_y$ clusters in the reactive atmosphere of O_2 and CH_4. In this plot $\Delta G(T,p)$ is computed (a) when only DFT total energies are included, (b) DFT+$F_{vibs}^{harmonic}$ are included and (c) DFT+$F_{vibs}^{anharmonic}$ are included to compute $F(T)$ of respective configurations as shown in Equation 3.2. Colored regions show the most stable compositions in a wide range of pressure at T = 800 K.

3.1.3.2 Comparing the role F_{vibs} in $\Delta G(T,p)$: Importance of capturing anharmonic effects

Herein, we have implemented a suite of three state-of-the-art techniques to plot $\Delta G(T,p)$. The first one is without any explicit contribution of F_{vibs} (as in Equation 3.9) i.e., only total DFT energy (E^{DFT}) of the cluster with and without ligands is considered (see Fig. 3.3a). In the second case, we have duly considered F_{vibs} upto harmonic approximation to calculate $\Delta G(T,p)$. $F_{vibs}^{harmonic}$ is computed using the following equation [48]:

$$F_{vibs}^{harmonic} = \sum_i \frac{h\nu_i}{2} + \sum_i k_B T \ln\left[1 - \exp\left(\frac{h\nu_i}{k_B T}\right)\right] \tag{3.10}$$

Note that after adding $F_{vibs}^{harmonic}$ with E^{DFT} (as in Equation 3.9), a new phase is introduced along with slight rearrangement of the existing phases, especially near the boundary region of competing configurations (see Fig. 3.3b). However, despite some small changes in Fig. 3.3a and 3.3b, we do not see any significant difference to identify the most stable phases at experimentally realistic pressure range. In this region, $Ni_4O_6CH_4$, $Ni_4O_7(CH_4)_2$ and $Ni_4O_8CH_4$ are the stable phases and if we see at the region, where $p_{O_2} = p_{CH_4} = 10^{-5}$ atm (T = 800 K), $Ni_4O_7(CH_4)_2$ comes out to be the most stable phase (see Fig. 3.3a and 3.3b) irrespective of $F_{vibs}^{harmonic}$ is taken into consideration or not.

Now here, it is assumed that at T = 800 K, the oscillations are constrained to vibrate under a harmonic potential. However, the real system does not necessarily follow this assumption.

And if so, the real anharmonic potential can be very different from harmonic potential. In such case, the expression for F_{vibs} can vary from one configuration to the other. Therefore, in an attempt to refine the expression of $\Delta G(T,p)$ at finite T,p, we have included anharmonic effects in the potential energy surface (see Fig. 3.3c). In order to quantitatively account for the anharmonic effects, we have performed the thermodynamic integration taking input from *ai*MD simulation to evaluate the excess free energy of clusters. Here, we have assumed that at low T (10K), both harmonic and anharmonic potentials do not diverge much. Taking such low T as our reference state, the Helmholtz free energy $F(T)$ is calculated according to the following equation:

$$\begin{aligned} F(T) = \underbrace{E^{\text{DFT}} + U^{ZPE}}_{U^{ref}} + \frac{T}{T_\circ} F_{vibs}^{harmonic}(T_\circ) \\ - T \underbrace{\int_{T_\circ}^{T} \frac{dT}{T^2} (\langle U \rangle_T - U^{ref})}_{thermodynamic\ \ integration} - k_B T \, \frac{N}{2} \ln \frac{T}{T_\circ} \end{aligned} \tag{3.11}$$

where $T_\circ$ and T represent the initial and final temperatures, respectively. E^{DFT}, U^{ref}, $F_{vibs}^{harmonic}(T_\circ)$, N and $\langle U \rangle_T$ are respectively the total DFT energy, zero point energy, Helmholtz free energy at temperature $T_\circ$ (10 K) under harmonic approximation, total number of atoms and canonical average of the total energy at temperature T (800 K) of the clusters. We have run *ai*MD simulations in canonical ensemble for 8 ps at five different temperatures, from T = 10 K to T = 800 K to obtain the average energy ($\langle U \rangle_T$). After that, we have performed quadratic curve fitting for this data and numerically integrated the corresponding function over the limits, $T_\circ$ = 10 K to T = 800 K to get the value of $F(T)$ at $T = 800$ K. After evaluating $F(T)$, we have minimized $\Delta G(T,p)$ using the same aforementioned procedure and obtained the phase diagram with the anharmonic effects. Interestingly, we have noticed, a completely new phase viz., $Ni_4O_6(CH_4)_2$ appears to be stable alongside three existing phases [viz., $Ni_4O_6CH_4$, $Ni_4O_8CH_4$ and $Ni_4O_7(CH_4)_2$] at reaction condition ($p_{O_2} = p_{CH_4} = 10^{-5}$ atm and T = 800 K). On comparing Fig. 3.3a, 3.3b and 3.3c, we infer that stable phases have not only been destabilized erroneously but also the new phases have a high probability of being missed at reaction conditions, if the anharmonic effects are not taken into consideration for this class of materials. Hence, it manifests that the inclusion of anharmonicity in these clusters affects the thermodynamic stability under operational conditions.

To clearly examine the relative probability of all the competing isomers simultaneously, we have estimated the probability of occurrence of all (meta)stable phases using all the three

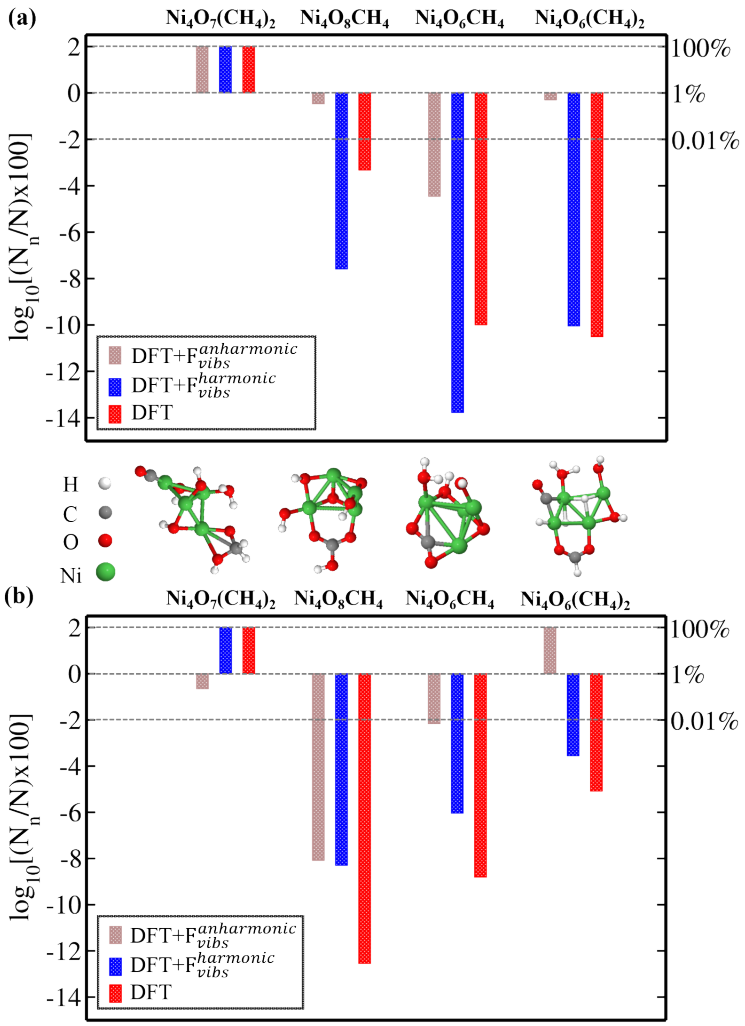

Figure 3.4: Logarithm of probability of occurrence (in %) of $Ni_4O_7(CH_4)_2$, $Ni_4O_8CH_4$, $Ni_4O_6CH_4$ and $Ni_4O_6(CH_4)_2$ clusters in all the three cases (DFT, DFT+$F_{vibs}^{harmonic}$ and DFT+$F_{vibs}^{anharmonic}$) at (a) T = 800 K and p_{O_2} = 1 atm, p_{CH_4} = 1 atm (b) T = 800 K and p_{O_2} = 10^{-10} atm, p_{CH_4} = 1 atm.

methods (viz., DFT, DFT+$F_{vibs}^{harmonic}$ and DFT+$F_{vibs}^{anharmonic}$) under different reaction conditions. It is calculated by the following equation:

$$\frac{N_n}{N} = \frac{\exp(\beta \Delta G_n)}{1 + \sum_m \exp(\beta \Delta G_m)} \tag{3.12}$$

Here, we assume total N different configurations are possible out of which N_n is the number of a given type (say n) and it's occurrence is given as per Fermi-Dirac statistics. Thus $\frac{N_n}{N}$ is the probability of occurrence of type-n configuration. ΔG_n is the Gibbs free energy of formation of type-n configuration. N_m is any other considered configuration type. As the range of $\frac{N_n}{N} \times 100\%$

is significantly large, we have taken logarithm of the above equation in the plots (see Fig. 3.4).

$$\log_{10}\left[\left(\frac{\mathrm{N_n}}{\mathrm{N}}\right)\times 100\right] \tag{3.13}$$

Therefore, the maximum possible value on y-axis is 2 for $\mathrm{N_n} = \mathrm{N}$. In Fig. 3.4a, we can clearly see that the first structure [viz., $Ni_4O_7(CH_4)_2$] is most likely to be stable by all three methods. But after that for the next three structures (viz., $Ni_4O_8CH_4$, $Ni_4O_6CH_4$ and $Ni_4O_6(CH_4)_2$), DFT+$F_{vibs}^{harmonic}$ and DFT+$F_{vibs}^{anharmonic}$ work counter to each other. Moreover, if we see Fig. 3.4b, the situation is even worse and inclusion of DFT+$F_{vibs}^{anharmonic}$ is absolutely essential as both DFT and DFT+$F_{vibs}^{harmonic}$ find different structures to be thermodynamically more stable and vice versa.

Next, we have shown two important applications of this finding by computing the IR spectra of two test cases: (i) $Ni_4O_6(CH_4)_2$ and (ii) $Ni_4O_7(CH_4)_2$.

3.1.3.3 $Ni_4O_6(CH_4)_2$ cluster: Harmonic IR vs Anharmonic IR

IR spectroscopy covers the infrared region of the electromagnetic spectrum with frequencies ranging from 4000 cm^{-1} to 40 cm^{-1} [122, 123, 124, 125, 126]. In IR spectroscopy, specific frequencies are absorbed by the molecules that are the characteristic of their structure. Here, we have simulated the IR spectra of one of the clusters viz., $Ni_4O_6(CH_4)_2$, that is explicitly stable on including the anharmonic contribution to the free energy, to determine its characteristic vibrational normal modes. For this, we have run 8 ps *ai*MD simulation in the canonical ensemble with Bussi-Donadio-Parrinello (BDP) [127] thermostat. From Fig. 3.5, we have noticed significant dissimilarities between the harmonic and anharmonic IR spectra of $Ni_4O_6(CH_4)_2$. Aside from the usual difference in peak intensities, the O−H stretching mode as per harmonic IR analysis near 2300 cm^{-1} (see Fig. 3.5 upper panel) is just a negligible hump in anharmonic IR (see Fig. 3.5 lower panel). Similarly, the C−H stretching mode around 3000 cm^{-1} is also not contributing in anharmonic IR. Hence, it is evident that there is a fundamental difference in the characteristic frequencies of vibration of this structure as computed with harmonic approximation and that of after capturing the anharmonic effects. As a result, they contribute differently to the free energy of vibration. This makes $Ni_4O_6(CH_4)_2$ stable in the anharmonic case, whereas unstable under the harmonic approximation. Note that we have taken just a prototypical model system here viz., Ni_4 cluster to study its stable phases under the reactive atmosphere of O_2 and

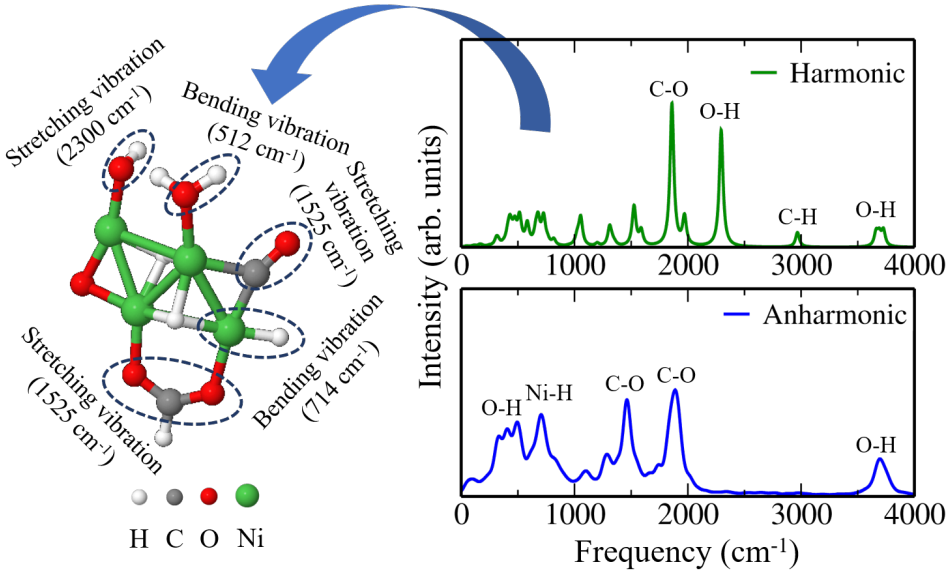

Figure 3.5: Infrared (IR) spectra of $Ni_4O_6(CH_4)_2$ for both harmonic (upper panel) as well as the anharmonic (lower panel) case. The possible vibrational modes are also shown corresponding to those respective peaks.

CH_4. Nevertheless, this model system is relevant and sufficient to convey the underlying message that there is a high chance of leaving important stable phases of the catalyst while ignoring the anharmonic effects during reaction condition.

3.1.3.4 $Ni_4O_7(CH_4)_2$ cluster and C−H bond activation

Apart from the above important facts, we notice that incorporation of anharmonic effects helps in predicting the potential catalyst for C−H bond activation. For this, we have considered a test case viz., $Ni_4O_7(CH_4)_2$ cluster, which is stable in all the three cases as shown in Fig. 3.3a, 3.3b and 3.3c. We have plotted its IR spectra (harmonic vs anharmonic) and compared in Fig. 3.6a. From Fig. 3.6a, we have noticed that O−H stretching presents significant anharmonic red-shifts in comparison to harmonic case around 273 cm^{-1}. These red-shift corrections lead to change in IR spectrum shape due to a reorganization of the vibrational modes. Primarily, we have observed some remarkable dissimilarities between harmonic and anharmonic IR spectra, for e.g., the intensity of C−O stretching peak has reduced significantly after the inclusion of anharmonic effects. Moreover, in the anharmonic IR spectrum, we have found an intense peak around 995 cm^{-1} corresponding to C−H bending vibration. This type of highly intense IR absorption is due to the change in dipole moment that occurs during a vibration, especially when the bond is highly polar in nature so that its dipole moment changes considerably as the bond

stretches. However, the harmonic IR spectrum completely fails to capture this information. To

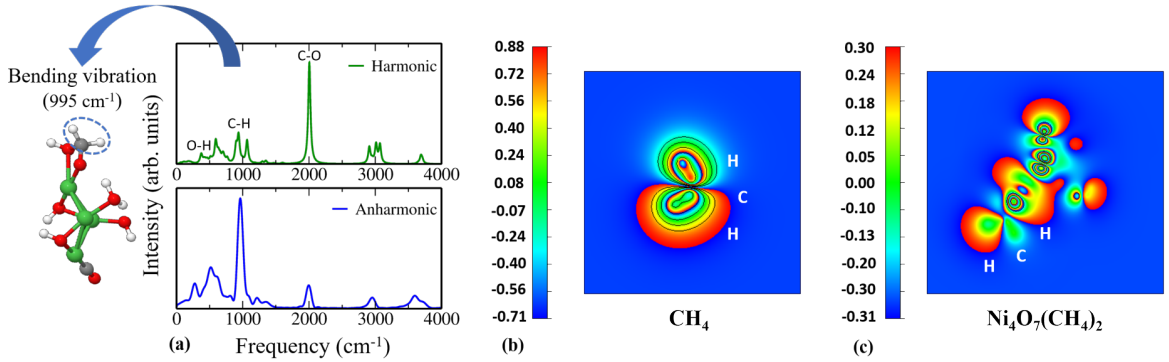

Figure 3.6: (a) Infrared (IR) spectra of $Ni_4O_7(CH_4)_2$ for both harmonic as well as the anharmonic case. Contour plots of electronic charge density associated with (001) plane of (b) CH_4 (delocalization of charge within C−H bonds) and (c) $Ni_4O_7(CH_4)_2$ cluster (localization of charge within C−H bonds).

validate this enhance dipolar interaction into this structure, we have plotted the charge density of $Ni_4O_7(CH_4)_2$ cluster and compared the same with CH_4 (see Fig. 3.6b and 3.6c). To obtain the charge density contour analysis, we have plotted the electron charge density for CH_4 and $Ni_4O_7(CH_4)_2$ cluster for the electronic levels near respective Highest Occupied Molecular Orbitals (HOMO). The constant slicing plane is chosen such that both the C and H atoms of the C−H bond is covered. The value of electron charge density varies from maximum (red color) to minimum (blue color). Now, if we notice the nature of the C−H bond in either case, we can clearly see the difference in charge localization. In conventional CH_4, the C−H bond is purely covalent, which makes it rather inert to get functionalized easily. However, in the $Ni_4O_7(CH_4)_2$ cluster, the C−H bond is very much polar with the localized charge on C and H respectively. This unusual localization of charge in the C−H bond gives rise to enhanced dipolar interactions (see Fig. 3.6c), and as a consequence of this, Ni_4 is expected to be a reliable catalyst in activating the C−H bonds in methane. This can be further explored by performing NEB/kMC simulations on the cluster. However, if this entire analysis is done using only harmonic approximation, this stable configuration would not even be considered for C−H bond activation as its peak in the IR spectrum is pretty small and delocalized. This further concludes the importance of capturing the anharmonic contribution to this class of materials.

3.1.4 Conclusions

In summary, we have carried out state-of-the-art hybrid density functional theory (DFT) calculations combined with $ab\ initio$ atomistic thermodynamics (aiAT) and $ab\ initio$ molecular dynamics (aiMD) simulation. Our aim was to explore how the thermodynamic stability of transition metal (TM) oxide clusters evolves in response to changes in temperature and pressure (T, p_{O_2} and p_{CH_4}). The inclusion of anharmonicity in our analysis unveiled the existence of previously ignored stable phases, which were not accounted for by conventional DFT and DFT+$F_{vibs}^{harmonic}$ methods. This discovery has profound implications, particularly in the context of CH bond activation. Harmonic IR methods proved inadequate in accurately depicting the vibrational modes necessary for understanding the activation of stable CH bonds in methane using a metal oxide cluster as a catalyst. Therefore, it is imperative to consider anharmonic effects when dealing with these materials, particularly in the context of catalytic processes.

3.2 O-vacancy mediated partially inverted ferrospinels for enhanced activity in the sulfuric acid decomposition for hydrogen production

3.2.1 Introduction

Over recent decades, the increasing global demand for energy has led to a significant rise in greenhouse gas emissions, primarily resulting from the burning of non-renewable fossil fuels like coal, natural gas, and petroleum oils. These sources release substantial amounts of greenhouse gases into the environment, emphasizing the need to explore cleaner and sustainable energy alternatives [128, 129, 130, 131]. Hydrogen emerges as a highly promising option, serving as a clean and sustainable energy carrier that emits no harmful greenhouse gases during combustion [132, 133, 134, 135, 136, 137, 138]. It can be generated from various raw materials, including water, through indirect techniques for water splitting [139, 140, 141, 142]. One such method, the Iodine-Sulfur (IS) cycle, is a non-carbon, thermochemical process with a reported efficiency of approximately 51% for hydrogen production [143, 144]. This multi-step cycle involves three key reactions: the Bunsen reaction, sulfuric acid decomposition, and hydroiodide decomposition [143]. Notably, the thermochemical decomposition of sulfuric acid is an extremely endothermic and corrosive process, characterized by significant kinetic barriers [145, 146, 147, 148]. This reaction occurs in two distinct steps. Initially, sulfuric acid undergoes thermal decomposition, yielding SO_3 and H_2O. Subsequently, in the second step, SO_3 undergoes catalytic decomposition into SO_2 and O_2 [149]. The latter step, known as the SO_3 decomposition or oxygen-evolving step, is particularly energy-intensive and requires the presence of a highly efficient and stable catalyst to facilitate the conversion of SO_3 into SO_2 and O_2 [150, 151].

Efforts to develop a highly active and thermally stable catalyst have led to numerous studies employing various materials, including precious metals, transition metal oxides, and complex metal oxides, such as perovskites and spinels [152, 153, 154, 155, 156, 157, 158]. Notably, supported transition metal oxides and complex metal oxides have garnered significant attention as potential alternatives to precious metal oxides due to their cost-effectiveness and enhanced stability [152, 159, 160, 161]. Complex metal oxides, particularly perovskites and spinels, stand

out as promising alternatives to platinum-based catalysts, owing to their robust thermal stability, especially under high-temperature conditions. Spinel structures are typically described by the formula AB_2O_4, where A and B represent the cation sites within the tetrahedral and octahedral arrangements, respectively. These cations are strategically arranged in a cubic close-packing of oxygen atoms, thereby exhibiting cubic symmetry with the space group $Fd\bar{3}m$. The structure of spinel oxides substantially influences their physical and chemical properties by accommodating diverse cations [162, 163, 164]. These cations can occupy various oxidation states across the A and B geometric sites. It is imperative to determine the degree of inversion and cation distribution, as these factors impact the material's physical and chemical characteristics. In the case of normal spinels, divalent and trivalent cations exclusively occupy the sites, resulting in an inversion degree of zero. Conversely, completely inverted spinels exhibit an inversion degree of 1. The preferences of cations for either tetrahedral or octahedral sites, coupled with parameters like temperature, cooling rate, and the method of synthesis, significantly influence the spatial arrangement of cations in spinel structures.

In this regard, Banerjee and colleagues synthesized AFe_2O_4 spinels (A = Cu, Ni, Co) utilizing the glycine-nitrate gel combustion method [165]. Among these spinels, $CuFe_2O_4$ exhibited superior catalytic performance, achieving 78% conversion at 1073 K. This exceptional activity of $CuFe_2O_4$ can be attributed to the high electronegativity of the Cu^{2+} ion in comparison to Fe^{2+} and Ni^{2+}, which weakens the S-O bond within mixed metal oxides. Consequently, $CuFe_2O_4$ exhibits a reduced susceptibility to sulfation in comparison to other metal oxides. The estimated activation energies for $CoFe_2O_4$, $CuFe_2O_4$, and $NiFe_2O_4$ were determined as 168.23, 116.91, and 229.16 kJ/mol, respectively. This same research group also investigated metal oxides based on chromium ($Fe_{2(1-x)}Cr_{2x}O_3$) and discovered that the maximum SO_2 yield was achieved at 1073 K, with no evidence of deactivation [166]. In the process of SO_3 decomposition, SO_3 interacts at available anchor sites on these metal surfaces, leading to the formation of metal sulfates. Subsequently, these metal sulfates decompose into SO_2 and oxygen via the dissociation of S-O bonds, underscoring the significance of the thermal stability of metal sulfates [165, 167]. The degree of thermal stability within a sulfate governs its susceptibility to S-O bond dissociation. The thermal stability of the S-O bond within the M-O-S linkage of a metal sulfate depends on the electronegativity of the metal M and, consequently, the polarization of the S-O bond. Specifically, a higher electronegativity of the metal M results in a weaker S-O bond, and vice versa. In the case of ferrospinels, their electronegativity follows the order of

$Fe^{3+} > > Cu^{2+} > Ni^{2+} > Co^{2+}$. Consequently, the catalytic activity and activation energy of the three ferrospinels AFe_2O_4 (A = Cu, Ni, Co) are arranged in the order of $CuFe_2O_4$ > $NiFe_2O_4$ > $CoFe_2O_4$ [165]. Nonetheless, it is noteworthy that Co^{3+} has a higher electronegativity than Fe^{2+} and Cu^{2+} [168]. Hence, $FeCo_2O_4$ ferrospinels possess the potential to serve as active catalysts in the high-temperature sulfuric acid decomposition reaction for thermochemical oxygen evolution.

Although these bimetallic catalysts have been widely explored for their exceptional bifunctional performance, there is still a need to investigate the role of their surface states, given the higher diversity of cations involved. The introduction of a secondary metal through doping leads to the formation of a double spinel, which combines characteristics of both normal and inverted spinels. This dual-phase structure allows us to enhance catalytic properties by generating additional oxygen vacancies, which not only act as active sites but also contribute to improved thermal stability. Therefore, the incorporation of a secondary metal into Co_3O_4 is a judicious choice for obtaining a catalyst with an increased number of active sites. In practice, the effective utilization of these active metals requires their stabilization on a support material. This approach facilitates superior heat distribution and helps prevent metal agglomeration, ensuring prolonged catalyst performance. To mitigate issues such as support sulfation, agglomeration, and metal loss during extended exposure to high temperatures, our research focuses on employing SiC-based support materials, which offer enhanced metal-support interaction [159]. SiC, with its high thermal conductivity, stability, and inert properties, has emerged as a promising catalyst support for high-temperature reactions. Our prior investigations have highlighted the critical role of strong metal-support interaction in enhancing activity and prolonging the stability of iron oxide when supported on pretreated SiC [159].

In this chapter, we focuse on stability and catalytic performance of both cobalt-rich ($FeCo_2O_4$) and iron-rich ($CoFe_2O_4$) spinel over support material for the SO_3 decomposition. Our methodology combines state-of-the-art theoretical approaches to provide a comprehensive understanding for the design of potential catalysts. The resulting catalyst, consisting of complex metal oxide nanoparticles supported on SiO_2 grown on SiC and mesoporous silica, exhibits remarkable activity and stability. To the best of our knowledge, this is the first attempt to investigate the catalytic activity of cobalt-rich ($FeCo_2O_4$) and iron-rich ($CoFe_2O_4$) spinels for this reaction. Thus, the present study enables us to engineer a highly active and stable catalyst for high-temperature reactions.

3.2.2 Computational methods

The spin-polarized density functional theory (DFT) calculations were performed using the plane-wave-based pseudopotential approach as implemented in the Vienna Ab initio Simulation Package (VASP) [169, 170]. To optimize the modeled geometries, the Perdew–Burke–Ernzerholf (PBE) exchange-correlation ϵ_{xc} functional was utilized within the generalized gradient approximation (GGA) [171]. For high-precision calculations, the electron wave function was expanded with an energy cutoff of 500 eV. The self-consistency loop was converged to a total energy threshold of 0.01 meV, and the structures were fully relaxed until the Heymann–Feynman forces on each atom were less than 10^{-5} eVÅ using conjugate gradient (CG) minimization. The Brillouin zone was sampled at the Γ point for all DFT calculations. It is well known that the local and semi-local functionals are insufficient to predict the stability and adsorption of oxide systems accurately. Therefore, the change in Gibbs free energy (ΔG) for the adsorption and dissociation of SO_3 molecules on the supported cluster was determined using a hybrid functional (HSE06) [31]. For the different reaction steps, the change in Gibbs free energy (ΔG) is calculated according to the following equations:

$$\Delta G_1 = G_{\text{catalyst+SO}_3} - G_{\text{SO}_3} - G_{\text{catalyst}} \tag{3.14}$$

$$\Delta G_2 = G_{\text{SO}_2-\text{catalyst}-\text{O}} - G_{\text{catalyst+SO}_3} \tag{3.15}$$

where G_{catalyst}, G_{SO_3}, $G_{\text{catalyst+SO}_3}$ and $G_{\text{SO}_2-\text{catalyst}-\text{O}}$ represent the total energy of the catalyst ($CoFe_2O_4$/SiC-Pretrt and $FeCo_2O_4$/SiC-Pretrt), the gas-phase adsorbate, the adsorbate adsorbed on the catalyst, and the adsorbate dissociated on the catalyst, respectively. An electron density difference analysis was conducted to gain insight into the nature of the bonding between the adsorbate and the catalyst. The electron density difference ($\Delta\rho$) was determined as:

$$\Delta\rho = \rho(\text{catalyst} + \text{SO}_3) - \rho(\text{SO}_3) - \rho(\text{catalyst}) \tag{3.16}$$

In order to identify the transition states (TSs) along the minimum energy path, we have employed the climbing-image nudged elastic band (CI-NEB) method [43, 172]. We extracted a nanocluster of $CoFe_2O_4$/$FeCo_2O_4$-np with a radius of 5 Å from its bulk cubic crystal (space group $Fd\bar{3}m$) and referred to this cluster as $CoFe_2O_4$/$FeCo_2O_4$ throughout this study. To construct the computational model of SiC that supports $CoFe_2O_4$/$FeCo_2O_4$, we utilized the $\{111\}$

facet of the "β-SiC" phase. To mimic our experimental model system, we added a layer of SiO_2 on top of the SiC support. To prevent unintended interactions between periodic images, a vacuum layer with a thickness of 20 Å was used.

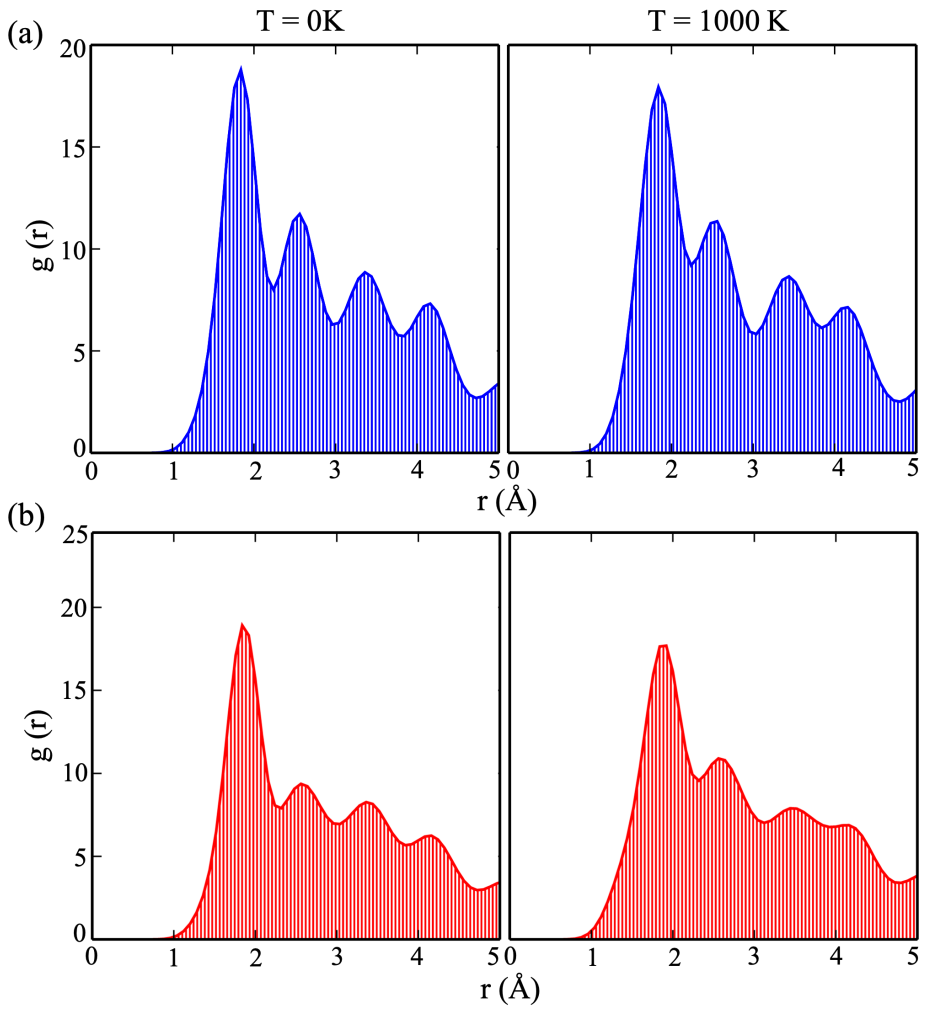

Figure 3.7: Radial distribution function (RDF) plot at 0 K and 1000 K for (a) $FeCo_2O_4$ and $CoFe_2O_4$ clusters over SiC-Pretrt, respectively.

3.2.3 Results and discussion

3.2.3.1 Thermodynamic stability and activation barrier

To gain a deeper understanding of catalytic performance in the spinels, we modeled a supercell consisting of a substrate (SiO_2/SiC) and a catalyst ($FeCo_2O_4$/$CoFe_2O_4$) bonded to it. Firstly, we conducted 8 ps *ab initio* molecular dynamics simulations to assess the structural stability of the catalysts at high temperatures. This was accomplished by plotting the radial distribu-

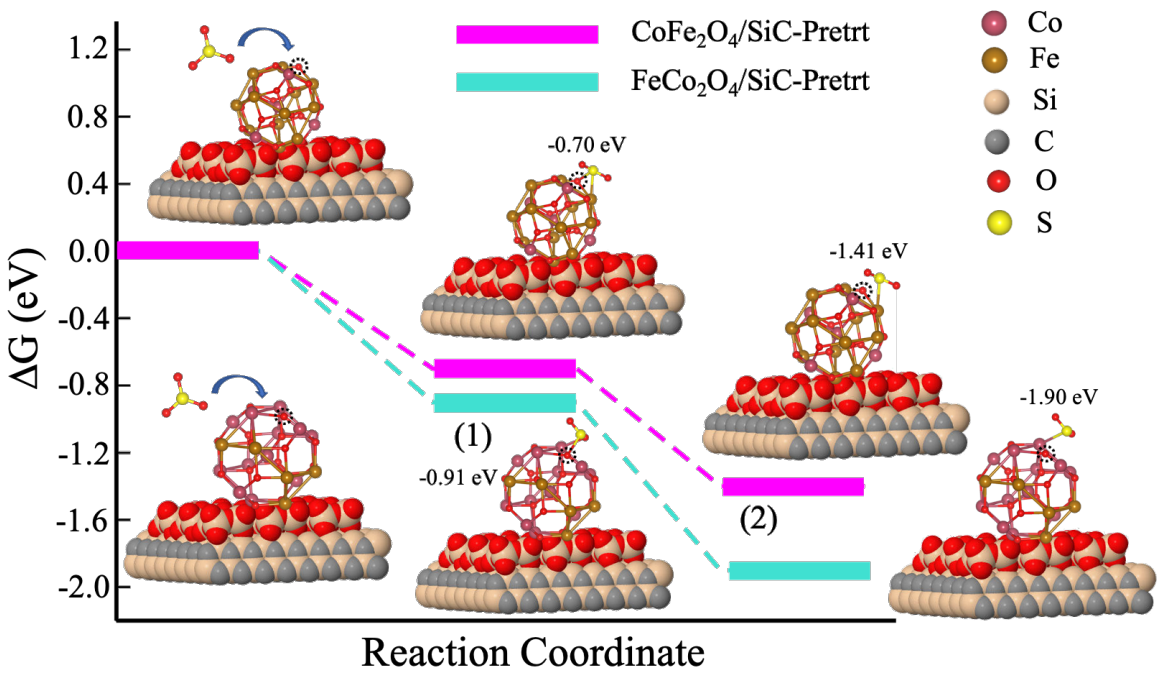

Figure 3.8: Free energy profiles for the adsorption and dissociation of SO_3 on the surfaces of $CoFe_2O_4$/SiC-Pretrt and $FeCo_2O_4$/SiC-Pretrt catalysts, respectively, were calculated using HSE06 ϵ_{xc} functional.

tion function (RDF) for $FeCo_2O_4$ and $CoFe_2O_4$ clusters over the SiC-Pretrt layer. The RDF analysis provides insights into the average distribution of atoms around a given atom within the system. Fig. 3.7 illustrates the RDF plots, indicating that there were no significant changes at 0 K and 1000 K for the clusters. These results suggest that our modeled systems maintain stability at high temperatures. Subsequently, we calculated the change in Gibbs free energy (ΔG) for the adsorption (the first step) and dissociation (the second step) of SO_3 on top of $CoFe_2O_4$/SiC-Pretrt and $FeCo_2O_4$/SiC-Pretrt (see Fig. 3.8). These calculations employed the Heyd–Scuseria–Ernzerhof (HSE06) ϵ_{xc} functional. Both adsorption and dissociation processes for SO_3 were found to be exergonic, with negative ΔG values for both systems. This indicates the thermodynamic stability of these systems. The $FeCo_2O_4$/SiC-Pretrt system exhibited a more negative ΔG, highlighting its higher stability in comparison to $CoFe_2O_4$/SiC-Pretreated. To gain further insight into the reaction mechanism, we calculated the activation barrier using the climbing image nudge elastic band (CI-NEB) method. It is important to note that conducting NEB calculations with a support structure consisting of over 200 atoms is computationally demanding. Therefore, we simplified the estimation of the activation barrier for SO_3 dissociation by excluding the support effect. Fig. 3.9 illustrates the reaction profile for the dis-

sociation of SO_3 on the catalyst surface. We evaluated the activation barrier for both $CoFe_2O_4$ and $FeCo_2O_4$ systems. The $FeCo_2O_4$ system displayed a lower activation barrier, facilitating the decomposition of SO_3. Therefore, from the stability and activation barrier analysis, we observed that $FeCo_2O_4$/SiC-Pretrt exhibits better catalytic performance.

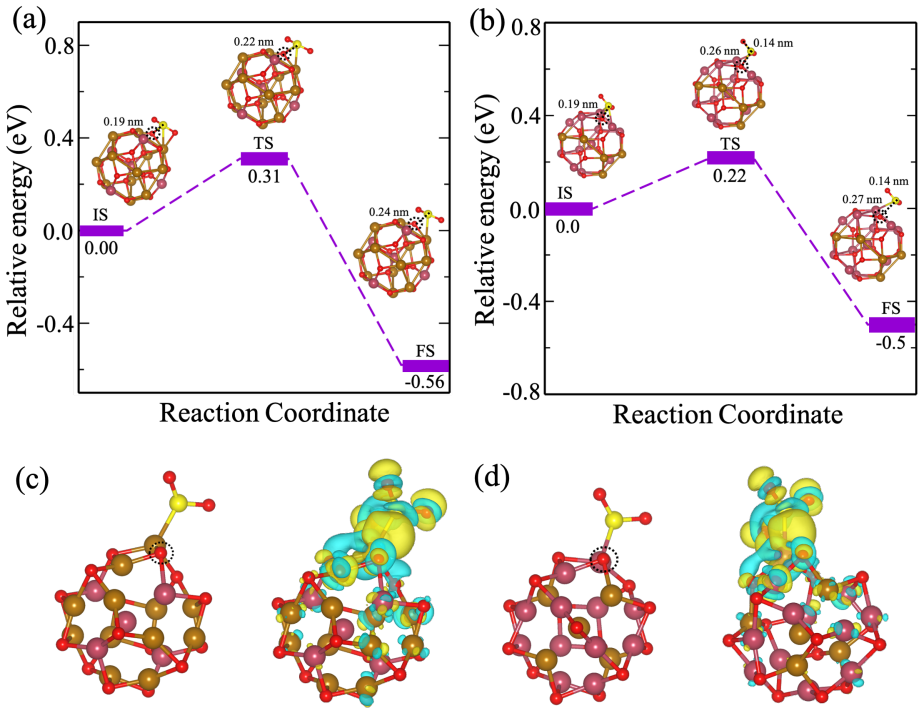

Figure 3.9: Reaction profiles for the decomposition of SO_3 with the initial state (IS), transition state (TS), and final state (FS) on (a) $CoFe_2O_4$ and (b) $FeCo_2O_4$ clusters with oxygen (O) vacancy were calculated using HSE06 ϵ_{xc} functional. Structures and charge density difference contours for SO_3 adsorbed on top of (c) $CoFe_2O_4$ and (d) $FeCo_2O_4$ clusters with O-vacancy. Cyan and yellow colors represent the negative and positive charge, respectively.

Next, to investigate the underlying reasons behind the catalytic performance of the spinel, we conducted an analysis of the atom-projected density of states (pDOS), as illustrated in Fig. 3.10. In the pDOS of isolated SO_3, distinctive and sharp peaks are observed. The HOMO level is primarily contributed by O atoms, while the LUMO level is associated with unoccupied states of S and O (see Fig. 3.10). Upon the adsorption of SO_3 onto the catalyst, we observed noteworthy changes in the S states. These states displayed dispersion, broadening, and a shift toward higher energy levels. This shift can be attributed to a charge transfer from the catalyst to the SO_3 molecule, leading to the elongation and weakening of one of the S-O bonds.

The presence of S states near the Fermi level signifies the occurrence of charge transfer from the cluster to SO_3. A greater number of S states in proximity to the Fermi level indicates a higher degree of charge transfer and a more pronounced elongation of the S-O bond. For instance, when SO_3 adsorbs at the oxygen vacancy of $FeCo_2O_4$, it results in more S states near the Fermi level in comparison to SO_3 adsorption on $CoFe_2O_4$. To depict this charge transfer, charge difference density maps for both configurations were plotted. The charge transfer plays a pivotal role in influencing the elongation and dissociation of the S-O bond, thereby signifying the catalytic activity of the cluster. Notably, the localization of the charge is found to be more pronounced when SO_3 is adsorbed at the O-vacancy of $FeCo_2O_4$, as demonstrated in Fig. 3.9. Consequently, the $FeCo_2O_4$ catalyst with an O-vacancy exhibits enhanced catalytic activity in the decomposition of SO_3 compared to the $CoFe_2O_4$ catalyst.

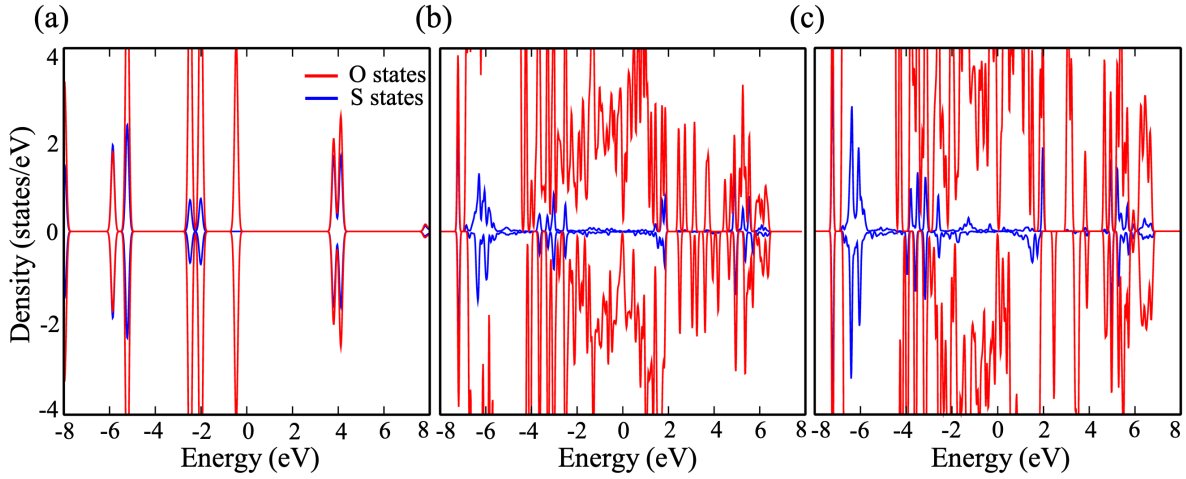

Figure 3.10: Projected density of states (pDOS) for (a) isolated SO_3, and SO_3, adsorbed over the cluster (b) $CoFe_2O_4$ and $FeCo_2O_4$ clusters, respectively. Here, red and blue colors correspond to O and S states, respectively. The energy range (y-axis) is the same for all figures.

3.2.4 Conclusions

In summary, we have carried out density functional theory (DFT) calculations combined with *ab initio* atomistic thermodynamics (*ai*AT) and *ab initio* molecular dynamics (*ai*MD) simulation to study the thermodynamic stability and catalytic performance in $CoFe_2O_4$/SiC-Pretrt and $FeCo_2O_4$/SiC-Pretrt systems. The negative value of Gibbs free energy shows the thermodynamic stability of the spinel systems. Our activation barrier calculations indicate that $FeCo_2O_4$/SiC-Pretrt exhibits better catalytic performance for the SO_3 decomposition. The

charge transfer between SO_3 and spinel results in the elongation of the S-O bond, which in turn facilitates the SO_3 decomposition. The enhanced performance can be attributed to the high electronegativity of Co^{3+}, the presence of oxygen vacancies, and the robust metal-support interaction.

CHAPTER 4

Origin of Rashba spin-splitting and strain tunability in ferroelectric bulk $CsPbF_3$

4.1 Introduction

Lead halide perovskites have become an excellent choice in optoelectronics due to their remarkable properties, including a suitable optical band gap, high absorption coefficient, low trap density, and cost-effective manufacturing [173, 174, 175, 176, 177, 178, 179, 180, 181]. These captivating materials find extensive use as absorbers in high-efficiency solar cells [182, 183, 184]. Over the last decade, dedicated research efforts have led to a remarkable increase in power conversion efficiency, exceeding 25% [185, 186]. Moreover, the significant influence of spin-orbit coupling (SOC), attributed to the presence of the heavy element Pb, plays a pivotal role in shaping the electronic characteristics of lead halide perovskites [187, 188]. SOC's impact on the band structures of these perovskites has been extensively documented [188]. Intriguingly, when combined with broken inversion symmetry, SOC becomes a critical component giving rise to various exotic phenomena, such as persistent spin textures [189, 190], topological surface states [191], and Rashba-Dresselhaus (RD) effects [192, 193, 194, 195, 196].

In the absence of inversion symmetry, the crystal experiences an effective magnetic field generated by spin-orbit coupling (SOC). This field, combined with the spin moment, results in the momentum-dependent splitting of energy bands, a phenomenon referred to as Rashba-Dresselhaus (RD) splitting. Originally, these effects, known as the Dresselhaus effect [197] and the Rashba effect [198], were identified in different crystal structures: zinc-blende and wurtzite, respectively. The key distinction between these effects lies in their origins of noncentrosymmetry. While the Rashba effect is associated with site inversion asymmetry, the Dresselhaus effect arises from bulk inversion asymmetry. Over the past decade, the RD effect has been

the focus of extensive research due to its potential applications in the emerging field of spintronics [199, 200]. Consequently, lead halide perovskites have been investigated as promising materials for spin-based applications [201, 202, 203, 204, 205]. Recently, a noteworthy Rashba effect has been observed in the tetragonal phase of $MAPbI_3$ (MA = $CH_3NH_3^+$), a phenomenon attributed to the reorientations of MA ions [206, 207]. Furthermore, predictions indicate that similar effects may be present in $CsPbBr_3$ and $MAPbBr_3$ perovskites [208, 209]. In recent studies, researchers have explored the potential of harnessing ferroelectric-coupled Rashba effects in halide perovskites (e.g., β-$MAPbI_3$, β-$MASnI_3$, ortho-$MASnBr_3$, $FASnI_3$ (FA = $HC(NH_2)_2^+$), opening up new avenues for spin-based devices utilizing perovskites [201, 210]. However, the stability of these perovskites in the presence of heat and moisture remains a challenge due to the volatile nature of organic molecules [211]. Hence, our current study aims to investigate the manifestation of the Rashba-Dresselhaus (RD) effect in inorganic ferroelectric (FE) perovskites. Notably, the intriguing interplay between ferroelectricity and the Rashba effect opens up the potential for electrically controlling the bulk Rashba effect, giving rise to a fascinating category of materials known as Ferroelectric Rashba Semiconductors (FERSCs) [212, 213, 214]. The quantification of this effect can be theoretically approached using ***k.p*** perturbation theory. According to this theory, the fundamental RD Hamiltonian can be expressed as [215, 216].

$$H_{RD}(\boldsymbol{k}) = \alpha_R(\sigma_x k_y - \sigma_y k_x) + \alpha_D(\sigma_x k_x - \sigma_y k_y) \tag{4.1}$$

In this equation, σ_x and σ_y denote Pauli spin matrices, k_i represents the crystal momentum ($i = x, y, z$), α_R and α_D correspond to the Rashba and Dresselhaus coefficients, respectively. When these terms are incorporated into the free-electron Hamiltonian, we get two distinct spin-split states with opposite spin polarizations. Although Rashba and Dresselhaus effects both produce a type of energy band splitting, the spin's orientation in momentum space, known as spin texture, provides insights into the nature of the splitting. In the pursuit of achieving a substantial Rashba-type energy band splitting, $CsPbF_3$ perovskite emerges as a promising candidate. To the best of our knowledge, a comprehensive quantitative investigation of the RD effect in this material is lacking in the existing literature. The presence of lead (Pb) and the noncentrosymmetric ferroelectric phase in $CsPbF_3$ suggests the potential occurrence of the RD effect within this material.

With this inspiration, we conducted a theoretical study based on the perturbative ***k.p*** for-

malism and backed by the first-principles calculations. In the present work, we have studied $Pm\bar{3}m$ and $R3c$ phases of $CsPbF_3$. Firstly, we have examined the electronic band structures in the above mentioned phases. After that, we have estimated the band gap of these phases using first-principles based approaches combined with SOC, viz., density functional theory (DFT) [14, 15] with semi-local exchange-correlation (ϵ_{xc}) functional (PBE [217]), hybrid DFT with HSE06 [31, 32] and single-shot GW (G_0W_0) [19, 218] under the many body perturbation theory (MBPT) and Wannier model approach. Subsequently, we have analyzed the electronic band structure of $R3c$ phase in terms of Rashba splitting under the combined framework of DFT and perturbative ***k.p*** formalism. We have also investigated the effect of strain on electronic band gap and Rashba parameters of $R3c$ phase. Finally, we have determined the minimum energy pathway of the FE transition using climbing image nudged elastic band (CINEB) method.

4.2 Computational methods

The DFT based first-principles calculations have been performed using the Vienna *ab initio* simulation package (VASP) [219, 220]. The ion-electron interactions in all the elemental constituents are described using projector augmented wave (PAW) [36, 170] method as implemented in VASP. We have considered pseudopotentials with the following valence states: Cs, $5s^25p^66s^1$; Pb, $6s^25d^{10}6p^2$; F, $2s^22p^5$. The structures are optimized using Perdew-Burke-Ernzerhof generalized gradient approximation (PBE-GGA), relaxing all ions until Hellmann-Feynman forces are less than 0.001 eV/Å. The cutoff energy of 520 eV is used for the plane-wave basis set such that the total energy calculations are converged within 10^{-5} eV. The Γ-centered 6×6×6 and 9×9×4 k-grid are used to sample the irreducible Brillouin zones of cubic phase with $Pm\bar{3}m$ space group and rhombohedral phase with $R3c$ space group of bulk $CsPbF_3$, respectively. The phonon calculations are performed for 3×3×3 and 2×2×2 super-cells in $Pm\bar{3}m$ and $R3c$ phases using PHONOPY package [221, 222]. In order to predict band gap, single-shot GW (G_0W_0) calculations have been performed on top of the orbitals obtained from HSE06+SOC ϵ_{xc} functional [G_0W_0@HSE06+SOC]. For this, we have used 6×6×6 and 4×4×2 k-grids in $Pm\bar{3}m$ and $R3c$ phases, respectively. The number of bands is set to four times the number of occupied bands. The polarizability calculations are performed on a grid of 50 frequency points. FE polarization is evaluated in the framework of Berry-phase theory of polarization [223, 224]. The minimum energy pathways of FE transitions are determined through

the climbing image nudged elastic band (CINEB) method [43]. Spin textures are plotted by calculating expectation values of spin operators S_i ($i = x, y, z$), given by

$$\langle S_i \rangle = \frac{1}{2} \langle \Psi_k | \, \sigma_i \, | \Psi_k \rangle \tag{4.2}$$

where σ_i are the pauli matrices and Ψ_k is the spinor eigenfunction obtained from noncollinear spin calculations. The spin texture is calculated with closely spaced 12×12 k-grid around high symmetry points. The PyProcar code is used to calculate the constant energy contour plots of the spin texture [225].

4.3 Results and discussion

4.3.1 Crystal structure

$CsPbF_3$ is primarily found in two phases: cubic ($Pm\bar{3}m$) and rhombohedral ($R3c$) phases [226, 227]. The $Pm\bar{3}m$ phase is centrosymmetric, meaning it contains an inversion center. In contrast, the noncentrosymmetric rhombohedral $R3c$ phase displays ferroelectric (FE) behavior due to cationic distortions away from anionic polyhedra [227]. The unit cell of the $R3c$ phase comprises 6 Cs atoms, 6 Pb atoms, and 18 F atoms. In comparison, the $Pm\bar{3}m$ phase features 1 Cs atom, 1 Pb atom, and 3 F atoms (as depicted in Fig. 4.1(a) and 4.1(b)). The calculated change in FE polarization for the rhombohedral ($R3c$) phase, relative to the centrosymmetric structure, is 34 μC/cm^2 along the [0001] direction in the hexagonal setting (or along the [111] direction in the rhombohedral setting). The details of optimized lattice parameters of $Pm\bar{3}m$ and $R3c$ phase are provided in Table 4.1 and 4.2.

Table 4.1: Optimized lattice parameters of $Pm\bar{3}m$ phase, a = 4.80652 Å.

Atom	x	y	z
Cs (1a)	0	0	0
Pb (1b)	0.5	0.5	0.5
F (3c)	0	0.5	0.5

Table 4.2: Optimized lattice parameters of $R3c$ phase, a = 6.80864 Å, c = 16.30620 Å. Hexagonal settings are used.

Atom	x	y	z
Cs (6a)	0	0	0
Pb (6b)	0	0.5	0.5
F (18e)	0.44	0	0.25

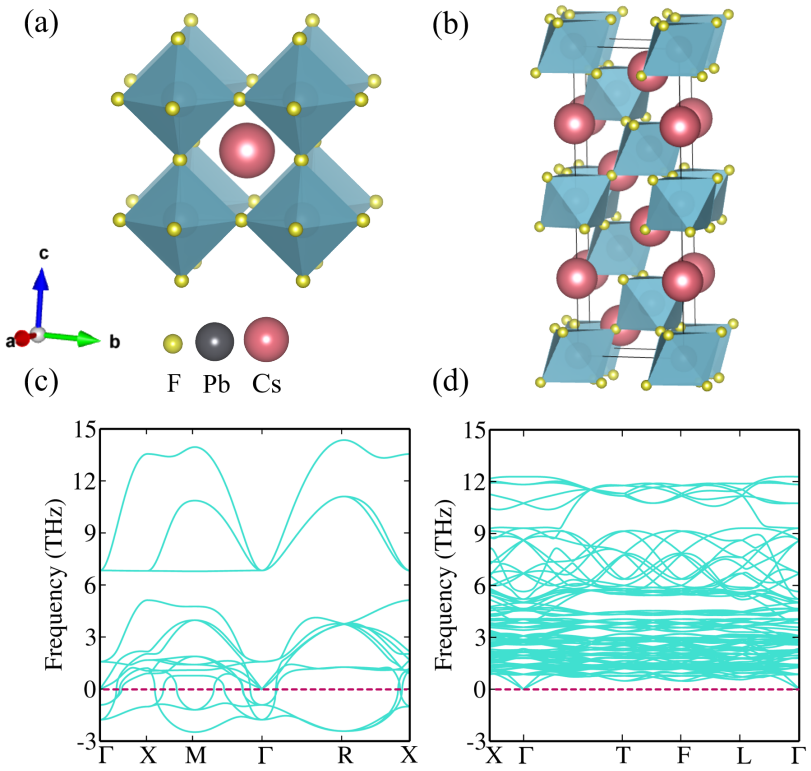

Figure 4.1: Crystal structure of $CsPbF_3$ (a) cubic $Pm\bar{3}m$ phase and (b) rhombohedral $R3c$ phase. Cs, Pb and F atoms are indicated by red, grey and yellow colors, respectively. Phonon band structure of $CsPbF_3$ (c) cubic $Pm\bar{3}m$ phase and (d) rhombohedral $R3c$ phase.

4.3.2 Electronic structure analysis

We have examined the electronic band structures of $Pm\bar{3}m$ and $R3c$ phases. As shown in Fig. 4.2, the band structure of $Pm\bar{3}m$ phase in presence of SOC reveals that there is no momentum-dependent splitting owing to its centrosymmetric structure. In addition, the cubic $Pm\bar{3}m$ phase is not dynamically stable due to the presence of negative frequencies in phonon

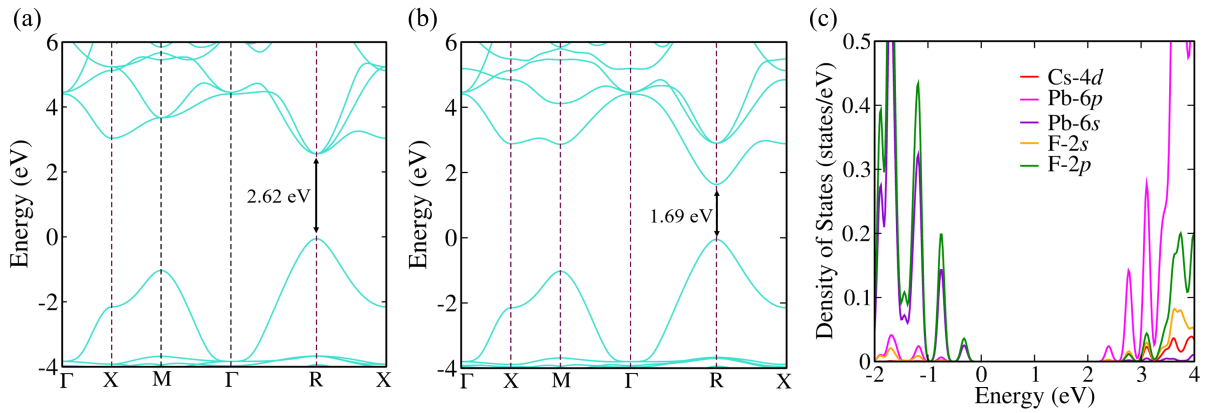

Figure 4.2: Band structure of cubic $Pm\bar{3}m$ phase of $CsPbF_3$, calculated using (a) PBE (b) PBE+SOC. (c) Projected density of states (pDOS), calculated using HSE06+SOC.

bandstructure (see Fig. 4.1(c)). Therefore, we have explored RD splitting in the latter phase (i.e., *R*3*c*). Also, we have plotted the band structure of FE *R*3*c* phase along the high symmetry path using hexagonal setting (as shown in Fig. 4.3(b)). Firstly, we have performed non-spin polarized calculations. After that, we have considered SOC in the calculation of electronic band structure. Fig. 4.3(c) and 4.3(d) show the electronic band structures calculated using PBE and PBE+SOC, respectively. A direct band gap of 3.26 eV is observed without SOC, whereas on including SOC, the band gap is reduced to 2.42 eV (indirect) around the Γ point. This change in band gap is attributed to SOC arising from the presence of Pb-6*p* orbitals in the conduction band (see pDOS in Fig. 4.3(g)). Hence, SOC is indispensable and duly considered in all further calculations. Note that PBE ϵ_{xc} functional is well known to underestimate the band gap due to its inability to capture the electron's self-interaction error. Therefore, we have also calculated the band gap with hybrid ϵ_{xc} functional HSE06 (with SOC), which comes out to be 3.57 eV. To date, there is no theoretical or experimental report on the band gap of *R*3*c* phase. In view of this, for a better estimation of the band gap, we have employed G_0W_0 approximation on top of HSE06+SOC orbitals, that results in the band gap of 5.01 eV (see Fig. 4.4(a)).

Subsequently, we have also plotted the imaginary part (Im (ε)) of dielectric function with converged *k*-grid for *R*3*c* phase of $CsPbF_3$ using HSE06+SOC and G_0W_0@HSE06+SOC (see Fig. 4.4(b)). The first peak of Im (ε) corresponds to the electronic band gap, which is the same as we get from band structure calculations. For imaginary part (Im (ε)) of dielectric function of $Pm\bar{3}m$ phase, see Fig. 4.5. The values of band gaps are listed in Table 4.3. It is worth quoting that HSE06+SOC/G_0W_0@HSE06+SOC only enhances the band gap without any notable change in the nature of band structure and strength of Rashba splitting [199, 206]. To confirm

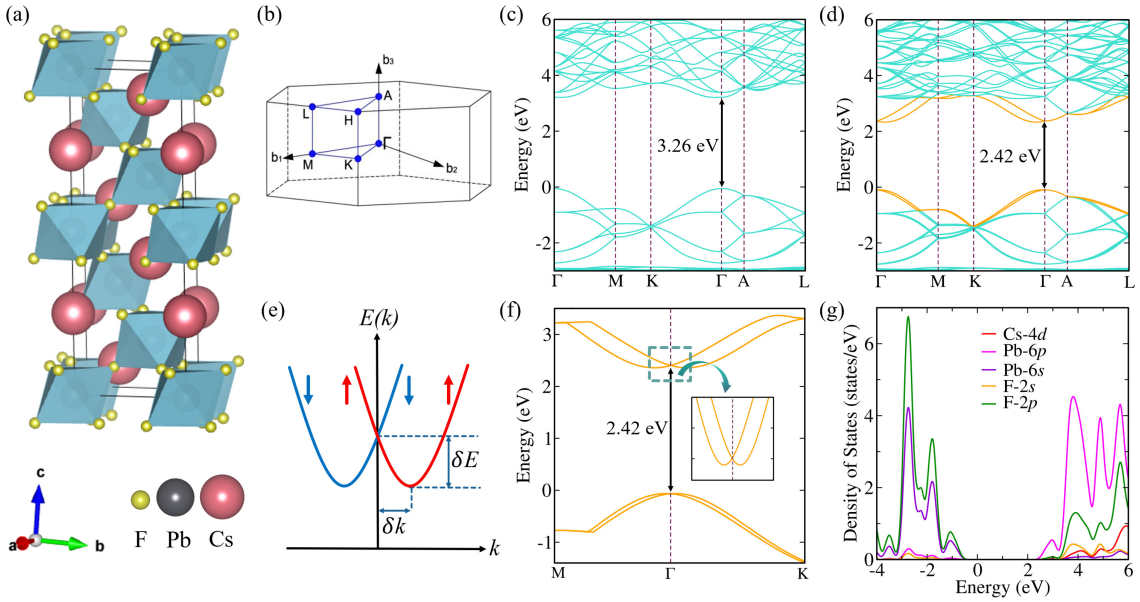

Figure 4.3: (a) Optimized crystal structure of $CsPbF_3$ in rhombohedral *R*3*c* phase. Cs, Pb and F atoms are indicated by red, grey and yellow colors, respectively. (b) The first hexagonal Brillouin zone showing the high symmetry path for band structure calculations in *R*3*c* phase of $CsPbF_3$. Electronic band structure of $CsPbF_3$ for *R*3*c* phase, calculated using (c) PBE (d) PBE+SOC. The conduction and valence bands considered in the discussion are indicated by orange color. (e) Schematic representation of bands showing Rashba splitting. (f) Splitting of conduction band minimum (CBm) and valence band maximum (VBM) of the chosen bands along the M-Γ-K path. The inset shows the enlarged view of Cbm. (g) Projected density of states (pDOS) in *R*3*c* phase of $CsPbF_3$ calculated using HSE06+SOC. The Fermi energy is set to zero in the energy axis.

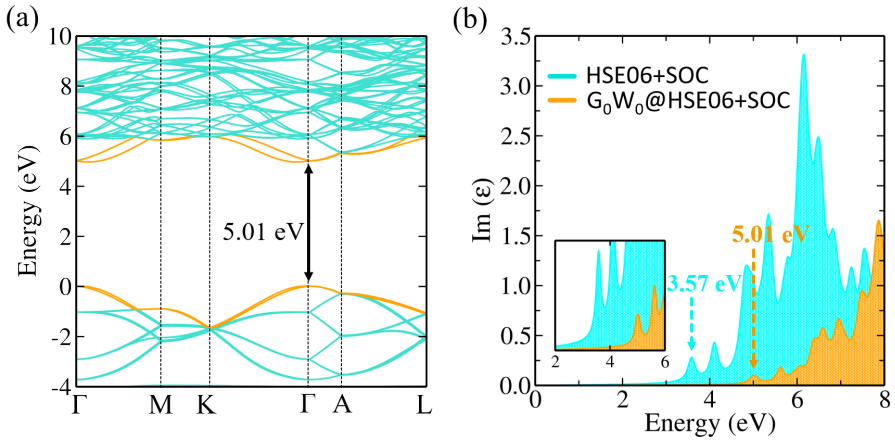

Figure 4.4: (a) Band structure of $R3c$ phase using G_0W_0@HSE+SOC. (b) Imaginary part (Im (ε)) of the dielectric function for $R3c$ phase of $CsPbF_3$ calculated using HSE06+SOC and G_0W_0@HSE+SOC.

Table 4.3: Band gap (in eV) of $Pm\bar{3}m$ and $R3c$ phases using different ϵ_{xc} functionals.

Structure	**PBE**	**PBE+SOC**	**HSE06**	**HSE06+SOC**	**G_0W_0@HSE06+SOC**
$Pm\bar{3}m$	2.62	1.69	3.61 [228, 229]	2.71	4.38
$R3c$	3.26	2.42	4.34	3.57	5.01

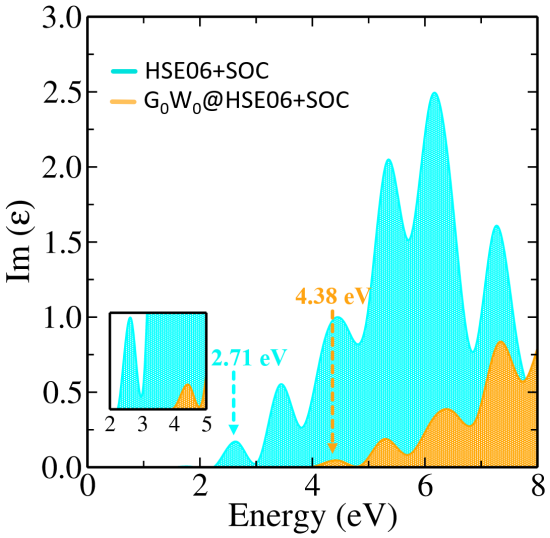

Figure 4.5: Imaginary part (Im (ε)) of the dielectric function for $Pm\bar{3}m$ phase of $CsPbF_3$ calculated using HSE06+SOC and G_0W_0@HSE+SOC ϵ_{xc} functional, respectively.

this, we have compared the band structures of $Pm\bar{3}m$ phase using PBE+SOC, HSE06+SOC, G_0W_0@HSE06+SOC and have found that the band profile remains same (see Fig. 4.6). There-

fore, in view of computational cost PBE+SOC is considered to compute RD parameters.

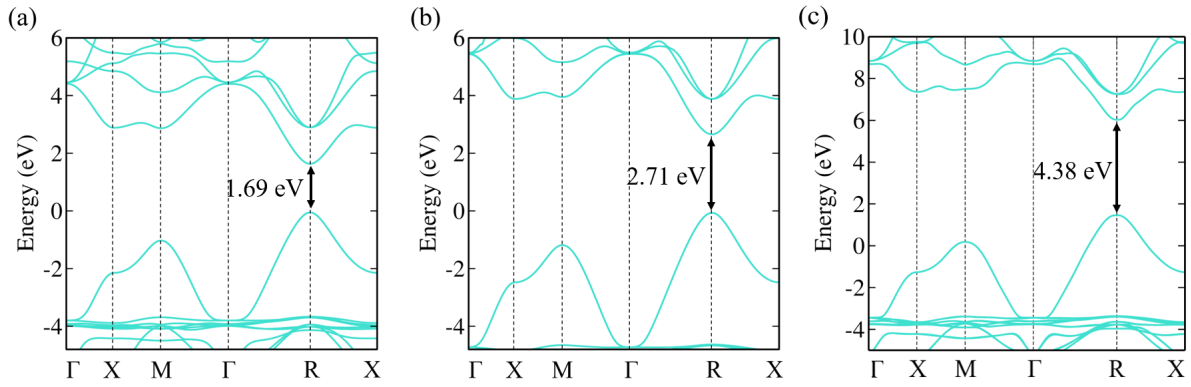

Figure 4.6: Band structure of cubic $Pm\bar{3}m$ phase of $CsPbF_3$, calculated using (a) PBE+SOC (b) HSE+SOC (c) G_0W_0@HSE+SOC, respectively.

4.3.3 Rashba and Dresselhaus spin-splitting in *R3c* phase

Inclusion of SOC leads to the splitting of bands in k_z=$\frac{\pi}{c}$ plane, which is perpendicular to the direction of polarization (see Fig. 4.3(d)). On the contrary, splitting is completely absent along Γ-A i.e., in direction parallel to polarization axis, indicating that the momentum dependent splitting around Γ point is the Rashba-type splitting. As a consequence, the CBm and VBM are located slightly off the Γ point. The CBm shifts from Γ towards M and K by 0.075 $Å^{-1}$ and 0.061 $Å^{-1}$, respectively. The VBM shifts from Γ towards M and K by 0.022 $Å^{-1}$ and 0.012 $Å^{-1}$, respectively (see Fig. 4.3(f)). This shift from Γ point in either direction is known as offset momentum (δk) (see Fig. 4.3(e)). The difference of energies at Γ and extremum point is known as Rashba spin-splitting energy (δE).

To grasp the overall nature of splitting, the constant energy 2D contour plots of spin texture are plotted in k_x-k_y plane centered at Γ point (see Fig. 4.7(a)) for schematic representation of spin textures). Fig. 4.7(b) and 4.7(c) show x, y and z components of spin at constant energies around CBm and VBM, respectively. As we can see from spin textures of CBm and VBM, the in-plane spin components (S_x and S_y) are perpendicular to the crystal momentum and out-of-plane component (S_z) is completely absent. This results in the helical shape of spin texture with inner and outer bands having opposite orientation, which confirms the existence of dominant Rashba splitting. In order to have a quantitative study of the RD effect, we have considered the ***k.p*** Hamiltonian. The model Hamiltonian of $R3c$ structure possessing C_{3v} point group

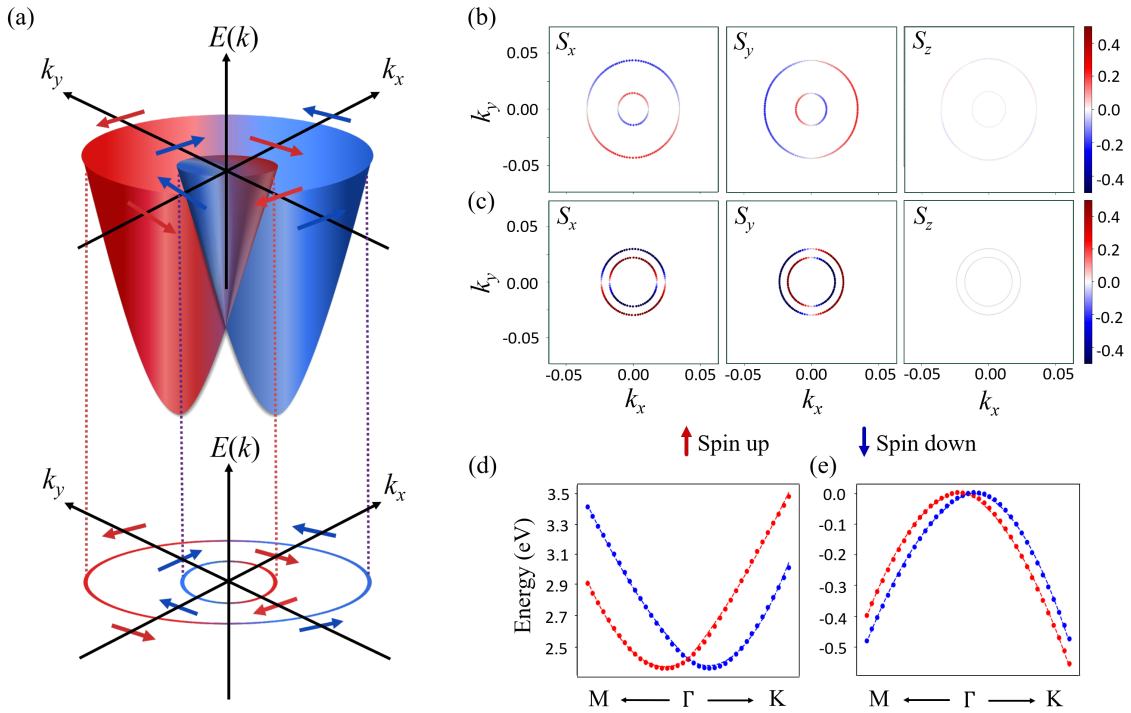

Figure 4.7: (a) Schematic representation of spin textures in Rashba splitting. Spin projected constant energy contour plots of spin texture calculated in k_x-k_y plane centered at Γ point. The upper and lower panels represent the spin textures calculated at constant energy: (b) E=E_F + 2.5 eV and (c) E=E_F − 0.2 eV, respectively. Electronic band structures showing spin-splitting of (d) CBm and (e) VBM around Γ point, respectively. Band structure is plotted along $(\frac{2\pi}{a}0.25, 0, 0) - (0, 0, 0) - (\frac{2\pi}{a}0.16, \frac{2\pi}{b}0.16, 0)$ direction of momentum space, which is M − Γ − K direction. DFT and ***k.p*** band structures are plotted with dashed lines and dots, respectively. In the color scale, red depicts spin-up while blue depicts spin-down states.

symmetry near Γ point in the presence of SOC can be written as [230, 231, 232]:

$$H_\Gamma(\boldsymbol{k}) = H_o(\boldsymbol{k}) + \alpha\sigma_y k_x + \beta\sigma_x k_y + \gamma\sigma_z[(k_x^3 + k_y^3) - 3(k_x k_y^2 + k_y k_x^2)] \tag{4.3}$$

Here $H_o(\boldsymbol{k})$ is the Hamiltonian of the free electrons with eigenvalues $E_o(\boldsymbol{k})$. α, β are the coefficients of the linear term and γ is the coefficient of the higher order term in the Hamiltonian. Since we have not noticed out-of-plane spin component in the spin texture, therefore, we have neglected the higher order terms in the Hamiltonian. Hence, the Hamiltonian for Γ point (con-

sidering only linear terms) can now be written as:

$$\begin{aligned} H_\Gamma(k) &= H_o(k) + \alpha k_x \sigma_y + \beta k_y \sigma_x \\ &= H_o(k) + \alpha_R(\sigma_x k_y - \sigma_y k_x) \\ &+ \ \alpha_D(\sigma_x k_x - \sigma_y k_y) \end{aligned} \tag{4.4}$$

The energy eigen values corresponding to this Hamiltonian is given as, $E_o(k) = \frac{\hbar^2 k_x^2}{2m_x^*} + \frac{\hbar^2 k_y^2}{2m_y^*}$ and m_x^*, m_y^* are the effective masses in x and y directions, respectively. Rashba and Dresselhaus coefficients are defined as $\alpha_R = (\alpha - \beta)/2$ and $\alpha_D = (\alpha + \beta)/2$, respectively [233]. On diagonalizing Eq. 4.4, we get energy eigenvalues as:

$$E_\pm(k) = E_o(k) \pm \sqrt{\alpha^2 k_x^2 + \beta^2 k_y^2} \tag{4.5}$$

The band structures obtained from DFT and the model Hamiltonian around Γ point are shown with dashed lines and dots in Fig. 4.7(d) and 4.7(e), respectively. The good agreement between both the band structures justifies the reliability of the chosen Hamiltonian. The DFT calculations for CBm give δE = 43.5 meV, δk = 0.075 Å^{-1} along Γ-M direction, where k_y = 0. Hence, the value of $\alpha = \frac{2\delta E}{\delta k}$ = 1.16 eVÅ. Along Γ-K direction, where $k_x = k_y$, δE = 43.5 meV, δk = 0.061 Å^{-1} and the calculated value of $\sqrt{\alpha^2 + \beta^2} = \frac{2\delta E}{\delta k}$ = 1.43 eVÅ. On putting the value of α, we get β = - 0.84 eVÅ, which results in α_R = 1.00 eVÅ and α_D = 0.16 eVÅ. Similarly, for VBM, δE = 3.4 meV, δk = 0.022 Å^{-1} along Γ-M direction. So, the value of $\alpha = \frac{2\delta E}{\delta k}$ = 0.31 eVÅ. Along Γ-K direction, δE = 3.4 meV and δk = 0.012 Å^{-1}. Therefore, $\sqrt{\alpha^2 + \beta^2} = \frac{2\delta E}{\delta k}$ = 0.57 eVÅ, which gives β = - 0.48 eVÅ. Using α and β parameters, the estimated values of α_R and α_D are 0.40 eVÅ and α_D = 0.09 eVÅ, respectively. The values are summed up in Table 4.4. As we can see from the values of RD parameters, the Rashba effect dominates in the

Table 4.4: Rashba parameters for band-splitting at Γ point in $R3c$ phase.

Position	δE **(meV)**	$\delta \boldsymbol{k}_{\Gamma-\mathbf{M}}$ **(Å^{-1})**	$\delta \boldsymbol{k}_{\Gamma-\mathbf{K}}$ **(Å^{-1})**	α_R **(eVÅ)**	α_D **(eVÅ)**
CBm	43.5	0.075	0.061	1.05	0.15
VBM	3.4	0.022	0.012	0.41	0.08

conduction band. The origin of large Rashba effect in CBm can be attributed to the stronger SOC stemming from higher contribution of Pb-6p orbital in conduction band (see Fig. 4.3(g)).

This large contribution of SOC in CBm compared to VBM is in well agreement with the previous findings [234]. On fitting the DFT band structure around Γ point for CBm, we find α = -0.90 eVÅ and β = 1.20 eVÅ. This gives α_R = 1.05 eVÅ and α_D = 0.15 eVÅ. Similarly, fitting the band structure for VBM, gives α = -0.33 eVÅ and β = 0.49 eVÅ and hence α_R = 0.41 eVÅ and α_D = 0.08 eVÅ. These values are in well agreement with the predicted values based on DFT calculation. The calculated values of RD parameters also confirm that the splitting around Γ point is mainly dominated by the Rashba effect.

4.3.4 Effect of strain on Rashba spin-splitting

After thorough analysis of RD spin-splitting, we have investigated the effect of strain on the band structure of $R3c$ phase. For this, we have applied uniaxial strain in z-direction, which is defined as

$$x = \frac{c - c_0}{c_0} \times 100\% \tag{4.6}$$

where c_0 is the equilibrium lattice constant and c is the strained lattice constant. The lattice vector c is varied from -5% to +5%, where "+" and "−" are used to denote tensile and compressive strain, respectively. After optimizing the structures at a given strain, we have plotted the band structures along high symmetry path. Fig. 4.8(a) shows the band structure of $R3c$ phase along Γ-M-K-Γ-A-L path, under the uniaxial strain of ±5%. To clearly examine the shift, we have also plotted the band structures along M-Γ-K (see Fig. 4.8(b)). Here, we have focused on CBm as there is large Rashba splitting in comparison to VBM. From the band structures in Fig. 4.8(b), we infer that strain causes a shift in momentum (δk) on either side of Γ point. The arrows represent the direction of shift. We have taken the equilibrium band structure (i.e., with 0% strain) as the reference for all the strained band structures. Interestingly, under compressive strain, the bands shift off from Γ on either side towards M and K. On the contrary, under tensile strain, the bands shift towards Γ from either side. This in turn changes δk and δE as a function of strain, and the overall effect of these parameters will change α_R and α_D accordingly. To quantify the effect of strain on Rashba parameters, we have calculated their values at a given strain within the framework of DFT. The values of Rashba parameters are mentioned in Table 4.5. Fig. 4.8(c-e) show δE, δk, α_R and α_D as a function of strain. From Fig. 4.8(c), we have observed that under compressive strain α_R is significantly enhanced from 1.05 to 1.48 eVÅ making the material tunable for spintronics application. Also, we have seen notable change in electronic band gap on the application of strain. The band gap values are

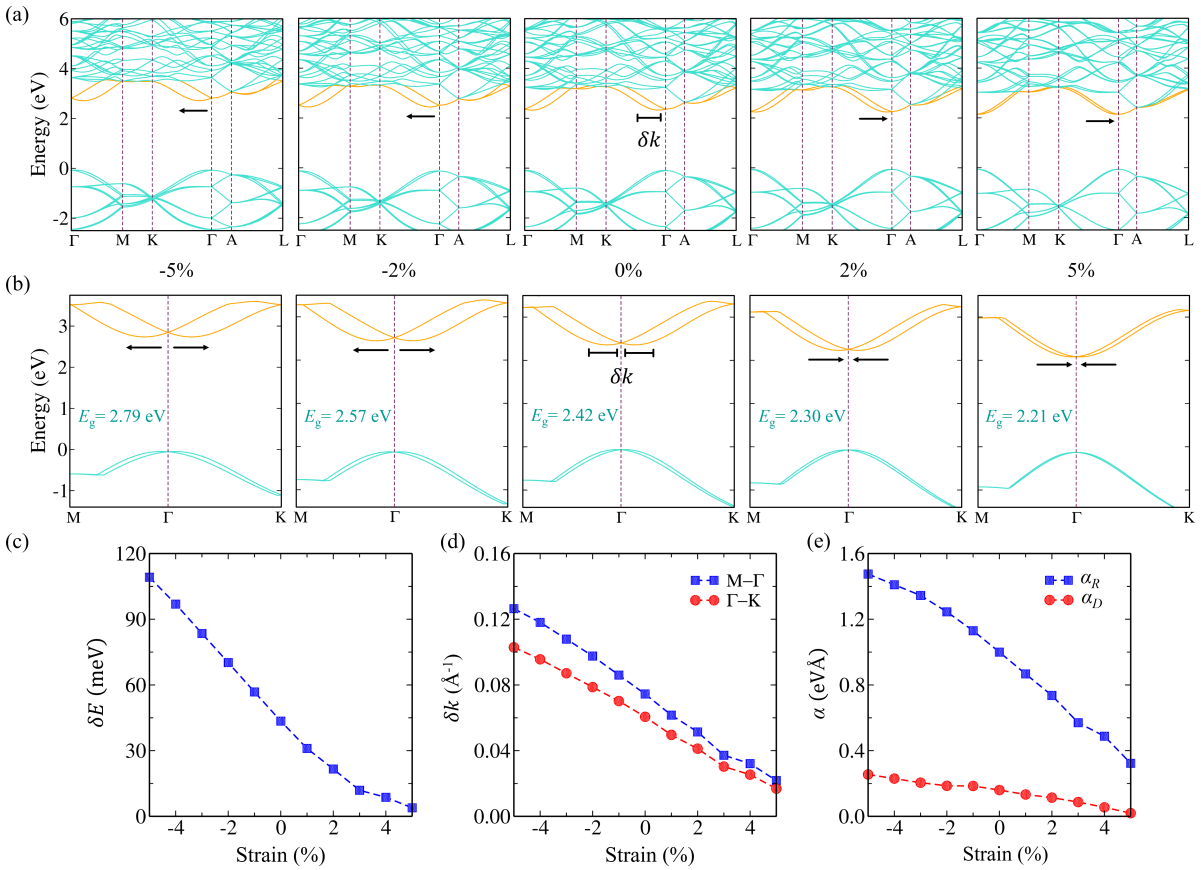

Figure 4.8: Band structures of $CsPbF_3$ ($R3c$ phase) under uniaxial strain of $\pm 5\%$, calculated using PBE+SOC for path (a) Γ-M-K-Γ-A-L and (b) M-Γ-K. (c) Rashba spin-splitting energy (δE) (d) offset momentum (δk) (e) Rashba parameters (α_R and α_D) as a function of strain. The values are calculated for CBm in $R3c$ phase. Note that δE is same along both M-Γ and Γ-K directions.

mentioned in Fig. 4.8(b).

Lastly, we have explored the possibility of polarization switching in FE $CsPbF_3$ using strain effects. To predict the feasibility of this phenomenon, we have analyzed the minimum energy pathway of the FE transition using CINEB method [235, 236]. For this, we have chosen the structure deformation path between two FE states with opposite spontaneous polarization through a centrosymmetric reference. As shown in Fig. 4.9, the E_b denotes the activation barrier for the polarization switching, which comes out to be 0.75 eV. This suggests that a switchable FE polarization is plausible in the material. The strain tunability and reversible spin textures owing to FE switching in $CsPbF_3$ give electrical control of spins and provide an all-semiconductor design for spintronic devices such as in spin-field effect transistor [237, 238].

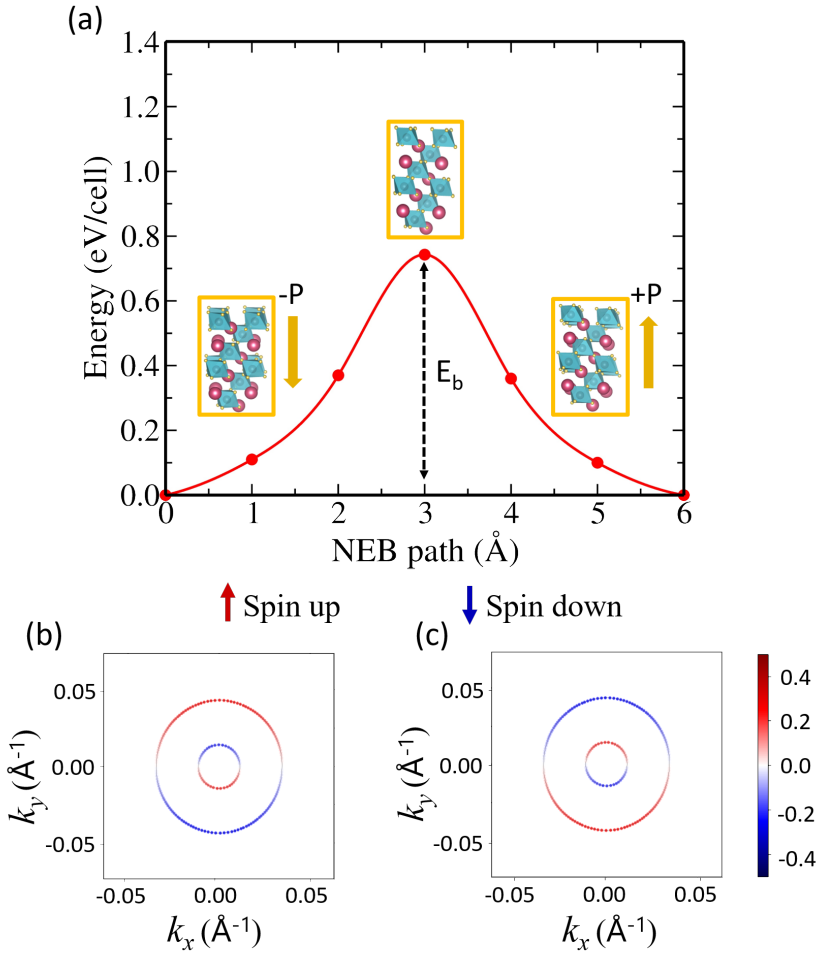

Figure 4.9: (a) Climbing image nudged elastic band (CINEB) calculation for the polarization switching process in $CsPbF_3$ perovskite. Two ferroelectric (FE) structures in the ground state with opposite direction of electric polarization are shown. E_b is the activation barrier energy for the polarization switching process. Reversible in-plane spin textures calculated at constant energy E = E_F+2.5 eV with oppposite spin polarization: (b) -P (c) +P.

Table 4.5: RD parameters as a function of strain for CBm in *R*3*c* phase.

Strain (%)	δE **(meV)**	$\delta \boldsymbol{k}_{\Gamma-\mathbf{M}}$ **(Å^{-1})**	$\delta \boldsymbol{k}_{\Gamma-\mathbf{K}}$ **(Å^{-1})**	α_R **(eVÅ)**	α_D **(eVÅ)**
-5	109.2	0.126	0.103	1.48	0.25
-4	96.9	0.118	0.096	1.41	0.23
-3	83.5	0.108	0.087	1.35	0.21
-2	70.2	0.098	0.079	1.25	0.19
-1	56.8	0.086	0.070	1.13	0.18
0	43.5	0.075	0.061	1.00	0.16
1	31.0	0.062	0.050	0.87	0.13
2	21.6	0.051	0.041	0.74	0.11
3	11.9	0.037	0.030	0.55	0.09
4	8.7	0.032	0.025	0.49	0.05
5	3.9	0.022	0.017	0.32	0.02

4.4 Conclusions

In summary, we conducted a comprehensive study on the electronic properties of $CsPbF_3$ in its *Pm*$\bar{3}$*m* and *R*3*c* phases using first-principles based methodologies viz., PBE, HSE06 and many-body perturbation theory (G_0W_0). Notably, we considered the influence of SOC in all our calculations. For the noncentrosymmetric *R*3*c* phase, we performed a detailed analysis of its Rashba-Dresselhaus (RD) splitting characteristics. We employed a symmetry-adapted ***k.p*** model Hamiltonian to validate our DFT results. Our analysis revealed that the material predominantly exhibits the Rashba effect, with a minimal contribution from the Dresselhaus effect. We also found that the Rashba effect is more prominent in the conduction band minimum (CBm) compared to the valence band maximum (VBM) of the *R*3*c* phase, primarily due to the significant contribution of the Pb-6p orbital in the conduction band. Furthermore, we observed that the Rashba parameters, viz., δk, δE, α_R, and α_D increase linearly under compressive strain. Applying strain significantly tuned the band gap of $CsPbF_3$. Lastly, we noticed

reversible changes in spin textures during ferroelectric switching, indicating that $CsPbF_3$ holds great potential in the field of spintronics.

CHAPTER 5

Vacancy-ordered double perovskites Cs_2BI_6 (B = Pt, Pd, Te, Sn): an emerging class of thermoelectric materials

5.1 Introduction

The pursuit of sustainable and renewable energy sources has long been a global priority [173, 184, 239, 240]. In addition to solar energy, one prominent avenue for renewable energy is the conversion of waste heat into electricity. To harness this waste heat effectively, we require highly efficient thermoelectric materials [241, 242, 243]. Advantageously, thermoelectric generators offer durability, robustness, scalability, compactness, and lack of moving parts. In order to achieve the maximum thermoelectric figure of merit (zT, as explained below), the material needs to have substantial Seebeck coefficient (S), coupled with high electrical conductivity (σ) and low thermal conductivity (κ) [244, 245, 246].

$$zT = \frac{S^2 \sigma T}{\kappa} \tag{5.1}$$

However, achieving a high zT in a single system is challenging due to the strong coupling and trade-off relationship between these parameters.

Halide-based perovskites have introduced a paradigm shift in the pursuit of high-performance materials [173, 247, 248]. This can be attributed to their diverse compositions and structures, which offer a wide range of functional properties [249]. More recently, halide perovskites have garnered attention for thermoelectric energy conversion due to their unique structural characteristics and lattice dynamics [250, 251, 252, 253, 254]. Yang *et al.* [251] reported an ultralow thermal conductivity of 0.5 $Wm^{-1}K^{-1}$ in halide perovskite nanowires made from $CsPbI_3$, $CsPbBr_3$, and $CsSnI_3$. Furthermore, various strategies, such as introducing lattice

defects [255, 256], creating artificial superlattices, and developing composite materials [257], have been explored to reduce lattice thermal conductivities in materials. Most of the thermoelectric materials reported, like SnSe [258, 259], PbTe [260, 261, 262, 263], Cu_2Se [264], and BiCuSeO [265, 266], exhibit low intrinsic lattice thermal conductivity, similar in magnitude to that observed in halide perovskites. This exceptionally low thermal conductivity of halide perovskites, coupled with their high carrier mobility, positions them as promising candidates for thermoelectric applications [252, 267, 268]. Unfortunately, these promising materials are plagued by lead toxicity and long-term instability. Consequently, these drawbacks have spurred the scientific community to explore alternative perovskite compositions and structures.

One alternative category of materials includes inorganic lead-free double perovskites, characterized by the general formula A_2BX_6. These are commonly referred to as vacancy-ordered double perovskites. This variation of halide perovskite structures is achieved by doubling the ABX_3 unit cell along all three crystallographic axes and eliminating every other B-site cation, as depicted in Fig. 5.1. These perovskite materials offer promising prospects for environmentally friendly and stable substitutes for both lead (Pb) and tin (Sn). In recent studies, vacancy-ordered double perovskites have garnered attention in the field of thermoelectrics due to their exceptional ability to minimize lattice thermal conductivity. This exceptional property can be attributed to their highly anharmonic lattice dynamics [250, 252, 269]. For instance, recent research by Jong et al. has highlighted the significant role of twofold rattling modes involving Cs atoms and SnI_6 clusters in achieving ultralow thermal conductivity in Cs_2SnI_6 [270].

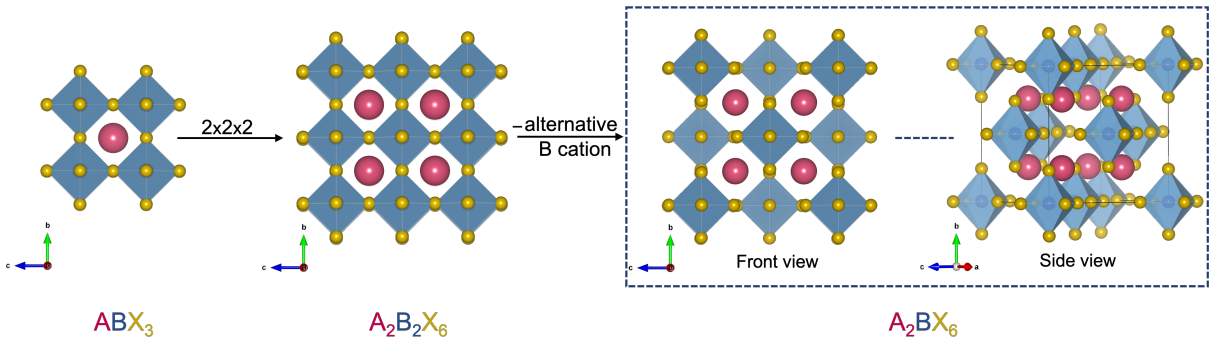

Figure 5.1: Schematic of the relationship between ABX_3 perovskite and A_2BX_6 (vacancy-ordered) double perovskite.

In this chapter, we have studied the vacancy-ordered double perovskites Cs_2BI_6 (B = Pt, Pd, Te, Sn) using state-of-the-art first-principles based methodologies under the framework of density functional theory (DFT) [14, 15] with suitable exchange-correlation (ϵ_{xc}) functionals

combined with many-body perturbative approaches (G_0W_0) [19, 218] and spin-orbit coupling (SOC). First, we have examined the structural, mechanical and thermodynamic stability of these materials. After that, we have studied the thermoelectric properties, where we find reasonably high zT values, calculated as a function of temperature (T). Interestingly, we have observed the presence of anharmonic effects, which are quantified by computing the harmonic and anharmonic energy contribution as a function of temperature in these vacancy-ordered double perovskites. In order to further explore the underlying mechanisms, we have examined the dynamical stability and anharmonicity by computing the phonon bandstructures and electron localization function (ELF). The ELF further confirms the presence of anharmonicity in this class of systems. As a consequence, we find that the study of electron-phonon interaction is important. The electron-phonon interaction is well captured by studying Fröhlich mesoscopic model [271, 272] to investigate the interaction of longitudinal optical phonon modes with the carriers that strongly influence the carrier mobility.

5.2 Computational methods

All the DFT [14, 15] calculations have been performed using the Vienna $ab\ initio$ simulation package (VASP) [219, 220]. The ion-electron interactions in all the elemental constituents are described using the projector augmented wave (PAW) [36, 170] method as implemented in VASP. The structural optimization is performed using generalized gradient approximation (PBE) [30] and optB86 [273] ϵ_{xc} functional with vdW corrections, relaxing all ions until Hellmann-Feynman forces are less than 0.001 eV/Å. The two-body vdW interaction, devised by Tkatchenko-Scheffler has been used during optimization [117]. The cutoff energy of 600 eV is used for the plane wave basis set such that the total energy calculations are converged within 10^{-5} eV. The Γ-centered $4\times4\times4$ k-grid is used to sample the Brillouin zone except when stated otherwise. The band gap is calculated using hybrid ϵ_{xc} functional (HSE06) [31, 32] and many-body perturbation theory. Note that the single-shot GW (G_0W_0) [19, 218] calculations have been performed on top of the orbitals obtained from PBE/HSE06 (with SOC) ϵ_{xc} functional [G_0W_0@PBE+SOC/HSE06+SOC]. The number of bands is set to four times the number of occupied bands. The polarizability calculation is performed on a grid of 50 frequency points. The effective mass is calculated by SUMO [274] using a parabolic fitting of the band edges. The phonon calculation is performed for $2\times2\times2$ supercell using the PHONOPY

package [221, 222]. The BoltzTrap Code [275] based on Boltzmann transport theory and phono3py [276] are used to evaluate thermoelectric properties. The self-consistent process described by Hellwarth is used to calculate the electron-phonon coupling strength [271]. Static dielectric constant is calculated using density functional perturbation theory (DFPT) [277] with a denser k-grid (6×6×6). To calculate the anharmonic energy, we have carried out *ab initio* molecular dynamics (AIMD) simulation employing Nose-Hoover thermostat [119] and pyHMA package [278].

5.3 Results and discussion

5.3.1 Crystal structure

Cs_2BI_6 (B = Pt, Pd, Te, Sn) vacancy-ordered double perovskites have a face-centered cubic crystal structure with the space group $Fm\bar{3}m$ (no. 225). In this structure, the Cs atoms are situated at the 8c Wyckoff positions and (0.25, 0.25, 0.25) coordinates, B atoms at 4a Wyckoff positions and (0, 0, 0) coordinates, and I atoms at 24e Wyckoff positions and (x, 0, 0) coordinates, where the value of x is around 0.20. Each of the Cs atoms resides between the [BI_6] octahedra and is surrounded by 12 I atoms, while the B atoms are at the corners and face-centered positions of [BI_6] octahedra. The Cs atoms located in the octahedral cage can act as heavy rattlers and lead to lattice anharmonicity [270]. Table 5.1 shows the optimized lattice parameters of vacancy-ordered double perovskites calculated using PBE and optB86 exchange-correlation (ε_{xc}) functionals along with van der Waals (vdW) forces. The two-body vdW interaction, devised by Tkatchenko-Scheffler, has been used during optimization. The optB86-vdW ε_{xc} functional reproduces the lattice parameters of vacancy-ordered double perovskites close to experimental ones.

5.3.2 Stability of Cs_2BI_6 (B = Pt, Pd, Te, Sn) vacancy-ordered double perovskites

5.3.2.1 Structural stability

Firstly, we have examined the stability of material as it is an essential factor in achieving a high-performance device applications. In order to predict the structural stability of the vacancy-ordered double perovskites, we have calculated the Goldschmidt tolerance factor (t) [281, 282]

Table 5.1: Calculated lattice parameters (Å) of Cs_2BI_6 (B = Pt, Pd, Te, Sn) vacancy-ordered double perovskites using different exchange-correlation (ε_{xc}) functionals.

Configurations	**Experimental**	**PBE**	**PBE-vdW**	**optB86-vdW**
Cs_2PtI_6	11.37 [279]	11.74	11.47	11.29
Cs_2PdI_6	11.33 [280]	11.67	11.42	11.23
Cs_2TeI_6	11.70 [249]	12.06	11.87	11.65
Cs_2SnI_6	11.65 [249]	12.00	11.82	11.57

and octahedral factor (μ) [283], given as:

$$t = \frac{r_A + r_X}{\sqrt{2}(r_B + r_X)}, \quad \mu = \frac{r_B}{r_X} \tag{5.2}$$

where r_A, r_B, and r_X are the Shannon ionic radii [284] for A, B and X ions, respectively. The Shannon radii for Cs^{+}, Pt^{4+}, Pd^{4+}, Te^{4+}, Sn^{4+} and I^{-} are 1.88, 0.63, 0.62, 0.69 and 0.97 Å, respectively. For stable cubic perovskites, the ranges of t and μ are $0.8 \leq t \leq 1.0$ and $0.29 \leq \mu \leq 0.55$. Recently, Bartel *et al.* have reported a new tolerance factor (τ) [285] to predict the stability of a perovskite, which is given as:

$$\tau = \frac{r_X}{r_B} - n_A\left(n_A - \frac{r_A/r_B}{ln(r_A/r_B)}\right) \tag{5.3}$$

where n_A is the oxidation state of cation A, r_i is the ionic radius of ion i and $r_A > r_B$ by definition. $\tau < 4.18$ indicates the formation of perovskite (92% accuracy). Since the range of τ is calculated for ABX_3 and $A_2BB^{'}X_6$ double perovskites, this may deviate for vacancy-ordered double perovskites (due to defects). The calculated values given in Table 5.2 show that the considered perovskites are stable in cubic structures.

Table 5.2: Goldschmidt tolerance factor (t), octahedral factor (μ) and new tolerance factor (τ) of Cs_2BI_6 vacancy-ordered double perovskites.

Configurations	***t***	μ	τ
Cs_2PtI_6	1.02	0.28	5.25
Cs_2PdI_6	1.02	0.28	5.31
Cs_2TeI_6	0.91	0.44	4.19
Cs_2SnI_6	0.99	0.31	4.90

5.3.2.2 Thermodynamic stability

Besides structural stability, we have also calculated the thermodynamic stability [286, 287] of Cs_2BI_6 (B = Pt, Pd, Te, Sn) vacancy-ordered double perovskites. For this, we have calculated the Gibbs free energies (ΔG) of perovskites as per the equations:

$$Cs_2PtI_6 \longrightarrow 2CsI + PtI_4 \tag{5.4}$$

$$Cs_2PdI_6 \longrightarrow CsI_3 + PdI_2 + CsI \tag{5.5}$$

$$Cs_2TeI_6 \longrightarrow 2CsI + TeI_4 \tag{5.6}$$

$$Cs_2SnI_6 \longrightarrow 2CsI + SnI_4 \tag{5.7}$$

Here $E(Cs_2BI_6)$, $E(CsI_3)$, E(CsI) and $E(BI_4)$ are respectively the total DFT energies of Cs_2BI_6, CsI_3, CsI and BI_4 and ΔH_D is the decomposition energy. The $\Delta G(T, P)$ values are listed in Table 5.3. The negative values confirm the thermodynamic stability of these vacancy-ordered double perovskites (see Fig. 5.2).

Table 5.3: $\Delta G(T, P)$ of Cs_2BI_6 perovskites calculated using PBE and HSE06 ε_{xc} functionals

Configurations	$\mathbf{\Delta G\ (eV/atom)(PBE)}$	$\mathbf{\Delta G\ (eV/atom)(HSE06)}$
Cs_2PtI_6	-0.62	-0.77
Cs_2PdI_6	-0.04	-0.16
Cs_2TeI_6	-1.09	-1.17
Cs_2SnI_6	-0.35	-0.44

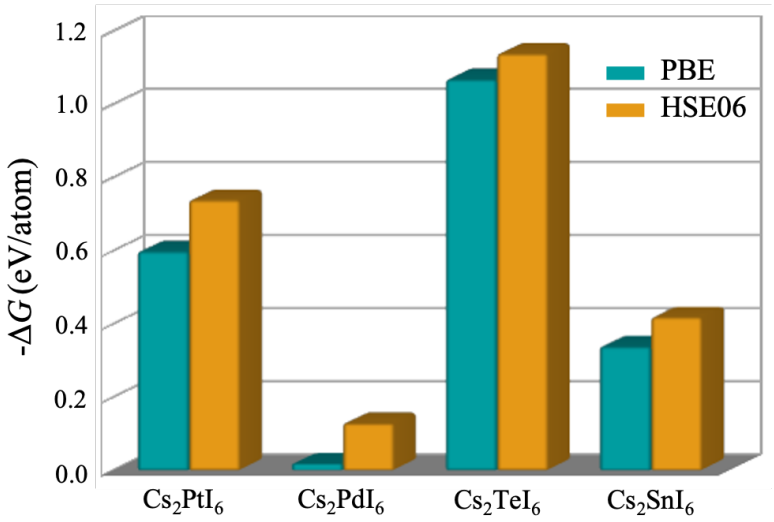

Figure 5.2: $\Delta G\ (T, P)$ of Cs_2BI_6 vacancy-ordered double perovskites calculated using PBE and HSE06 ε_{xc} functionals.

5.3.2.3 Mechanical stability

To determine the mechanical stability of the perovskites, we have calculated the elastic constants of the materials using the finite strain theory [288]. For cubic symmetry, three independent elastic constants viz., C_{11}, C_{12} and C_{44} are sufficient to explain the mechanical stability and related properties of the crystal. The corresponding mechanical stability criterion [289, 290] is given as follows:

$$C_{11} > 0,\ \ C_{44} > 0,\ \ C_{11} - C_{12} > 0,\ \ C_{11} + 2C_{12} > 0 \tag{5.8}$$

Using these elastic constants, we can calculate Bulk (B), Shear (G) and Young's modulus (E) of the perovskites. The Voigt bulk (B_V) and shear (G_V) moduli, Reuss bulk (B_R) and shear

(G_R) moduli are calculated using the following relations:

$$B_V = B_R = \frac{(C_{11} + 2C_{12})}{3} \tag{5.9}$$

$$G_V = \frac{(C_{11} - C_{12} + 3C_{44})}{5} \tag{5.10}$$

$$G_R = \frac{5(C_{11} - C_{12})C_{44}}{4C_{44} + 3(C_{11} - C_{12})} \tag{5.11}$$

According to Voigt-Reuss-Hill approximations [291], Young's modulus (E) and Poissons's ratio (ν) are obtained as:

$$B = \frac{B_V + B_R}{2}, \quad G = \frac{G_V + G_R}{2} \tag{5.12}$$

$$E = \frac{9BG}{3B + G} \tag{5.13}$$

$$\nu = \frac{3B - 2G}{3B + G} \tag{5.14}$$

The ductility of these perovskites is studied in terms of Pugh's (B/G) and Poisson's ratio (ν). If the $B/$G is found to be greater (or lower) than 1.75, the material is ductile (or brittle). For ν, the limiting value is 0.26. The calculated elastic constants and moduli are given in Table 5.4. As

Table 5.4: Calculated elastic constants C_{ij} (GPa), Bulk modulus *B* (GPa), Shear modulus *G* (GPa), Young's modulus *E* (GPa), Pugh's ratio *B/G*, Poisson's ratio ν and elastic anisotropy ***A*** of Cs_2BI_6 vacancy-ordered double perovskites.

Configurations	C_{11}	C_{12}	C_{44}	***B***	***G***	***E***	***B/G***	ν	***A***
Cs_2PtI_6	9.58	4.51	3.93	6.20	3.30	8.40	1.88	0.27	1.55
Cs_2PdI_6	16.64	8.98	7.36	11.53	5.66	11.39	2.04	0.29	1.92
Cs_2TeI_6	20.30	10.55	8.70	13.80	6.90	17.74	2.00	0.29	1.78
Cs_2SnI_6	14.36	8.20	6.65	10.25	4.88	12.63	2.10	0.29	2.16

we can see, the elastic constants satisfy the stability criteria, indicating the mechanical stability of these vacancy-ordered double perovskites. The calculated values of B/G (> 1.75) and ν

(> 0.26) show that the studied vacancy-ordered double perovskites are ductile (see Table 5.4). Also, we have calculated the elastic anisotropy (A) of these materials, given by the equation:

$$A = \frac{2C_{44}}{C_{11} - C_{12}} \tag{5.15}$$

where A represents the elastic anisotropy coefficient. The value of A is equal to 1 for an isotropic crystal. The deviation from this value measures the degree of elastic anisotropy possessed by the crystal. According to the calculated values, all the considered double perovskites are anisotropic in nature.

5.3.3 Electronic structure analysis

After studying the stability, we have calculated the electronic band gaps (with and without SOC) of the vacancy-ordered double perovskites. Since simple local/semi-local ϵ_{xc} functionals (viz., LDA, GGA) are unable to predict the band gaps correctly due to their incapability of capturing the electron's self-interaction error, we have employed HSE06 ϵ_{xc} functional and many-body perturbation theory (G_0W_0) to calculate the band gaps more accurately. The calculated band gaps of Cs_2PtI_6, Cs_2PdI_6, Cs_2TeI_6 and Cs_2SnI_6 are 1.35, 1.43, 1.49 and 1.23 eV, respectively. This implies that all these perovskites have band gaps in the visible region, expanding their scope for energy-harvesting applications. The values of band gaps are listed in Table 5.5, which agree well with the experimental values. Also, we have plotted the bandstructures of perovskites using HSE06+SOC ϵ_{xc} functional (see Fig. 5.3).

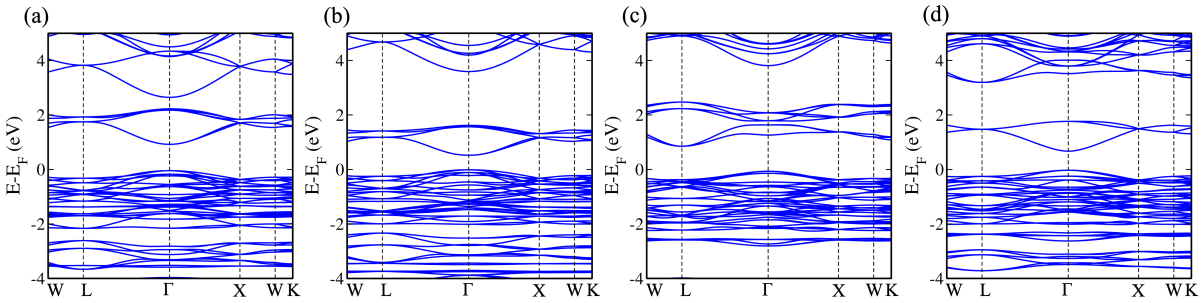

Figure 5.3: Band structures of (a) Cs_2PtI_6, (b) Cs_2PdI_6, (c) Cs_2TeI_6 and (d) Cs_2SnI_6 vacancy-ordered double perovskites, calculated using HSE06+SOC ε_{xc} functional.

Fig. 5.4 shows the pDOS of all four vacancy-ordered double perovskites. The valence band maximum (VBM) of these perovskites are mostly dominated by I-p orbitals, while conduction band minimum (CBm) are contributed by I-p orbitals along with Pt-d, Pd-d, Te-p and Sn-s

Table 5.5: Band gap (eV) of Cs_2BI_6 vacancy-ordered double perovskites calculated using different ϵ_{xc} functionals.

Configurations	PBE	PBE+SOC	HSE06	HSE06+SOC	G_0W_0@PBE+SOC	G_0W_0@HSE06+SOC	Experimental
Cs_2PtI_6	0.36	0.29	1.07	0.96	**1.35**	2.20	1.37 [292]
Cs_2PdI_6	0.06	0.02	0.62	0.51	0.59	**1.43**	1.41 [293]
Cs_2TeI_6	1.14	0.91	1.70	**1.49**	2.12	2.44	1.50 [294]
Cs_2SnI_6	0.09	0.06	0.84	0.70	**1.23**	2.31	1.25 [249]

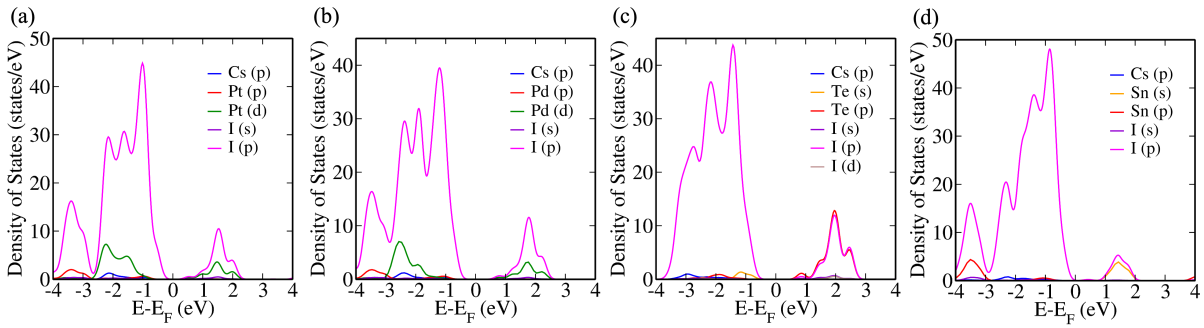

Figure 5.4: Projected density of states (pDOS) of (a) Cs_2PtI_6, (b) Cs_2PdI_6, (c) Cs_2TeI_6 and (d) Cs_2SnI_6 vacancy-ordered double perovskites, calculated using HSE06+SOC ε_{xc} functional.

orbitals in Cs_2PtI_6, Cs_2PdI_6, Cs_2TeI_6 and Cs_2SnI_6, respectively. The VBM is also composed of Pt-d, Pd-d and Te-s orbitals in Cs_2PtI_6, Cs_2PdI_6 and Cs_2TeI_6, respectively. There is a strong hybridization of Te-p and I-p orbitals in Cs_2TeI_6 and Sn-s and I-p orbitals in Cs_2SnI_6. For the reliability of the calculations, we have checked the convergence of the properties viz., energy (E), imaginary (Im(ε)) and real (Re(ε)) part of the dielectric function in the vacancy-ordered double perovskites with k-grid. The energies of the Cs_2BI_6 perovskites in Table 5.6 show that 4×4×4 k-grid is sufficient to calculate E.

5.3.4 Thermoelectric properties of Cs_2BI_6 (B = Pt, Pd, Te, Sn) vacancy-ordered double perovskites

Next, we have calculated the thermoelectric properties of the perovskites using the BoltzTrap Code [275]. Fig. 5.5(a) shows the Seebeck coefficient (S) as a function of chemical potential (μ) for Cs_2BI_6 perovskites. S measures the induced thermoelectric voltage (ΔV) in response to a temperature difference (ΔT) across the material and is given as S=$\Delta V/\Delta T$, while μ shows

Table 5.6: Energies (eV) of Cs_2BI_6 (B = Pt, Pd, Te, Sn) vacancy-ordered double perovskites at different *k*-grids calculated using PBE ε_{xc} functional.

	***E* (eV)**				
Configurations	**2×2×2**	**3×3×3**	**4×4×4**	**5×5×5**	**6×6×6**
Cs_2PtI_6	-110.5206	-110.5481	-110.5493	-110.5493	-110.5494
Cs_2PdI_6	-106.3718	-106.4057	-106.4056	-106.4057	-106.4052
Cs_2TeI_6	-98.7717	-98.7872	-98.7873	-98.7874	-98.7873
Cs_2SnI_6	-105.2440	-105.2542	-105.2547	-105.2550	-105.2532

the addition or removal of electrons (doping) against the repulsive forces of electrons already present in the material. Advantageously, the position of μ determines the fraction of electrons in the conduction or valence band which take part in the electronic transport and hence influences S. Thus, S can be determined from the change in the chemical potential of electrons induced by the temperature difference. By definition, μ=0 coincides with the top of the valence band in semiconductors. This implies that at μ=0, the nature of S determines the type of semiconductor. From Fig. 5.5(a), we can see that at μ=0, the value of S is positive for Cs_2PtI_6 and Cs_2TeI_6 at various temperatures, indicating that these perovskites are p-type semiconductors. The maximum values of S for Cs_2PtI_6 and Cs_2TeI_6 are 710 and 190 µV/K, respectively, at 300 K. On the other hand, S is negative for Cs_2PdI_6 and Cs_2SnI_6, which indicates the n-type character in these perovskites [295]. For Cs_2PdI_6 and Cs_2SnI_6, the maximum values of S are 148 and 290 µV/K, respectively, at 300 K. Also, we have observed that the value of S decreases with an increase in temperature for all the considered Cs_2BI_6 perovskites. Fig. 5.5(b) shows the variation of S with carrier concentration (n) [296, 297] at different temperatures. Subsequently, to calculate the efficiency of material to convert heat into electrical energy, we have calculated the zT as a function of temperature (see Fig. 5.5(c)) for Cs_2BI_6 perovskites. The computed average zT for Cs_2PtI_6, Cs_2PdI_6, Cs_2TeI_6 and Cs_2SnI_6 are 0.88, 0.85, 0.95 and 0.78, respectively, which make them promising for thermoelectric applications.

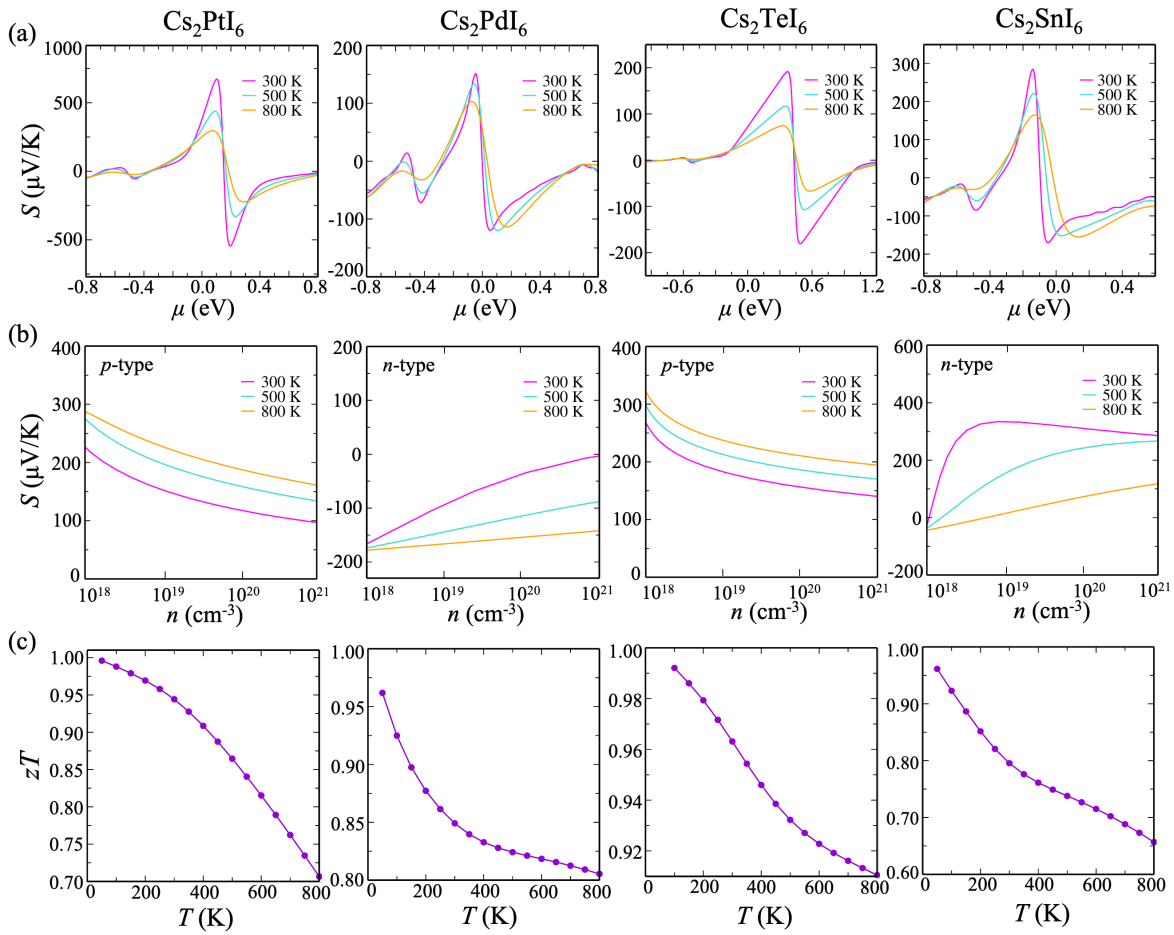

Figure 5.5: Seebeck coefficient (S) as a function of (a) chemical potential (μ) and (b) carrier concentration (n) at 300, 500 and 800 K. (c) Thermoelectric figure of merit (zT) as a function of temperature (T) for Cs_2PtI_6, Cs_2PdI_6, Cs_2TeI_6 and Cs_2SnI_6, calculated using HSE06 ϵ_{xc} functional.

5.3.5 Relation between anharmonicity and lattice thermal conductivity

Low thermal conductivity is desirable for efficient thermoelectric materials, which in turn depends on lattice dynamics [298, 299]. Lattice dynamics play a pivotal role in governing materials properties such as thermal conductivity [300], ionic and electronic transport [301], optical emission [302], ferroelectricity and superconductivity [303]. Deviation from harmonic vibrational potential results in high amplitude anharmonic vibrations that introduce vibrational disorder in the system. This results in significant phonon-phonon scattering, which leads to low thermal conductivities and better thermoelectric performance [304, 305, 306] (see Fig. 5.6).

To examine this deviation at high temperatures, we have calculated the harmonic (U_h) as well as anharmonic energy (U_{ah}) in vacancy-ordered double perovskites. U_h is calculated un-

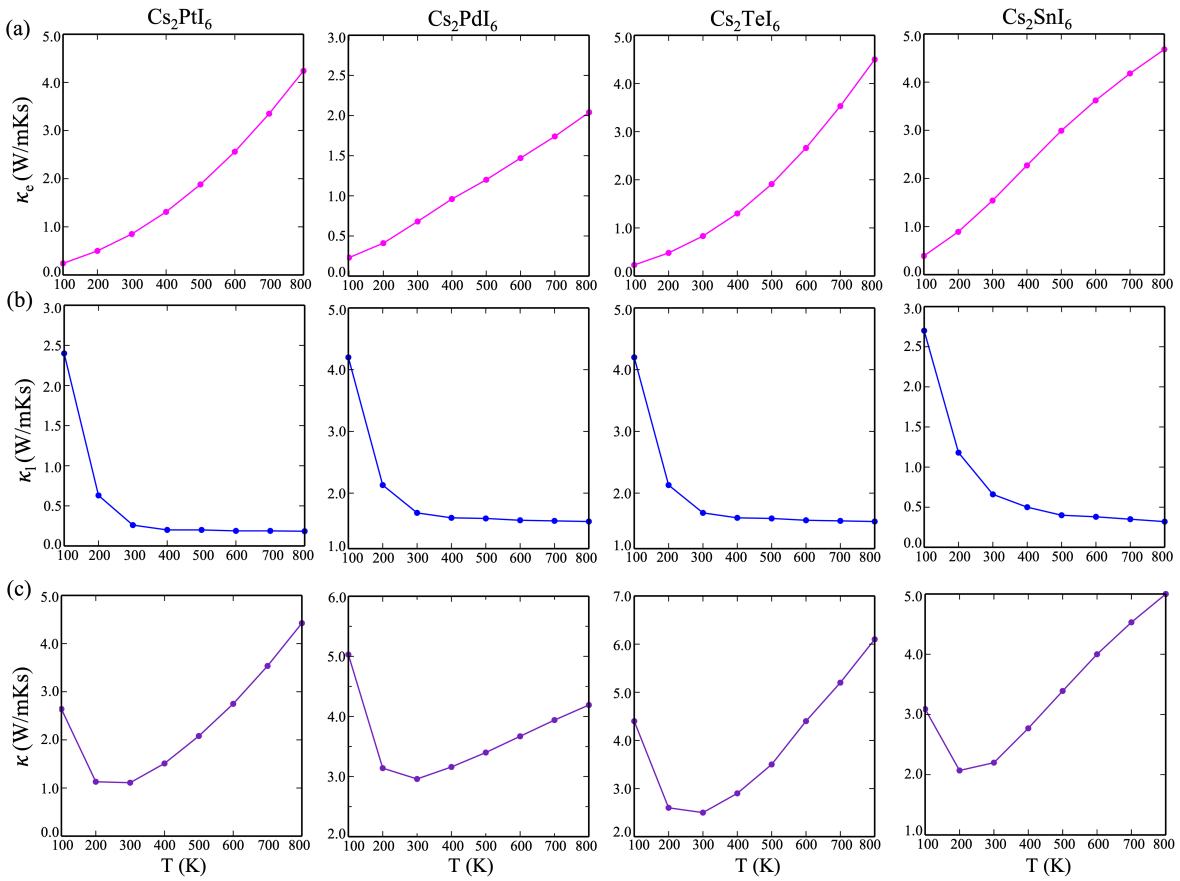

Figure 5.6: Calculated (a) electronic thermal conductivity, (b) lattice thermal conductivity and (c) total thermal conductivity in Cs_2BI_6 vacancy-ordered double perovskites, calculated using PBE ε_{xc} functional.

der harmonic approximation for all perovskites. To quantify U_{ah} in Cs_2BI_6 vacancy-ordered double perovskites, we have performed AIMD calculations at different temperatures using Nose-Hoover thermostat [119]. This data is then fed to a post-processing python package pyHMA [278], which determines the anharmonic energy. Fig. 5.7(a-d) show the variation of U_{ah} with temperature. As the temperature increases, we observe a deviation from harmonic potential leading to lattice anharmonicity.

The intimate connection between anharmonic lattice dynamics and functional properties motivates a fundamental understanding of anharmonicity in this class of materials. To further assess anharmonicity in our system, we have first examined the dynamical stability by plotting the phonon dispersion bandstructures of all Cs_2BI_6 perovskites using density functional perturbation theory (DFPT) [277], as shown in Fig. 5.8(a). For vacancy-ordered double perovskites, the structural symmetry confirms 108 phonon modes as they contain 36 atoms per unit cell.

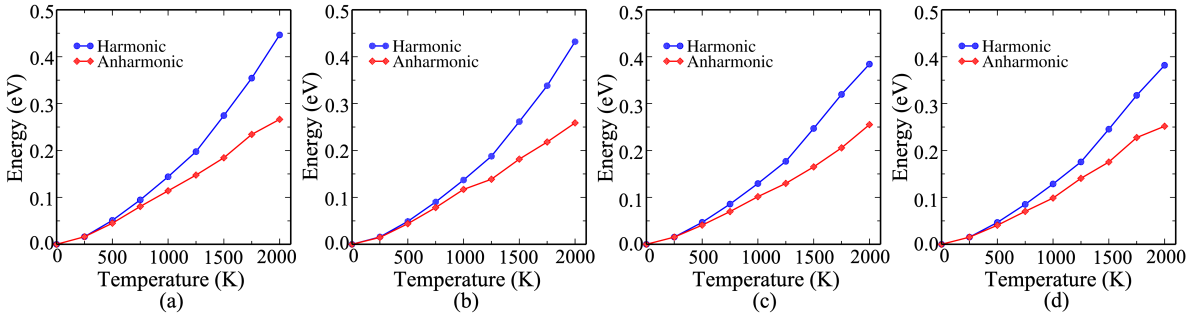

Figure 5.7: Harmonic (U_h) and anharmonic energy (U_{ah}) of (a) Cs_2PtI_6 (b) Cs_2PdI_6 (c) Cs_2TeI_6 and (d) Cs_2SnI_6 as a function of temperature (T), calculated using HSE06 ϵ_{xc} functional.

Out of these 108 phonon modes, there are 3 acoustic modes, while the remaining modes are optical, characterized as low and high-frequency phonons, respectively. The absence of negative frequencies confirms the dynamical stability of these perovskites. After examining the phonon modes, we try to explore the interaction between the atoms of these perovskites. The spatial distribution of the electron density around atom gives the measure of phonon anharmonicity. Therefore, we have computed the ELF to study materials bonding and anharmonicity (see Fig. 5.8(b)). The localization of electrons is estimated by a dimensionless ELF probability density ranging between 0 and 1. With the increase in ELF value, the electrons get more localized, and hence the bonds become stronger. As we can see in Fig. 5.8(b), I atoms draw more charge because of its higher electronegativity in comparison to B atoms. Nevertheless, there is significant charge sharing among B-I bonds due to the small electronegativity difference, indicating the possibility of covalent bonding. On the other hand, no charge is shared between Cs and B/I atoms. However, physical interaction between Cs and [BI_6] octahedra results in nonspherical electron density around Cs and I atoms, which explains the origin of the phonon anharmonicity. Also, there is no charge transfer between the neighbouring octahedra owing to the vacancies in Cs_2BI_6 perovskites. This indicates that [BI_6] octahedra in Cs_2BI_6 are loosely bound and may lead to cluster-rattling vibrations along with Cs atom rattlers [270]. This in turn, increases the phonon scattering followed by suppression of κ [305, 306].

Anharmonic lattice dynamics give rise to stronger electron-phonon coupling in the material as electrons interact with lattice vibrations via the formation of polarons [307, 308]. To study these electron-phonon interactions, we have calculated the electron-phonon coupling strength using Fröhlich's polaron model [272]. The dimensionless Fröhlich electron-phonon coupling

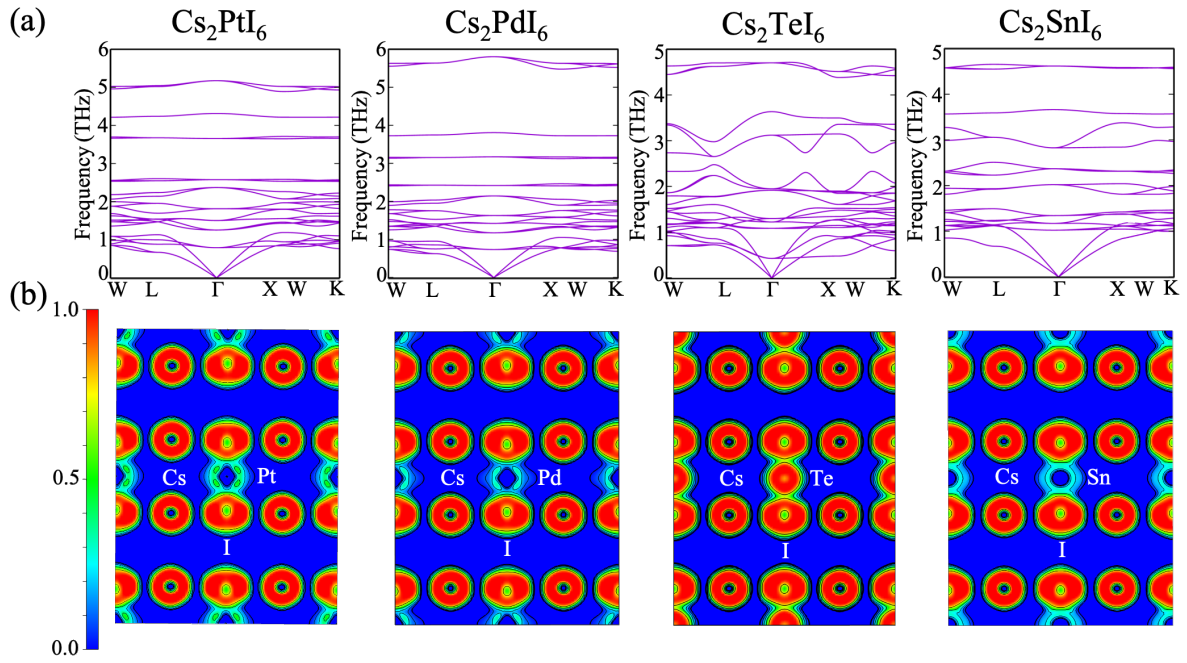

Figure 5.8: (a) Phonon dispersion plots and (b) two dimensional ELF of (110) plane passing through Cs, Pt, Pd, Te, Sn and I atoms of Cs_2PtI_6, Cs_2PdI_6, Cs_2TeI_6 and Cs_2SnI_6, calculated using PBE ϵ_{xc} functional. The ELF values of 0.0, 0.5, and 1.0 are interpreted as absence, uniform electron gas like, and localized electrons, respectively.

parameter (α) measures the electron-phonon coupling strength of the material and is given as:

$$\alpha = \frac{1}{4\pi\epsilon_0}\frac{1}{2}\left(\frac{1}{\epsilon_\infty} - \frac{1}{\epsilon_{\text{static}}}\right)\frac{e^2}{\hbar\omega_{\text{LO}}}\left(\frac{2m^*\omega_{\text{LO}}}{\hbar}\right)^{1/2} \tag{5.16}$$

The α depends on the material-specific properties, viz., electronic (ϵ_∞) and ionic static (ϵ_{static}) dielectric constants, permittivity of free space (ϵ_0), the effective carrier mass (m^*), and a characteristic longitudinal optical phonon angular frequency (ω_{LO}). For a system having multiple phonon branches, an average LO frequency is calculated by considering all the infrared active optical phonon branches and taking a spectral average of them [309]. The values of α for Cs_2BI_6 perovskites are listed in Table 5.7 and follow the order: Cs_2PtI_6 > Cs_2PdI_6 > Cs_2TeI_6 > Cs_2SnI_6. The ELF and strong electron-phonon coupling validate the presence of anharmonicity in our considered perovskites. Also, the heavy atoms present in the system act as phonon rattlers and help suppress the lattice thermal conductivity effectively. This leads to their effective utilization in high-performance thermoelectric device applications.

Table 5.7: Effective mass of electrons m^* in terms of rest mass of electron m_0, electronic dielectric constant ϵ_∞ and ionic static dielectric constant ϵ_{static} of Cs_2BI_6 perovskites.

Configurations	m^*	ϵ_∞	ϵ_{static}
Cs_2PtI_6	0.49	3.41	4.55
Cs_2PdI_6	0.47	2.80	3.30
Cs_2TeI_6	0.40	3.59	5.55
Cs_2SnI_6	0.33	2.67	3.46

Table 5.8: Calculated polaron parameters corresponding to electrons in Cs_2BI_6 perovskites. ω_{LO} (THz), α_e, m_P, l_P (Å) and μ_P ($cm^2V^{-1}s^{-1}$) are the optical phonon frequency, Fröhlich coupling constant, polaron mass, polaron radii and polaron mobility, respectively.

Configurations	ω_{LO} **(THz)**	α_e	m_P/m^*	l_P **(Å)**	μ_P **($cm^2V^{-1}s^{-1}$)**
Cs_2PtI_6	1.74	2.24	1.29	22.90	42.15
Cs_2PdI_6	1.62	1.81	1.19	25.10	64.90
Cs_2TeI_6	4.26	1.73	1.35	50.98	45.30
Cs_2SnI_6	3.52	1.50	1.27	47.43	71.12

5.3.6 Conclusions

In summary, we have carried out an extensive study to investigate the structural, elastic and thermoelectric properties of Cs_2BI_6 (B = Pt, Pd, Te, Sn) vacancy-ordered perovskites under the framework of density functional theory. The Pugh's and Poisson's ratios show the ductile nature of the perovskites. Furthermore, the negative Gibbs free energies and phonon band structures affirm the stability of these materials. The band gaps calculated using different ϵ_{xc} functionals fall within the visible region, which is advantageous for energy-harvesting properties. The zT values for Cs_2PtI_6, Cs_2PdI_6, Cs_2TeI_6 and Cs_2SnI_6 are 0.88, 0.85, 0.95 and 0.78, respectively, which show that these perovskites are promising for thermoelectric applications. To examine the role of anharmonicity, the ELFs are plotted for these perovskites, which indi-

cates the presence of lattice anharmonicity. The calculation of the harmonic and anharmonic energy confirm the anharmonicity in this class of materials. As a result of anharmonicity, these compounds have strong electron-phonon coupling and the strength of this coupling is quantified using Fröhlich's polaron model. The observed phonon-phonon scattering, driven by anharmonicity and the influence of heavy atoms as phonon rattlers, contributes to the low thermal conductivity and enhanced thermoelectric properties.

CHAPTER 6

Low lattice thermal conductivity and its role in thermoelectric performance of CsNaS and RbNaS alkali metal sulfides

6.1 Introduction

Thermoelectric (TE) materials hold significant importance in energy generation as they possess the capability to convert heat into electricity and vice versa, without the requirement for any mechanical components. These materials have emerged as promising solutions to tackle waste heat challenges and enhance energy efficiency in response to the growing energy demands of contemporary technology [241, 310]. The evaluation of a TE device's performance typically revolves around a dimensionless parameter known as the figure of merit, denoted as zT. This parameter relies on various crucial physical parameters, including the Seebeck coefficient (α), electrical conductivity (σ), total thermal conductivity (κ, consisting of electronic (κ_e) and lattice (κ_{ph}) contributions), and temperature (T). Mathematically, zT is represented as $zT = \alpha^2\sigma T/(\kappa = \kappa_e+\kappa_{ph})$. Achieving a high zT in a TE material poses a significant challenge due to the intricate interplay among these TE parameters.

To tackle this challenge, researchers have explored various innovative approaches aimed at decoupling the transport of electrons and phonons within materials, thereby improving the zT parameter. These methods encompass a diverse array of techniques, such as band-structure engineering [311, 312, 313, 314, 315], nanostructuring [316], composite materials [317, 318, 319, 320], and the application of the high-entropy concept [321, 322]. Essentially, the simultaneous enhancement of electronic transport and the suppression of phonon propagation stand as critical criteria for the advancement of high-performance TE materials, as demonstrated by materials like PbTe [323], SnSe [258], skutterudites [324], and half-Heusler

compounds [325]. In this chapter, we have studied the thermoelectric properties of CsNaS and RbNaS alkali metal sulfides. This class of materials represents environmentally friendly alternatives to lead halide perovskites.

6.2 Computational methods

The density functional theory (DFT) [14, 15] calculations were carried out using the plane-wave-based pseudopotential approach, as implemented in the Vienna Ab initio Simulation Package (VASP) [169, 170]. The structural optimization of all the modeled structures was performed using generalized gradient approximation (GGA) expressed by the Perdew–Burke–Ernzerhof (PBE) [217] exchange-correlation (ϵ_{xc}) functional. The self-consistency loop was converged with a total energy threshold of 0.01 meV by conjugate gradient (CG) minimization. The structures were fully relaxed until the Heymann–Feynman forces on each atom were less than 10^{-5} eV/Å. All the structures were visualized through VESTA (Visualization for Electronic and STructural Analysis) [339] software. A $6 \times 6 \times 2$ k-mesh was used for Brillouin zone sampling. The electron wave function was expanded in a plane-wave basis set with an energy cutoff of 600 eV. Phonon calculations were obtained within the harmonic approximation and using a finite displacement method [340]. The phonon dispersion plots and group velocities were calculated using the PHONOPY package [222, 221]. Lattice thermal conductivity (κ_l) is calculated using phono3py. The BoltzTrap Code [275], based on Boltzmann transport theory, was used to evaluate thermoelectric properties.

6.3 Results and discussion

6.3.1 Dynamical stability

CsNaS and RbNaS exhibit an ABX-type structure with P4/nmm symmetry. The structures of these alkali metal sulfides are shown in Fig. 6.1a and 6.1b. To examine the dynamical stabilities of these sulfides, we have calculated the phonon dispersion (ω vs k) plots. As illustrated in Fig. 6.1c and 6.1d, there are no negative frequencies in the phonon spectrums, suggesting the dynamical stability of CsNaS and RbNaS alkali metal sulfides.

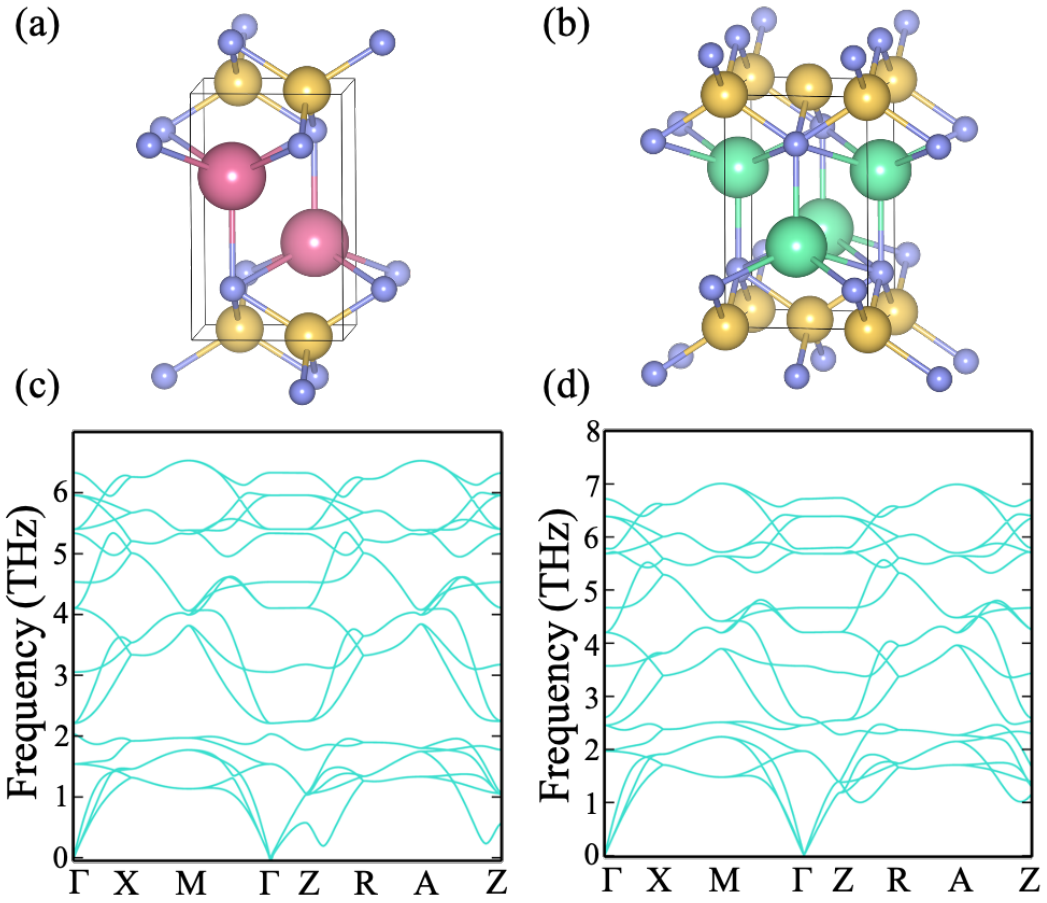

Figure 6.1: Crystal structure of (a) CsNaS (b) RbNaS having P4/nmm symmetry. Cs, Rb, Na and S atoms are indicated by pink, green, yellow and purple colors, respectively. Phonon band structure of (a) CsNaS (b) RbNaS alkali metal sulfides.

6.3.2 Electronic properties

Next, to gain a deeper understanding of the electronic transport, we conducted DFT calculations to analyze the electronic band structures of CsNaS and RbNaS alkali metal sulfides. The bandstructures, calculated using PBE functional, are shown in Fig. 6.2. The band gaps for CsNaS and RbNaS are 2.52 and 2.41 eV, respectively, which are favorable for thermoelectric applications.

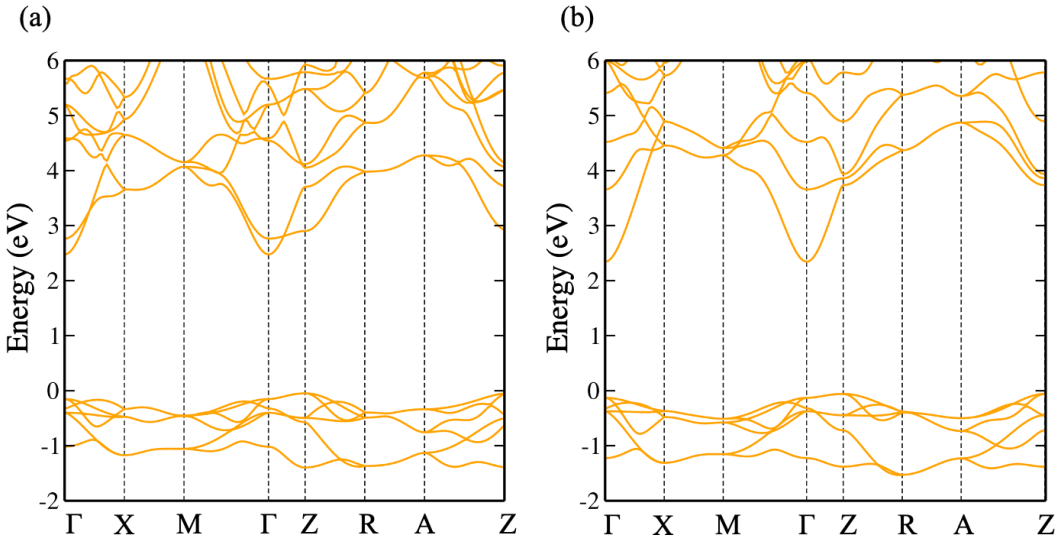

Figure 6.2: Band structures of (a) CsNaS and (b) RbNaS, calculated using PBE ϵ_{xc} functional.

6.3.3 Lattice thermal conductivity (κ_l)

Subsequently, to investigate the thermal transport, we have determined the lattice thermal conductivity (κ_l) as a function of temperature for CsNaS and RbNaS alkali metal sulfides using the second-order and third-order IFCs by solving the linearized phonon Boltzmann transport equation (PBTE) (see Fig. 6.3). From the calculations, we observe that the calculated lattice thermal conductivity of CsNaS and RbNaS are 0.25 $Wm^{-1}K^{-1}$ and 0.65 $Wm^{-1}K^{-1}$ at 300 K, which is much lower than that for commonly known thermoelectrics, such as PbSe (2.64 $Wm^{-1}K^{-1}$) and PbTe (2.30 $Wm^{-1}K^{-1}$). Lower values of κ_l makes these materials promising for thermoelectric applications. Additionally, it is observed that the κ_l has anisotropic nature. The estimated values are higher along the x-direction as compared to those along the z-direction, suggesting the thermal conduction along z as more beneficial for TE applications.

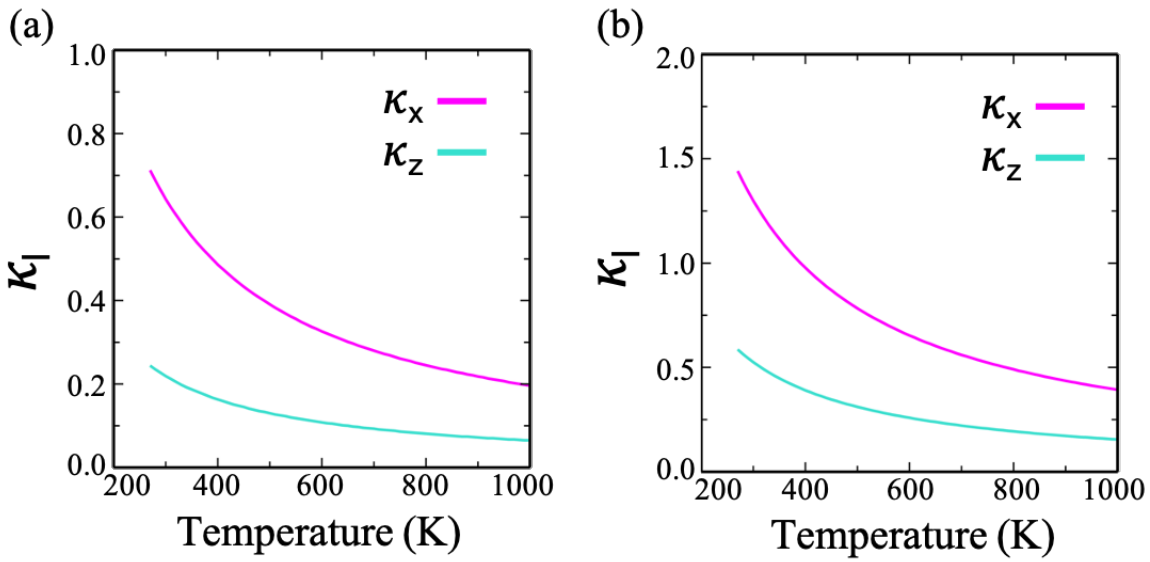

Figure 6.3: Lattice thermal conductivity as a function of temperature of (a) CsNaS and (b) RbNaS alkali metal sulfides.

6.3.4 Gruneisen parameter (γ) and phonon lifetime (τ)

To analyze the origin of this low thermal conductivity, we have determined the Gruneisen parameter (γ). This parameter gives a estimation of the phonon's anharmonicity and predominantly determines the magnitude of phonon scattering. The γ is found to vary from 0.2 to 5.1 for CsNaS and 0 to 3.7 for RbNaS over the entire range of frequencies (see Fig. 6.4), which is higher than the value estimated for PbTe (1.66) and PbSe (1.52). This shows that the anharmonicity in both materials is very pronounced and thus assists in reducing the phonon thermal conductivity. To further analyze the lattice conductivity, we focus on the phonon lifetime (τ) for the frequency range of interest (see Fig. 6.5). The phonon modes are depicted as black spots in the picture; as the color thermometer shows, red and blue are the regions of most significant phonon mode density. The spread of phonon lifetimes indicates that the maximum value for the materials is 6 ps, which is quite promising being less than the highest phonon lifetime of 8 ps for the good TE performer PbTe. Short lifetimes imply the phonon–phonon scattering rates will be remarkably higher, consequently leading to a low κ_l value.

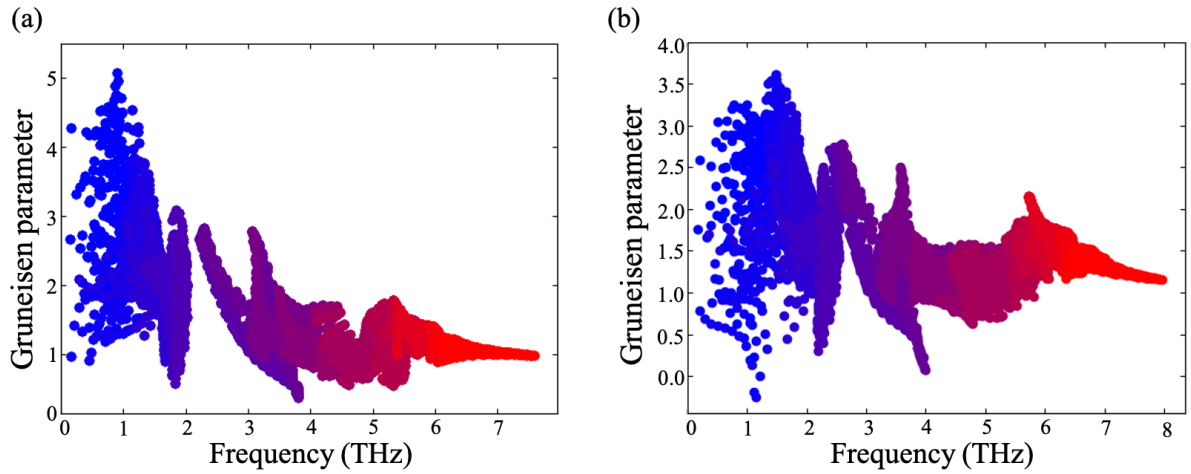

Figure 6.4: Gruneisen parameter (γ) of (a) CsNaS and (b) RbNaS alkali metal sulfides.

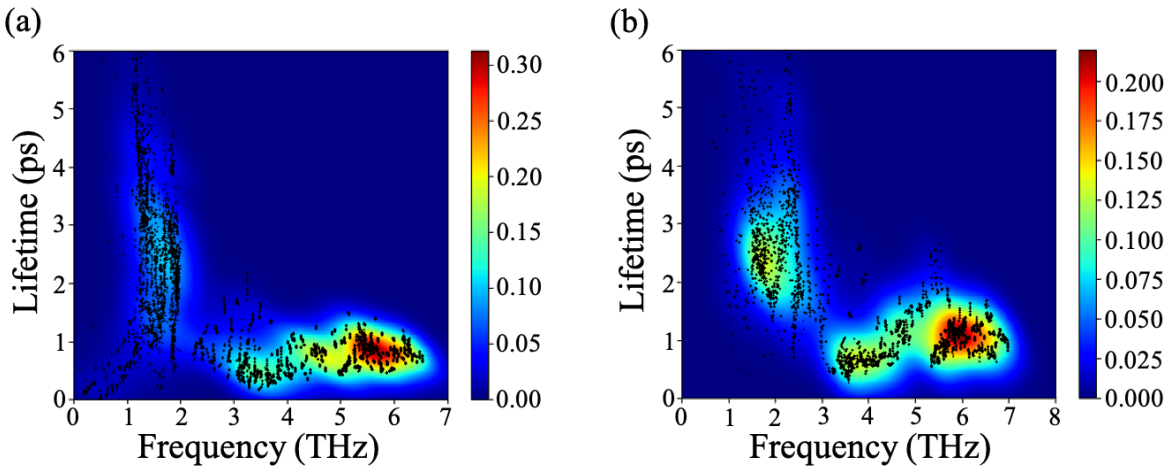

Figure 6.5: Phonon lifetimes (τ) of (a) CsNaS and (b) RbNaS alkali metal sulfides.

6.4 Conclusions

In summary, our investigation has focused on the thermoelectric properties of CsNaS and RbNaS alkali metal sulfides within the framework of density functional theory. Specifically, we have analyzed the lattice thermal conductivity (κ_l) of these sulfides across varying temperatures. Our computational findings indicate that these materials exhibit low κ_l values, suggesting their potential suitability for thermoelectric applications. Additionally, we have explored several contributing factors to this low κ_l, including strong anharmonicity and a reduced phonon lifetime primarily influenced by intense phonon-phonon scattering.

CHAPTER 7

Enhancing thermoelectric properties via crystal field engineering and low thermal conductivity

7.1 Engineering electronic structure and lattice dynamics to achieve enhanced thermoelectric performance of Mn–Sb co-doped GeTe

7.1.1 Introduction

Thermoelectric (TE) materials, which have the unique ability to convert heat energy into electrical power bidirectionally, offer promising solutions to address the global energy challenge [241, 343]. Recent advancements in TE properties have been driven by innovative transport mechanisms, focusing on (a) optimizing electrical transport performance [311, 312, 344, 345] and (b) reducing thermal conductivity within a single system [346, 347, 348]. Within the realm of notable TE materials, IV–VI-based chalcogenides like GeTe, PbTe, and SnTe stand out due to their attractive TE properties in the intermediate temperature range ($\sim$ 500–800 K). These materials owe their remarkable characteristics to their distinct band structure, high carrier mobility, and intrinsically low κ_{ph} (phonon thermal conductivity) [349, 350, 351]. However, the GeTe system contains inherent Ge vacancies, resulting in a high hole carrier concentration (n $\sim$ 10^{21} cm^{-3}), high electrical conductivity ($\sigma \sim$ 8000 S/cm), and a small Seebeck coefficient ($\alpha \sim$ 28 μV/K at 300 K), which collectively lead to inferior TE properties. Additionally, GeTe undergoes a second-order phase transition ($\sim$ 700 K) from a high-temperature cubic (Fm-3m) to a low-temperature rhombohedral structure ($R3m$). Recent research has focused on optimizing GeTe's TE properties and lowering the transition temperature to enhance its practical utility [352, 353]. Achieving a high zT (thermoelectric figure of merit) relies on optimizing carrier

concentration (n ~10^{19}–10^{20} cm^{-3}), band engineering [354], and reducing κ_{ph} through various techniques, including hierarchical architecture engineering [245], defect engineering [260], composite approaches [317, 355], and the incorporation of multiscale scattering centers [356].

As discussed earlier, various strategies have been explored to reduce the high hole carrier concentration and enhance α in GeTe [338]. Aliovalent dopants such as Bi^{3+} and Sb^{3+} at the Ge^{2+} site have been employed to lower carrier concentration and decrease κ_{ph} through phonon scattering via solid-solution point defects. While such doping also reduces the phase transition temperature to $\sim$ 300 K at a doping concentration of ~10%, it significantly diminishes electrical conductivity [357]. In contrast, Mn doping in GeTe has effectively promoted band convergence by decreasing the energy difference between the light and heavy hole bands and increasing symmetry through a hexagonal-to-cubic transition, ultimately leading to an increase in the carriers' effective mass [358]. Mn doping also improves carrier concentration (n) in GeTe. Notably, intrinsic vacancies in GeTe result in a high carrier concentration ($\sim 10^{21}$ cm^{-3}) and deepens the Fermi level (E_F) in the valence band. Increasing Mn doping in GeTe further deepens E_F in the valence band, which does not benefit TE performance. Moreover, a higher Mn content ($\sim$ 10%) at the Ge site significantly reduces carrier mobility due to induced spin scattering and does not improve the overall zT [341]. Therefore, optimizing co-doping of Mn and Sb in GeTe is essential to achieve a synergistic effect of enhanced band convergence and an optimized Fermi level position, leading to an improved α for high TE performance in GeTe. This study showcases improved TE properties in Mn and Sb co-doped GeTe through the manipulation of electronic structure (optimized Fermi level position, carrier concentration, and band convergence) and lattice dynamics (reduced phonon velocity). A systematic band-structure calculation for Mn-Sb co-doped GeTe was performed to corroborate experimental results, employing density functional theory (DFT) calculations. Furthermore, a phonon dispersion calculation that accounts for Ge vacancies in GeTe and Mn-Sb co-doped GeTe was conducted to shed light on the reduction of κ_{ph}.

7.1.2 Computational methods

All of the density functional theory (DFT) calculations were performed using the plane-wave-based pseudopotential approach, as implemented in the Vienna Ab initio Simulation Package (VASP). The self-consistency loop was converged with a total energy threshold of 0.01 meV. The structures were fully relaxed until the Heymann-Feynman forces on each atom were

less than 10^{-5} eV/Åfor both pure and doped configurations. The effects of doping were considered by substituting Mn and Sb atoms at the specific sites of Ge atoms in a 2×2×2 supercell (originally in rhombohedral phase) consisting of 48 atoms. The structural optimization was carried out using generalized gradient approximation (GGA) expressed by the Perdew–Burke–Ernzerhof (PBE) exchange-correlation functional. Spin-orbit coupling interactions owing to heavy atoms were included when calculating the electronic structures. A 6×6×2 k-mesh was used for Brillouin zone sampling. The electron wave function was expanded in a plane-wave basis set with an energy cutoff of 600 eV. Phonon calculations were obtained within the harmonic approximation and using a finite displacement method. A 2×2×2 supercell was set for the cubic GeTe containing 64 atoms, whereas, for the rhombohedral phase, a 3×3×1 supercell containing 54 atoms was built. In the Mn–Sb co-doped rhombohedral system, we used a 2×2×1 supercell consisting of 96 atoms.

7.1.3 Results and discussion

7.1.3.1 Electronic structure

In order to gain insights into the electronic transport properties in the Mn–Sb co-doped GeTe system, we conducted DFT calculations to analyze the electronic band structure and density of states (DOS) for pristine GeTe, Mn-doped GeTe, and Mn–Sb co-doped GeTe. The structures are illustrated in Fig. 7.1). In our calculations, we observed that in the electronic structures of both cubic and rhombohedral $Ge_{24}Te_{24}$, the principal valence band (light hole) maximum (VBM) and the conduction band minimum (CBM) occur at the Γ point due to the folding of the L point onto Γ. We determined that the band gap (e_g) for cubic and rhombohedral $Ge_{24}Te_{24}$ is 0.22 eV and 0.52 eV, respectively. These values align with earlier theoretical predictions and experimental findings [334, 359]. It is important to note that pristine GeTe exhibits a high hole carrier concentration, primarily due to the presence of intrinsic Ge vacancies. In our electronic structure calculations, we considered this high carrier concentration, which experimentally ranges from 8×10^{20} to 1.5×10^{21} cm^{-3} for pure GeTe. This range approximately corresponds to Ge vacancy concentrations of 4.3% to 8.1% if we assume one hole per atom [332].

In Fig. 7.2a, the electronic band structure of $Ge_{22}Te_{24}$ is shown. Additionally, we systematically investigated the effects of doping on the band structure: (i) the introduction of one Mn

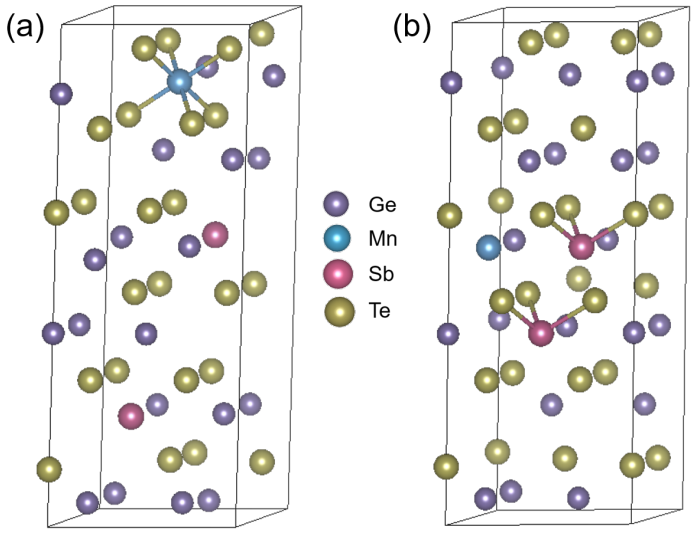

Figure 7.1: (a) and (b) are two configurations of Mn–Sb co-doped system with different energies.

atom (Fig. 7.2b), (ii) the incorporation of one Mn atom and one Sb atom (Fig. 7.2c), and (iii) the substitution of one Mn atom and two Sb atoms for Ge in the GeTe supercell (Fig. 7.2d). The introduction of Mn in Mn-doped GeTe gives rise to a new impurity/donor band attributed to the Mn state [358]. This impurity band results in a reduction of the band gap in GeTe. In the case of Mn–Sb co-doping, we assessed the energies of two distinct configurations: (i) where Mn and Sb atoms are in close proximity and (ii) where they are located farther apart as shown in Fig. 7.1. It was determined that the latter configuration, where Mn and Sb atoms are further apart, is more energetically favorable, thus making it the more stable configuration. As such, our calculations focused on this second configuration [334]. In the context of co-doping Mn and Sb in GeTe (specifically, $Ge_{19}MnSb_2Te_{24}$), the energy separation between the two valence bands, denoted as ΔE_Γ, is further reduced to 0.09 eV. Consequently, the carrier transport in this system is notably influenced by heavy holes. Therefore, our calculations confirm that Mn–Sb co-doping in GeTe leads to enhanced valence band convergence and validates the observed increase in the α.

Next, we computed DOS for all the compositions: pristine $Ge_{24}Te_{24}$, $Ge_{22}Te_{24}$ (with Ge vacancies), $Ge_{21}MnTe_{24}$ (Mn-doped), $Ge_{20}MnSbTe_{24}$, and $Ge_{19}MnSb_2Te_{24}$, as depicted in Fig. 7.2e. The positioning of the Fermi level plays a critical role in optimizing the thermoelectric (TE) performance of any material. In the case of GeTe, its high hole carrier concentration due to intrinsic Ge vacancies results in a deep positioning of the Fermi level within the valence

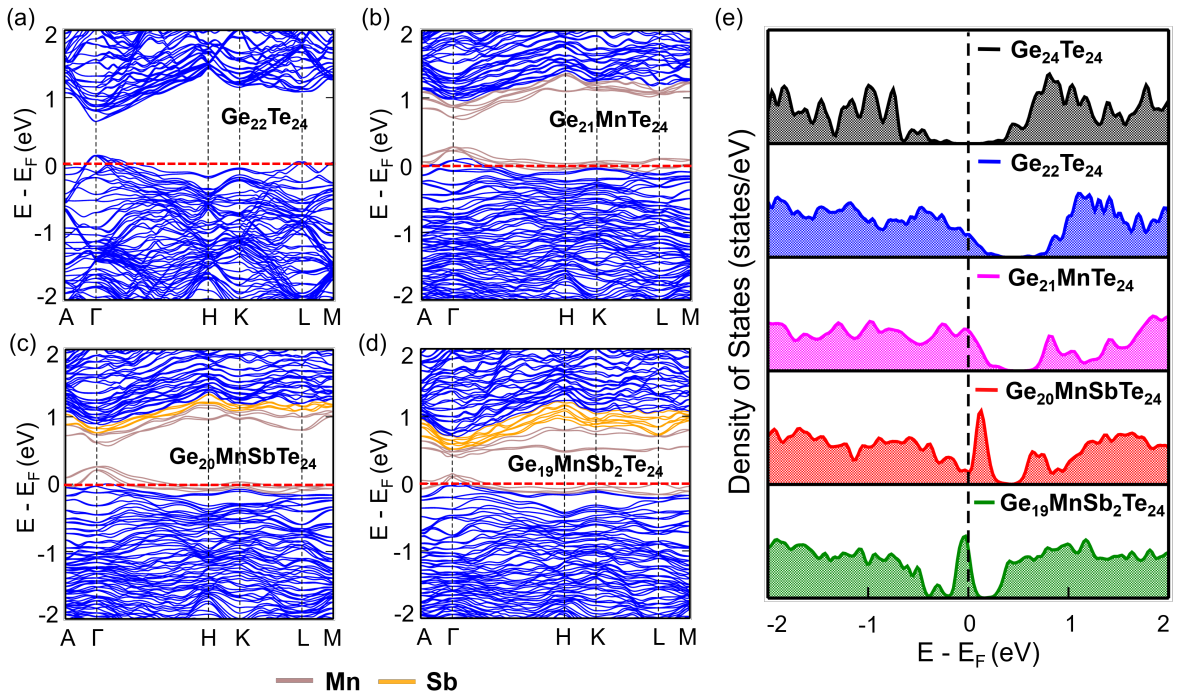

Figure 7.2: Electronic band structures of rhombohedral (a) $Ge_{22}Te_{24}$, (b) $Ge_{21}MnTe_{24}$, (c) $Ge_{20}MnSbTe_{24}$, and (d) $Ge_{19}MnSb_2Te_{24}$. The Ge vacancies are considered during the calculation to attest to the high carrier concentration. The band gap appears at the Γ point in a $2\times2\times2$ supercell containing 48 atoms. The VBM and CBM occur at the L point in the pristine GeTe fold onto the Γ point in the supercell. (e) Density of states of pristine GeTe ($Ge_{24}Te_{24}$), GeTe with Ge vacancies ($Ge_{22}Te_{24}$), Mn-doped GeTe ($Ge_{21}MnSb_{24}$), and Mn–Sb co-doped GeTe ($Ge_{20}MnSbTe_{24}$, $Ge_{19}MnSb_2Te_{24}$) samples.

band. Consequently, the charge carriers below the Fermi level contribute energy transport that compensates for the charge carriers above the Fermi level, leading to a lower α [315]. The DOS plot illustrates that the Fermi level resides at the center of the band gap in pristine $Ge_{24}Te_{24}$. However, with the introduction of Ge vacancies, the Fermi level shifts deep into the valence band, aligning with the high carrier concentration characteristic of GeTe. Mn doping in GeTe also leads to an increase in carrier concentration, which drives the Fermi level even deeper into the valence band. This decrease in the energy offset between the edges of the valence band, as revealed by band-structure calculations, results in band convergence. Hence, the combined effects of band convergence and the deeper positioning of the Fermi level explain the observed rise in the α with increasing carrier concentration in Mn-doped GeTe. Sb doping introduces donor states below the conduction band of pure GeTe, causing the Fermi level to shift towards

the valence band edge and, consequently, a reduction in hole carrier concentration is observed. A similar density of states behavior is noted for Sb–Bi co-doped GeTe [334]. Furthermore, Mn–Sb co-doping accentuates the steepness of the DOS, particularly in the vicinity of the valence band edge. This heightened DOS characteristic indicates a higher effective mass and holds promise for enhancing the α [341]. The Fermi level, influenced by the theoretical consideration of larger Ge vacancies, is positioned within the valence band in both Mn and Sb co-doping cases [332].

The DFT results closely align with the experimental measurements of the α. In the case of pristine GeTe, the heavy hole band is situated approximately 0.21 eV deeper than the light hole band. Even at high carrier concentrations, reaching up to 10^{21} cm^{-3}, the light hole band predominantly governs carrier transport, as indicated by the Fermi level's estimated position being only approximately 0.091 eV (rendering the effect of the heavy hole band negligible). Upon introducing Mn doping, the energy offset between the valence band edges (heavy and light bands) diminishes concomitantly with an increase in carrier concentration. This shift results in the joint transport of heavy and light holes, logically leading to an increase in effective mass and an enhancement of the α. The introduction of Sb in co-doping causes a shift of the Fermi level toward the conduction band, facilitated by the self-compensation effect of holes through the introduction of electrons. Finally, in the Mn–Sb co-doped GeTe system, we observe a significant enhancement of the α. As such, the synergistic effects of Mn and Sb co-doping yield an overall improvement in the thermoelectric performance of GeTe.

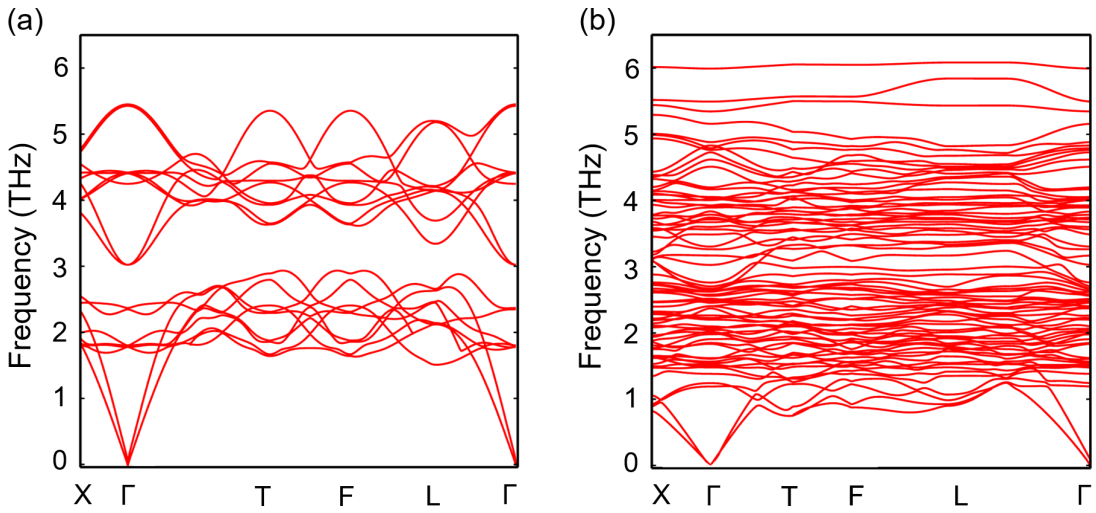

Figure 7.3: Phonon dispersion curve for (a) $Ge_{24}Te_{24}$ and (b) $Ge_{21}MnSb_2Te_{24}$ in a rhombohedral structure.

7.1.3.2 Lattice thermal conductivity (κ_{ph})

Subsequently, the reason behind the reduction in lattice thermal conductivity in Mn–Sb co-doped GeTe can be illuminated by examining the phonon dispersion curve. We conducted phonon dispersion calculations for both pristine GeTe and Mn–Sb co-doped GeTe. Fig. 7.3a and 7.3b show the phonon dispersion plots for $Ge_{24}Te_{24}$ and $Ge_{21}MnSb_2Te_{24}$, respectively, both within the rhombohedral structure. The phonon dispersion curve for pristine GeTe is consistent with prior research findings [341, 342]. Importantly, the introduction of Mn through doping in GeTe (specifically, $Ge_{23}MnTe_{24}$) does not significantly alter the phonon dispersion curve, encompassing both acoustic and optical modes at lower frequencies. This outcome is in line with the findings reported by Liu et al. [341]. However, a noteworthy departure is observed in the phonon dispersion curve for Mn–Sb co-doped GeTe ($Ge_{21}MnSb_2Te_{24}$), as illustrated in Fig. 7.3b. In general, the phonon dispersion is elucidated by the ω vs k plot, where the gradient

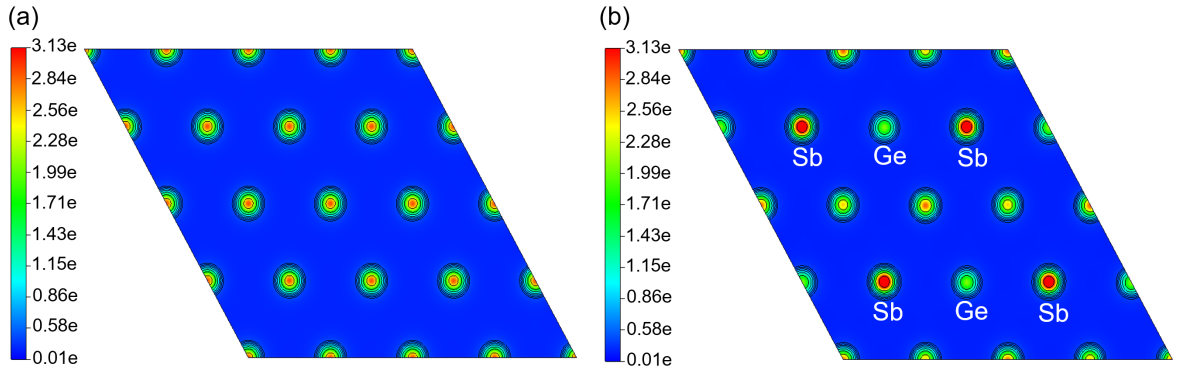

Figure 7.4: Charge density plot for a plane with Miller indices (001) at a distance of 13Åfrom the origin for (a) $Ge_{24}Te_{24}$ showing all Ge atoms and (b) $Ge_{21}MnSb_2Te_{24}$ showing Ge and Sb atoms.

of the ω vs k curve provides the phonon group velocity (v_g), defined as $v_g = d\omega/dk$. As Fig. 7.3b illustrates, the gradient or slope of the phonon curve for the Mn–Sb co-doped system is notably lower than that of pristine GeTe. This phenomenon indicates a decrease in the mean phonon group velocity for Mn–Sb co-doped samples compared to pristine GeTe, consequently leading to a reduction in lattice thermal conductivity. The observed decrease in the slope of the phonon dispersion curve associated with Sb doping can be attributed to the relatively large mass (M) of Sb, as the phonon frequency ω scales inversely with the square root of mass, $\omega \propto M^{-1/2}$. To gain insights into charge transfer effects, we examined the charge density contours for $Ge_{24}Te_{24}$ and $Ge_{21}MnSb_2Te_{24}$, depicted in Fig. 7.4. It is evident that charge transfer occurs between Sb

and Ge atoms, strengthening the chemical bonds between them. This reinforced bond, resulting from charge transfer, restricts the free vibrations of atoms, consequently reducing the phonon group velocity.

7.1.4 Conclusions

In summary, this investigation highlights the improved thermoelectric characteristics observed in GeTe doped with both Mn and Sb, elucidating the underlying mechanisms of electronic structure manipulation and lattice dynamics. The DFT calculations indicate that Mn–Sb co-doping sharpens the density of states and enhances band convergence, while also optimizing the Fermi level position, thereby contributing to the observed increase in α. As a result, the power factor of all samples increases with temperature, predominantly due to the amplified α values. Additionally, the investigation reveals a decrease in the κ at 300 K and with increasing temperature for Mn–Sb-doped samples. Analysis of phonon thermal conductivity (κ_{ph}) at 300 K indicates strong phonon scattering, aligning with reduced phonon group velocity as observed in phonon dispersion curves. These reductions in κ and enhancements in α collectively lead to a superior thermoelectric figure of merit (zT) in Mn–Sb co-doped GeTe.

7.2 Effect of crystal field engineering and Fermi level optimization on thermoelectric properties of $Ge_{1.01}Te$

7.2.1 Introduction

Thermoelectric (TE) materials play a significant role in power generation and solid-state cooling due to their ability to convert heat into electricity and vice versa without the need for any moving parts. They have emerged as viable solutions for addressing thermal management and enhancing energy efficiency, in response to the increasing prevalence of waste heat in modern technology [241, 310]. The performance of a TE device is typically evaluated using a dimensionless parameter known as the figure of merit, denoted as zT. This metric depends on several key physical parameters, including the Seebeck coefficient (α), electrical conductivity (σ), total thermal conductivity (κ, which consists of electronic (κ_e) and lattice (κ_{ph}) contributions), and temperature (T). Mathematically, zT is expressed as zT = $\alpha^2\sigma T/(\kappa = \kappa_e+\kappa_{ph})$. Achieving a high zT in a TE material is a challenging task due to the intricate relationships between these TE parameters. To address this challenge, numerous innovative strategies have been employed to decouple the transport of electrons and phonons within materials, thereby enhancing zT. These strategies encompass approaches such as band-structure engineering [311, 312, 313, 314, 315], nanostructuring [316], composite materials [317, 318, 319, 320], and the utilization of the high-entropy concept [321, 322]. In essence, the simultaneous improvement of electronic transport and the inhibition of phonon propagation are crucial criteria for the development of high-performance TE materials, as evidenced in materials like PbTe [323], SnSe [258], skutterudites [324], and half-Heusler compounds [325].

Doped semiconductor holds the potential to improve TE properties due to their favorable electronic structure. GeTe-based materials serve as a notable example, demonstrating their suitability for mid-temperature applications. However, the high p-type carrier concentration ($\sim 10^{21}$ cm^{-3}) at 300 K in GeTe, primarily arising from intrinsic Ge, leads to a low α and a high κ_e. These factors collectively result in inferior TE performance [326]. Additionally, the large energy gap (ΔE) between the light and heavy valence bands places constraints on increasing α. Furthermore, the room temperature κ_{ph} for pristine GeTe ($\sim$ 3 W·m^{-1}·K^{-1}) exceeds the theoretically predicted minimum value (0.44 W·m^{-1}·K^{-1}) estimated using Cahill's model [327].

As the absolute value of the α decreases while σ and κ_e increase with carrier concentration (n), optimizing carrier concentration becomes a critical initial step. This optimization is followed by engineering electronic and phonon band structures to achieve the desired TE parameters. Strategies for reducing κ_{ph} include hierarchical architecture engineering [328], defect engineering [329], composite approaches [257], and the integration of multiscale scattering center techniques [245, 330]. To address the challenge of high hole carrier concentration and to enhance α in GeTe, several innovative strategies have been employed, such as alloying and band structure modifications [331, 332, 333]. Aliovalent doping with ions like Bi^{3+} and Sb^{3+} at the Ge^{2+} site has been utilized to decrease the carrier concentration and reduce κ_{ph} through phonon scattering by solid-solution point defects [334]. This type of aliovalent doping also leads to a convergence of the energy gap (ΔE) between the light and heavy bands, thereby improving α. However, it's worth noting that extensive aliovalent doping can significantly reduce σ. Alternatively, transition metal doping, including elements like Ti, Zn, Mn, and others, has been explored in the literature to achieve ΔE convergence and, consequently, enhance α [335, 336, 337].

As previously mentioned, optimizing the Fermi level (carrier concentration), is of paramount importance in achieving higher zT values in TE materials [255]. In the case of pristine GeTe, the exceptionally high n, mainly due to intrinsic Ge vacancies, results in the Fermi level sinking deep into the valence band. Shuai et al. achieved an enhanced zT within the Ge-rich GeTe system through the manipulation of Ge vacancies [338]. In this study, we employ a combination of strategies to significantly enhance zT (1.75 at 773 K). This improvement is achieved by systematically doping Ti and Bi into vacancy-engineered $Ge_{1.01}Te$, leveraging the synergistic effects of crystal field engineering, valence band convergence, and point-defect scattering. Excess Ge manipulation adjusts n, enhancing α and reducing κ_e at 300 K. The introduction of Ti doping further enhances α through crystal field engineering, achieved by reducing the c/a ratio. Ti–Bi co-doping further improves the band convergence and increases α, and reduces κ_{ph} through point-defect scattering. Additionally, theoretical insights into crystal field and band structure engineering for electronic transport, followed by the calculation of TE parameters using the Boltzmann transport equation are provided. Phonon dispersion calculations support the engineered reduction in lattice thermal conductivity, demonstrating the impact of phonon engineering.

7.2.2 Computational methods

The density functional theory (DFT) [14, 15] calculations were carried out using the plane-wave-based pseudopotential approach, as implemented in the Vienna Ab initio Simulation Package (VASP) [169, 170]. The structural optimization of all the modeled structures was performed using generalized gradient approximation (GGA) expressed by the Perdew–Burke–Ernzerhof (PBE) [217] exchange-correlation (ϵ_{xc}) functional. The self-consistency loop was converged with a total energy threshold of 0.01 meV by conjugate gradient (CG) minimization. The structures were fully relaxed until the Heymann–Feynman forces on each atom were less than 10^{-5} eV/Å for both pure and doped configurations. The effects of doping were considered by substituting Ti and Bi atoms at the specific sites of Ge atoms in a 2 × 2 × 2 supercell consisting of 48 atoms. All the structures were visualized through VESTA (Visualization for Electronic and STructural Analysis) [339] software. Spin–orbit coupling (SOC) interactions owing to heavy atoms were included when calculating the electronic band structures and density of states. A 6 × 6 × 2 k-mesh was used for Brillouin zone sampling. The electron wave function was expanded in a plane-wave basis set with an energy cutoff of 600 eV. Phonon calculations were obtained within the harmonic approximation and using a finite displacement method [340]. The phonon dispersion plots and group velocities were calculated using the PHONOPY package [222, 221]. A 2 × 2 × 2 supercell was set for the cubic GeTe containing 64 atoms, whereas, for the rhombohedral phase, a 3 × 3 × 1 supercell containing 54 atoms was built. In the Ti–Bi co-doped rhombohedral system, we used a 2 × 2 × 2 supercell consisting of 96 atoms. The BoltzTrap Code [275], based on Boltzmann transport theory, was used to evaluate thermoelectric properties. The starting parameters for the calculations were the values obtained from the refinement.

7.2.3 Results and discussion

7.2.3.1 Electronic properties

First, we modeled $Ge_{1.01}Te$ with excess Ge at interstitial sites in the pristine GeTe system. Subsequently, we introduced Ti and Bi doping at Ge sites in $Ge_{1.01}Te$. Dopants were substituted at various sites, and the total energies of the respective systems were computed (see Fig. 7.5). The configuration with the lowest energy was selected for further analysis. Additionally, we theoretically induced Ge vacancies during the calculations to match

the experimentally observed high carrier concentration. Therefore, $Ge_{23}Te_{24}$, $Ge_{22}TiTe_{24}$, $Ge_{21}TiBiTe_{24}$, and $Ge_{20}TiBi_2Te_{24}$ corresponds to $Ge_{1.01}Te$, $Ge_{0.99}Ti_{0.02}Te$, $Ge_{0.97}Ti_{0.02}Bi_{0.02}Te$, and $Ge_{0.91}Ti_{0.02}Bi_{0.08}Te$ in $Ge_{1.01-x-y}Ti_xBi_yTe$ ($0.00 \leq x \leq 0.02$, $0.00 \leq y \leq 0.08$). The lattice parameters are listed in Table 7.1. To gain a deeper understanding of the electronic

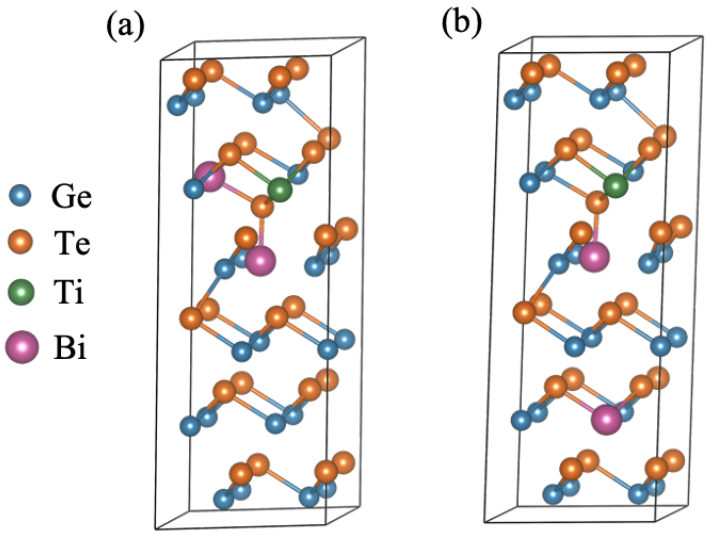

Figure 7.5: (a) and (b) represent two configurations of $Ge_{20}TiBi_2Te_{24}$ with different relative energies, calculated using PBE exchange-correlation functional.

Table 7.1: Lattice parameters (a, c), c/a for $Ge_{1.01-x-y}Ti_xBi_yTe$ ($0.00 \leq x \leq 0.02$, $0.00 \leq y \leq 0.08$) at 300 K.

sample x, y	a (Å)	c (Å)	c/a
0.00, 0.00	4.1624	10.6762	2.5649
0.02, 0.00	4.1627	10.6718	2.5636
0.02, 0.02	4.1642	10.6502	2.5575
0.02, 0.08	4.1696	10.5816	2.5377

transport within the Ti–Bi co-doped GeTe system, we conducted DFT calculations to analyze the electronic band structures and density of states (DOS) for pristine GeTe, Ti-doped GeTe, and Ti–Bi co-doped GeTe. A systematic approach was employed, involving the doping of Ge, Ti, and Ti–Bi within the GeTe system to generate all required configurations. Our calculations revealed that the principal valence band (light hole) maximum (VBM) and conduction

band minimum (CBM) are situated at the Γ point due to the folding of the L point onto Γ (see Fig. 7.6). Pristine GeTe exhibits a high hole carrier concentration due to intrinsic Ge vacan-

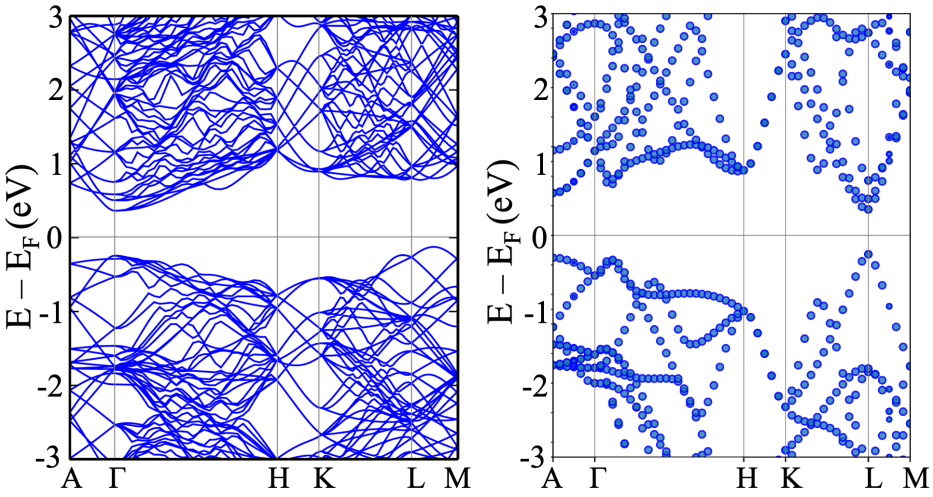

Figure 7.6: (a) Band structure of $Ge_{25}Te_{24}$ supercell, where the principal valence band (light hole) maximum (VBM) and conduction band minimum (CBM) occur at the Γ point due to the folding of the L point onto Γ. (b) The unfolded band structure of $Ge_{25}Te_{24}$ supercell showing VBM and CBM at L point.

cies, which was taken into account in our DFT calculations. The electronic band structure for $Ge_{23}Te_{24}$ is depicted in Fig. 7.7(a). (i) For the Ti-doped case [Fig. 7.7(b)], (ii) one Ti and one Bi atom [Fig. 7.7(c)], and (iii) one Ti and two Bi atoms were substituted in place of Ge within the GeTe supercell. In the case of Ti–Bi co-doping, the energies of two configurations were computed, with the results showing that (i) Ti and Bi atoms are close to each other and (ii) they are farther apart. The latter configuration displayed lower energy, signifying greater stability, and was consequently selected for all subsequent calculations (see Fig. 7.5). Fig. 7.7(b) illustrates the emergence of new impurity bands resulting from Ti states near the conduction band, which reduces the band gap. These resonant levels manifest below the conduction band due to the high-energy Ti d orbitals, consistent with prior studies [338]. The co-doping of Ti and Bi at Ge sites in GeTe ($Ge_{21}TiBiTe_{24}$) further reduces the energy separation between the valence bands (ΔE_Γ), from 0.21 to 0.13 eV, which is further decreased to 0.08 eV in $Ge_{20}TiBi_2Te_{24}$, ultimately leading to band convergence in GeTe. This implies that heavy holes significantly influence carrier transport, and Ti–Bi co-doping in GeTe enhances valence band convergence, confirming the observed increase in the Seebeck coefficient. Furthermore, we computed density of states (DOS) plots for $Ge_{25}Te_{24}$ (with excess Ge), followed by $Ge_{23}Te_{24}$ (with Ge vacancies),

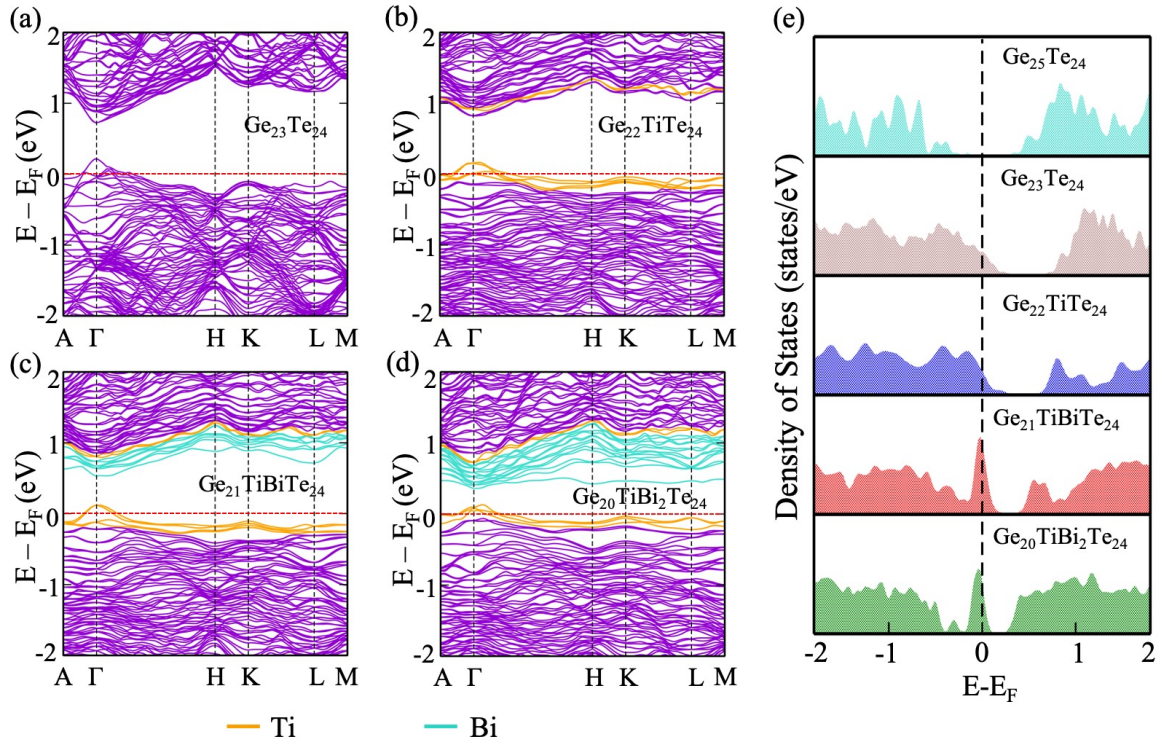

Figure 7.7: Electronic band structures of (a) $Ge_{23}Te_{24}$, (b) $Ge_{22}TiTe_{24}$, (c) $Ge_{21}TiBiTe_{24}$, and (d) $Ge_{20}TiBi_2Te_{24}$. The Ge vacancies are theoretically induced during the calculation to attest to the large experimental value of carrier concentration. The band gap appears at the Γ point in a $2 \times 2 \times 2$ supercell containing 48 atoms. The VBM and CBM occur at the L point in the pristine GeTe fold onto the Γ point in the supercell. (e) Density of states of GeTe with excess Ge ($Ge_{25}Te_{24}$), GeTe with Ge vacancies ($Ge_{23}Te_{24}$), Ti-doped GeTe ($Ge_{22}TiTe_{24}$), and Ti–Bi co-doped GeTe ($Ge_{21}TiBiTe_{24}$, $Ge_{20}TiBi_2Te_{24}$) samples.

$Ge_{22}TiTe_{24}$ (Ti-doped), and $Ge_{21}TiBiTe_{24}$ and $Ge_{20}TiBi_2Te_{24}$ (Ti–Bi co-doped). The position of the Fermi level plays a crucial role in optimizing the thermoelectric (TE) performance of any system. In the presence of a high hole carrier concentration in GeTe, the Fermi level is positioned deep within the valence band. However, the DOS plot indicates that the Fermi level falls in the middle of the band gap for pristine $Ge_{24}Te_{24}$ [255]. To align with the experimentally observed high carrier concentration in GeTe, we introduced Ge vacancies theoretically, causing the Fermi level to reside deep within the valence band. With excess Ge ($Ge_{25}Te_{24}$), the Fermi level tends to shift towards the conduction band. Ti doping in GeTe (with excess Ge) increases the carrier concentration, causing the Fermi level (E_F) to shift deeper into the valence band. Bi doping, on the other hand, reduces the hole carrier concentration due to the donor

properties of Bi. This reduction in the energy offset between the valence band edges results in band convergence in the co-doped system, as demonstrated in the band structure calculations. Hence, the combination of both band convergence and the position of the Fermi level indicates an increased Seebeck coefficient in co-doped samples. Furthermore, Ti–Bi co-doping results in a steeper DOS, particularly near the valence band edge. This sharper DOS feature signifies a higher effective mass and contributes to the enhancement of the Seebeck coefficient [341]. The Fermi level lies within the valence band in the case of Ti and Bi co-doping, primarily due to the consideration of larger Ge vacancies during the theoretical calculations.

7.2.3.2 Thermoelectric properties

Subsequently, to investigate the thermoelectric properties, we conducted calculations for electrical conductivity (σ), Seebeck coefficient (α), thermal conductivity (κ), power factor ($\alpha^2\sigma$), and thermoelectric figure of merit (zT) for the $Ge_{23}Te_{24}$, $Ge_{22}TiTe_{24}$, $Ge_{21}TiBiTe_{24}$ and $Ge_{20}TiBi_2Te_{24}$ systems while varying the chemical potential (μ). It's important to note that all transport properties dependent on μ were calculated by keeping the temperature constant and allowing the carrier concentration (n) to change. This implies that, for a fixed temperature (in this case, 300 K), μ is a function of n, providing insight into the doping of carriers by illustrating the addition or removal of electrons from the system. The position of μ, in turn, determines the fraction of electrons in the conduction or valence band, influencing transport properties. Consequently, we determined the thermoelectric parameters as a function of μ. Fig. 7.8(b) illustrates the change in the α with respect to μ. The α quantifies the induced thermoelectric voltage (ΔV) in response to a temperature difference (ΔT) in the material and is mathematically expressed as $\alpha = \Delta V/\Delta T$. When $\mu = 0$, it coincides with the top of the valence band in semiconductors, indicating that at $\mu = 0$, the sign of α determines the semiconductor type. Fig. 7.8(b) demonstrates that at $\mu = 0$, α is positive for all GeTe systems, indicating their p-type semiconductor nature. Additionally, α is depicted as a function of temperature for the GeTe systems (see Fig. 7.9). Since the calculation of κ_{ph} for all doped configurations using state-of-the-art advanced methods is computationally expensive, we opted to use the experimental κ_{ph} value at 300 K to calculate zT, following the equation: $zT=\alpha^2\sigma T/(\kappa=\kappa_e+\kappa_{ph})$. Fig. 7.8(a) and 7.8(c) reveal that electrical conductivity and thermal conductivity decrease with Ti–Bi doping, consistent with experimental findings. The increase in α due to doping results in higher power factor values when compared to the pristine system (see Fig. 7.8(d)). Notably, resonant

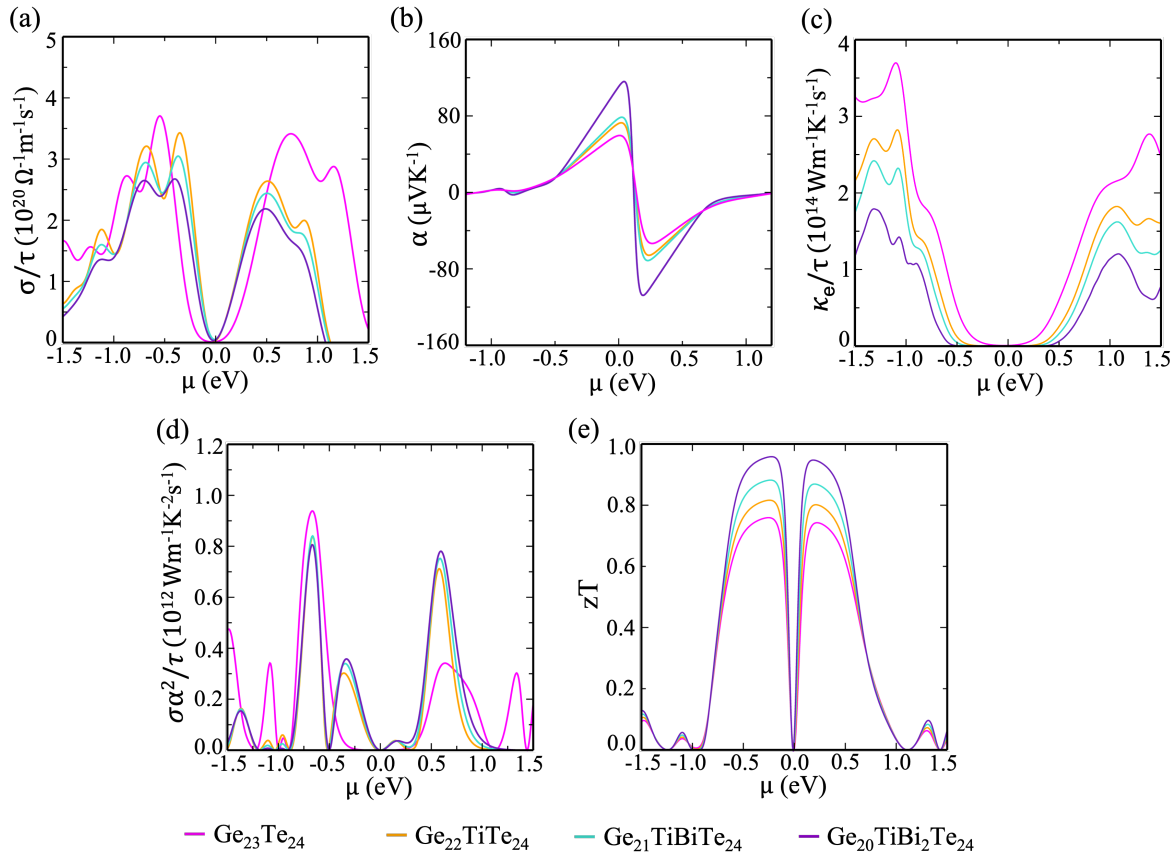

Figure 7.8: (a) Electrical conductivity (σ), (b) Seebeck coefficient (α), (c) electronic thermal conductivity (κ_e), (d) power factor ($\alpha^2\sigma$), and (e) figure of merit (zT) as a function of chemical potential (μ) are calculated at 300 K for different GeTe compositions: $Ge_{23}Te_{24}$, $Ge_{22}TiTe_{24}$, $Ge_{21}TiBiTe_{24}$ and $Ge_{20}TiBi_2Te_{24}$. Electrical conductivity, Seebeck coefficient, thermal conductivity, power factor, and figure of merit are reported by scaling them with τ.

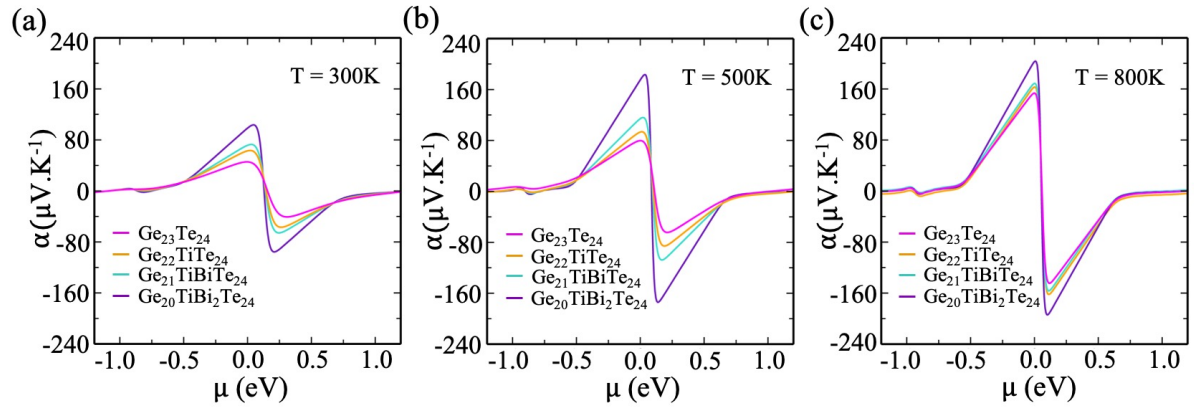

Figure 7.9: (a) Calculated Seebeck coefficient (α) as a function of chemical potential (μ) for different GeTe compositions at (a) 300 K, (b) 500 K, and (c) 800 K.

peaks are observed near the Fermi level in the positive "μ" region. Furthermore, zT values (Fig. 7.8(e)) are higher in the negative "μ" region compared to the positive region, indicating that p-type doping yields higher zT values. This observation underscores the potential of the considered co-doped systems as promising p-type thermoelectric materials.

7.2.3.3 Phonon dispersion calculation

Low thermal conductivity is desirable for efficient TE materials. To investigate the lattice thermal conductivity in Ti–Bi co-doped GeTe, we performed phonon dispersion calculations for both GeTe ($Ge_{24}Te_{24}$) and Ti–Bi co-doped ($Ge_{21}TiBi_2Te_{24}$). Notably, we did not consider vacancies when calculating the phonon dispersion curves due to technical complexities related to accommodating numerous defects within a supercell [255]. The objective of these calculations was to assess the dynamical stability of the materials. Fig. 7.10(a) and 7.10(b) illustrate

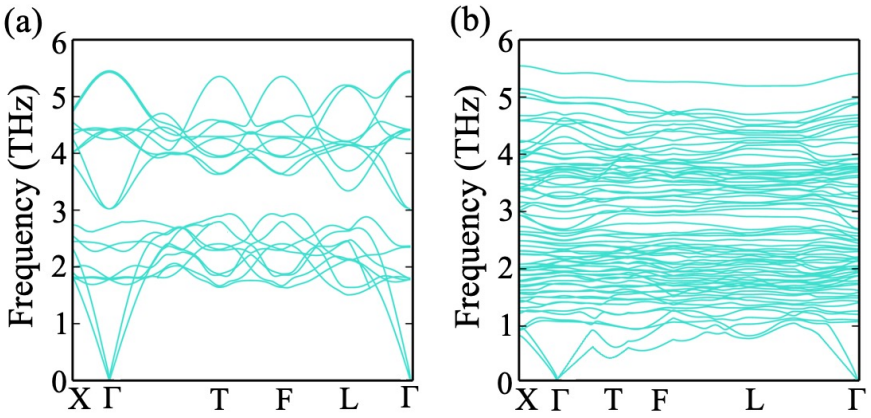

Figure 7.10: Phonon dispersion curve for (a) $Ge_{24}Te_{24}$ and (b) $Ge_{21}TiBi_2Te_{24}$ in a rhombohedral structure.

the phonon dispersion plots for $Ge_{24}Te_{24}$ and $Ge_{21}TiBi_2Te_{24}$, in their rhombohedral structure. The phonon dispersion curve for pure GeTe aligns with previous studies [342]. However, the phonon dispersion curve for Ti–Bi co-doping exhibits a significant reduction in slope, as depicted in Fig. 7.10(b). Typically, the phonon dispersion is represented as a plot of ω vs k, and the gradient of this curve corresponds to the phonon group velocity (v_g), where $v_g = d\omega/dk$. In Fig. 7.10(b), it's evident that the gradient of the phonon curve for the Ti–Bi co-doped system is lower than that of GeTe at the point shown in Fig. 7.10(a). This indicates a decrease in the average phonon group velocity for the Ti–Bi co-doped sample compared to GeTe, resulting in reduced lattice thermal conductivity. The decrease in the gradient of the dispersion curve for

Bi doping can be attributed to the relatively large atomic mass (M) of Bi, as indicated by the relationship $\omega \propto M^{-1/2}$. Additionally, we conducted an analysis of charge density contours for $Ge_{24}Te_{24}$ and $Ge_{21}TiBi_2Te_{24}$, shown in Fig. 7.11. This analysis revealed a charge transfer between the Bi and Ge atoms, further enhancing the stability of chemical bonds. This increased bond stability restricts the free vibrations of atoms, resulting in a decrease in the phonon group velocity, which, in turn, contributes to the lower lattice thermal conductivity. Therefore, the lower thermal conductivity and higher zT values result in potential thermoelectric properties in these doped GeTe systems.

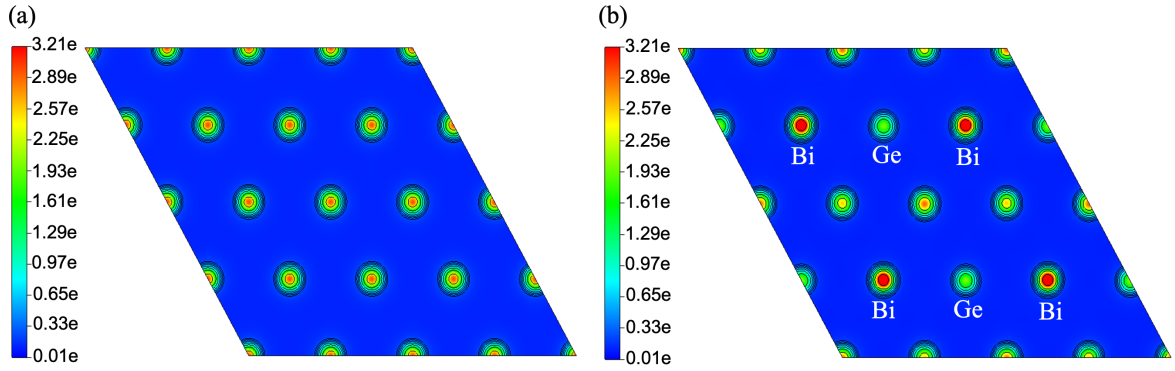

Figure 7.11: Charge density plot of a plane with Miller indices (001) at a distance of 9.5 Å from the origin for (a) $Ge_{25}Te_{24}$ supercell showing all Ge atoms, and (b) $Ge_{20}TiBi_2Te_{24}$ supercell showing Ge and Bi atoms.

7.2.4 Conclusions

In summary, this density functional theory study has demonstrated the enhancement of thermoelectric properties in $Ge_{1.01}Te$ through Ti–Bi co-doping in conjunction with vacancy engineering. The introduction of excess Ge plays a pivotal role in reducing carrier concentration (n) and thereby adjusting the Fermi level position, ultimately enhancing the thermoelectric performance of $Ge_{1.01}Te$. Moreover, Ti doping contributes to the improvement in α by means of crystal field engineering, facilitated by a decreased c/a ratio. This effect is further amplified by the reduction in carrier concentration through Bi doping. The Ti–Bi co-doped $Ge_{1.01}Te$ showcases increased band degeneracy, further enhancing α. Phonon dispersion calculations indicated a decrease in phonon group velocity in the Ti–Bi co-doped system, attributed to the larger atomic mass of Bi and the charge transfer occurring between Bi and Ge atoms. The combined effects of optimizing carrier concentration, enhancing band degeneracy, and reducing

phonon thermal conductivity (κ_{ph}) culminated in a high zT value for $Ge_{21}TiBi_2Te_{24}$, making it promising for thermoelectric applications.

CHAPTER 8

Epilogue and outlook

Energy materials include a broad spectrum of materials with pivotal roles in numerous energy-related processes, such as energy generation, storage, and conversion. These materials serve as fundamental components for harnessing and controlling energy across various applications. In line with this, we have explored the domains of catalysis, optoelectronics, and thermoelectricity, offering promising pathways to address the global energy crisis. Particularly, we have studied energy materials viz., catalysts for methane activation and hydrogen production, as well as perovskites utilized in solar cells and thermoelectric devices.

Methane, a primary component of natural gas, is a plentiful, cost-effective, and eco-friendly energy source. However, it is also a notable greenhouse gas, making its conversion into valuable products crucial. One key route for this conversion is the generation of synthesis gas (syngas) from methane. Syngas serves as a precursor for producing various valuable chemicals, including methanol, liquid hydrocarbons, ammonia, and dimethyl ether. Despite its abundance, the efficient activation of methane presents a significant challenge due to its strong C-H bonds (4.5 eV), low polarizability, and negligible electron affinity. To overcome this challenge, a suitable catalyst is essential. Transition metal (TM) clusters, in particular, are well-known for their efficient catalytic activity, both in homogeneous and heterogeneous settings. This can be attributed to the presence of partially occupied d-shells in transition metals, enabling them to exhibit multiple oxidation states in their complexes. In our study, we have focused on a representative model system: nickel (Ni_4), which has already been experimentally synthesized and exhibits high selectivity. We considered its behavior in a reactive atmosphere consisting of O_2 and CH_4 gas molecules under realistic conditions. In the presence of such an atmosphere, clusters adsorb surrounding gas molecules and form intermediate phases [$Ni_4O_x(CH_4)_y$], which are generally active materials for applications in heterogeneous catalysis. Our investigation revealed the influence of environmental factors, specifically temperature (T), partial pressure of

oxygen (p_{O_2}), and partial pressure of methane (p_{CH_4}), on the thermodynamic stability of these $Ni_4O_x(CH_4)_y$ ($0 \leq x \leq 8, 0 \leq y \leq 3$) clusters. Additionally, to account for anharmonicity in the vibrational free energy contribution to the configurational entropy, we numerically assessed the excess free energy of the clusters. We employed the thermodynamic integration method with *ab initio* molecular dynamics (*ai*MD) simulation inputs. While seeking precise thermodynamic stability, we observed that accounting for anharmonicity revealed new stable phases that were previously overlooked by DFT and DFT+Fharmonic methods. This inclusion significantly impacted our ability to detect the activation of the C-H bond, where the harmonic IR approach failed to capture the correct vibrational modes

Lead halide perovskites have gained considerable attention in the field of optoelectronics due to their unique characteristics, including an appropriate optical band gap, high absorption coefficient, low trap density, and cost-effectiveness. Notably, the inclusion of heavy elements like Pb in these materials results in strong spin-orbit coupling (SOC), a pivotal factor influencing their electronic properties. In the absence of inversion symmetry, these crystals experience an effective magnetic field due to SOC. This magnetic field, coupled with spin moments, gives rise to a momentum-dependent splitting of bands, referred to as Rashba-Dresselhaus (RD) splitting. The presence of Pb and ferroelectricity in the non-centrosymmetric phase of $CsPbF_3$ indicates the potential for the RD effect in this material. We have studied the $Pm3\ m$ and $R3c$ phases of $CsPbF_3$, employing the perturbative ***k.p*** formalism alongside first-principles calculations. Initially, we assessed the dynamical stability of these phases, identifying the lack of dynamical stability in the $Pm3\ m$ phase due to the presence of negative frequencies in the phonon bandstructure. Subsequently, we determined the band gap of these phases using first-principles-based methodologies in conjunction with SOC. This involved DFT with semilocal exchange-correlation (ϵ_{xc}) functional (PBE), hybrid DFT with HSE06, and single-shot GW (G_0W_0) within the many-body perturbation theory (MBPT). Our examination of the electronic band structure of the $R3c$ phase unveiled the presence of Rashba splitting and distinctive spin textures. We also explored the impact of strain on the band gap and Rashba parameters, observing significant modulation of Rashba spin splitting through the application of uniaxial strain (±5%). Additionally, our investigation revealed reversible spin textures in $CsPbF_3$ perovskite, enhancing its potential for perovskite-based spintronic applications.

Howerver, the issues of lead toxicity and long-term stability have limited the promising prospects of lead halide perovskites. These concerns have prompted researchers to seek out

alternative compositions and structural configurations. One such promising avenue is the exploration of inorganic lead-free double perovskites, often referred to as vacancy-ordered double perovskites (VODPs) and denoted by the general formula A_2BX_6. VODPs are a defect variant of halide perovskites, resulting from the duplication of the ABX_3 unit cell along all three crystallographic axes, with the removal of every alternate B-site cation. In our investigation, our initial focus revolved around assessing the stability of these materials, a paramount consideration for their potential in high-performance device applications. To gauge their structural stability, we calculated the Goldschmidt tolerance factor (t) and octahedral factor (μ). Our computations revealed that these perovskites exhibit structural stability in cubic phases. Furthermore, we delved into the evaluation of their thermodynamic and mechanical stability. Thermodynamic stability was assessed through the calculation of Gibbs free energies (ΔG), which consistently yielded negative values, signifying the thermodynamic stability of these materials. The evaluation of mechanical stability involved determining the elastic constants using the finite strain theory, and they met the criteria for mechanical stability. With the stability of these materials confirmed, we proceeded to compute their electronic band gaps, both with and without the inclusion of spin-orbit coupling (SOC). The obtained band gap values for Cs_2PtI_6, Cs_2PdI_6, Cs_2TeI_6, and Cs_2SnI_6 were found to be 1.35 eV, 1.43 eV, 1.49 eV, and 1.23 eV, respectively. These band gap values indicate that all of these perovskites possess band gaps within the visible spectrum, which holds great promise for energy-harvesting applications. Notably, these calculated band gap values align well with experimental observations.

Lately, VODPs have garnered attention in the field of thermoelectrics due to their exceptionally low lattice thermal conductivity, attributed to their highly anharmonic lattice dynamics. To ascertain the dynamical stability, we plotted the phonon dispersion band structures for all Cs_2BI_6 perovskites using the density functional perturbation theory (DFPT), and the absence of negative frequencies affirmed their dynamical stability. The existence of anharmonicity in these materials was examined by computing the Electron Localization Function (ELF), which confirmed the presence of anharmonicity in this class of systems. To quantify the anharmonic energy (U_{ah}) in Cs_2BI_6 VODPs, we conducted *ab initio* molecular dynamics (*ai*MD) simulations at varying temperatures, employing the Nose-Hoover thermostat. Subsequently, we calculated the thermoelectric properties of these perovskites using the BoltzTraP code, leading to the computation of average zT values for Cs_2PtI_6, Cs_2PdI_6, Cs_2TeI_6, and Cs_2SnI_6, which were found to be 0.88, 0.85, 0.95, and 0.78, respectively. These values underscore the potential

of these materials in thermoelectric applications.

In addition, we have explored the thermoelectric properties (TE) of GeTe semiconductor. GeTe is characterized by the presence of intrinsic Ge vacancies, which leads to high hole carrier concentration (10^{21} cm^{-3}), a significant electrical conductivity (approximately 8000 S/cm), and a relatively low Seebeck coefficient (around 28 μV/K at 300 K). These properties collectively result in inferior TE properties. To overcome these issues, we have explored the Mn-Sb and Ti-Bi co-doping at cation sites in GeTe. DFT simulations have revealed that the introduction of doping leads to improved band convergence and fine-tuning of the Fermi level position. Consequently, this adjustment aids in the enhancement of the Seebeck coefficient (α). The optimized α, combined with an increase in electrical conductivity (σ), results in a significantly improved power factor ($\alpha^2\sigma$) for the co-doped GeTe system. This, in turn, leads to high zT values, which suggest the promising TE properties of the system.

Overall, energy materials present a wide array of prospects for energy-related applications, paving the way for more efficient and stable catalysts, photovoltaic and thermoelectric devices. The insights into various parameters and the theoretical framework discussed in this thesis can serve as valuable guidance for future endeavors in exploring and creating energy materials tailored for thermoelectric and photovoltaic applications.

Bibliography

[1] Vladimir S Arutyunov and Georgiy V Lisichkin. Energy resources of the 21st century: Problems and forecasts. can renewable energy sources replace fossil fuels. *Russian Chemical Reviews*, 86(8):777, 2017.

[2] John P Holdren. Energy in transition. *Scientific American*, 263(3):156–163, 1990.

[3] Abdeen Mustafa Omer. Energy, environment and sustainable development. *Renewable and sustainable energy reviews*, 12(9):2265–2300, 2008.

[4] Anam Kalair, Naeem Abas, Muhammad Shoaib Saleem, Ali Raza Kalair, and Nasrullah Khan. Role of energy storage systems in energy transition from fossil fuels to renewables. *Energy Storage*, 3(1):e135, 2021.

[5] Ib Chorkendorff and Johannes W Niemantsverdriet. *Concepts of modern catalysis and kinetics*. John Wiley & Sons, 2017.

[6] A Mahmoudi, M Fazli, and MR Morad. A recent review of waste heat recovery by organic rankine cycle. *Applied Thermal Engineering*, 143:660–675, 2018.

[7] Hussam Jouhara, Navid Khordehgah, Sulaiman Almahmoud, Bertrand Delpech, Amisha Chauhan, and Savvas A Tassou. Waste heat recovery technologies and applications. *Thermal Science and Engineering Progress*, 6:268–289, 2018.

[8] Bradley Orr, Aliakbar Akbarzadeh, Masataka Mochizuki, and Randeep Singh. A review of car waste heat recovery systems utilising thermoelectric generators and heat pipes. *Applied thermal engineering*, 101:490–495, 2016.

[9] Stefan K Estreicher. Hydrogen-related defects in crystalline semiconductors: a theorist's perspective. *Materials Science and Engineering: R: Reports*, 14(7-8):319–412, 1995.

[10] Chris G Van de Walle and Jörg Neugebauer. First-principles calculations for defects and impurities: Applications to iii-nitrides. *Journal of applied physics*, 95(8):3851–3879, 2004.

[11] David A Drabold and Stefan K Estreicher. *Theory of defects in semiconductors*. Springer, 2007.

[12] Neil W Ashcroft and ND Mermin. Solid state. *Physics (New York: Holt, Rinehart and Winston) Appendix C*, 1976.

[13] William Hume-Rothery, W Mabbott, Gilbert, and KM Channel Evans. The freezing points, melting points, and solid solubility limits of the alloys of sliver and copper with the elements of the b sub-groups. *Philosophical Transactions of the Royal Society of London. Series A, Containing Papers of a Mathematical or Physical Character*, 233(721-730):1–97, 1934.

[14] Pierre Hohenberg and Walter Kohn. Inhomogeneous electron gas. *Physical review*, 136(3B):B864, 1964.

[15] Walter Kohn and Lu Jeu Sham. Self-consistent equations including exchange and correlation effects. *Physical review*, 140(4A):A1133, 1965.

[16] Nicola Marzari, Andrea Ferretti, and Chris Wolverton. Electronic-structure methods for materials design. *Nature materials*, 20(6):736–749, 2021.

[17] Jörg Neugebauer and Tilmann Hickel. Density functional theory in materials science. *Wiley Interdisciplinary Reviews: Computational Molecular Science*, 3(5):438–448, 2013.

[18] Audrius Alkauskas, Peter Broqvist, and Alfredo Pasquarello. Defect levels through hybrid density functionals: Insights and applications. *physica status solidi (b)*, 248(4):775–789, 2011.

[19] Lars Hedin. New method for calculating the one-particle green's function with application to the electron-gas problem. *Physical Review*, 139(3A):A796, 1965.

[20] Stefan Albrecht, Lucia Reining, Rodolfo Del Sole, and Giovanni Onida. Ab initio calculation of excitonic effects in the optical spectra of semiconductors. *Physical review letters*, 80(20):4510, 1998.

[21] Michael Rohlfing and Steven G Louie. Electron-hole excitations in semiconductors and insulators. *Physical review letters*, 81(11):2312, 1998.

[22] David J Griffiths and Darrell F Schroeter. *Introduction to quantum mechanics*. Cambridge university press, 2018.

[23] P. Hohenberg and W. Kohn. Inhomogeneous electron gas. *Phys. Rev.*, 136:B864–B871, Nov 1964.

[24] Richard M Martin. *Electronic structure: basic theory and practical methods*. Cambridge university press, 2004.

[25] Robert G Parr and Yang Weitao. *Density-functional theory of atoms and molecules*. Oxford university press, 1994.

[26] W. Kohn and L. J. Sham. Self-consistent equations including exchange and correlation effects. *Phys. Rev.*, 140:A1133–A1138, Nov 1965.

[27] John P. Perdew and Karla Schmidt. Jacob's ladder of density functional approximations for the exchange-correlation energy. 577(1):1–20, 2001.

[28] David C Langreth and MJ Mehl. Beyond the local-density approximation in calculations of ground-state electronic properties. *Physical Review B*, 28(4):1809, 1983.

[29] KEITH A BRUECKNER et al. Correlation energy of an electron gas with a slowly varying high density. *Physical Review*, 165(1):18, 1968.

[30] John P. Perdew, Kieron Burke, and Matthias Ernzerhof. Generalized gradient approximation made simple. *Phys. Rev. Lett.*, 77:3865–3868, Oct 1996.

[31] Jochen Heyd, Gustavo E Scuseria, and Matthias Ernzerhof. Hybrid functionals based on a screened coulomb potential. *The Journal of chemical physics*, 118(18):8207–8215, 2003.

[32] Aliaksandr V Krukau, Oleg A Vydrov, Artur F Izmaylov, and Gustavo E Scuseria. Influence of the exchange screening parameter on the performance of screened hybrid functionals. *The Journal of chemical physics*, 125(22):224106, 2006.

[33] Mike C Payne, Michael P Teter, Douglas C Allan, TA Arias, and ad JD Joannopoulos. Iterative minimization techniques for ab initio total-energy calculations: molecular dynamics and conjugate gradients. *Reviews of modern physics*, 64(4):1045, 1992.

[34] DR Hamann, M Schlüter, and C Chiang. Norm-conserving pseudopotentials. *Physical Review Letters*, 43(20):1494, 1979.

[35] David Vanderbilt. Soft self-consistent pseudopotentials in a generalized eigenvalue formalism. *Physical review B*, 41(11):7892, 1990.

[36] Peter E Blöchl. Projector augmented-wave method. *Physical review B*, 50(24):17953, 1994.

[37] O Krogh Andersen. Linear methods in band theory. *Physical Review B*, 12(8):3060, 1975.

[38] John C Slater. Wave functions in a periodic potential. *Physical Review*, 51(10):846, 1937.

[39] Dorothea Golze, Marc Dvorak, and Patrick Rinke. The gw compendium: A practical guide to theoretical photoemission spectroscopy. *Frontiers in chemistry*, 7:377, 2019.

[40] Richard Phillips Feynman. Forces in molecules. *Physical review*, 56(4):340, 1939.

[41] OH Nielsen and Richard M Martin. First-principles calculation of stress. *Physical Review Letters*, 50(9):697, 1983.

[42] Graeme Henkelman and Hannes Jónsson. Improved tangent estimate in the nudged elastic band method for finding minimum energy paths and saddle points. *The Journal of chemical physics*, 113(22):9978–9985, 2000.

[43] Graeme Henkelman, Blas P Uberuaga, and Hannes Jónsson. A climbing image nudged elastic band method for finding saddle points and minimum energy paths. *The Journal of chemical physics*, 113(22):9901–9904, 2000.

[44] Gregory Mills, Hannes Jónsson, and Gregory K Schenter. Reversible work transition state theory: application to dissociative adsorption of hydrogen. *Surface Science*, 324(2-3):305–337, 1995.

[45] Daniel Sheppard, Rye Terrell, and Graeme Henkelman. Optimization methods for finding minimum energy paths. *The Journal of chemical physics*, 128(13), 2008.

[46] R Elber and M Karplus. A method for determining reaction paths in large molecules: Application to myoglobin. *Chemical Physics Letters*, 139(5):375–380, 1987.

[47] Ryszard Czerminski and Ron Elber. Reaction path study of conformational transitions in flexible systems: applications to peptides. *The Journal of chemical physics*, 92(9):5580–5601, 1990.

[48] Saswata Bhattacharya, Sergey V Levchenko, Luca M Ghiringhelli, and Matthias Scheffler. Efficient ab initio schemes for finding thermodynamically stable and metastable atomic structures: Benchmark of cascade genetic algorithms. *New Journal of Physics*, 16(12):123016, 2014.

[49] Jutta Rogal and Karsten Reuter. Ab initio atomistic thermodynamics for surfaces: A primer. Technical report, 2006.

[50] DA McQuarrie. Statistical mechanics, harper &, 1976.

[51] Lu Jeu Sham and Walter Kohn. One-particle properties of an inhomogeneous interacting electron gas. *Physical Review*, 145(2):561, 1966.

[52] John P Perdew, Robert G Parr, Mel Levy, and Jose L Balduz Jr. Density-functional theory for fractional particle number: Derivative discontinuities of the energy. *Physical Review Letters*, 49(23):1691, 1982.

[53] Giovanni Onida, Lucia Reining, and Angel Rubio. Electronic excitations: density-functional versus many-body green's-function approaches. *Reviews of modern physics*, 74(2):601, 2002.

[54] Maxim Shishkin and Georg Kresse. Self-consistent g w calculations for semiconductors and insulators. *Physical Review B*, 75(23):235102, 2007.

[55] M Shishkin and G Kresse. Implementation and performance of the frequency-dependent g w method within the paw framework. *Physical Review B*, 74(3):035101, 2006.

[56] Sergey V Faleev, Mark Van Schilfgaarde, and Takao Kotani. All-electron self-consistent g w approximation: Application to si, mno, and nio. *Physical review letters*, 93(12):126406, 2004.

[57] Manuel Grumet, Peitao Liu, Merzuk Kaltak, Jiří Klimeš, and Georg Kresse. Beyond the quasiparticle approximation: Fully self-consistent g w calculations. *Physical Review B*, 98(15):155143, 2018.

[58] Hector Prats, Ramon A. Gutierrez, Juan Jose Pinero, Francesc Vines, Stefan T. Bromley, Pedro J. Ramirez, Jose A. Rodriguez, and Francesc Illas. Room temperature methane capture and activation by ni clusters supported on tic(001): Effects of metal−carbide interactions on the cleavage of the c−h bond. *Journal of the American Chemical Society*, 141(13):5303–5313, 2019.

[59] Emmett D. Goodman, Allegra A. Latimer, An-Chih Yang, Liheng Wu, Nadia Tahsini, Frank Abild-Pedersen, and Matteo Cargnello. Low-temperature methane partial oxidation to syngas with modular nanocrystal catalysts. *ACS Applied Nano Materials*, 1(9):5258–5267, 2018.

[60] Provas Pal, Rajib Kumar Singha, Arka Saha, Rajaram Bal, and Asit Baran Panda. Defect-induced efficient partial oxidation of methane over nonstoichiometric ni/ceo_2 nanocrystals. *The Journal of Physical Chemistry C*, 119(24):13610–13618, 2015.

[61] Jiacan Su, Liehu Cao, Liang Li, Jie Wei, Gengnan Li, and Yinyin Yuan. Highly sensitive methane catalytic combustion micro-sensor based on mesoporous structure and nano-catalyst. *Nanoscale*, 5:9720–9725, 2013.

[62] Bjørn Christian Enger, Rune Lodeng, and Anders Holmen. A review of catalytic partial oxidation of methane to synthesis gas with emphasis on reaction mechanisms over transition metal catalysts. *Applied Catalysis A: General*, 346(1-2):1–27, 2008.

[63] Stefan HAM Leenders, Rafael Gramage-Doria, Bas de Bruin, and Joost NH Reek. Transition metal catalysis in confined spaces. *Chemical Society Reviews*, 44(2):433–448, 2015.

[64] K Aasberg-Petersen, J-H Bak Hansen, TS Christensen, I Dybkjaer, P Seier Christensen, C Stub Nielsen, SEL Winter Madsen, and JR Rostrup-Nielsen. Technologies for large-scale gas conversion. *Applied Catalysis A: General*, 221(1-2):379–387, 2001.

[65] Subhasis Das, Manideepa Sengupta, Arijit Bag, Mumtaj Shah, and Ankur Bordoloi. Facile synthesis of highly disperse ni–co nanoparticles over mesoporous silica for enhanced methane dry reforming. *Nanoscale*, 10:6409–6425, 2018.

[66] Pei Tang, Qingjun Zhu, Zhaoxuan Wu, and Ding Ma. Methane activation: the past and future. *Energy Environ. Sci.*, 7:2580–2591, 2014.

[67] Ho Ting Luk, Cecilia Mondelli, Daniel Curulla Ferre, Joseph A. Stewart, and Javier Perez-Ramrez. Status and prospects in higher alcohols synthesis from syngas. *Chem. Soc. Rev.*, 46:1358–1426, 2017.

[68] Yan-Xia Zhao, Zi-Yu Li, Yuan Yang, and Sheng-Gui He. Methane activation by gas phase atomic clusters. *Accounts of Chemical Research*, 51(11):2603–2610, 2018.

[69] Hai-Fang Li, Yan-Xia Zhao, Zhen Yuan, Qing-Yu Liu, Zi-Yu Li, Xiao-Na Li, Chuan-Gang Ning, and Sheng-Gui He. Methane activation by tantalum carbide cluster anions ta2c4–. *The Journal of Physical Chemistry Letters*, 8(3):605–610, 2017.

[70] Hai-Fang Li, Zi-Yu Li, Qing-Yu Liu, Xiao-Na Li, Yan-Xia Zhao, and Sheng-Gui He. Methane activation by iron-carbide cluster anions fec6–. *The Journal of Physical Chemistry Letters*, 6(12):2287–2291, 2015.

[71] Matthieu Fleys, Yves Simon, Dariusz Swierczynski, Alain Kiennemann, and Paul-Marie Marquaire. Investigation of the reaction of partial oxidation of methane over ni/la2o3 catalyst. *Energy & Fuels*, 20(6):2321–2329, 2006.

[72] Miryam Gil-Calvo, Cristina Jimenez-Gonzalez, Beatriz de Rivas, Jose I. Gutierrez−Ortiz, and Ruben Lopez-Fonseca. Novel nickel aluminate-derived catalysts supported on ceria and ceria−zirconia for partial oxidation of methane. *Industrial & Engineering Chemistry Research*, 56(21):6186–6197, 2017.

[73] Saurabh Bhavsar and Götz Veser. Chemical looping beyond combustion: production of synthesis gas via chemical looping partial oxidation of methane. *RSC Adv.*, 4:47254–47267, 2014.

[74] D. A. Hickman and L. D. Schmidt. Production of syngas by direct catalytic oxidation of methane. *Science*, 259(5093):343–346, 1993.

[75] Dirk Neumann, Mark Kirchhoff, and Götz Veser. Towards an efficient process for small-scale, decentralized conversion of methane to synthesis gas: combined reactor engineering and catalyst synthesis. *Catalysis Today*, 98(4):565 – 574, 2004.

[76] AT Ashcroft, AK Cheetham, JS al Foord, MLH Green, CP Grey, AJ Murrell, and PDF Vernon. Selective oxidation of methane to synthesis gas using transition metal catalysts. *Nature*, 344(6264):319–321, 1990.

[77] Patrick DF Vernon, Malcolm LH Green, Anthony K Cheetham, and Alexander T Ashcroft. Partial oxidation of methane to synthesis gas. *Catalysis Letters*, 6(2):181–186, 1990.

[78] R. C. Ramaswamy, P. A. Ramachandran, and M. P. Dudukovic. Modeling catalytic partial oxidation of methane to syngas in short-contact-time packed-bed reactors. *Industrial & Engineering Chemistry Research*, 46(25):8638–8651, 2007.

[79] Yun Hang Hu and Eli Ruckenstein. Catalyst temperature oscillations during partial oxidation of methane. *Industrial & Engineering Chemistry Research*, 37(6):2333–2335, 1998.

[80] S.S. Bharadwaj and L.D. Schmidt. Catalytic partial oxidation of natural gas to syngas. *Fuel Processing Technology*, 42(2):109 – 127, 1995.

[81] A. Hellman, A. Resta, N. M. Martin, J. Gustafson, A. Trinchero, P.-A. Carlsson, O. Balmes, R. Felici, R. van Rijn, J. W. M. Frenken, J. N. Andersen, E. Lundgren, and H. Gronbeck. The active phase of palladium during methane oxidation. *The Journal of Physical Chemistry Letters*, 3(6):678–682, 2012.

[82] P. Morten Hundt, Maarten E. van Reijzen, Hirokazu Ueta, and Rainer D. Beck. Vibrational activation of methane chemisorption: The role of symmetry. *The Journal of Physical Chemistry Letters*, 5(11):1963–1967, 2014.

[83] John D Aiken III and Richard G Finke. A review of modern transition-metal nanoclusters: their synthesis, characterization, and applications in catalysis. *Journal of Molecular Catalysis A: Chemical*, 145(1-2):1–44, 1999.

[84] Craig L Hill and Christina M Prosser-McCartha. Homogeneous catalysis by transition metal oxygen anion clusters. *Coordination Chemistry Reviews*, 143:407–455, 1995.

[85] Han Guo, Philippe Sautet, and Anastassia N. Alexandrova. Reagent triggers isomerization of fluxional cluster catalyst via dynamic coupling. *The Journal of Physical Chemistry Letters*, 0(ja):null, 0.

[86] Husileng Lee, Xiujuan Wu, and Licheng Sun. Copper-based homogeneous and heterogeneous catalysts for electrochemical water oxidation. *Nanoscale*, 2020.

[87] Shaohong Zhu, Xinyi Lian, Tingting Fan, Zhou Chen, Yunyun Dong, Weizheng Weng, Xiaodong Yi, and Weiping Fang. Thermally stable core–shell ni/nanorod-ceo2@sio2 catalyst for partial oxidation of methane at high temperatures. *Nanoscale*, 10:14031–14038, 2018.

[88] Dong Wang and Didier Astruc. The recent development of efficient earth-abundant transition-metal nanocatalysts. *Chem. Soc. Rev.*, 46:816–854, 2017.

[89] Antonio Ruiz Puigdollers, Philomena Schlexer, Sergio Tosoni, and Gianfranco Pacchioni. Increasing oxide reducibility: The role of metal/oxide interfaces in the formation of oxygen vacancies. *ACS Catalysis*, 7(10):6493–6513, 2017.

[90] Mark T. Greiner, Lily Chai, Michael G. Helander, Wing-Man Tang, and Zheng-Hong Lu. Transition metal oxide work functions: The influence of cation oxidation state and oxygen vacancies. *Advanced Functional Materials*, 22(21):4557–4568, 2012.

[91] Jurgen Kauhler, Jen-Hui Chang, and Myung-Hwan Whangbo. Bonding and oxidation state of a transition metal atom encapsulated in an isolated octahedral cluster cation of main group elements: synthesis, crystal structure, and electronic structure of pt2in14ga3o8f15 containing highly positive 18-electron complex [ptin6]10+ and low-valent in+ ions. *Journal of the American Chemical Society*, 127(7):2277–2284, 2005.

[92] Shikha Saini, Pooja Basera, Ekta Arora, and Saswata Bhattacharya. Unraveling thermodynamic stability, catalytic activity, and electronic structure of [tm$_x$mg$_y$o$_z$]+/0/–clusters at realistic conditions: A hybrid dft and ab initio thermodynamics study. *The Journal of Physical Chemistry C*, 123(25):15495–15502, 2019.

[93] Mie Andersen, Chiara Panosetti, and Karsten Reuter. A practical guide to surface kinetic monte carlo simulations. *Frontiers in chemistry*, 7:202, 2019.

[94] Amrita Bhattacharya and Saswata Bhattacharya. Exploring n-rich phases in lixny clusters for hydrogen storage at nanoscale. *The Journal of Physical Chemistry Letters*, 6(18):3726–3730, 2015.

[95] Manfred T. Reetz and Wolfgang Helbig. Size-selective synthesis of nanostructured transition metal clusters. *Journal of the American Chemical Society*, 116(16):7401–7402, 1994.

[96] V Sudheeshkumar, Kazeem O Sulaiman, and Robert WJ Scott. Activation of atom-precise clusters for catalysis. *Nanoscale Advances*, 2020.

[97] Saswata Bhattacharya, Benjamin H. Sonin, Christopher J. Jumonville, Luca M. Ghiringhelli, and Noa Marom. Computational design of nanoclusters by property-based genetic algorithms: Tuning the electronic properties of $(\mathrm{tio}_2)_n$ clusters. *Phys. Rev. B*, 91:241115, Jun 2015.

[98] Thomas M. Soini and Notker Rausch. Size-dependent properties of transition metal clusters: from molecules to crystals and surfaces – computational studies with the program paragauss. *Phys. Chem. Chem. Phys.*, 17:28463–28483, 2015.

[99] Emil Roduner. Size matters: why nanomaterials are different. *Chem. Soc. Rev.*, 35:583–592, 2006.

[100] Lin Li, Ask H. Larsen, Nichols A. Romero, Vitali A. Morozov, Christian Glinsvad, Frank Abild-Pedersen, Jeff Greeley, Karsten W. Jacobsen, and Jens K. Nørskov. Investigation of catalytic finite-size-effects of platinum metal clusters. *The Journal of Physical Chemistry Letters*, 4(1):222–226, 2013.

[101] P. L. Rodriguez Kessler and A. R. Rodriguez Dominguez. Stability of ni clusters and the adsorption of ch4: First-principles calculations. *The Journal of Physical Chemistry C*, 119(22):12378–12384, 2015.

[102] Andreas Sieber, Colette Boskovic, Roland Bircher, Oliver Waldmann, Stefan T. Ochsenbein, Grégory Chaboussant, Hans U. Güdel, Nadeschda Kirchner, Joris van Slageren,

Wolfgang Wernsdorfer, Antonia Neels, Helen Stoeckli-Evans, Stefan Janssen, Fanni Juranyi, and Hannu Mutka. Synthesis and spectroscopic characterization of a new family of ni4 spin clusters. *Inorganic Chemistry*, 44(12):4315–4325, 2005. PMID: 15934762.

[103] Jingyun Ye, Laura Gagliardi, Christopher J. Cramer, and Donald G. Truhlar. Single ni atoms and ni4 clusters have similar catalytic activity for ethylene dimerization. *Journal of Catalysis*, 354:278 – 286, 2017.

[104] Sarah Z Tasker, Eric A Standley, and Timothy F Jamison. Recent advances in homogeneous nickel catalysis. *Nature*, 509(7500):299–309, 2014.

[105] Wilhelm Keim. Nickel: an element with wide application in industrial homogeneous catalysis. *Angewandte Chemie International Edition in English*, 29(3):235–244, 1990.

[106] Enrico Monachino, Mark Greiner, Axel Knop-Gericke, Robert Schlogl, Carlo Dri, Erik Vesselli, and Giovanni Comelli. Reactivity of carbon dioxide on nickel: Role of co in the competing interplay between oxygen and graphene. *The Journal of Physical Chemistry Letters*, 5(11):1929–1934, 2014.

[107] Sudipta De, Jiaguang Zhang, Rafael Luque, and Ning Yan. Ni-based bimetallic heterogeneous catalysts for energy and environmental applications. *Energy Environ. Sci.*, 9:3314–3347, 2016.

[108] Fengwang Li, Douglas R. MacFarlane, and Jie Zhang. Recent advances in the nanoengineering of electrocatalysts for co2 reduction. *Nanoscale*, 10:6235–6260, 2018.

[109] Pallavi Bothra and Swapan K. Pati. Improved catalytic activity of rhodium monolayer modified nickel (110) surface for the methane dehydrogenation reaction: a first-principles study. *Nanoscale*, 6:6738–6744, 2014.

[110] Saswata Bhattacharya, Sergey V Levchenko, Luca M Ghiringhelli, and Matthias Scheffler. Stability and metastability of clusters in a reactive atmosphere: Theoretical evidence for unexpected stoichiometries of mg_mo_x. *Physical review letters*, 111(13):135501, 2013.

[111] Saswata Bhattacharya, Benjamin H Sonin, Christopher J Jumonville, Luca M Ghiringhelli, and Noa Marom. Computational design of nanoclusters by property-based

genetic algorithms: Tuning the electronic properties of (tio_2) n clusters. *Physical Review B*, 91(24):241115, 2015.

[112] Ekta Arora, Shikha Saini, Pooja Basera, Manish Kumar, Arunima Singh, and Saswata Bhattacharya. Elucidating the role of temperature and pressure to the thermodynamic stability of charged defects in complex metal-hydrides: A case study of naalh4. *The Journal of Physical Chemistry C*, 123(1):62–69, 2019.

[113] Shikha Saini, Debalaya Sarker, Pooja Basera, Sergey V Levchenko, Luca M Ghiringhelli, and Saswata Bhattacharya. Structure and electronic properties of transition-metal/mg bimetallic clusters at realistic temperatures and oxygen partial pressures. *The Journal of Physical Chemistry C*, 122(29):16788–16794, 2018.

[114] John P Perdew, Matthias Ernzerhof, and Kieron Burke. Rationale for mixing exact exchange with density functional approximations. *The Journal of chemical physics*, 105(22):9982–9985, 1996.

[115] Volker Blum, Ralf Gehrke, Felix Hanke, Paula Havu, Ville Havu, Xinguo Ren, Karsten Reuter, and Matthias Scheffler. Ab initio molecular simulations with numeric atom-centered orbitals. *Computer Physics Communications*, 180(11):2175 – 2196, 2009.

[116] E. van Lenthe, E. J. Baerends, and J. G. Snijders. Relativistic regular two−component hamiltonians. *The Journal of Chemical Physics*, 99(6):4597–4610, 1993.

[117] Alexandre Tkatchenko and Matthias Scheffler. Accurate molecular van der waals interactions from ground-state electron density and free-atom reference data. *Physical review letters*, 102(7):073005, 2009.

[118] Nicos S. Martys and Raymond D. Mountain. Velocity verlet algorithm for dissipative-particle-dynamics-based models of suspensions. *Phys. Rev. E*, 59:3733–3736, Mar 1999.

[119] Denis J Evans and Brad Lee Holian. The nose–hoover thermostat. *The Journal of chemical physics*, 83(8):4069–4074, 1985.

[120] Pooja Basera, Shikha Saini, Ekta Arora, Arunima Singh, Manish Kumar, and Saswata Bhattacharya. Stability of non-metal dopants to tune the photo-absorption of tio 2 at realistic temperatures and oxygen partial pressures: A hybrid dft study. *Scientific reports*, 9(1):1–13, 2019.

[121] Manish Kumar, Pooja Basera, Shikha Saini, and Saswata Bhattacharya. Role of defects in photocatalytic water splitting: Monodoped vs codoped srtio3. *The Journal of Physical Chemistry C*, 2020.

[122] Barbara Stuart. *Infrared Spectroscopy*, pages 1–18. American Cancer Society, 2015.

[123] Wei Zheng Weng, Ming Shu Chen, Qian Gu Yan, Ting Hua Wu, Zi Sheng Chao, Yuan Yan Liao, and Hui Lin Wan. Mechanistic study of partial oxidation of methane to synthesis gas over supported rhodium and ruthenium catalysts using in situ time-resolved ftir spectroscopy. *Catalysis today*, 63(2-4):317–326, 2000.

[124] Vitaly L. Sushkevich, Rene Verel, and Jeroen A. van Bokhoven. Pathways of methane transformation over copper-exchanged mordenite as revealed by in situ nmr and ir spectroscopy. *Angewandte Chemie International Edition*, 59(2):910–918, 2020.

[125] Sheedeh Fouladvand, Magnus Skoglundh, and Per-Anders Carlsson. A transient in situ infrared spectroscopy study on methane oxidation over supported pt catalysts. *Catal. Sci. Technol.*, 4:3463–3473, 2014.

[126] Xueting Wang, Natalia M Martin, Johan Nilsson, Stefan Carlson, Johan Gustafson, Magnus Skoglundh, and Per-Anders Carlsson. Copper-modified zeolites and silica for conversion of methane to methanol. *Catalysts*, 8(11):545, 2018.

[127] José Ruiz-Franco, Lorenzo Rovigatti, and Emanuela Zaccarelli. On the effect of the thermostat in non-equilibrium molecular dynamics simulations. *The European Physical Journal E*, 41(7):80, 2018.

[128] Farid Safari and Ibrahim Dincer. A review and comparative evaluation of thermochemical water splitting cycles for hydrogen production. *Energy Conversion and Management*, 205:112182, 2020.

[129] Shintaro Ida and Tatsumi Ishihara. Recent progress in two-dimensional oxide photocatalysts for water splitting. *The Journal of Physical Chemistry Letters*, 5(15):2533–2542, 2014.

[130] Lilac Amirav and A Paul Alivisatos. Photocatalytic hydrogen production with tunable nanorod heterostructures. *The Journal of Physical Chemistry Letters*, 1(7):1051–1054, 2010.

[131] Rulin Sun, Ruimin Wang, Xinlu Liu, Xiao Chen, Li Che, Hongjun Fan, Xueming Yang, and Qing Guo. Hydrogen production on pt/tio2: Synergistic catalysis between pt clusters and interfacial adsorbates. *The Journal of Physical Chemistry Letters*, 13(14):3182–3187, 2022.

[132] IP Jain. Hydrogen the fuel for 21st century. *International journal of hydrogen energy*, 34(17):7368–7378, 2009.

[133] Neubi F Xavier Jr, Glauco F Bauerfeldt, and Marco Sacchi. First-principles microkinetic modeling unravelling the performance of edge-decorated nanocarbons for hydrogen production from methane. *ACS applied materials & interfaces*, 15(5):6951–6962, 2023.

[134] Haisu Wu, Tifang Miao, Qinghua Deng, Yun Xu, Haixia Shi, Ying Huang, and Xianliang Fu. Accelerating nickel-based molecular construction via dft guidance for advanced photocatalytic hydrogen production. *ACS Applied Materials & Interfaces*, 14(15):17486–17499, 2022.

[135] Yanqi Wang, Jianrong Li, Qianqian Hu, Minting Hao, Yifan Liu, Liaokuo Gong, Renfu Li, and Xiaoying Huang. Boosting visible-light-driven photocatalytic hydrogen production through sensitizing tio2 via novel nanoclusters. *ACS Applied Materials & Interfaces*, 13(34):40562–40570, 2021.

[136] Ce Hu, Zhenzhen Jiang, Wenda Zhou, Manman Guo, Ting Yu, Xingfang Luo, and Cailei Yuan. Wafer-scale sulfur vacancy-rich monolayer mos2 for massive hydrogen production. *The Journal of Physical Chemistry Letters*, 10(16):4763–4768, 2019.

[137] Dechao Wang, Rong Chen, Xun Zhu, Dingding Ye, Yang Yang, Youxu Yu, Jinwang Li, Yuxin Liu, Hang Zhao, and Qiang Liao. Synergetic photo-thermo catalytic hydrogen production by carbon materials. *The Journal of Physical Chemistry Letters*, 13(6):1602–1608, 2022.

[138] Wilbert Mtangi, Vankayala Kiran, Claudio Fontanesi, and Ron Naaman. Role of the electron spin polarization in water splitting. *The journal of physical chemistry letters*, 6(24):4916–4922, 2015.

[139] Andrea Rossin, Giulia Tuci, Lapo Luconi, and Giuliano Giambastiani. Metal–organic frameworks as heterogeneous catalysts in hydrogen production from lightweight inorganic hydrides. *Acs Catalysis*, 7(8):5035–5045, 2017.

[140] Kohsuke Mori, Kohei Miyawaki, and Hiromi Yamashita. Ru and ru–ni nanoparticles on tio2 support as extremely active catalysts for hydrogen production from ammonia–borane. *ACS Catalysis*, 6(5):3128–3135, 2016.

[141] SS Shinde, Dong-Hyung Kim, Jin-Young Yu, and Jung-Ho Lee. Self-assembled air-stable magnesium hydride embedded in 3-d activated carbon for reversible hydrogen storage. *Nanoscale*, 9(21):7094–7103, 2017.

[142] Yinwu Li, Peifeng Su, Jingxing Jiang, and Zhuofeng Ke. Bifunctional effect of a triple-bond heterobimetallic zr/co system for hydrogen activation. *ACS Catalysis*, 11(21):13452–13462, 2021.

[143] Shailesh Pathak and Sreedevi Upadhyayula. High temperature sulfuric acid decomposition in iodine-sulfur process–thermodynamics, concentrator and reactor, product separation, materials, and energy analysis. *International Journal of Hydrogen Energy*, 46(69):34148–34174, 2021.

[144] Lloyd C Brown, Ryan D Lentsch, Gottfried E Besenbruch, Kenneth R Schultz, and James E Funk. Alternative flowsheets for the sulfur-iodine thermochemical hydrogen cycle. Technical report, General Atomics, San Diego, CA (United States), 2003.

[145] Ashish Nadar, Atindra Mohan Banerjee, MR Pai, Sher Singh Meena, RV Pai, R Tewari, SM Yusuf, AK Tripathi, and SR Bharadwaj. Nanostructured fe2o3 dispersed on sio2 as catalyst for high temperature sulfuric acid decomposition—structural and morphological modifications on catalytic use and relevance of fe2o3-sio2 interactions. *Applied Catalysis B: Environmental*, 217:154–168, 2017.

[146] Yanwei Zhang, Rui Wang, Xiangdong Lin, Zhihua Wang, Jianzhong Liu, Junhu Zhou, and Kefa Cen. Catalytic performance of different carbon materials for hydrogen production in sulfur–iodine thermochemical cycle. *Applied Catalysis B: Environmental*, 166:413–422, 2015.

[147] Nicholas R Brown and Shripad T Revankar. A review of catalytic sulfur (vi) oxide decomposition experiments. *international journal of hydrogen energy*, 37(3):2685–2698, 2012.

[148] Shailesh Pathak, Anshuman Goswami, and Sreedevi Upadhyayula. Kinetic modeling and simulation of catalyst pellet in the high temperature sulfuric acid decomposition section of iodine-sulfur process. *International Journal of Hydrogen Energy*, 44(59):30850–30864, 2019.

[149] Kishore Kondamudi and Sreedevi Upadhyayula. Kinetic studies of sulfuric acid decomposition over al–fe2o3 catalyst in the sulfur-iodine cycle for hydrogen production. *International journal of hydrogen energy*, 37(4):3586–3594, 2012.

[150] Sandeep Nigam and Chiranjib Majumder. Single atom alloy catalyst for so 3 decomposition: enhancement of platinum catalyst's performance by ag atom embedding. *Nanoscale*, 10(44):20599–20610, 2018.

[151] Sandeep Nigam and Chiranjib Majumder. Are deposited bimetallic clusters more effective for so3 decomposition? a systematic study using first principles theory. *The Journal of Physical Chemistry C*, 116(48):25594–25601, 2012.

[152] AM Banerjee, AR Shirole, MR Pai, AK Tripathi, SR Bharadwaj, D Das, and PK Sinha. Catalytic activities of fe2o3 and chromium doped fe2o3 for sulfuric acid decomposition reaction in an integrated boiler, preheater, and catalytic decomposer. *Applied Catalysis B: Environmental*, 127:36–46, 2012.

[153] AM Banerjee, MR Pai, R Tewari, Naina Raje, AK Tripathi, SR Bharadwaj, and D Das. A comprehensive study on pt/al2o3 granular catalyst used for sulfuric acid decomposition step in sulfur–iodine thermochemical cycle: Changes in catalyst structure, morphology and metal-support interaction. *Applied Catalysis B: Environmental*, 162:327–337, 2015.

[154] Masato Machida, Yui Miyazaki, Yuichi Matsunaga, and Keita Ikeue. Efficient catalytic decomposition of sulfuric acid with copper vanadates as an oxygen-generating reaction for solar thermochemical water splitting cycles. *Chemical Communications*, 47(34):9591–9593, 2011.

[155] George Karagiannakis, Christos C Agrafiotis, Alexandra Zygogianni, Chrysoula Pagkoura, and Athanasios G Konstandopoulos. Hydrogen production via sulfur-based thermochemical cycles: Part 1: Synthesis and evaluation of metal oxide-based candidate catalyst powders for the sulfuric acid decomposition step. *international journal of hydrogen energy*, 36(4):2831–2844, 2011.

[156] Haznan Abimanyu, Kwang-Deog Jung, Ki-Won Jun, Jinsoo Kim, and Kye Sang Yoo. Preparation and characterization of fe/cu/al2o3-composite granules for so3 decomposition to assist hydrogen production. *Applied Catalysis A: General*, 343(1-2):134–141, 2008.

[157] Daniel M Ginosar, Harry W Rollins, Lucia M Petkovic, Kyle C Burch, and Michael J Rush. High-temperature sulfuric acid decomposition over complex metal oxide catalysts. *International journal of hydrogen energy*, 34(9):4065–4073, 2009.

[158] Bhari Mallanna Nagaraja, Kwang Deog Jung, and Kye Sang Yoo. Synthesis of cu/fe/ti/al 2 o 3 composite granules for so 3 decomposition in si cycle. *Catalysis letters*, 128:248–252, 2009.

[159] Shailesh Pathak, Shikha Saini, Kishore Kondamudi, Sreedevi Upadhyayula, and Saswata Bhattacharya. Insights into enhanced stability and activity of silica modified sic supported iron oxide catalyst in sulfuric acid decomposition. *Applied Catalysis B: Environmental*, 284:119613, 2021.

[160] Ashish Nadar, Atindra Mohan Banerjee, MR Pai, Sher Singh Meena, AK Patra, PU Sastry, R Singh, MK Singh, and AK Tripathi. Immobilization of crystalline fe2o3 nanoparticles over sio2 for creating an active and stable catalyst: A demand for high temperature sulfuric acid decomposition. *Applied Catalysis B: Environmental*, 283:119610, 2021.

[161] Ashish Nadar, Atindra Mohan Banerjee, MR Pai, RV Pai, Sher Singh Meena, R Tewari, and AK Tripathi. Catalytic properties of dispersed iron oxides fe2o3/mo2 (m= zr, ce, ti and si) for sulfuric acid decomposition reaction: Role of support. *International journal of hydrogen energy*, 43(1):37–52, 2018.

[162] TAS Ferreira, JC Waerenborgh, MHRM Mendonça, MR Nunes, and FM Costa. Structural and morphological characterization of feco2o4 and cofe2o4 spinels prepared by a coprecipitation method. *Solid State Sciences*, 5(2):383–392, 2003.

[163] Vancho Kocevski, Ghanshyam Pilania, and Blas P Uberuaga. High-throughput investigation of the formation of double spinels. *Journal of Materials Chemistry A*, 8(48):25756–25767, 2020.

[164] Yinye Chen, Zhen Zhang, Xin Wang, Yidian Lin, Jiachang Zuo, Xuhui Yang, Songhua Chen, Yongjin Luo, Qingrong Qian, and Qinghua Chen. Crystal plane effect of co3o4 on styrene catalytic oxidation: Insights into the role of co3+ and oxygen mobility at diverse temperatures. *ACS Applied Materials & Interfaces*, 15(27):32404–32415, 2023.

[165] AM Banerjee, MR Pai, SS Meena, AK Tripathi, and SR Bharadwaj. Catalytic activities of cobalt, nickel and copper ferrospinels for sulfuric acid decomposition: the high temperature step in the sulfur based thermochemical water splitting cycles. *international journal of hydrogen energy*, 36(8):4768–4780, 2011.

[166] AM Banerjee, MR Pai, K Bhattacharya, AK Tripathi, VS Kamble, SR Bharadwaj, and SK Kulshreshtha. Catalytic decomposition of sulfuric acid on mixed cr/fe oxide samples and its application in sulfur–iodine cycle for hydrogen production. *International Journal of Hydrogen Energy*, 33(1):319–326, 2008.

[167] Shailesh Pathak and Sreedevi Upadhyayula. A review on the development of supported non-noble metal catalysts for the endothermic high temperature sulfuric acid decomposition step in the iodine–sulfur cycle for hydrogen production. *International Journal of Hydrogen Energy*, 47(31):14186–14210, 2022.

[168] Michael Laing. The electronegativity of a metal and its e o: should they correlate? *South African journal of science*, 98(11):573–580, 2002.

[169] Georg Kresse and Jürgen Furthmüller. Efficiency of ab-initio total energy calculations for metals and semiconductors using a plane-wave basis set. *Computational materials science*, 6(1):15–50, 1996.

[170] Georg Kresse and Daniel Joubert. From ultrasoft pseudopotentials to the projector augmented-wave method. *Physical review b*, 59(3):1758, 1999.

[171] John P Perdew, Kieron Burke, and Matthias Ernzerhof. Phys rev lett 77: 3865. *Errata:(1997) Phys Rev Lett*, 78:1396, 1996.

[172] Hushan Chand, Ashish Kumar, Preeti Bhumla, Banavath Raju Naik, Viswanath Balakrishnan, Saswata Bhattacharya, and Venkata Krishnan. Scalable production of ultrathin boron nanosheets from a low-cost precursor. *Advanced materials interfaces*, 9(23):2200508, 2022.

[173] Akihiro Kojima, Kenjiro Teshima, Yasuo Shirai, and Tsutomu Miyasaka. Organometal halide perovskites as visible-light sensitizers for photovoltaic cells. *Journal of the American Chemical Society*, 131(17):6050–6051, 2009.

[174] Henry J Snaith. Perovskites: the emergence of a new era for low-cost, high-efficiency solar cells. *The journal of physical chemistry letters*, 4(21):3623–3630, 2013.

[175] Martin A Green, Anita Ho-Baillie, and Henry J Snaith. The emergence of perovskite solar cells. *Nature photonics*, 8(7):506–514, 2014.

[176] Michael Grätzel. The light and shade of perovskite solar cells. *Nature materials*, 13(9):838–842, 2014.

[177] Michael M Lee, Joël Teuscher, Tsutomu Miyasaka, Takurou N Murakami, and Henry J Snaith. Efficient hybrid solar cells based on meso-superstructured organometal halide perovskites. *Science*, 338(6107):643–647, 2012.

[178] Guichuan Xing, Nripan Mathews, Shuangyong Sun, Swee Sien Lim, Yeng Ming Lam, Michael Grätzel, Subodh Mhaisalkar, and Tze Chien Sum. Long-range balanced electron-and hole-transport lengths in organic-inorganic ch3nh3pbi3. *Science*, 342(6156):344–347, 2013.

[179] Joseph S Manser, Jeffrey A Christians, and Prashant V Kamat. Intriguing optoelectronic properties of metal halide perovskites. *Chemical reviews*, 116(21):12956–13008, 2016.

[180] A Swarnkar, AR Marshall, and EM Sanehira. bd chernomordik, d. t. moore, ja christians, t. chakrabarti and jm luther, quantum dot–induced phase stabilization of a-cspbi3 perovskite for high-efficiency photovoltaics. *Science*, 354(6308):92–95, 2016.

[181] Samuel D Stranks and Henry J Snaith. Metal-halide perovskites for photovoltaic and light-emitting devices. *Nature nanotechnology*, 10(5):391–402, 2015.

[182] Jae Keun Nam, Do Hyung Chun, Ryan Joon Kyu Rhee, Jung Hwan Lee, and Jong Hyeok Park. Methodologies toward efficient and stable cesium lead halide perovskite-based solar cells. *Advanced Science*, 5(8):1800509, 2018.

[183] Sekai Tombe, Getachew Adam, Herwig Heilbrunner, Dogukan Hazar Apaydin, Christoph Ulbricht, Niyazi Serdar Sariciftci, Christopher J Arendse, Emmanuel Iwuoha, and Markus C Scharber. Optical and electronic properties of mixed halide (x= i, cl, br) methylammonium lead perovskite solar cells. *Journal of Materials Chemistry C*, 5(7):1714–1723, 2017.

[184] Julian Burschka, Norman Pellet, Soo-Jin Moon, Robin Humphry-Baker, Peng Gao, Mohammad K Nazeeruddin, and Michael Grätzel. Sequential deposition as a route to high-performance perovskite-sensitized solar cells. *Nature*, 499(7458):316–319, 2013.

[185] NREL NREL. Best research-cell efficiency chart. 2019.

[186] Florent Sahli, Jérémie Werner, Brett A Kamino, Matthias Bräuninger, Raphaël Monnard, Bertrand Paviet-Salomon, Loris Barraud, Laura Ding, Juan J Diaz Leon, Davide Sacchetto, et al. Fully textured monolithic perovskite/silicon tandem solar cells with 25.2% power conversion efficiency. *Nature materials*, 17(9):820–826, 2018.

[187] Jacky Even, Laurent Pedesseau, M-A Dupertuis, J-M Jancu, and Claudine Katan. Electronic model for self-assembled hybrid organic/perovskite semiconductors: Reverse band edge electronic states ordering and spin-orbit coupling. *Physical Review B*, 86(20):205301, 2012.

[188] Jacky Even, Laurent Pedesseau, Jean-Marc Jancu, and Claudine Katan. Importance of spin–orbit coupling in hybrid organic/inorganic perovskites for photovoltaic applications. *The Journal of Physical Chemistry Letters*, 4(17):2999–3005, 2013.

[189] LL Tao and Evgeny Y Tsymbal. Persistent spin texture enforced by symmetry. *Nature communications*, 9(1):1–7, 2018.

[190] Hong Jian Zhao, Hiro Nakamura, Rémi Arras, Charles Paillard, Peng Chen, Julien Gosteau, Xu Li, Yurong Yang, and Laurent Bellaiche. Purely cubic spin splittings with persistent spin textures. *Physical Review Letters*, 125(21):216405, 2020.

[191] Frank Schindler, Zhijun Wang, Maia G Vergniory, Ashley M Cook, Anil Murani, Shamashis Sengupta, Alik Yu Kasumov, Richard Deblock, Sangjun Jeon, Ilya Drozdov, et al. Higher-order topology in bismuth. *Nature physics*, 14(9):918–924, 2018.

[192] MA Toloza Sandoval, A Ferreira da Silva, EA de Andrada e Silva, and GC La Rocca. Rashba and dresselhaus spin-orbit interaction strength in gaas/gaalas heterojunctions. *Physics Procedia*, 28:95–98, 2012.

[193] Louis Ponet and S Artyukhin. First-principles theory of giant rashba-like spin splitting in bulk gete. *Physical Revdi2013electriciew B*, 98(17):174102, 2018.

[194] Domenico Di Sante, Paolo Barone, Alessandro Stroppa, Kevin F Garrity, David Vanderbilt, and Silvia Picozzi. Intertwined rashba, dirac, and weyl fermions in hexagonal hyperferroelectrics. *Physical review letters*, 117(7):076401, 2016.

[195] Kunihiko Yamauchi, Paolo Barone, Tatsuya Shishidou, Tamio Oguchi, and Silvia Picozzi. Coupling ferroelectricity with spin-valley physics in oxide-based heterostructures. *Phys. Rev. Lett.*, 115:037602, Jul 2015.

[196] L. L. Tao, Tula R. Paudel, Alexey A. Kovalev, and Evgeny Y. Tsymbal. Reversible spin texture in ferroelectric $\mathrm{Hfo_2}$. *Phys. Rev. B*, 95:245141, Jun 2017.

[197] Gene Dresselhaus. Spin-orbit coupling effects in zinc blende structures. *Physical Review*, 100(2):580, 1955.

[198] Emmanuel I Rashba. Properties of semiconductors with an extremum loop. i. cyclotron and combinational resonance in a magnetic field perpendicular to the plane of the loop. *Soviet Physics, Solid State*, 2:1109–1122, 1960.

[199] Domenico Di Sante, Paolo Barone, Riccardo Bertacco, and Silvia Picozzi. Electric control of the giant rashba effect in bulk gete. *Advanced materials*, 25(4):509–513, 2013.

[200] Evgeny Plekhanov, Paolo Barone, Domenico Di Sante, and Silvia Picozzi. Engineering relativistic effects in ferroelectric snte. *Physical Review B*, 90(16):161108, 2014.

[201] Minsung Kim, Jino Im, Arthur J Freeman, Jisoon Ihm, and Hosub Jin. Switchable s= 1/2 and j= 1/2 rashba bands in ferroelectric halide perovskites. *Proceedings of the National Academy of Sciences*, 111(19):6900–6904, 2014.

[202] Yasemin Kutes, Linghan Ye, Yuanyuan Zhou, Shuping Pang, Bryan D Huey, and Nitin P Padture. Direct observation of ferroelectric domains in solution-processed ch3nh3pbi3 perovskite thin films. *The journal of physical chemistry letters*, 5(19):3335–3339, 2014.

[203] David Giovanni, Hong Ma, Julianto Chua, Michael Gratzel, Ramamoorthy Ramesh, Subodh Mhaisalkar, Nripan Mathews, and Tze Chien Sum. Highly spin-polarized carrier dynamics and ultralarge photoinduced magnetization in ch3nh3pbi3 perovskite thin films. *Nano letters*, 15(3):1553–1558, 2015.

[204] Mikael Kepenekian and Jacky Even. Rashba and dresselhaus couplings in halide perovskites: Accomplishments and opportunities for spintronics and spin–orbitronics. *The journal of physical chemistry letters*, 8(14):3362–3370, 2017.

[205] Christian Rinaldi, Sara Varotto, Marco Asa, Jagoda Sławinska, Jun Fujii, Giovanni Vinai, Stefano Cecchi, Domenico Di Sante, Raffaella Calarco, Ivana Vobornik, et al. Ferroelectric control of the spin texture in gete. *Nano letters*, 18(5):2751–2758, 2018.

[206] Linn Leppert, Sebastian E. Reyes-Lillo, and Jeffrey B. Neaton. Electric field- and strain-induced rashba effect in hybrid halide perovskites. *The Journal of Physical Chemistry Letters*, 7(18):3683–3689, 2016. PMID: 27577732.

[207] Linn Leppert, Sebastian E Reyes-Lillo, and Jeffrey B Neaton. Electric field-and strain-induced rashba effect in hybrid halide perovskites. *The journal of physical chemistry letters*, 7(18):3683–3689, 2016.

[208] Maya Isarov, Liang Z Tan, Maryna I Bodnarchuk, Maksym V Kovalenko, Andrew M Rappe, and Efrat Lifshitz. Rashba effect in a single colloidal cspbbr3 perovskite nanocrystal detected by magneto-optical measurements. *Nano letters*, 17(8):5020–5026, 2017.

[209] Daniel Niesner, Max Wilhelm, Ievgen Levchuk, Andres Osvet, Shreetu Shrestha, Miroslaw Batentschuk, Christoph Brabec, and Thomas Fauster. Giant rashba splitting in

ch 3 nh 3 pbbr 3 organic-inorganic perovskite. *Physical review letters*, 117(12):126401, 2016.

[210] Alessandro Stroppa, Domenico Di Sante, Paolo Barone, Menno Bokdam, Georg Kresse, Cesare Franchini, Myung-Hwan Whangbo, and Silvia Picozzi. Tunable ferroelectric polarization and its interplay with spin–orbit coupling in tin iodide perovskites. *Nature communications*, 5(1):1–8, 2014.

[211] Nabonswende Aida Nadege Ouedraogo, Yichuan Chen, Yue Yue Xiao, Qi Meng, Chang Bao Han, Hui Yan, and Yongzhe Zhang. Stability of all-inorganic perovskite solar cells. *Nano Energy*, 67:104249, 2020.

[212] Silvia Picozzi. Ferroelectric rashba semiconductors as a novel class of multifunctional materials. *Frontiers in Physics*, 2:10, 2014.

[213] Marcus Liebmann, Christian Rinaldi, Domenico Di Sante, Jens Kellner, Christian Pauly, Rui Ning Wang, Jos Emiel Boschker, Alessandro Giussani, Stefano Bertoli, Matteo Cantoni, et al. Giant rashba-type spin splitting in ferroelectric gete (111). *Advanced Materials*, 28(3):560–565, 2016.

[214] Awadhesh Narayan. Class of rashba ferroelectrics in hexagonal semiconductors. *Phys. Rev. B*, 92:220101, Dec 2015.

[215] Aurelien Manchon, Hyun Cheol Koo, Junsaku Nitta, SM Frolov, and RA Duine. New perspectives for rashba spin–orbit coupling. *Nature materials*, 14(9):871–882, 2015.

[216] Chang Woo Myung, Saqib Javaid, Kwang S Kim, and Geunsik Lee. Rashba–dresselhaus effect in inorganic/organic lead iodide perovskite interfaces. *ACS Energy Letters*, 3(6):1294–1300, 2018.

[217] John P Perdew, Kieron Burke, and Matthias Ernzerhof. Generalized gradient approximation made simple. *Physical review letters*, 77(18):3865, 1996.

[218] Mark S Hybertsen and Steven G Louie. First-principles theory of quasiparticles: calculation of band gaps in semiconductors and insulators. *Physical review letters*, 55(13):1418, 1985.

[219] Georg Kresse and Jürgen Hafner. Ab initio molecular dynamics for liquid metals. *Physical Review B*, 47(1):558, 1993.

[220] Georg Kresse and Jürgen Furthmüller. Efficient iterative schemes for ab initio total-energy calculations using a plane-wave basis set. *Physical review B*, 54(16):11169, 1996.

[221] Atsushi Togo, Fumiyasu Oba, and Isao Tanaka. First-principles calculations of the ferroelastic transition between rutile-type and cacl 2-type sio 2 at high pressures. *Physical Review B*, 78(13):134106, 2008.

[222] Atsushi Togo and Isao Tanaka. First principles phonon calculations in materials science. *Scripta Materialia*, 108:1–5, 2015.

[223] RD King-Smith and David Vanderbilt. Theory of polarization of crystalline solids. *Physical Review B*, 47(3):1651, 1993.

[224] Raffaele Resta. Macroscopic polarization in crystalline dielectrics: the geometric phase approach. *Reviews of modern physics*, 66(3):899, 1994.

[225] Uthpala Herath, Pedram Tavadze, Xu He, Eric Bousquet, Sobhit Singh, Francisco Muñoz, and Aldo H. Romero. Pyprocar: A python library for electronic structure pre/post-processing. *Computer Physics Communications*, 251:107080, 2020.

[226] P Berastegui, S Hull, and SG Eriksson. A low-temperature structural phase transition in cspbf3. *Journal of Physics: Condensed Matter*, 13(22):5077, 2001.

[227] Eva H Smith, Nicole A Benedek, and Craig J Fennie. Interplay of octahedral rotations and lone pair ferroelectricity in cspbf3. *Inorganic chemistry*, 54(17):8536–8543, 2015.

[228] Jingyu Qian, Bin Xu, and Wenjing Tian. A comprehensive theoretical study of halide perovskites abx3. *Organic Electronics*, 37:61–73, 2016.

[229] G Murtaza, Iftikhar Ahmad, M Maqbool, HA Rahnamaye Aliabad, and A Afaq. Structural and optoelectronic properties of cubic cspbf3 for novel applications. *Chinese Physics Letters*, 28(11):117803, 2011.

[230] Subhadeep Bandyopadhyay, Atanu Paul, and I. Dasgupta. Origin of rashba-dresselhaus effect in the ferroelectric nitride perovskite $\mathrm{lawn_3}$. *Phys. Rev. B*, 101:014109, Jan 2020.

[231] Moh. Adhib Ulil Absor, Iman Santoso, Harsojo, Kamsul Abraha, Hiroki Kotaka, Fumiyuki Ishii, and Mineo Saito. Strong rashba effect in the localized impurity states of halogen-doped monolayer ptse_2. *Phys. Rev. B*, 97:205138, May 2018.

[232] Luiz Gustavo Davanse da Silveira, Paolo Barone, and Silvia Picozzi. Rashba-dresselhaus spin-splitting in the bulk ferroelectric oxide bialo_3. *Phys. Rev. B*, 93:245159, Jun 2016.

[233] Sajjan Sheoran, Manish Kumar, Preeti Bhumla, and Saswata Bhattacharya. Rashba dominated spin-splitting in the bulk ferroelectric oxide perovskite kio3, 2021.

[234] Samuel D Stranks and Paulina Plochocka. The influence of the rashba effect. *Nature materials*, 17(5):381–382, 2018.

[235] Moh. Adhib Ulil Absor and Fumiyuki Ishii. Intrinsic persistent spin helix state in two-dimensional group-iv monochalcogenide mx monolayers ($m = \mathrm{Sn}$ or ge and $x = \mathrm{S}$, se, or te). *Phys. Rev. B*, 100:115104, Sep 2019.

[236] Julien Varignon, Jacobo Santamaria, and Manuel Bibes. Electrically switchable and tunable rashba-type spin splitting in covalent perovskite oxides. *Phys. Rev. Lett.*, 122:116401, Mar 2019.

[237] Mikaël Kepenekian, Roberto Robles, Claudine Katan, Daniel Sapori, Laurent Pedesseau, and Jacky Even. Rashba and dresselhaus effects in hybrid organic–inorganic perovskites: from basics to devices. *ACS nano*, 9(12):11557–11567, 2015.

[238] Jiajia Chen, Kai Wu, Wei Hu, and Jinlong Yang. Tunable rashba spin splitting in two-dimensional polar perovskites. *The Journal of Physical Chemistry Letters*, 12(7):1932–1939, 2021.

[239] Idris A Ajia, Paul R Edwards, Yusin Pak, Ermek Belekov, Manuel A Roldan, Nini Wei, Zhiqiang Liu, Robert W Martin, and Iman S Roqan. Generated carrier dynamics in v-pit-enhanced ingan/gan light-emitting diode. *ACS Photonics*, 5(3):820–826, 2017.

[240] Huanping Zhou, Qi Chen, Gang Li, Song Luo, Tze-bing Song, Hsin-Sheng Duan, Ziruo Hong, Jingbi You, Yongsheng Liu, and Yang Yang. Interface engineering of highly efficient perovskite solar cells. *Science*, 345(6196):542–546, 2014.

[241] Gangjian Tan, Li-Dong Zhao, and Mercouri G Kanatzidis. Rationally designing high-performance bulk thermoelectric materials. *Chem. Rev.*, 116(19):12123–12149, 2016.

[242] Ziang Jing, Hangyu Wang, Xianghui Feng, Bing Xiao, Yingchun Ding, Kai Wu, and Yonghong Cheng. Superior thermoelectric performance of ordered double transition metal mxenes: $Cr_2tic_2t_2$ (t=-oh or-f). *J. Phys. Chem. Lett.*, 10(19):5721–5728, 2019.

[243] Saikat Mukhopadhyay and Thomas L Reinecke. Lone-pair electron-driven thermoelectrics at room temperature. *J. Phys. Chem. Lett.*, 10(14):4117–4122, 2019.

[244] H Julian Goldsmid et al. *Introduction to thermoelectricity*, volume 121. Springer, 2010.

[245] Tiejun Zhu, Yintu Liu, Chenguang Fu, Joseph P Heremans, Jeffrey G Snyder, and Xinbing Zhao. Compromise and synergy in high-efficiency thermoelectric materials. *Adv. Mater.*, 29(14):1605884, 2017.

[246] Hongyao Xie, Xianli Su, Trevor P Bailey, Cheng Zhang, Wei Liu, Ctirad Uher, Xinfeng Tang, and Mercouri G Kanatzidis. Anomalously large seebeck coefficient of $cufes_2$ derives from large asymmetry in the energy dependence of carrier relaxation time. *Chem. Mater.*, 32(6):2639–2646, 2020.

[247] Weijun Ke, Constantinos C Stoumpos, and Mercouri G Kanatzidis. "unleaded" perovskites: status quo and future prospects of tin-based perovskite solar cells. *Adv. Mater.*, 31(47):1803230, 2019.

[248] Constantinos C Stoumpos, Christos D Malliakas, and Mercouri G Kanatzidis. Semiconducting tin and lead iodide perovskites with organic cations: phase transitions, high mobilities, and near-infrared photoluminescent properties. *Inorg. Chem.*, 52(15):9019–9038, 2013.

[249] Annalise E Maughan, Alex M Ganose, Mitchell M Bordelon, Elisa M Miller, David O Scanlon, and James R Neilson. Defect tolerance to intolerance in the vacancy-ordered double perovskite semiconductors cs_2sni_6 and cs_2tei_6. *J. Am. Chem. Soc.*, 138(27):8453–8464, 2016.

[250] Paribesh Acharyya, Tanmoy Ghosh, Koushik Pal, Kaushik Kundu, Kewal Singh Rana, Juhi Pandey, Ajay Soni, Umesh V Waghmare, and Kanishka Biswas. Intrinsically

ultralow thermal conductivity in ruddlesden–popper 2d perovskite $cs_2pbi_2cl_2$: localized anharmonic vibrations and dynamic octahedral distortions. *J. Am. Chem. Soc.*, 142(36):15595–15603, 2020.

[251] Woochul Lee, Huashan Li, Andrew B Wong, Dandan Zhang, Minliang Lai, Yi Yu, Qiao Kong, Elbert Lin, Jeffrey J Urban, Jeffrey C Grossman, et al. Ultralow thermal conductivity in all-inorganic halide perovskites. *Proc. Natl. Acad. Sci.*, 114(33):8693–8697, 2017.

[252] Hongyao Xie, Shiqiang Hao, Jinke Bao, Tyler J Slade, G Jeffrey Snyder, Christopher Wolverton, and Mercouri G Kanatzidis. All-inorganic halide perovskites as potential thermoelectric materials: dynamic cation off-centering induces ultralow thermal conductivity. *J. Am. Chem. Soc.*, 142(20):9553–9563, 2020.

[253] Md Azimul Haque, Seyoung Kee, Diego Rosas Villalva, Wee-Liat Ong, and Derya Baran. Halide perovskites: thermal transport and prospects for thermoelectricity. *Adv. Sci.*, 7(10):1903389, 2020.

[254] Huile Jin, Jun Li, James Iocozzia, Xin Zeng, Pai-Chun Wei, Chao Yang, Nan Li, Zhaoping Liu, Jr Hau He, Tiejun Zhu, et al. Hybrid organic–inorganic thermoelectric materials and devices. *Angew. Chem. Int. Ed.*, 58(43):15206–15226, 2019.

[255] Ashutosh Kumar, Preeti Bhumla, Taras Parashchuk, Stanislaw Baran, Saswata Bhattacharya, and Krzysztof T Wojciechowski. Engineering electronic structure and lattice dynamics to achieve enhanced thermoelectric performance of mn–sb co-doped gete. *Chemistry of Materials*, 33(10):3611–3620, 2021.

[256] Ashutosh Kumar, Preeti Bhumla, Duraisamy Sivaprahasam, Saswata Bhattacharya, and Nita Dragoe. Effect of crystal field engineering and fermi level optimization on thermoelectric properties of ge 1.01 te: Experimental investigation and theoretical insight. *Physical Review Materials*, 7(4):045402, 2023.

[257] Ashutosh Kumar, Preeti Bhumla, Artur Kosonowski, Karol Wolski, Szczepan Zapotoczny, Saswata Bhattacharya, and Krzysztof T Wojciechowski. Synergistic effect of work function and acoustic impedance mismatch for improved thermoelectric performance in gete-wc composite. *ACS Applied Materials & Interfaces*, 14(39):44527–44538, 2022.

[258] Li-Dong Zhao, Shih-Han Lo, Yongsheng Zhang, Hui Sun, Gangjian Tan, Ctirad Uher, Christopher Wolverton, Vinayak P Dravid, and Mercouri G Kanatzidis. Ultralow thermal conductivity and high thermoelectric figure of merit in snse crystals. *Nature*, 508(7496):373–377, 2014.

[259] Li-Dong Zhao, Gangjian Tan, Shiqiang Hao, Jiaqing He, Yanling Pei, Hang Chi, Heng Wang, Shengkai Gong, Huibin Xu, Vinayak P Dravid, et al. Ultrahigh power factor and thermoelectric performance in hole-doped single-crystal snse. *Science*, 351(6269):141–144, 2016.

[260] Kanishka Biswas, Jiaqing He, Ivan D Blum, Chun-I Wu, Timothy P Hogan, David N Seidman, Vinayak P Dravid, and Mercouri G Kanatzidis. High-performance bulk thermoelectrics with all-scale hierarchical architectures. *Nature*, 489(7416):414–418, 2012.

[261] Yanzhong Pei, Andrew F May, and G Jeffrey Snyder. Self-tuning the carrier concentration of pbte/ag_2te composites with excess ag for high thermoelectric performance. *Adv. Energy Mater.*, 1(2):291–296, 2011.

[262] Yanzhong Pei, Xiaoya Shi, Aaron LaLonde, Heng Wang, Lidong Chen, and G Jeffrey Snyder. Convergence of electronic bands for high performance bulk thermoelectrics. *Nature*, 473(7345):66–69, 2011.

[263] Yongan Yang, David K Taggart, Ming H Cheng, John C Hemminger, and Reginald M Penner. High-throughput measurement of the seebeck coefficient and the electrical conductivity of lithographically patterned polycrystalline pbte nanowires. *J. Phys. Chem. Lett.*, 1(20):3004–3011, 2010.

[264] Trevor P Bailey, Si Hui, Hongyao Xie, Alan Olvera, Pierre FP Poudeu, Xinfeng Tang, and Ctirad Uher. Enhanced zt and attempts to chemically stabilize cu_2se via sn doping. *J. Mater. Chem. A*, 4(43):17225–17235, 2016.

[265] Zhou Li, Chong Xiao, Shaojuan Fan, Yu Deng, Wenshuai Zhang, Bangjiao Ye, and Yi Xie. Dual vacancies: an effective strategy realizing synergistic optimization of thermoelectric property in bicuseo. *J. Am. Chem. Soc.*, 137(20):6587–6593, 2015.

[266] Dongwang Yang, Xianli Su, Yonggao Yan, Tiezheng Hu, Hongyao Xie, Jian He, Ctirad Uher, Mercouri G Kanatzidis, and Xinfeng Tang. Manipulating the combustion wave

during self-propagating synthesis for high thermoelectric performance of layered oxychalcogenide $bi_{1-x}pb_{x}cuseo$. *Chem. Mater.*, 28(13):4628–4640, 2016.

[267] Xin Qian, Xiaokun Gu, and Ronggui Yang. Lattice thermal conductivity of organic-inorganic hybrid perovskite $ch_3nh_3pbi_3$. *Appl. Phys. Lett.*, 108(6):063902, 2016.

[268] Mandvi Saxena, Pinku Roy, Megha Acharya, Imon Bose, Khagesh Tanwar, and Tanmoy Maiti. Enhanced thermoelectric figure-of-merit in environmentally benign $ba_{x}sr_{2-x}ticoo_6$ double perovskites. *Appl. Phys. Lett.*, 109(26):263903, 2016.

[269] Johan Klarbring, Olle Hellman, Igor A Abrikosov, and Sergei I Simak. Anharmonicity and ultralow thermal conductivity in lead-free halide double perovskites. *Phys. Rev. Lett.*, 125(4):045701, 2020.

[270] Un-Gi Jong, Yun-Sim Kim, Chol-Hyok Ri, Yun-Hyok Kye, Chol-Jin Pak, Stefaan Cottenier, and Chol-Jun Yu. Twofold rattling mode-induced ultralow thermal conductivity in vacancy-ordered double perovskite cs_2sni_6. *Chem. Commun.*, 58(26):4223–4226, 2022.

[271] Jarvist Moore Frost. Calculating polaron mobility in halide perovskites. *Phys. Rev. B*, 96(19):195202, 2017.

[272] Herbert Fröhlich. Electrons in lattice fields. *Adv. Phys.*, 3(11):325–361, 1954.

[273] Timo Thonhauser, Valentino R Cooper, Shen Li, Aaron Puzder, Per Hyldgaard, and David C Langreth. Van der waals density functional: Self-consistent potential and the nature of the van der waals bond. *Phys. Rev. B*, 76(12):125112, 2007.

[274] Alex M Ganose, Adam J Jackson, and David O Scanlon. sumo: Command-line tools for plotting and analysis of periodic* ab initio* calculations. *J. Open Source Softw.*, 3(28):717, 2018.

[275] Georg KH Madsen and David J Singh. Boltztrap. a code for calculating band-structure dependent quantities. *Comput. Phys. Commun.*, 175(1):67–71, 2006.

[276] Atsushi Togo, Laurent Chaput, and Isao Tanaka. Distributions of phonon lifetimes in brillouin zones. *Phys. Rev. B*, 91:094306, Mar 2015.

[277] M Gajdoš, K Hummer, G Kresse, J Furthmüller, and FJPRB Bechstedt. Linear optical properties in the projector-augmented wave methodology. *Phys. Rev. B*, 73(4):045112, 2006.

[278] Sabry G Moustafa, Apoorva Purohit, Andrew J Schultz, and David A Kofke. pyhma: A vasp post-processor for precise measurement of crystalline anharmonic properties using harmonically mapped averaging. *Comput. Phys. Commun.*, 258:107554, 2021.

[279] Muhammad Faizan, KC Bhamu, Ghulam Murtaza, Xin He, Neeraj Kulhari, Murefah Mana AL-Anazy, and Shah Haidar Khan. Electronic and optical properties of vacancy ordered double perovskites a_2bx_6 (a= rb, cs; b= sn, pd, pt; and x= cl, br, i): a first principles study. *Sci. Rep.*, 11(1):1–9, 2021.

[280] B Schupp, P Heines, A Savin, and H-L Keller. Crystal structures and pressure-induced redox reaction of $cs_2pdi_4.i_2$ to cs_2pdi_6. *Inorg. Chem.*, 39(4):732–735, 2000.

[281] Victor Moritz Goldschmidt. Die gesetze der krystallochemie. *Sci. Nat.*, 14(21):477–485, 1926.

[282] Qingde Sun and Wan-Jian Yin. Thermodynamic stability trend of cubic perovskites. *J. Am. Chem. Soc.*, 139(42):14905–14908, 2017.

[283] W Travis, ENK Glover, Hugo Bronstein, DO Scanlon, and RG Palgrave. On the application of the tolerance factor to inorganic and hybrid halide perovskites: a revised system. *Chem. Sci.*, 7(7):4548–4556, 2016.

[284] Robert D Shannon. Revised effective ionic radii and systematic studies of interatomic distances in halides and chalcogenides. *Acta Crystallographica A*, 32(5):751–767, 1976.

[285] Christopher J Bartel, Christopher Sutton, Bryan R Goldsmith, Runhai Ouyang, Charles B Musgrave, Luca M Ghiringhelli, and Matthias Scheffler. New tolerance factor to predict the stability of perovskite oxides and halides. *Sci. Adv.*, 5(2):eaav0693, 2019.

[286] Un-Gi Jong, Chol-Jun Yu, Yun-Hyok Kye, Song-Hyok Choe, Jin-Song Kim, and Yong-Guk Choe. Anharmonic phonons and phase transitions in the vacancy-ordered double perovskite $\mathrm{cs_2sni_6}$ from first-principles predictions. *Phys. Rev. B*, 99:184105, May 2019.

[287] Un-Gi Jong, Chol-Jun Yu, Yun-Hyok Kye, Yun-Sim Kim, Chol-Ho Kim, and Son-Guk Ri. A first-principles study on the chemical stability of inorganic perovskite solid solutions cs 1- x rb x pbi 3 at finite temperature and pressure. *J. Mater. Chem. A*, 6(37):17994–18002, 2018.

[288] Francis Dominic Murnaghan. Finite deformations of an elastic solid. *Am. J. Math.*, 59(2):235–260, 1937.

[289] O. Beckstein, J. E. Klepeis, G. L. W. Hart, and O. Pankratov. First-principles elastic constants and electronic structure of $\alpha - \mathrm{pt_2Si}$ and ptsi. *Phys. Rev. B*, 63:134112, Mar 2001.

[290] Félix Mouhat and François-Xavier Coudert. Necessary and sufficient elastic stability conditions in various crystal systems. *Phys. Rev. B*, 90(22):224104, 2014.

[291] WOLDEMAR Voigt. Lehrbuch der kristallphysik, 1910. *Leipzig etrived, Nov*, 29, 2016.

[292] Shuzhang Yang, Liang Wang, Shuai Zhao, Anmin Liu, Yi Zhou, Qianji Han, Fengyang Yu, Liguo Gao, Chu Zhang, and Tingli Ma. Novel lead-free material $\mathrm{cs_2pti_6}$ with narrow bandgap and ultra-stability for its photovoltaic application. *ACS Appl. Mater. Interfaces*, 12(40):44700–44709, 2020.

[293] Lei Zhou, Jin-Feng Liao, Zeng-Guang Huang, Xu-Dong Wang, Yang-Fan Xu, Hong-Yan Chen, Dai-Bin Kuang, and Cheng-Yong Su. All-inorganic lead-free $\mathrm{cs_2pdx_6}$ (x= br, i) perovskite nanocrystals with single unit cell thickness and high stability. *ACS Energy Lett.*, 3(10):2613–2619, 2018.

[294] Isabel Vazquez-Fernandez, Silvia Mariotti, Oliver S Hutter, Max Birkett, Tim D Veal, Theodore DC Hobson, Laurie J Phillips, Lefteris Danos, Pabitra K Nayak, Henry J Snaith, et al. Vacancy-ordered double perovskite $\mathrm{cs_2tei_6}$ thin films for optoelectronics. *Chem. Mater.*, 32(15):6676–6684, 2020.

[295] Animesh Bhui, Tanmoy Ghosh, Koushik Pal, Kewal Singh Rana, Kaushik Kundu, Ajay Soni, and Kanishka Biswas. Intrinsically low thermal conductivity in the n-type vacancy-ordered double perovskite $\mathrm{cs_2sni_6}$: Octahedral rotation and anharmonic rattling. *Chem. Mater.*, 34(7):3301–3310, 2022.

[296] Muhammad Sajjad, Qasim Mahmood, Nirpendra Singh, and J Andreas Larsson. Ultralow lattice thermal conductivity in double perovskite cs_2pti_6: a promising thermoelectric material. *ACS Appl. Energy Mater.*, 3(11):11293–11299, 2020.

[297] Muhammad Faizan, Shah Haidar Khan, Houari Khachai, Taieb Seddik, Saad Bin Omran, Rabah Khenata, Jiahao Xie, and Murefah mana AL-Anazy. Electronic, optical, and thermoelectric properties of perovskite variants a_2bx_6: Insight and design via first-principles calculations. *Int. J. Energy Res.*, 45(3):4495–4507, 2021.

[298] Ayelet Graff and Yaron Amouyal. Reduced thermal conductivity in niobium-doped calcium-manganate compounds for thermoelectric applications. *Appl. Phys. Lett.*, 105(18):181906, 2014.

[299] Weibing Chen and Jingbo Li. Origin of the low thermal conductivity of the thermoelectric material β-zn_4 sb_3: An ab initio theoretical study. *Appl. Phys. Lett.*, 98(24):241901, 2011.

[300] JS Dugdale and DKC MacDonald. Lattice thermal conductivity. *Phys. Rev.*, 98(6):1751, 1955.

[301] Sokseiha Muy, John C Bachman, Livia Giordano, Hao-Hsun Chang, Douglas L Abernathy, Dipanshu Bansal, Olivier Delaire, Satoshi Hori, Ryoji Kanno, Filippo Maglia, et al. Tuning mobility and stability of lithium ion conductors based on lattice dynamics. *Energy Environ. Sci.*, 11(4):850–859, 2018.

[302] SL Chodos, AM Black, and CD Flint. Vibronic spectra and lattice dynamics of cs_2mnf_6 and $a_{12}mivf_6$: $Mnf_2{}^{-6}$. *J. Chem. Phys.*, 65(11):4816–4824, 1976.

[303] John Bardeen, Leon N Cooper, and John Robert Schrieffer. Theory of superconductivity. *Phys. Rev.*, 108(5):1175, 1957.

[304] Manoj K Jana and Kanishka Biswas. Crystalline solids with intrinsically low lattice thermal conductivity for thermoelectric energy conversion. *ACS Energy Lett.*, 3(6):1315–1324, 2018.

[305] MI Katsnelson. Lattice dynamics: Anharmonic effects. *Encyclopedia of Condensed Matter Physics*, page 77, 2005.

[306] Suvodeep Paul, Saheb Karak, Annie Mathew, Ankita Ram, and Surajit Saha. Electron-phonon and phonon-phonon anharmonic interactions in 2h-mox$_2$ (x= s, te): A comprehensive resonant raman study. *Phys. Rev. B*, 104(7):075418, 2021.

[307] Wei Wang, Jiafa Sun, Bin Li, and Junqi He. Dynamical instability, strong anharmonicity and electron-phonon coupling in kos$_2$o$_6$: First-principles calculations. *AIP Adv.*, 7(9):095221, 2017.

[308] Joshua Leveillee, George Volonakis, and Feliciano Giustino. Phonon-limited mobility and electron–phonon coupling in lead-free halide double perovskites. *J. Phys. Chem. Lett.*, 12(18):4474–4482, 2021.

[309] Robert W Hellwarth and Ivan Biaggio. Mobility of an electron in a multimode polar lattice. *Phys. Rev. B*, 60(1):299, 1999.

[310] Jun Mao, Hangtian Zhu, Zhiwei Ding, Zihang Liu, Geethal Amila Gamage, Gang Chen, and Zhifeng Ren. High thermoelectric cooling performance of n-type mg3bi2-based materials. *Science*, 365(6452):495–498, 2019.

[311] Yu Xiao, Haijun Wu, Juan Cui, Dongyang Wang, Liangwei Fu, Yang Zhang, Yue Chen, Jiaqing He, Stephen J Pennycook, and Li-Dong Zhao. Realizing high performance n-type pbte by synergistically optimizing effective mass and carrier mobility and suppressing bipolar thermal conductivity. *Energy & Environmental Science*, 11(9):2486–2495, 2018.

[312] Lei Yang, Zhi-Gang Chen, Matthew S Dargusch, and Jin Zou. High performance thermoelectric materials: progress and their applications. *Advanced Energy Materials*, 8(6):1701797, 2018.

[313] Takao Mori. Novel principles and nanostructuring methods for enhanced thermoelectrics. *Small*, 13(45):1702013, 2017.

[314] Li Xie, Yongjin Chen, Ruiheng Liu, Erhong Song, Tong Xing, Tingting Deng, Qingfeng Song, Jianjun Liu, Renkui Zheng, Xiang Gao, et al. Stacking faults modulation for scattering optimization in gete-based thermoelectric materials. *Nano Energy*, 68:104347, 2020.

[315] Yuan Yu, Matteo Cagnoni, Oana Cojocaru-Mirédin, and Matthias Wuttig. Chalcogenide thermoelectrics empowered by an unconventional bonding mechanism. *Advanced Functional Materials*, 30(8):1904862, 2020.

[316] D Sivaprahasam, SB Chandrasekhar, S Kashyap, Ashutosh Kumar, and R Gopalan. Thermal conductivity of nanostructured fe0. 04co0. 96sb3 skutterudite. *Materials Letters*, 252:231–234, 2019.

[317] Ashutosh Kumar, Artur Kosonowski, Piotr Wyzga, and Krzysztof T Wojciechowski. Effective thermal conductivity of srbi4ti4o15-la0. 7sr0. 3mno3 oxide composite: Role of particle size and interface thermal resistance. *Journal of the European Ceramic Society*, 41(1):451–458, 2021.

[318] Ashutosh Kumar and Krzysztof T Wojciechowski. Effect of interface thermal resistance on thermoelectric properties of acoustically mismatched composite. *Journal of the European Ceramic Society*, 42(10):4227–4232, 2022.

[319] Artur Kosonowski, Ashutosh Kumar, Taras Parashchuk, Raul Cardoso-Gil, and Krzysztof T Wojciechowski. Thermal conductivity of pbte–cosb 3 bulk polycrystalline composite: role of microstructure and interface thermal resistance. *Dalton Transactions*, 50(4):1261–1273, 2021.

[320] Artur Kosonowski, Ashutosh Kumar, Karol Wolski, Szczepan Zapotoczny, and Krzysztof T Wojciechowski. Origin of electrical contact resistance and its dominating effect on electrical conductivity in pbte/cosb3 composite. *Journal of the European Ceramic Society*, 42(6):2844–2852, 2022.

[321] Binbin Jiang, Yong Yu, Juan Cui, Xixi Liu, Lin Xie, Jincheng Liao, Qihao Zhang, Yi Huang, Shoucong Ning, Baohai Jia, et al. High-entropy-stabilized chalcogenides with high thermoelectric performance. *Science*, 371(6531):830–834, 2021.

[322] Ashutosh Kumar, Diana Dragoe, David Berardan, and Nita Dragoe. Thermoelectric properties of high-entropy rare-earth cobaltates. *Journal of Materiomics*, 9(1):191–196, 2023.

[323] Yanzhong Pei, Aaron LaLonde, Shiho Iwanaga, and G Jeffrey Snyder. High thermoelectric figure of merit in heavy hole dominated pbte. *Energy & Environmental Science*, 4(6):2085–2089, 2011.

[324] Yinglu Tang, Zachary M Gibbs, Luis A Agapito, Guodong Li, Hyun-Sik Kim, Marco Buongiorno Nardelli, Stefano Curtarolo, and G Jeffrey Snyder. Convergence of multi-valley bands as the electronic origin of high thermoelectric performance in cosb3 skutterudites. *Nature materials*, 14(12):1223–1228, 2015.

[325] B Hinterleitner, I Knapp, M Poneder, Yongpeng Shi, H Müller, G Eguchi, C Eisenmenger-Sittner, M Stöger-Pollach, Y Kakefuda, N Kawamoto, et al. Thermoelectric performance of a metastable thin-film heusler alloy. *Nature*, 576(7785):85–90, 2019.

[326] Suresh Perumal, Subhajit Roychowdhury, and Kanishka Biswas. High performance thermoelectric materials and devices based on gete. *Journal of Materials Chemistry C*, 4(32):7520–7536, 2016.

[327] David G Cahill and RO Pohl. Heat flow and lattice vibrations in glasses. *Solid State Communications*, 70(10):927–930, 1989.

[328] Yanling Pei, Gangjian Tan, Dan Feng, Lei Zheng, Qing Tan, Xiaobing Xie, Shengkai Gong, Yue Chen, Jing-Feng Li, Jiaqing He, et al. Integrating band structure engineering with all-scale hierarchical structuring for high thermoelectric performance in pbte system. *Advanced Energy Materials*, 7(3):1601450, 2017.

[329] Jun Mao, Yixuan Wu, Shaowei Song, Qing Zhu, Jing Shuai, Zihang Liu, Yanzhong Pei, and Zhifeng Ren. Defect engineering for realizing high thermoelectric performance in n-type mg3sb2-based materials. *ACS Energy Letters*, 2(10):2245–2250, 2017.

[330] Hangtian Liu, Zhiyu Chen, Jing Tang, Yan Zhong, Xuming Guo, Fujie Zhang, and Ran Ang. High quality factor enabled by multiscale phonon scattering for enhancing thermoelectrics in low-solubility n-type pbte–cu2te alloys. *ACS Applied Materials & Interfaces*, 12(47):52952–52958, 2020.

[331] Xinyue Zhang, Juan Li, Xiao Wang, Zhiwei Chen, Jianjun Mao, Yue Chen, and Yanzhong Pei. Vacancy manipulation for thermoelectric enhancements in gete alloys. *Journal of the American Chemical Society*, 140(46):15883–15888, 2018.

[332] Xinyue Zhang, Zhonglin Bu, Siqi Lin, Zhiwei Chen, Wen Li, and Yanzhong Pei. Gete thermoelectrics. *Joule*, 4(5):986–1003, 2020.

[333] Di Wu, Li-Dong Zhao, Shiqiang Hao, Qike Jiang, Fengshan Zheng, Jeff W Doak, Haijun Wu, Hang Chi, Y Gelbstein, C Uher, et al. Origin of the high performance in gete-based thermoelectric materials upon bi2te3 doping. *Journal of the American Chemical Society*, 136(32):11412–11419, 2014.

[334] Suresh Perumal, Pavithra Bellare, U Sandhya Shenoy, Umesh V Waghmare, and Kanishka Biswas. Low thermal conductivity and high thermoelectric performance in sb and bi codoped gete: complementary effect of band convergence and nanostructuring. *Chemistry of Materials*, 29(24):10426–10435, 2017.

[335] Luo Yue, Wenlin Cui, Shuqi Zheng, Yue Wu, Lijun Wang, Pengpeng Bai, and Ximeng Dong. Band engineering and thermoelectric performance optimization of p-type gete-based alloys through ti/sb co-doping. *The Journal of Physical Chemistry C*, 124(10):5583–5590, 2020.

[336] Takao Mori, David Berthebaud, Toshiyuki Nishimura, Akiko Nomura, Toetsu Shishido, and Kazuo Nakajima. Effect of zn doping on improving crystal quality and thermoelectric properties of borosilicides. *Dalton Transactions*, 39(4):1027–1030, 2010.

[337] JK Lee, MW Oh, BS Kim, BK Min, HW Lee, and SD Park. Influence of mn on crystal structure and thermoelectric properties of gete compounds. *Electronic Materials Letters*, 10:813–817, 2014.

[338] Jing Shuai, Yang Sun, Xiaojian Tan, and Takao Mori. Manipulating the ge vacancies and ge precipitates through cr doping for realizing the high-performance gete thermoelectric material. *Small*, 16(13):1906921, 2020.

[339] Koichi Momma and Fujio Izumi. Vesta 3 for three-dimensional visualization of crystal, volumetric and morphology data. *Journal of applied crystallography*, 44(6):1272–1276, 2011.

[340] K Parlinski, ZQ Li, and Y Kawazoe. First-principles determination of the soft mode in cubic zro 2. *Physical Review Letters*, 78(21):4063, 1997.

[341] Zihang Liu, Jifeng Sun, Jun Mao, Hangtian Zhu, Wuyang Ren, Jingchao Zhou, Zhiming Wang, David J Singh, Jiehe Sui, Ching-Wu Chu, et al. Phase-transition temperature suppression to achieve cubic gete and high thermoelectric performance by bi and mn codoping. *Proceedings of the National Academy of Sciences*, 115(21):5332–5337, 2018.

[342] Urszula D Wdowik, Krzysztof Parlinski, Stéphane Rols, and Tapan Chatterji. Soft-phonon mediated structural phase transition in gete. *Physical Review B*, 89(22):224306, 2014.

[343] C Wood. Materials for thermoelectric energy conversion. *Reports on progress in physics*, 51(4):459, 1988.

[344] Subhajit Roychowdhury, Manisha Samanta, Suresh Perumal, and Kanishka Biswas. Germanium chalcogenide thermoelectrics: electronic structure modulation and low lattice thermal conductivity. *Chemistry of Materials*, 30(17):5799–5813, 2018.

[345] Yanzhong Pei, Heng Wang, and GJ Snyder. Thermoelectric materials: band engineering of thermoelectric materials (adv. mater. 46/2012). *Advanced Materials*, 24(46):6124–6124, 2012.

[346] Yang Jin, Yu Xiao, Dongyang Wang, Zhiwei Huang, Yuting Qiu, and Li-Dong Zhao. Realizing high thermoelectric performance in gete through optimizing ge vacancies and manipulating ge precipitates. *ACS Applied Energy Materials*, 2(10):7594–7601, 2019.

[347] Suresh Perumal, Subhajit Roychowdhury, and Kanishka Biswas. Reduction of thermal conductivity through nanostructuring enhances the thermoelectric figure of merit in ge 1- x bi x te. *Inorganic Chemistry Frontiers*, 3(1):125–132, 2016.

[348] Heng Wang, Anek Charoenphakdee, Ken Kurosaki, Shinsuke Yamanaka, and G Jeffrey Snyder. Reduction of thermal conductivity in pbte: Tl by alloying with tlsbt e 2. *Physical Review B*, 83(2):024303, 2011.

[349] Xiaoxiao Qiu, Qi Zheng, Xiaofang Lu, Shengjie Fan, Xiying Zhou, Lianjun Wang, and Wan Jiang. Effect of bi doping on thermoelectric properties of ge0. 90- xpb0. 10bixte compounds. *Materials Science in Semiconductor Processing*, 109:104955, 2020.

[350] Jiaqing He, Steven N Girard, Mercouri G Kanatzidis, and Vinayak P Dravid. Microstructure-lattice thermal conductivity correlation in nanostructured pbte0. 7s0. 3 thermoelectric materials. *Advanced Functional Materials*, 20(5):764–772, 2010.

[351] Debattam Sarkar, Tanmoy Ghosh, Ananya Banik, Subhajit Roychowdhury, Dirtha Sanyal, and Kanishka Biswas. Highly converged valence bands and ultralow lattice thermal conductivity for high-performance snte thermoelectrics. *Angewandte Chemie International Edition*, 59(27):11115–11122, 2020.

[352] Wei-Di Liu, Zhi-Gang Chen, and Jin Zou. Eco-friendly higher manganese silicide thermoelectric materials: progress and future challenges. *Advanced Energy Materials*, 8(19):1800056, 2018.

[353] Xinyue Zhang and Yanzhong Pei. Manipulation of charge transport in thermoelectrics. *npj Quantum Materials*, 2(1):68, 2017.

[354] Luo Yue, Teng Fang, Shuqi Zheng, Wenlin Cui, Yue Wu, Siyi Chang, Lijun Wang, Pengpeng Bai, and Huaizhou Zhao. Cu/sb codoping for tuning carrier concentration and thermoelectric performance of gete-based alloys with ultralow lattice thermal conductivity. *ACS Applied Energy Materials*, 2(4):2596–2603, 2019.

[355] Ashutosh Kumar, Ravi Kumar, and Dillip K Satapathy. Bi2se3-pvdf composite: A flexible thermoelectric system. *Physica B: Condensed Matter*, 593:412275, 2020.

[356] Gangjian Tan, Shiqiang Hao, Songting Cai, Trevor P Bailey, Zhongzhen Luo, Ido Hadar, Ctirad Uher, Vinayak P Dravid, Christopher Wolverton, and Mercouri G Kanatzidis. All-scale hierarchically structured p-type pbse alloys with high thermoelectric performance enabled by improved band degeneracy. *Journal of the American Chemical Society*, 141(10):4480–4486, 2019.

[357] Suresh Perumal, Subhajit Roychowdhury, Devendra S Negi, Ranjan Datta, and Kanishka Biswas. High thermoelectric performance and enhanced mechanical stability of p-type ge1–x sb x te. *Chemistry of Materials*, 27(20):7171–7178, 2015.

[358] Zheng Zheng, Xianli Su, Rigui Deng, Constantinos Stoumpos, Hongyao Xie, Wei Liu, Yonggao Yan, Shiqiang Hao, Ctirad Uher, Chris Wolverton, et al. Rhombohedral to

cubic conversion of gete via mnte alloying leads to ultralow thermal conductivity, electronic band convergence, and high thermoelectric performance. *Journal of the American Chemical Society*, 140(7):2673–2686, 2018.

[359] Kostiantyn Shportko, Stephan Kremers, Michael Woda, Dominic Lencer, John Robertson, and Matthias Wuttig. Resonant bonding in crystalline phase-change materials. *Nature materials*, 7(8):653–658, 2008.